

Dissertation zur Erlangung des Doktorgrades
der Fakultät für Chemie und Pharmazie
der Ludwig-Maximilians-Universität München

Structural Basis of Translational Recycling and Bacterial Ribosome Rescue

Hanna Kratzat

aus

Hamburg, Deutschland

2021

Erklärung

Diese Dissertation wurde im Sinne von § 7 der Promotionsordnung vom 28. November 2011 von Herrn Prof. Dr. Roland Beckmann betreut.

Eidesstattliche Versicherung

Diese Dissertation wurde eigenständig und ohne unerlaubte Hilfe erarbeitet.

München, 20.12.2021

Hanna Kratzat

Dissertation eingereicht am 20.12.2021

1. Gutachter: Prof. Dr. Roland Beckmann
2. Gutachter: Prof. Dr. Karl-Peter Hopfner

Mündliche Prüfung am 09.02.2022

List of publications

Molecular analysis of the ribosome recycling factor ABCE1 bound to the 30S post-splitting complex.

Nürnberg-Goloub E*, [Kratzat H*](#), Heinemann H*, Heuer A, Kötter P, Berninghausen O, Becker T, Tampé R, Beckmann R.

EMBO J. 2020 May 4;39(9):e103788. doi: 10.15252/embj.2019103788. Epub 2020 Feb 17. PMID: 32064661; PMCID: PMC7196836.

Structure and function of yeast Lso2 and human CCDC124 bound to hibernating ribosomes.

Wells JN*, Buschauer R*, Mackens-Kiani T, Best K, [Kratzat H](#), Berninghausen O, Becker T, Gilbert W, Cheng J, Beckmann R.

PLoS Biol. 2020 Jul 20;18(7):e3000780. doi: 10.1371/journal.pbio.3000780. PMID: 32687489; PMCID: PMC7392345.

An ATP-dependent partner switch links flagellar C-ring assembly with gene expression.

Blagotinsek V*, Schwan M*, Steinchen W, Mrusek D, Hook JC, Rossmann F, Freibert SA, [Kratzat H](#), Murat G, Kressler D, Beckmann R, Beeby M, Thormann KM, Bange G.

Proc Natl Acad Sci U S A. 2020 Aug 25;117(34):20826-20835. doi: 10.1073/pnas.2006470117. Epub 2020 Aug 11. PMID: 32788349; PMCID: PMC7456076.

Structural basis for translational shutdown and immune evasion by the Nsp1 protein of SARS-CoV-2.

Thoms M*, Buschauer R*, Ameismeier M*, Koepke L, Denk T, Hirschenberger M, [Kratzat H](#), Hayn M, Mackens-Kiani T, Cheng J, Straub JH, Stürzel CM, Fröhlich T, Berninghausen O, Becker T, Kirchhoff F, Sparrer KMJ, Beckmann R.

Science. 2020 Sep 4;369(6508):1249-1255. doi: 10.1126/science.abc8665. Epub 2020 Jul 17. PMID: 32680882; PMCID: PMC7402621.

A structural inventory of native ribosomal ABCE1-43S pre-initiation complexes.

[Kratzat H*](#), Mackens-Kiani T*, Ameismeier M, Potocnjak M, Cheng J, Dacheux E, Namane A, Berninghausen O, Herzog F, Fromont-Racine M, Becker T, Beckmann R.

EMBO J. 2021 Jan 4;40(1):e105179. doi: 10.15252/embj.2020105179. Epub 2020 Dec 8. PMID: 33289941; PMCID: PMC7780240.

Ribosome collisions in bacteria promote ribosome rescue by triggering mRNA cleavage by SmrB.

Saito K*, Kratzat H, Campbell A, Buschauer R, Burroughs AM, Aravind L, Beckmann R, Green R, Buskirk AR.

biorxiv 2021 Aug 16; doi: 10.1101/2021.08.16.456513.

Ribosome collisions induce mRNA cleavage and ribosome rescue in bacteria.

Saito K*, Kratzat H*, Campbell A, Buschauer R, Burroughs AM, Berninghausen O, Aravind L, Green R, Beckmann R, Buskirk AR.

Nature. in press; doi: <https://doi.org/10.1038/s41586-022-04416-7>

Inhibition of SRP-dependent protein secretion by the bacterial alarmone (p)ppGpp.

Czech L*, Mais CN*, Kratzat H, Sarmah P, Giammarinaro P, Freibert SA, Esser HF, Musial J, Berninghausen O, Steinchen W, Beckmann R, Koch HG, Bange G.

Nat Commun. 2022 Feb 25;13(1):1069. doi: 10.1038/s41467-022-28675-0. PMID: 35217658.

* These authors contributed equally to this work.

Contributions report

This dissertation contains research that was conducted from November 2016 to November 2021 at the Gene Center of the Ludwig-Maximilians University in Munich, in the Laboratory of Prof. Roland Beckmann. Several projects are collaborative work with scientists from the labs of Prof. Gert Bange (Philipps University, Marburg), Prof. Robert Tampé (Goethe University, Frankfurt), Prof. Micheline Fromont-Racine (Institut Pasteur, Paris, France), and Prof. Rachel Green (Johns Hopkins University School of Medicine, Baltimore, US).

Publication 1 (Nürenberg-Goloub *et al.*, 2020)

In this publication, a structural and functional analysis of the ABCE1-bound 30S post-splitting complex was performed. I was involved in sample optimization and preparation for analysis by cryo-EM and I processed the cryo-EM data. Further, I built and refined molecular models and together with all authors interpreted the structure. Based on the results, I helped to design mutational and functional studies. I prepared all structural figures, the cartoon summarizing our findings, and I was involved in the preparation of the manuscript.

Publication 2 (Kratzat *et al.*, 2021)

This publication reports several cryo-EM structures of native ABCE1-bound initiation complexes from yeast and human and discusses their role in the process of translation initiation. I assisted in cryo-EM data processing, prepared and refined molecular models, and analyzed the structures. I helped with protein purifications to perform splitting assays. Further, I prepared all structural figures of the publication and was involved in writing the manuscript.

Publication 3 (Saito *et al.*, 2021)

This publication describes for the first time how ribosome collisions promote ribosome rescue in bacteria. I created and prepared all disome samples for *in vitro* splitting assays and for cryo-EM analysis. I processed all cryo-EM data sets. Further, I was involved in the preparation of the figures and the manuscript.

SUMMARY

In the last step of gene expression, a messenger RNA (mRNA) sequence is translated into a polypeptide. This highly regulated and dynamic process is carried out by the ribosome, a ribonucleoprotein complex composed of two unequal subunits. The translation cycle is initiated when the small ribosomal subunit (SSU) binds to an mRNA and recognizes the start codon of the open reading frame (ORF). Then the large ribosomal subunit (LSU) joins and the ribosome starts moving along the mRNA. A protein is synthesized until the ribosome reaches a stop codon. A cell needs thousands (prokaryotes) or millions (eukaryotes) of ribosomes for protein production and spends enormous amounts of energy on the assembly of this macromolecular machinery. Therefore, it is crucial to recycle the machinery after each successful round of translation. The recycling step allows release of mRNA, transfer RNA (tRNA) and the synthesized polypeptide from ribosomal subunits and subsequent binding of the next mRNA for protein synthesis.

The first part of this dissertation includes studies of the highly conserved and essential ribosome recycling factor ATP binding cassette (ABC) Subfamily E Member 1 (ABCE1). In eukaryotes and archaea, ABCE1 binds the ribosome and in concert with an A-site factor and splits the ribosome into large and small subunits. ABCE1 harbors two nucleotide binding sites (NBSs), which are formed at the interface of two nucleotide binding domains (NBDs). Prior to this work, the ABCE1-bound pre-splitting complex, as well as the ABCE1-bound post-splitting complex, had been visualized by cryo-electron microscopy (cryo-EM) at medium resolution. This structural analysis combined with functional studies led to a model for the mechanism of the splitting event. ATP-binding and the closure of the NBSs lead to repositioning of the iron-sulfur cluster domain, which results in collision with the A-site factor and ribosome splitting. Yet, how conformational changes during the splitting event are triggered and communicated to the NBSs of ABCE1, was not understood. To gain molecular insights into this process, a structure of a fully nucleotide-occluded (closed) state of ABCE1 bound to the archaeal 30S post-splitting complex was solved by cryo-EM. At a resolution of 2.8 Å a detailed molecular analysis of ABCE1 was performed and confirmed by a combination of mutational and functional studies. This allowed to propose a refined model of how the ATPase cycle is linked to ribosome splitting and which role the different domains of ABCE1 play.

In eukaryotes, the recycling phase is directly linked to translation initiation via the SSU. After being released from the mRNA 3' end, the SSU can engage with another or even the same mRNA at the 5' end. The recycling factor ABCE1 was found to be associated with initiation complexes, but whether it plays a role in initiation was not clear. Using cryo-EM, structures of native ABCE1-containing initiation

complexes were solved and intensive 3D classification allowed to distinguish different stages of initiation, during which ABCE1 may play a role. Surprisingly, ABCE1 adopted a previously unknown state for ABC-type ATPases that was termed “hybrid state”. Here, the NBSI is in a half open state with ADP bound and the NBSII is in a closed state with ATP bound. Further, eukaryotic initiation factor 3j (eIF3j) was found to stabilize this hybrid conformation via its N-terminus. Since eIF3j had already been described to assist ABCE1 in ribosome dissociation, *in vitro* splitting assays were performed demonstrating that eIF3j indeed actively enhances the splitting reaction. On top of this, the high-resolution structure allowed to describe the interaction network of eIF3j with the ribosome, initiation factors (IFs), and ABCE1.

Independent of ABCE1, the structures presented here allowed to provide an improved molecular model of the human 43S pre-initiation complex (PIC) and to analyze its sophisticated interaction network. In particular, new molecular insights into the large eIF3 complex encircling the 43S PIC, and the eIF2 ternary complex delivering the initiator tRNA are provided.

Equally important as canonical recycling is the recognition and recycling of ribosomes that result from translational failure. Aberrant translation elongation and ribosome stalling can be caused by a plethora of different stresses. In bacterial cells, multiple rescue systems are known such as trans-translation or alternative ribosome rescue factor-mediated termination, which act on ribosome nascent chain complexes with an empty A-site (non-stop complexes). It has been a long standing question how ribosomes that are stalled in the middle of an ORF (no-go complexes) are recognized and recycled. The second part of this dissertation reports a new bacterial rescue system that acts on no-go complexes. In eukaryotes, the concept of ribosome collisions as a trigger for ribosome rescue has been studied extensively. Here, it was found that a similar mechanism exists in bacteria and thus a structural analysis of collided disomes in *E. coli* and *B. subtilis* was conducted. In a genetic screen, the endonuclease SmrB was identified as one candidate for a collision sensor. Structural analysis of SmrB-bound disomes elucidated how this rescue factor is recruited to collided ribosomes. Its SMR domain binds to the disome interface between the stalled and the collided ribosome in close proximity to the mRNA and in a position ideal to perform endonucleolytic cleavage. Such cleavage then results in non-stop complexes that can be recycled by the pathways mentioned above. In conclusion, this work provides mechanistic insights into how a cell distinguishes stalled ribosomes from actively translating ribosomes and characterizes a novel ribosome rescue pathway.

Abbreviations

3D	three dimensional
A	adenine
aa	amino acid and their single or three letter code
ABC	ATP-binding cassette
aa-tRNA	aminoacyl transfer RNA
AMP-PNP	adenylyl-imidodiphosphate; non-hydrolysable analogue of ATP
A-site	aminoacyl-tRNA binding site on the ribosome
ATP	adenosine triphosphate
<i>B. subtilis</i>	<i>Bacillus subtilis</i>
C	cytosine
cryo-EM	cryo-electron microscopy
CTD	C-terminal domain
DNA	deoxyribonucleic acid
<i>E. coli</i>	<i>Escherichia coli</i>
EF	elongation factor
E-site	exit site for tRNAs on the ribosome
FeSD	iron-sulfur cluster domain
fMET	formyl-methionine
G	guanine
GAP	GTPase activating protein
GGQ motif	glycine-glycine-glutamine motif
GMP-PNP	guanylyl-imidodiphosphate; non-hydrolysable analogue of GTP
GTP	guanosine-triphosphate
h#	rRNA helix of the SSU
H#	rRNA helix of the LSU
HLH	helix-loop-helix
IF	initiation factor
IC	initiation complex
kDa	kilodalton
LSU	large ribosomal subunit
mRNA	messenger RNA
NBD	nucleotide binding domain
NBS	nucleotide binding site

nt	nucleotide
NTD	N-terminal domain
ORF	open reading frame
PABP	poly-A binding proteins
Pi	inorganic phosphate
PIC	pre-initiation complex
PTC	peptidyl transferase center
post-SC	post-splitting complex
pre-SC	pre-splitting complex
P-site	peptidyl-tRNA binding site on the ribosome
RBS	ribosome binding site
RF	release factor
RNA	ribonucleic acid
RNC	ribosome nascent chain complex
RQC	ribosome-associated quality control
rRNA	ribosomal RNA
RRM	RNA-recognition motif
<i>S. cerevisiae</i>	<i>Saccharomyces cerevisiae</i>
SD	Shine-Dalgarno sequence
SMR	small MutS-related
SRL	sarcin-ricin loop
<i>S. solfataricus</i>	<i>Sulfolobus solfataricus</i>
SSU	small ribosomal subunit
T	thymine
TAP	tandem affinity purification
<i>T. celer</i>	<i>Thermococcus celer</i>
tRNA	transfer RNA
tRNA _i	initiator tRNA
<i>T. thermophilus</i>	<i>Thermus thermophilus</i>
U	uracil
UTR	untranslated region
wt	wild-type

List of Figures

	page
Figure 1: Structure of the prokaryotic 70S ribosome.	2
Figure 2: Schematic overview of eukaryotic cap-dependent translation initiation.	9
Figure 3 Structure of ABCE1 and conformational changes of ABCE1 during ribosome splitting.	23
Figure 4: Schematic overview of ribosome rescue and ribosome-associated quality control.	27
Figure 5: Overview of initiation complexes.	45

Table of contents

List of publications	III
Contributions report	V
SUMMARY	VI
Abbreviations	VIII
List of Figures	X
Table of contents	XI
1. INTRODUCTION	1
1.1 The Ribosome	1
1.2 The Translation Cycle	6
1.2.1 Initiation	6
1.2.2 Elongation	15
1.2.3 Termination	17
1.2.4 Recycling	19
1.3 Ribosome rescue and ribosome-associated quality control pathways	26
1.3.1 Ribosome rescue and RQC in bacteria	26
1.3.2 Ribosome rescue and RQC in eukaryotes	30
2. AIMS AND OBJECTIVES	34
2.1 Structural analysis of ABCE1 in ribosome recycling and translation initiation	34
2.2 Structural basis of ribosome rescue in bacteria	35
3. SUMMARY AND DISCUSSION OF PUBLICATIONS	36
Publication 1 Molecular analysis of the ribosome recycling factor ABCE1 bound to the 30S post-splitting complex	36
Publication 2 Structural inventory of native ribosomal ABCE1-43S pre-initiation complexes.	40
Publication 3 Ribosome collisions in bacteria promote ribosome rescue by triggering mRNA cleavage by SmrB.	46
4. REFERENCES	51
5. ACKNOWLEDGEMENTS	83
6. PUBLICATIONS OF THIS DISSERTATION	85

1. INTRODUCTION

1.1 The Ribosome

In the conserved cellular process of protein translation, genetic information carried within the sequence of a messenger RNA (mRNA) is translated into an amino acid (aa) sequence of a protein (Crick, 1958, 1970). The central unit of this process is a megadalton RNA-protein complex – the ribosome. The ribosome is a molecular machinery, whose special architecture creates a confined space to catalyze the reaction and bind necessary factors. The following chapter describes its architecture and briefly summarize how a structural understanding of this machinery emerged over the last two decades.

The ribosome consists of two unequal subunits, often named by their sedimentation velocity in Svedberg units (S). The small subunit (SSU), 30S in bacteria and archaea and 40S in eukaryotes, harbors the mRNA binding channel and the decoding center, where codon nucleotides of the mRNA are exposed for selection of anticodons present on aa-charged transfer RNAs (tRNA) (Ogle *et al*, 2001; Schlutzen *et al*, 2000; Yusupova *et al*, 2001). A tRNA molecule fulfills its function of decoding by base pairing with three nucleotides of the mRNA and carrying the corresponding aa (Carter *et al*, 2000; Crick *et al*, 1961; Hoagland *et al*, 1958; Ogle *et al*, 2001; VanLoock *et al*, 2000). The tRNA specific aa is linked to the RNA molecule by an ester bond between the aa carboxyl group and the tRNA 3'-OH group, which is catalyzed by specific aminoacyl-tRNA synthetases (Gomez & Ibba, 2020; Hoagland *et al*, 1958; Pang *et al*, 2014). In bacteria, like for example the model organism *Escherichia coli* (*E. coli*), the SSU consists of a 1,542 nucleotide long ribosomal RNA (16S rRNA) and 21 different ribosomal proteins (numbers refer to *E. coli*). The 16S rRNA folds into four distinct domains, which together with the ribosomal proteins constitute the characteristic shape of the SSU with the structural landmarks “body”, “platform”, “shoulder”, “head”, and “beak” (Figure 1). The mRNA channel is positioned between head and body and during translation, the mRNA enters the SSU between head and shoulder. The entry site is formed like a latch, which surrounds the mRNA and elongates the curved mRNA channel. The mRNA exit is located between head and platform (Frank *et al*, 1995; Schlutzen *et al*, 2000; Wilson & Cate, 2012; Wimberly *et al*, 2000; Yusupova *et al*, 2001). In total, roughly 30 nucleotides are bound within the ribosomal mRNA channel (Yusupova *et al*, 2001).

On the large subunit (LSU), 50S in bacteria and archaea and 60S in eukaryotes, the aminoacyl end of the incoming tRNA and the peptidyl tRNA are positioned in the peptidyl transferase center (PTC). Further, the LSU forms the peptide exit tunnel, in which the nascent peptides grow and then exit the ribosome. The tunnel and the PTC are mainly formed by the 2,904 nucleotides long RNA (23S rRNA in *E. coli*) (Ban *et al*, 2000; Harms *et al*, 2001; Polacek & Mankin, 2005; Rodnina *et al*, 2007). Since the

catalytic center, as well as the decoding center, are formed by rRNA, the ribosome is considered as a ribozyme (Ban *et al*, 2000; Nissen *et al*, 2000; Schmeing *et al*, 2002; Steitz & Moore, 2003). Additionally, the LSU consists of a 5S rRNA and 33 different proteins (in *E. coli*), which together with the 23S rRNA form a hemispherical body with protuberances. Structural landmarks of the LSU are the “central protuberance”, the L1-stalk” and the “L7/L12-stalk” (“P-stalk” in eukaryotes) (Figure 1) (Frank *et al*, 1991; Radermacher *et al*, 1987; Yusupov *et al*, 2001).

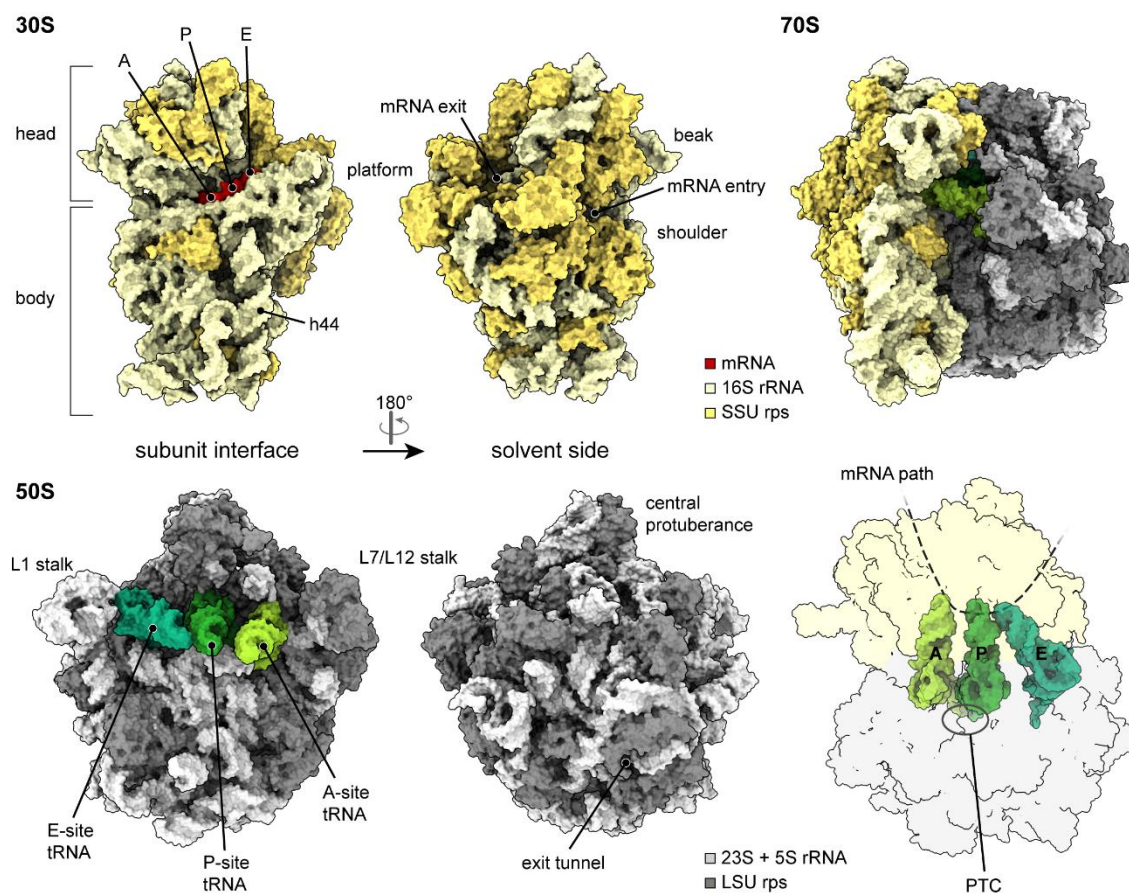


Figure 1: Structure of prokaryotic 70S ribosome. The ribosome consists of the 30S small ribosomal subunit (SSU) and the 50S large ribosomal subunit (LSU). Molecular models of the *E. coli* ribosome (PDB: 7K00, 4V4I, 5NWY) are displayed as surface representation. The small subunit is colored in yellow and the large subunit in grey, both with the darker color for ribosomal proteins and the lighter color for ribosomal RNA (rRNA). Structural landmarks as well as the positions of the peptidyl transferase center (PTC), exit tunnel, and mRNA path are labeled. The tRNAs bind to ribosomal A- (aminoacylation), P- (peptidyl), and E- (exit) sites that are located on the subunit interface of both subunits.

Together the subunits form a 70S ribosome in prokaryotes and archaea or 80S ribosome in eukaryotes. The interaction of the subunits creates an intersubunit space, to which tRNAs are delivered by translation factors and in turn interact with mRNA (Yusupov *et al*, 2001; Schuwirth *et al*, 2005; Selmer

et al, 2006). The unidirectional and rapid movement of mRNA and tRNA through the complex is a defined sequence of large and small conformational rearrangements. This includes for example opening and closing of the L1 stalk and movement of the SSU with respect to the LSU (Blanchard *et al*, 2004; Dunkle *et al*, 2011; Frank & Agrawal, 2000; Ogle *et al*, 2001). Different states during the translation process are defined by the orientation of the subunits towards each other and the way tRNAs are bound within the complex. Both subunits have three tRNA binding sites (A, P and E) located at the intersubunit sites (Figure 1). The aminoacyl tRNA binds to the A-site, the peptidyl tRNA to the P-site, and the dissociation of tRNA occurs from the exit (E) site (Agrawal *et al*, 1996; Selmer *et al*, 2006; Yusupov *et al*, 2001).

Both subunits have gained a lot in complexity during evolution. In this regard, the ribosomal structure can be divided into a highly conserved core composed mostly of rRNA and harboring the main functional sites and the surrounding periphery. In eukaryotes and even more so in mammals, the solvent sides of the subunits are decorated with additional ribosomal proteins, rRNA expansion segments (ES) and variable regions (Anger *et al*, 2013; Ben-Shem *et al*, 2011; Melnikov *et al*, 2012). This is also represented in the increased molecular weight, 2.3 MDa in bacteria to 4.3 MDa in higher eukaryotes, as well as the protein-to-rRNA ratio, which for the SSU is 1:2 in bacteria to 1:1 in eukaryotes (Melnikov *et al*, 2012; Wilson & Cate, 2012). Eukaryotic ribosomes contain over 1,000 more nucleotides than bacterial ribosomes and around 80 ribosomal proteins, of which 34 have a homolog in bacteria.

One example for how ribosomes have evolved differently is the mRNA entry and exit channel. As the mechanism to recruit mRNA to the ribosome is fundamentally different between bacteria and eukaryotes (see Chapter 1.2.1 Initiation), the structural architecture has adapted to its function. At the mRNA exit region in bacteria, bacteria-specific proteins surround the rRNA that recognizes the SD sequence of the mRNA. In eukaryotes, this part of the 18S rRNA is shortened and the mRNA exit contains eukaryotic-specific proteins. The conserved helix 16 (h16) at the mRNA entry is kept in one conformation by ribosomal proteins in bacteria but can adopt multiple conformations in eukaryotes. This flexibility allows initiation factors (IFs) to control whether the latch is in an open or closed conformation and thus can regulate mRNA scanning (Melnikov *et al*, 2012).

The analysis of the rRNA sequence itself has led to the discovery of archaea as a phylogenetically distinct third branch of life (Woese *et al*, 1990). Although archaeal ribosomes are very similar to bacterial ribosomes in size, the primary structure of the rRNAs and the ribosomal proteins are closer to eukaryotes (Lecompte *et al*, 2002; Timsit *et al*, 2021). Moreover, the archaeal and eukaryotic translation systems share several translation factors. Still, each kingdom of life has its own ribosomal

features. Because archaea can adapt to harsh environmental conditions, their ribosome structures are often more rigid and thus archaeal subunits were used early on for structural studies (Ban *et al*, 2000). Later, the structural analysis of the full ribosome revealed several copies of certain ribosomal proteins in archaea, which are absent in eukaryotes and bacteria. Overall, archaeal ribosomes exhibit an intermediate complexity compared to bacterial and eukaryotic counterparts (Armache *et al*, 2013; Becker *et al*, 2012).

Gaining knowledge about the architecture of the ribosome helped to draw a more and more detailed picture of the process of protein translation. A major breakthrough in the early 21st century was when crystal structures of bacterial and archaeal subunits were solved by X-ray crystallography (Ban *et al*, 2000; Wimberly *et al*, 2000; Schluenzen *et al*, 2000). These models helped to interpret low-resolution cryo-electron microscopy (cryo-EM) structures (Frank *et al*, 1995; Gabashvili *et al*, 2000; Malhotra *et al*, 1998; Matadeen *et al*, 1999; Stark *et al*, 1995) and could be used to solve X-ray crystallography structures of the empty *E. coli* ribosome at 3.5 Å resolution (Schuwirth *et al*, 2005) and the *T. thermophilus* ribosome in complex with mRNA and tRNA bound at 5.5 Å and 2.8 Å resolution (Selmer *et al*, 2006; Yusupov *et al*, 2001). For the first time, the intricate network of rRNA and proteins could be visualized. Moreover, interactions between the subunits, as well as interactions of the ribosome with mRNA and tRNA, could be described at molecular level. At the same time, cryo-EM had already been used to study the dynamics of the translation process. With this technique different functional states of ribosomes as well as their more flexible regions could be visualized (Connell *et al*, 2007; Frank & Agrawal, 2000; Frank, 2001). Yet, it took another decade in which cryo-EM techniques and software improved tremendously until cryo-EM structures could be visualized at resolutions similar to X-ray crystallography. This “resolution revolution” could mainly be attributed to higher speed and sensitivity of detectors. Electrons are sensed directly and not convert into photons first. Also, faster readout allowed to track and correct for specimen movements. Combined with improved imaging processing procedures, this had a huge impact on the field of structural biology (Kühlbrandt, 2014). Cryo-EM supersedes X-ray crystallography as the technique allows to computationally separate conformational and compositional states. Moreover, it only requires small amounts of samples, which not necessarily need to be homogeneous. Therefore, the ribosome emerged as a perfect specimen for cryo-EM. Over the last ten years the technique allowed to visualize dynamic ribosomal processes in different species and get a deeper understanding of the translational machinery and its interactome (Brown & Shao, 2018).

Today, the Electron Microscopy Data Bank (EMDB; www.emdataresource.org) contains over 1500 ribosome structures, and still, important questions remain to be answered as the ribosome is intertwined in so many crucial cellular pathways. Even at the core of the translation process, certain

details need to be discovered. This is especially true for short-lived intermediates and transient processes. Here, structural studies combined with biochemical and spectroscopic approaches will likely play an important role in finding answers and posing new questions.

1.2 The Translation Cycle

Each round of translation can be divided into four main phases, in which the ribosome binds to an mRNA and selects the start codon of an open reading frame (ORF) (initiation), translates it to protein (elongation) until it reaches a stop codon (termination), and is released from the mRNA and the newly synthesized protein (recycling). The following chapters will describe each phase in more detail and highlight differences that have evolved between the three different domains of life. A more thorough characterization of this process is for example reviewed by Sokabe and Fraser (Sokabe & Fraser, 2019), and Weisser and Ban (Weisser & Ban, 2019) for eukaryotes, and by Rodnina (Rodnina, 2018) for prokaryotes.

1.2.1 Initiation

The initial phase of translation assembles first the SSU and then the LSU on the mRNA. Among the four steps of protein translation, initiation varies the most between the three domains of life, and the process has gained a lot in complexity during evolution. The high regulation in eukaryotes reflects how important it is for a cell to tightly control this energy-consuming process.

Translation initiation in bacteria

In bacteria, translation and transcription are coupled (Kohler *et al*, 2017; Miller *et al*, 1970; Saxena *et al*, 2018; Wang *et al*, 2020; Washburn *et al*, 2020). Therefore, the ribosome can bind to the mRNA as soon as the ribosome binding site (RBS) emerges from the RNA polymerase. Then the accurate and efficient selection of the initiation codon (AUG, or GUG or UUG) is accomplished by base pairing of the Shine-Dalgarno (SD) sequence of the mRNA 5' end with the anti-SD sequence in the 16S rRNA 3'-region (Geissmann *et al*, 2009; Korostelev *et al*, 2008; Ringquist *et al*, 1992; Shine & Dalgarno, 1974; Steitz & Jakes, 1975; Yusupova *et al*, 2001). The SD sequence is located 8-10 nt upstream of the start codon and the mRNA can bind to the SSU independent of IFs. Only a partial relocation of mRNA by the IF into the correct position for decoding has been observed (La Teana *et al*, 1995; Yusupova *et al*, 2006). Translation initiation is also possible on leaderless mRNA (Chang *et al*, 2006), which are mRNAs with only a start codon and a tri-phosphate at the 5' end, but no SD sequence present. This very simple way of translation initiation can be found in all three domains of life (Schmitt *et al*, 2019), thus it might be the initiation pathway found in the last universal common ancestor (Nakagawa *et al*, 2010).

The secondary structure of the RBS and other properties of the mRNA determine the association rate within the first step of initiation (Rodnina, 2018). After mRNA binding, the 30S SSU head is fixed in a position that is favorable for tRNA delivery (Korostelev *et al*, 2007). The initiation factors IF1, IF2, and

IF3 help in recruiting the initiator fMet-tRNA (Antoun *et al*, 2003, 2006). The largest of the three - IF2 - specifically recognizes a formyl-methionyl-moiety of the tRNA and undergoes large conformational changes during the initiation process (Simonetti *et al*, 2008). IF2 is composed of three major parts and exhibits an elongated shape. The least conserved is the N-terminal domain (NTD) that interacts with the LSU upon subunit joining. The G-domain consists of three subdomains GI, GII, GIII, of which GII is responsible for GTP-binding and hydrolysis. This part is homologous to other translational GTPases such as EF-Tu. The C-terminal domain consists of two modules that are necessary to recognize fMet-tRNA^{fMet} (Antoun *et al*, 2006; Myasnikov *et al*, 2005; Simonetti *et al*, 2008, 2013b, 2013a). IF3 ensures the fidelity of fMet-tRNA^{fMet} selection and prevents premature subunit joining. It binds to the platform of the SSU (Carter *et al*, 2001; Hussain *et al*, 2016). The rather small protein IF1 binds to the A-site contacting uS12 and enhances the binding and activity of IF2 and IF3 (Carter *et al*, 2001). After the 30S initiation complex (30S IC) is formed by SSU-mRNA, IF1, IF2, IF3, and fMet-tRNA^{fMet}, start-codon recognition leads to dissociation of IF3 and LSU joining. Within the 70S pre-initiation complex (70S PIC) GTP-hydrolysis is triggered and the tRNA accommodates in the canonical P-site position. IF1 leaves the complex and IF2 is repositioned. The release of the Pi then leads to dissociation of IF2 and the 70S initiation complex (70S IC) is formed (Hussain *et al*, 2016). This complex can then enter the next phase of translation with an empty A-site allowing delivery of an aa-tRNA (Kaledhonkar *et al*, 2019).

Translation initiation in eukaryotes

Unlike bacterial translation, eukaryotic translation is spatially separated from transcription. Therefore, the first step of translation initiation can be divided into two separate processes: mRNA selection and activation by initiation factor complex eIF4F, and formation of the 43S pre-initiation complex (PIC) (Figure 2) (Hinnebusch, 2014, 2017; Merrick & Pavitt, 2018; Sokabe & Fraser, 2019). All eukaryotic mRNAs possess a 5' cap structure (m⁷GpppN) and a poly-A tail at the 3' end. This conserved structure is recognized by the cap-binding complex eIF4F, which consists of DEAD box RNA helicase eIF4A, scaffolding protein eIF4G, and the cap-binding protein eIF4E (Merrick, 2015). The subunit eIF4G in turn can interact with poly-A-binding protein (PABP) and helps in circularization of the mRNA (Archer *et al*, 2015; Costello *et al*, 2015; Tarun *et al*, 1997; Wells *et al*, 1998). The 43S PIC is a stable complex in which initiation factors eIF1, eIF1A, eIF3, eIF5, and the ternary complex (TC) composed of eIF2, GTP and Met-tRNA_i, encircle the 40S SSU. The 40S SSU within this complex can originate from free as well as recycled subunits. eIF1 and eIF1A bind cooperatively to the platform in proximity to the P- and A-site, respectively (Lomakin & Steitz, 2013; Maag *et al*, 2005; Passmore *et al*, 2007; Weissner *et al*, 2013). Unlike the rather small factors eIF1 and eIF1A, eIF3 is a multi-protein complex with a different number of subunits ranging from six subunits in yeast to thirteen subunits in human (designated eIF3a-m)

(Hinnebusch, 2006; Valásek, 2012). Its subunits bind mainly to the solvent side of the 40S SSU and span from the mRNA entry to the exit (Aylett *et al*, 2015; Erzberger *et al*, 2014; Hashem *et al*, 2013; Siridechadilok *et al*, 2005). The TC delivers the initiator Met-tRNA_i in the GTP-bound form of eIF2. It is not absolutely required for mRNA recruitment, but necessary for scanning and recognition of the initiation codon. Recruitment of the TC is promoted by eIF1, eIF1A and eIF3, which change the head conformation of the 40S SSU and allow positioning of the tRNA for scanning (Aitken *et al*, 2016; Majumdar *et al*, 2003; Olsen *et al*, 2003; Pestova *et al*, 1998; Sokabe & Fraser, 2014; Valásek, 2012). Moreover, eIF1 and eIF1A were suggested to open up the latch of the mRNA entry channel, which enables mRNA binding (Passmore *et al*, 2007; Hussain *et al*, 2014).

An alternative to this sequence of the 43S PIC assembly events is that first, a multi factor complex (MFC) is formed by eIF1, eIF3, eIF5, and the TC, which then binds the 40S SSU to build the 43S PIC (Asano *et al*, 2000; Dennis *et al*, 2009; Jivotovskaya *et al*, 2006; Sokabe *et al*, 2012; Valásek *et al*, 2002). Yet, further experiments are needed to define the function of such MFC.

The second step of initiation is the binding of the activated mRNA to the 43S PIC. This process is stimulated by eIF4B, a factor that is not part of the eIF4F complex and independently interacts with the PIC (Mitchell *et al*, 2010; Walker *et al*, 2013; Zhou *et al*, 2014). In mammals, the interaction between eIF3 and eIF4F is crucial for mRNA recruitment (Hinton *et al*, 2007; Korneeva *et al*, 2000; Lamphear *et al*, 1995; Morino *et al*, 2000; Villa *et al*, 2013). After successful binding, initiation can enter the next phase, in which the 5' untranslated region (5'-UTR) of the mRNA is scanned by the 48S IC in 3' direction until the Met-tRNA_i anticodon base pairs with three complementary bases on the mRNA. In this process, the helicase eIF4A unwinds the mRNA and allows the 43S PIC to migrate along the mRNA with a speed of ~8 nt per second (Grifo *et al*, 1984; Linder *et al*, 1989; Merrick, 2015; Vassilenko *et al*, 2011). The process can further be assisted by ATP-dependent DEAD-box RNA helicases, for example DHX29 (Pisareva *et al*, 2008; des Georges *et al*, 2015). During scanning, the IC features an "open" conformation with mRNA and tRNA loosely bound. This tRNA conformation is called P_{OUT} and allows mRNA to move through the mRNA channel as well as the tRNA probing successive triplets entering the P-site (Llácer *et al*, 2015).

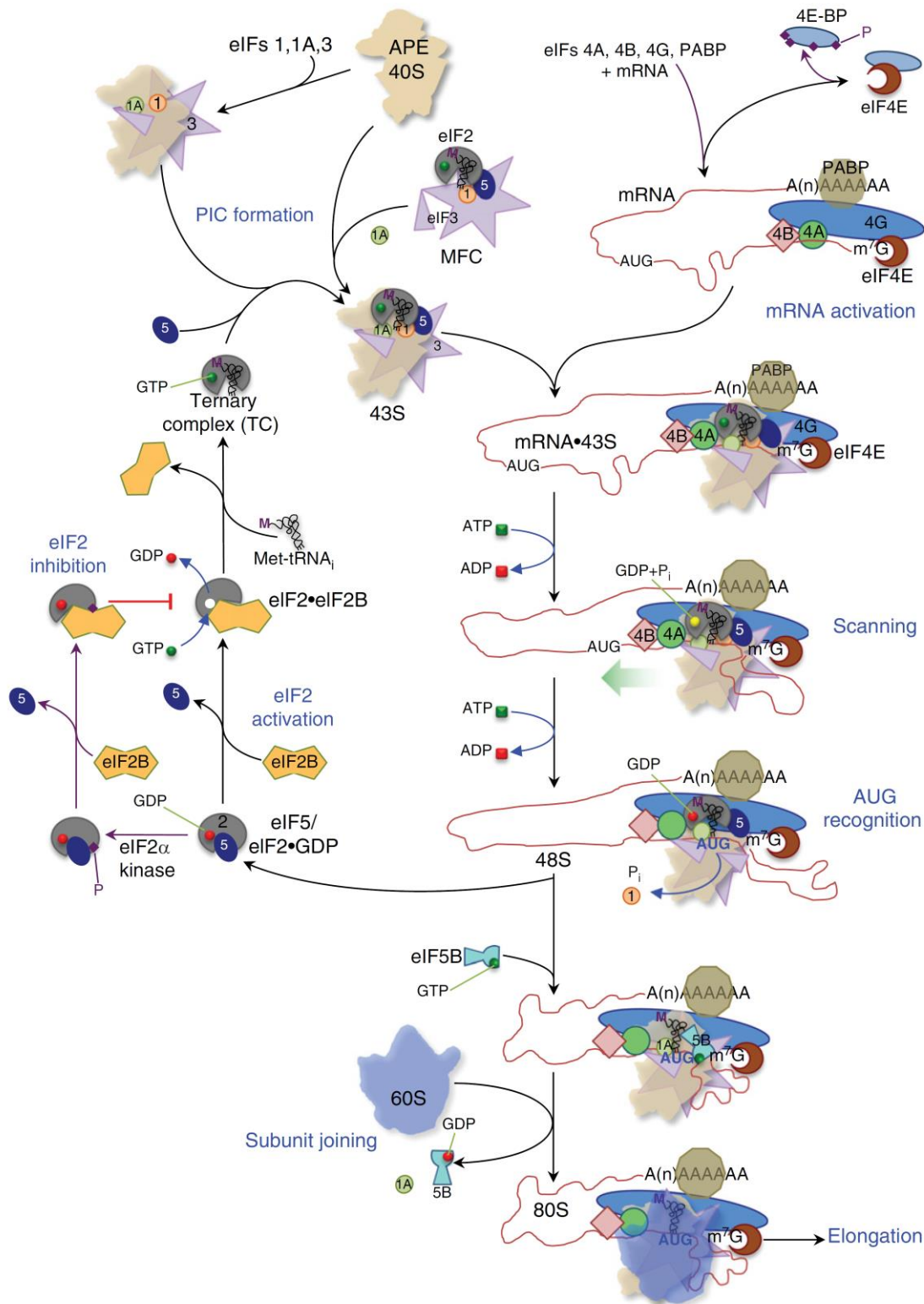


Figure 2: Schematic overview of eukaryotic cap-dependent translation initiation. Initiation factors (IFs) bind to the 40S SSU consecutively or as a multi factor complex to form the 43S pre-initiation complex (PIC). eIF2 is activated by eIF2B to form the ternary complex (TC), which delivers the Met-tRNA_i. The mRNA is activated by eIF4F and poly-A binding proteins (PABP). After recruitment of mRNA to the 43S PIC, the scanning 48S initiation complex (IC) is formed. Start codon recognition then leads to conformational changes and dissociation of eIF1, eIF2 and eIF5. In the last step, eIF5B promotes subunit joining, which enables the 80S ribosome to enter the elongation phase. The figure was adapted from (Merrick & Pavitt, 2018).

Once an AUG codon enters the P-site, it is only recognized if the surrounding sequence is the “Kozak” consensus with a purine at the -3 position and a G at +4 position relative to the AUG (+1) (Jackson *et al*, 2010; Kozak, 1986, 2005). In that case, initiation enters the next phase. Upon start codon recognition, the 48S IC undergoes structural rearrangements and changes to a “closed” conformation (Hussain *et al*, 2014; Ll  cer *et al*, 2015; Lorsch & Dever, 2010). The Met-tRNA_i forms base-pairs with the start codon in the P-site and changes to a so-called P_{IN} state. (Ll  cer *et al*, 2015). The GTP-hydrolysis by eIF2 can already happen during the scanning process and is stimulated by GTPase activating protein (GAP) eIF5. The release of the inorganic phosphate (Pi) though is blocked by eIF1.

The structural rearrangements after start codon recognition lead to release of eIF1, as well as an altered binding of eIF1A and eIF5 (Cheung *et al*, 2007; Unbehaun *et al*, 2004). Together this causes the release of P_i and thus makes this step irreversible (Algire *et al*, 2005; Majumdar & Maitra, 2005; Nanda *et al*, 2013; Saini *et al*, 2014). Furthermore, it is followed by the dissociation of eIF2-GDP from the tRNA and the 48S IC (Jennings *et al*, 2017; Kapp & Lorsch, 2004). Detachment of eIF2 in complex with eIF5 (Unbehaun *et al*, 2004) allows initiation to enter the last phase, in which the 60S LSU joins. This process is promoted by eIF5B, which is recruited by eIF1A (Pestova *et al*, 2000; Acker *et al*, 2006, 2009). The GTPase binds at the intersubunit space and GTP-hydrolysis leads to positioning of the Met-tRNA_i in the P-site. This is accompanied by large conformational changes of eIF5B bound to 80S, which eventually lead to dissociation of eIF5B-GDP and eIF1A (Fringer *et al*, 2007; Wang *et al*, 2019). Afterwards the 80S ribosome with vacant A-site and Met-tRNA_i in the P-site can enter the next phase of translation.

Eukaryotic translation initiation factors of the 43S PIC

This chapter describes the eukaryotic IFs of the 43S PIC in more detail and highlights their regulatory role during the initiation process.

eIF1A (Tif11p in *S. cerevisiae*), together with eIF1 and eIF3, promotes TC binding to the SSU. The homolog of bacterial IF1 is 16.5 kDa in size and has an S1-like domain as well as two flexible intrinsically disordered tails, which are eukaryotic specific (Battiste *et al*, 2000; Merrick & Pavitt, 2018). On the SSU, it binds to the A-site at the top of h44 (Yu *et al*, 2009; Weisser *et al*, 2013; Aylett *et al*, 2015). The positively charged N-terminal tail stabilizes the codon-anticodon duplex and the closed conformation of the IC (Fekete *et al*, 2007; Saini *et al*, 2010). The h44 rRNA base A1709 (*Tetrahymena thermophila*; A1493 in *E.coli*) can flip out to monitor start codon recognition and is recognized and stabilized by eIF1A (Ogle *et al*, 2001; Weisser *et al*, 2013). Further interactions of the NTT with the 40S head were observed (Hussain *et al*, 2014). The C-terminal tail of eIF1A is also positioned in the P-site but moves

away upon start codon recognition. It then interacts with the NTD of eIF5B, which is important for subunit joining. Thus, eIF1A stays bound to the SSU during all phases of initiation. After full assembly of the 80S IC, eIF5B, and eIF1A leave the complex together (Acker *et al*, 2006; Fringer *et al*, 2007; Wang *et al*, 2019).

The 13 kDa protein eIF1 (Sui1p in *S. cerevisiae*) binds close to the P-site and the mRNA channel in proximity to eIF1A, but there is no direct contact between the factors (Aylett *et al*, 2015; Hussain *et al*, 2014; Lomakin *et al*, 2003; Rabl *et al*, 2011; Weisser *et al*, 2013). The factor consists of an α/β -fold and an N-terminal tail (Reibarkh *et al*, 2008). During scanning, its position blocks the tRNA from adopting the P_{in} state. Moreover, eIF2 β connects eIF1 to the Met-tRNA_i and thereby stabilizes the open conformation of the IC (Llácer *et al*, 2015; Maag *et al*, 2005; Pestova & Kolupaeva, 2002). Further interactions are formed between eIF1 and the CTD of eIF5 as well as eIF3c (Erzberger *et al*, 2014; Reibarkh *et al*, 2008; Sokabe & Fraser, 2014). This interaction network allows to discriminate between cognate and near-cognate start codons. Mutations in eIF1 affect TC recruitment, scanning, and start codon recognition stringency (Cheung *et al*, 2007; Hinnebusch, 2017; Martin-Marcos *et al*, 2013; Yoon & Donahue, 1992). If mutations weaken the binding of eIF1 to the PIC, this leads to enhanced initiation at the near-cognate UUG codon (Sui⁻ phenotype), as well as a reduced rate of TC loading (Gcd⁻ phenotype). On the other hand, mutations that affect interactions within the closed conformation of the PIC increase discrimination against non-AUG codons (Ssu⁻ phenotype). These phenotypes can also be analyzed for other IFs and allow to map functions in start codon recognition stringency to the different elements of the IFs (Fekete *et al*, 2007; Saini *et al*, 2010; Hinnebusch, 2014, 2017).

The factor responsible for delivery of Met-tRNA_i, eIF2, consists of three subunits (α , β , γ ; Sui2p, Sui3p, Gcd11p in *S. cerevisiae*) (Schmitt *et al*, 2010). The L-shaped factor wraps around the tRNA. The α -subunit constitutes the longer side of the L-shape and has a molecular weight of 36 kDa. It consists of three domains (I, II, III). Domain I, possessing an OB-fold, contacts the 40S head in proximity to the E-site and together with the Met-tRNA_i docks eIF2 on the SSU (Hussain *et al*, 2014; Llácer *et al*, 2015). Further, Arg residues within this domain interact with mRNA upstream of the AUG codon, especially the nucleotides important for the Kozak consensus (Hinnebusch, 2017). Domain II is α -helical and contacts the D- and T-loops of the Met-tRNA_i. The C-terminal domain III with an α/β -fold connects to eIF2 γ and the acceptor arm of the Met-tRNA_i. The largest subunit of eIF2, eIF2 γ (52 kDa), consists of three domains and shows high similarity to EF-Tu (Hannig *et al*, 1993; Roll-Mecak *et al*, 2004; Schmitt *et al*, 2012). It is composed of an N-terminal GTP-binding domain and the β -barrel domains II and III. The subunit connects eIF2 α and eIF2 β and contacts Met-tRNA_i. Domain II forms a pocket, in which the acceptor stem and the aa are bound. This pocket is in close proximity to the GTP-binding site (Schmitt *et al*, 2012). eIF2 β is anchored to eIF2 γ by an N-terminal helix and consists of a central helix-turn helix

domain (HTH), which contacts eIF1 and eIF1A. When the 48S IC changes from an open to a closed state, the interaction pattern of this domain changes. The contact to the initiation factors gets lost and the tRNA interactions are changed. Moreover, eIF2 β consists of a C-terminal zinc-binding domain, which is positioned close to the GTPase center of eIF2 γ (Dever *et al*, 2016; Ll  cer *et al*, 2015; Schmitt *et al*, 2012; Stolboushkina *et al*, 2008). All subunits of eIF2 are required to bind and deliver tRNA (Kapp *et al*, 2006). The elements of the Met-tRNA_i that are specifically recognized by eIF2 are the A1:U72 and C3:G70 base pairs in the acceptor stem as well as A54, A60 in the T loop and three G:C base pairs in the anticodon stem (Kapp *et al*, 2006).

Different environmental conditions can influence the availability of the TC and thus the initiation rate of the cell (Pavitt *et al*, 1998; Rowlands *et al*, 1988). Before eIF2 can deliver the Met-tRNA_i to the 43S PIC, it has to be activated by the guanine exchange factor (GEF) eIF2B (Jennings *et al*, 2013) (Figure 2). Cellular stress can lead to phosphorylation of the α -subunit of eIF2 α at Ser51 and as a consequence, the TC is unable to form a complex with eIF2B. Thus, GDP is not exchanged to GTP and TC availability is reduced (Dever *et al*, 1992). Under normal conditions, the nucleotide exchange leads to Met-tRNA_i binding with high specificity and TC formation (Kapp & Lorsch, 2004; Kapp *et al*, 2006). The stable GDP-bound form of eIF2 has a high affinity to eIF5 (Algire *et al*, 2005; Singh *et al*, 2006). Both factors leave the IC at the same time and eIF5 can only be replaced by eIF2B, which ensures that GDP stays bound to eIF2. The CTD of eIF5 is the GDP-dissociation inhibitor, whereas the NTD of eIF5 has its role in GTPase activation of eIF2 during the initiation process (Alone & Dever, 2006; Jennings & Pavitt, 2010; Jennings *et al*, 2013).

eIF3 has been implicated to be functionally relevant throughout the initiation cycle, is important for mRNA recruitment to the PIC, and interacts with all other IFs (Aitken *et al*, 2016; Hinnebusch, 2011). The large eIF3 complex ranges between 600 and 800 kDa (Hinnebusch, 2006; Val  sek, 2012) and contains PCI (proteasome, COP9/signalosome, eIF3) and MPN (Mpr1-Pad1-N-terminal) modules (Enchev *et al*, 2010). Early low-resolution EM maps have determined the overall shape and position of yeast (Aylett *et al*, 2015; Erzberger *et al*, 2014) and mammalian eIF3 (Querol-Audi *et al*, 2013; Siridechadilok *et al*, 2005; Sun *et al*, 2011). In yeast, eIF3a (Tif32) and eIF3c (Nip1) form a dimer with their PCI modules at the mRNA exit, which connects to the eIF3b-g-i-j (Prt1, Tif35, Tif34, Hcr1) subcomplex via an interaction between the eIF3a-CTD and eIF3b (Erzberger *et al*, 2014; Val  sek, 2012). Moreover, the NTD of eIF3c connects to the intersubunit side of the 40S (Erzberger *et al*, 2014). The eIF3b-g-i-j subcomplex is called “yeast-like core” or “peripheral subunits” (des Georges *et al*, 2015; Simonetti *et al*, 2016) and sits at the solvent site of the SSU close to the mRNA entry. Within this complex, eIF3b serves as an interaction hub. The NTD of eIF3b contains an RNA-recognition motif (RRM) that connects to eIF3j and the C-terminal part of eIF3a (Dong *et al*, 2013; Elantak *et al*, 2007;

Erzberger *et al*, 2014). The central part of eIF3b, a 9-bladed β -propeller domain, anchors it on the 40S SSU, and the C-terminal helix of eIF3b binds eIF3i (Erzberger *et al*, 2014; Liu *et al*, 2014). The 7-bladed β -propeller domain of eIF3i in turn binds the NTD of eIF3g (Erzberger *et al*, 2014). eIF3g further consists of an RRM, that has not been visualized in the context of the 43S PIC. The RRM of eIF3b has been shown to promote 40S binding and AUG selection during scanning. This depends on its interaction with the NTD of eIF3j (Chiu *et al*, 2010; Elantak *et al*, 2007, 2010; Nielsen *et al*, 2006). The CTD of eIF3j binds directly to the mRNA entry channel in proximity to the A-site and the eIF1A binding site (Aylett *et al*, 2015; Fraser *et al*, 2007). The eIF3j subunit itself is only loosely associated with eIF3, which can independently bind to 40S SSU (Fraser *et al*, 2004; Valášek *et al*, 2017) and non-essential (Valášek *et al*, 1999). In the presence of mRNA, eIF4F and eIF4B were shown to lower the affinity of eIF3j for the 43S PIC (Sokabe & Fraser, 2017, 2019).

In higher eukaryotes, the PCI-MPN core of eIF3 forms a multi-lobed structure stabilized by a helical bundle and a PCI β -sheet arc (des Georges *et al*, 2015; Enchev *et al*, 2010; Erzberger *et al*, 2014). It comprises eIF3a and 3c and the additional mammalian subunit 3f, 3h, 3k, 3l, and 3m. The octameric complex is bound at the mRNA exit via eIF3a and 3c and folds into five lobes, which are composed of 3a (left arm), 3c (head), 3e (right arm), 3l/3k (right leg), and 3h/3f/3m (left leg). Although the 3e/3h/3k/3l subunits are not essential (Masutani *et al*, 2007) and also not involved in interactions with the 40S SSU, they play an important role in the interaction with mRNA and other regulatory factors such as eIF4G. The core structure is connected to the other subunits like in yeast by the CTD of eIF3a.

Another additional mammalian subunit of eIF3 is eIF3d. It consists of a cap-binding domain and an N-terminal extension. Whereas the NTD has not been visualized, the rest of the subunit is positioned behind RACK1 on the 40S head (des Georges *et al*, 2015). The crystal structure of the cap-binding domain revealed a complex fold that forms a cup-shaped architecture with a positively charged central tunnel that is negatively charged at its base. Further eIF3d shows structural homology to 5'cap-endonucleases, which together suggests that eIF3d is involved in an eIF4E-independent mRNA recruitment initiation pathway (Lee *et al*, 2016).

Together, eIF3 is responsible for assembly of the scanning complex, cap-dependent mRNA loading, start codon recognition, and LSU joining.

eIF5 (Tif5p) was found to co-purify with eIF3 (Phan *et al*, 1998). It is a two-lobed protein and, as mentioned above, the NTD acts as the GAP for eIF2 and binds to its G-domain (Alone & Dever, 2006; Bieniossek *et al*, 2006). The NTD structurally resembles eIF1 (Conte *et al*, 2006) and after start codon recognition and release of eIF1 relocates to its position and thus allows P_i release from eIF2 (Nanda *et al*, 2009). The CTD of eIF5 binds to eIF2 β , eIF1 and eIF3c (Obayashi *et al*, 2017; Yamamoto *et al*, 2005).

These interactions influence the stringency of AUG recognition and mutations in this region destabilize the closed state of the 48S IC (Luna *et al*, 2012).

Translation initiation in archaea

Features of both, eukaryotic and bacterial translation initiation, are present in archaeal initiation (Schmitt *et al*, 2019, 2020). The architecture of archaeal mRNAs is, depending on the organism, leaderless or contains a SD-sequence at the 5'-end. Although transcription and translation are coupled (French *et al*, 2007), the archaeal PIC is more similar to the eukaryotic PIC. It is formed by the TC aIF2-GTP-Met-tRNA_i, aIF1, and aIF1A, which are bound to the 30S SSU (Coureux *et al*, 2016, 2020; Hasenöhrl *et al*, 2006, 2009; Pedullà *et al*, 2005). For eIF3 and eIF4, no homologs exist, except for aIF4A, which was found to be non-essential (Gäbel *et al*, 2013). Start codon selection is orchestrated by the PIC similarly as in eukaryotes. The TC, aIF1, and aIF1A are positioned at the intersubunit side of the 30S SSU close to the A- and P-site (Coureux *et al*, 2016; Hasenöhrl *et al*, 2006, 2009). The tRNA can switch from a so-called P_{REMOTE} state, in which the tRNA is located outside of the P-site, to the P_{in} state. The conformation of the tRNA in the P_{REMOTE} state differs significantly from the P_{OUT} state, as the mRNA is not scanned, but start codon recognition relies on a SD-assisted mechanism (Coureux *et al*, 2016; Monestier *et al*, 2018). This is also reflected in the mRNA exit channel architecture as in eukaryotes initiation factors stabilize the mRNA after start codon recognition. These specific interactions are not present in archaea. The change to the P_{IN} state is accompanied by a 30S SSU head rotation, which locks the tRNA anticodon in the P-site. Then the release of P_i leads to dissociation of aIF2-GDP and aIF1 and in the next step aIF5B can bind and initiate subunit joining (Maone *et al*, 2007). Different than in eukaryotic initiation, aIF5B is not recruited via aIF1A as the C-terminal extension of eIF1A is not present. Still, subunit joining represents the most conserved stage of initiation as e/aIF5B and e/aIF1A are orthologues of the bacterial proteins IF2 and IF1, respectively (Schmitt *et al*, 2020).

Another archaeal initiation factor is aIF6, which is the homolog of eIF6 (Tif6 in yeast). It binds with affinity to the 50S LSU (Benelli *et al*, 2009; Greber *et al*, 2012) and acts as an anti-association factor. In eukaryotes, eIF6 was found to be involved in preventing premature 40S joining (Gartmann *et al*, 2010; Klinge *et al*, 2011) and can be released by an EF-G homolog Efl1 (Weis *et al*, 2015). In archaea, no homolog of Efl1 exists, but a recent study found that aEF2 induces the release of aIF6 from 50S LSU (Lo Gullo *et al*, 2021).

1.2.2 Elongation

During elongation phase, a protein chain is synthesized by repetitive cycles of decoding in the A-site, peptide bond formation in the PTC (Rodnina, 2018; Dever *et al*, 2018). This very dynamic process is accompanied by unidirectional movements of tRNAs and mRNA through the ribosome, called translocation. As the process is highly conserved from bacteria to mammals, it will be described for bacteria and the respective factors and differences for archaea and eukaryotes will be highlighted throughout the text.

After start codon recognition and translocation of the Met-tRNA_i to the P-site, the next codon on the mRNA is exposed in the A-site. At this point, the next aa-tRNA is delivered in a ternary complex with the GTPase EF-Tu (eEF1A and aEF1A in eukaryotes and archaea, respectively) and GTP, and is selected with high fidelity (Fischer *et al*, 2015; Loveland *et al*, 2020; Rodnina *et al*, 2017; Schmeing *et al*, 2009). The recruitment of the ternary complex takes place via an interaction with the bL12 stalk of the LSU (P-stalk in eukaryotes) (Diaconu *et al*, 2005; Kothe *et al*, 2004). To ensure the production of the right protein sequence, the correct Watson-Crick base pairing geometry needs to be recognized by key residues in the 16S rRNA (18S rRNA). Two adenosines (A1492, A1493 in *E. coli*, A1824, A1825 in *H. sapiens*, A1755, A1756 in *S. cerevisiae*) of h44 probe the minor groove of the codon-anticodon helix and only change to a “flipped-out” conformation if there is cognate base pairing (Fischer *et al*, 2015; Loveland *et al*, 2017; Ogle *et al*, 2001). The third base of the codon and the corresponding base of the anticodon are allowed to adopt a non-perfect wobble base pairing, which provides the structural basis for the degeneracy of the genetic code (Crick, 1966; Loveland *et al*, 2017). Further, a guanosine (G530 in *E. coli*, G626 in mammals, G577 in *S. cerevisiae*) of h18 acts as a latch that fastens the codon-anticodon helix into the decoding center. As a result, the ternary complex moves into a different position. This allows contact to the sarcin-ricin loop (SRL) of the 23SrRNA and triggers GTP hydrolysis by EF-Tu. This irreversible step is followed by conformational changes of EF-Tu, which lead to the release and accommodation of tRNA in the A-site of the LSU. Thereby, the acceptor stem is positioned in the PTC. Proper accommodation serves as a second checkpoint for selection of the cognate aa-tRNA (Geggier *et al*, 2010; Shao *et al*, 2016). EF-Tu - GDP dissociates from the ribosome and is recycled by the GEF EF-Ts (eEF1B and aEF1B in eukaryotes and archaea, respectively). If peptidyl-tRNA and aa-tRNA are located in the PTC, they can react and form a peptide bond. Positioning of rRNA and tRNA residues, ordering of water molecules, and electrostatic shielding catalyzes this reaction within the active center of the ribosome (Rodnina, 2018; Sharma *et al*, 2005; Wallin & Aqvist, 2010; Watson *et al*, 2020). A nucleophilic attack of the amino group of the aa-tRNA on the carbonyl ester bond in the peptidyl-tRNA results in a transfer of the nascent peptide onto the A-site tRNA (Simonović & Steitz, 2009). Once peptide bond formation happened, a counterclockwise rotation of the SSU can occur,

which leads to a so-called “rotated” state of the ribosome with the tRNAs in hybrid (A/P and P/E) states and uL1 stalk in a closed conformation (Moazed & Noller, 1989; Budkevich *et al*, 2011; Dunkle *et al*, 2011). At this stage the ribosome spontaneously fluctuates between the rotated and the unrotated conformation (Blanchard *et al*, 2004). The GTPase EF-G (eEF2 and aEF2 in eukaryotes and archaea, respectively) recognizes the hybrid state elongation complex and promotes the rearrangements from the pre-translocation state (PRE) to the post-translocation state (POST). After GTP-hydrolysis, the P_i stays bound to EF-G. A movement of the SSU body in clockwise direction, while the SSU head stays in a forward-swiveled state, opens up the decoding region. The changed interactions with the SSU body allow displacement of the tRNAs and mRNA (Spahn *et al*, 2004; Taylor *et al*, 2007). Next, the SSU head domain moves backwards and leaves the translocated tRNAs in P- and E-sites (Ermolenko & Noller, 2011; Ramrath *et al*, 2013; Ratje *et al*, 2010). This is accompanied by the release of P_i from EF-G. As the E-site tRNA moves further away from the P-site tRNA, the codon-anticodon interaction is lost and the SSU head moves further back. Dissociation of E-site tRNA and EF-G finally leaves a ribosome competent to bind a new aa-tRNA to the A-site. The binding of the next tRNA is uncoupled from tRNA dissociation from the E-site (Ferguson *et al*, 2015; Semenov *et al*, 1996; Uemura *et al*, 2010).

Another elongation factor is EF-P (eIF5A and aIF5A in eukaryotes and archaea, respectively), which was first identified as an initiation factor (Glick & Ganoza, 1975; Henderson & Hershey, 2011), but following studies reported impaired translation elongation upon depletion of eIF5A (Gregio *et al*, 2009; Saini *et al*, 2009). This was further supported by studies of EF-P, which showed that the factors can stimulate the synthesis of proteins with polyproline stretches (Doerfel *et al*, 2013). The unique structure of proline makes it a poor A-site peptidyl-acceptor and P-site peptidyl-donor and thus stretches of prolines lead to ribosomal stalling (Pavlov *et al*, 2009; Doerfel *et al*, 2013). It was found that eIF5A and its hypusine modification are required for the synthesis of these difficult aa stretches (Gutierrez *et al*, 2013; Park *et al*, 2010). Likewise in bacteria, EF-P is modified with a lysinylation, which is also essential for its function (Doerfel *et al*, 2013; Ude *et al*, 2013). From ribosome profiling data, it became apparent that eIF5A acts globally on translation elongation and not on specific mRNAs or translation initiation. In eukaryotes, eIF5A further acts on stop codons and assists in translation termination (Pelechano & Alepuz, 2017; Schuller *et al*, 2017). Structures of ribosome complexes with eIF5A bound, revealed that the factor binds to the E-site and reaches towards the PTC contacting the acceptor arm of the peptidyl-tRNA (Huter *et al*, 2017a; Melnikov *et al*, 2016; Schmidt *et al*, 2016). It then helps to position the substrates in the correct geometry. By binding to the E-site, eIF5A can monitor RNCs that have paused during elongation or termination and facilitate peptide bond formation or peptide release (Schuller *et al*, 2017; Dever *et al*, 2018).

1.2.3 Termination

Translation termination in bacteria

Unlike all other codons, the stop codons UAA, UAG, and UGA are recognized by class-1 release factors 1 (RF1) and 2 (RF2). Depending on which codon is present in the A-site, RF1 or RF2 binds to the A-site of the ribosome. The codon UAA can be read by both factors, UAG is only recognized by RF1 and UGA by RF2 (Capecci, 1967; Caskey *et al*, 1968; Scolnick *et al*, 1968; Youngman *et al*, 2008). Both factors have similar overall structures composed of four domains (Shin *et al*, 2004; Vestergaard *et al*, 2001). Domain II and IV bind to the decoding center and domain II interacts via the N-terminus of helix $\alpha 5$ to specifically recognize the uracil in the first position of the codon. Additionally, interactions between the stop codon recognition motif PVT (RF1) or SPV (RF2) and the other bases of the codon lead to stable binding of the RF (Ito *et al*, 2000; Petry *et al*, 2005). Together this results in conformational changes in the decoding center. G530 and A1492 (*E. coli* numbering) flip out as in canonical decoding, but A1493 stays stacked within h44 because it would clash with the RF. This is further stabilized by stacking of A1913 of 23S rRNA on A1493. The switch loop that connects domain III and IV of the RF senses these conformational changes by binding to a pocket formed by A1492, A1913, and uS12 (Korostelev *et al*, 2008, 2010; Laurberg *et al*, 2008; Weixlbaumer *et al*, 2008). Thus, recognition of the stop codon leads to a conformational change within RF1/RF2, which directs domain III into the PTC (Fu *et al*, 2019; Korostelev *et al*, 2008, 2010; Laurberg *et al*, 2008; Weixlbaumer *et al*, 2008; Shin *et al*, 2004). Domain III of both RFs harbors the conserved GGQ motif, which interacts with residues of the PTC as well as the P-site tRNA (Laurberg *et al*, 2008; Zavialov *et al*, 2002). The Gln in the motif is post-translationally methylated, which enhances the activity of the peptide release. The backbone of the Gln residue is oriented in a way that it is in hydrogen bonding distance to the 3'OH of A76 of the P-site tRNA. Conformational changes within the PTC allow for activation of a water molecule that attacks the ester bond and result in deacylated tRNA and free peptide (Laurberg *et al*, 2008; Pierson *et al*, 2016; Santos *et al*, 2013; Zeng & Jin, 2016).

In the last step of translation termination, RF1 or RF2 dissociate with the help of RF3 (Freistroffer *et al*, 1997). Class II release factor RF3 is a translational GTPase, which binds to the RF1/RF2- bound ribosome after peptide release (Adio *et al*, 2018; Gao *et al*, 2007a; Zavialov *et al*, 2002). Accommodation of the factor induces a rotation of the SSU relative to the LSU, which leads to destabilization in the binding of RF1/RF2 and positions the G domain of RF3 on the LSU. The sarcin-ricin loop then stimulates GTP hydrolysis and induces a conformational change and dissociation of RF3. Surprisingly, no direct interaction between the RFs is necessary to induce their dissociation (Adio *et al*, 2018; Fu *et al*, 2019; Gao *et al*, 2007a; Graf *et al*, 2018; Zavialov *et al*, 2002).

Translation termination in eukaryotes

Termination in eukaryotes is catalyzed by eukaryotic class I release factor 1 (eRF1) and eukaryotic class II release factor 3 (eRF3) (Alkalaeva *et al*, 2006; Schuller & Green, 2018; Stansfield *et al*, 1995; Zhouravleva *et al*, 1995). Although the termination process proceeds similarly, the factors involved are evolutionarily unrelated to their bacterial counterparts. First, eRF1 is delivered by the EF-Tu-like GTPase eRF3 and recognizes the Stop codon in the ribosomal A-site (Alkalaeva *et al*, 2006; Bertram *et al*, 2000; Frolova *et al*, 1996; Muhs *et al*, 2015; Salas-Marco & Bedwell, 2004). Stop codon recognition works on all three stop codons and is distinct from bacteria. The t-RNA-like shape of eRF1 is composed of three domains (N, M, and C) (Song *et al*, 2000). The N domain, which contains the conserved NIKS, GTS, and YxCxxxF motifs, binds to the decoding center and changes the mRNA codon conformation to a U-turn (Brown *et al*, 2015; Matheisl *et al*, 2015; Shao *et al*, 2016). The compaction of mRNA also includes the fourth nucleotide immediately following the stop codon. This geometry is stabilized by stacking of the flipped out A1825 (in *H. sapiens*; A1493 in *E. coli*) of h44 with the +2 and +3 nucleotide of the stop codon, as well as stacking interactions between G626 (G530 in *E. coli*) of the 18S rRNA and the +4 nucleotide. Further, interactions to eRF1 allow to specifically recognize stop codons. The NIKS sequence is located at the end of helix $\alpha 2$ and selects for a uridine in the +1 position. The YxCxxxF motif allows discrimination to sense codons by stabilizing stacking of +2 and +3 purines and the flipped-out position of A1825. This interaction network propagates a movement of the GTS motif, the interaction of Thr with the +3 base, and together forms the stop codon binding pocket (Brown *et al*, 2015; Matheisl *et al*, 2015). Collectively, this allows for a high level of discrimination between stop codons and sense codons (Brown *et al*, 2015; Matheisl *et al*, 2015; Salas-Marco & Bedwell, 2005).

Additionally, eRF3 can stimulate the stop codon recognition activity of eRF1 (Cheng *et al*, 2009; Frolova *et al*, 1999). The NTD of eRF3 was found to interact with PABP, and thus allows the recruitment of the ternary eRF1-eRF3-GTP complex by PABP to terminating ribosomes. For the termination process itself, this part of the protein is not important (Cosson *et al*, 2002; Hoshino *et al*, 1999; Ivanov *et al*, 2008). The C-terminal part of the factor is homologous to EF-Tu and eEF1A and is composed of three domains. Domain I is the G-domain that binds and hydrolyses GTP, which is stimulated by eRF1 and the ribosome (Frolova *et al*, 1996; Wada & Ito, 2014). As all GTPases, this domain contains switch I and switch II, which regulate the GTP-dependent conformational changes. Domain II and III, which are important for the interaction with eRF1, form β barrel structures (Kong *et al*, 2004; Atkinson *et al*, 2008). Upon binding to the termination complex the M domain of eRF1 harboring the GGQ motif is still bound by eRF3 (des Georges *et al*, 2014; Preis *et al*, 2014; Taylor *et al*, 2012). Stop codon recognition then triggers GTP hydrolysis by eRF3 and results in structural rearrangements and dissociation of eRF3 (Cheng *et al*, 2009; Frolova *et al*, 1996; Salas-Marco & Bedwell, 2004). Further, it

leads to positioning of the M domain of eRF1 in a way that the GGQ motif is inserted into the PTC (Matheisl *et al*, 2015; Muhs *et al*, 2015; Preis *et al*, 2014; Shao *et al*, 2016). In this new extended conformation eRF1 resembles a tRNA in the A-site and is in contact with P-site tRNA with its N- and M-domain. Comparison of structural studies in eukaryotes and bacteria regarding the release of the nascent chain suggest that the two systems function in a similar way. Hydrolysis of the nascent chain from the peptidyl tRNA results from a nucleophilic attack of a water molecule, which is catalyzed by the conserved GGQ tripeptide (Jin *et al*, 2010; Laurberg *et al*, 2008).

Translation termination in archaea

As in eukaryotes, archaeal translation termination relies on class I and class II RFs that form a ternary complex with GTP and bind to RNCs with a stop codon in the A-site. Both factors are structurally and functionally related (Franckenberg *et al*, 2012; Kobayashi *et al*, 2012). aRF1 shares the common sequence motifs GGQ, NIKS, YxCxxxF, and as eRF1 is composed of three domains (A, B, and C) (Dontsova *et al*, 2000; Kobayashi *et al*, 2012; Saito *et al*, 2010). A difference to the eukaryotic system is that the delivery of aRF1 is accomplished by aEF1 α as no dedicated RF-GTPase is present in archaea. Thus, this factor is involved in translation elongation by binding to tRNA, translation termination by binding to aRF1, and ribosome rescue by binding to aPelota (Kobayashi *et al*, 2012; Saito *et al*, 2010).

1.2.4 Recycling

Ribosome recycling in bacteria

After termination, the ribosome is split into subunits in order to release mRNA and tRNA (Schlessinger *et al*, 1967; Janosi *et al*, 1996). As for the termination process, the factors involved in this process differ between the three domains of life. In bacteria, EF-G and the ribosome recycling factor (RRF) catalyze recycling (Hirashima & Kaji, 1970; Pavlov *et al*, 1997; Peske *et al*, 2005). The post-termination complex itself is composed of deacylated P- and E-site tRNAs, mRNA, and ribosomal subunits. Peptide release during termination induces a rotated ribosomal conformation, which can fluctuate to a non-rotated state (Sternberg *et al*, 2009; Prabhakar *et al*, 2017). The binding of RRF then stabilizes the ribosome in a rotated state with the P-site tRNA in a hybrid P/E binding state and inhibits re-association of RF1 or RF2 (Dunkle *et al*, 2011). The L-shaped RRF consists of two domains: domain I consist of a three-helix bundle and is connected by two flexible linkers to domain II (Weixlbaumer *et al*, 2007). Domain I binds the ribosome by forming several contacts to 23S rRNA on the 50S subunit and the linker faces the L7/L12 stalk base as well as the SRL region. Domain II contacts uS12 and

intersubunit bridge B2a (Agrawal *et al*, 2004; Dunkle *et al*, 2011; Gao *et al*, 2005; Sternberg *et al*, 2009). The process requires energy from GTP, processed by EF-G as the binding of RRF alone is not sufficient to split the ribosome (Gao *et al*, 2007b; Hirokawa *et al*, 2006; Peske *et al*, 2005; Zavialov *et al*, 2005). Likewise, EF-G binding alone does not promote splitting. A study using time-resolved cryo-EM of the recycling process showed that binding of EF-G allows rotation of RRF domain II in respect to domain I (Fu *et al*, 2016). The factors interact via the hinge and domain II of RRF with domain III and IV of EF-G (Gao *et al*, 2007b). This leads to interruption of intersubunit bridge B2a by the movement of domain II, which was already suggested based on previous studies of the complex (Borg *et al*, 2016; Fu *et al*, 2016; Gao *et al*, 2007b; Wilson *et al*, 2005; Yokoyama *et al*, 2012). The movement is potentially triggered by binding of EF-G, GTP hydrolysis by EF-G, or P_i release. Together, the joint action of the factors leads to splitting of the ribosome.

Additionally, initiation factor 3 (IF3) is involved in ribosome recycling and links this phase to the initiation phase of translation (Hirokawa *et al*, 2006). The subunit splitting event results in the formation of two entities: a complex formed by the 50S LSU, EF-G, RRF, and E-site tRNA, and a complex formed by the 30S SSU, mRNA, and deacylated P-site tRNA (Fu *et al*, 2016). The latter is bound by IF3 via the intersubunit site of 30S SSU. This prevents re-association of the 50S LSU and thus the formation of unproductive 70S (Hirokawa *et al*, 2006; Prabhakar *et al*, 2017). Further, it activates tRNA dissociation, which triggers dissociation of mRNA (Fu *et al*, 2016; Karimi *et al*, 1999; Prabhakar *et al*, 2017) or vice-versa (Chen *et al*, 2017). Whether IF3 plays an active role in the disassembly of the post-splitting complex (post-SC) or just inhibits rebinding of 50S is not yet clear.

Ribosome recycling in eukaryotes and archaea

After termination, ABCE1 is recruited to eRF1-bound 80S (aRF1-bound 70S in archaea) and interacts with eRF1, SSU, and LSU forming the pre-splitting complex (pre-SC). ABCE1 interaction with eRF1 promotes peptidyl hydrolysis (Hellen, 2018; Khoshnevis *et al*, 2010; Shoemaker & Green, 2011). For splitting, conformational changes within ABCE1 and movement of its iron-sulfur (Fe-S) cluster domain (FeSD) were suggested to push eRF1 into the intersubunit space, which leads to destabilization of intersubunit bridges (Becker *et al*, 2012; Gouridis *et al*, 2019; Heuer *et al*, 2017; Kiosze-Becker *et al*, 2016). Further, it was shown that ABCE1 is a crucial factor for ribosome recycling *in vivo* (Young *et al*, 2015). The conformational states of ABCE1 during the splitting process and the dependency on nucleotide binding and hydrolysis are discussed in more detail below (see chapter 1.2.4.3 Ribosome recycling factor ABCE1).

Another factor that was suggested to enhance and control ribosome splitting is eIF3j (Hcr1 in *S. cerevisiae*) (Beznosková *et al*, 2013; Young & Guydosh, 2019). Although the factor was also reported as a substoichiometric subunit of eIF3 (Elantak *et al*, 2010; Valásek *et al*, 1999), further studies showed that deletion of eIF3j (Δ eIF3j) promotes readthrough at stop codons (Beznosková *et al*, 2013). A ribosome profiling study confirmed that eIF3j is indeed recruited to ribosomes at stop codons and inhibits re-initiation of translation in the 3' UTR (Young & Guydosh, 2019). A role in ribosome recycling is further supported by the finding that overexpression of ABCE1 can fully suppress the slow growth phenotype of Δ eIF3j (Beznosková *et al*, 2013). The molecular mechanism of this is not understood yet.

Subunit splitting results in a 40S SSU with deacylated tRNA, mRNA and ABCE1 bound. In the second step of ribosome recycling, the post-SC needs to be disassembled. Binding of eIF1, eIF1A, eIF3 can lead to release of mRNA and tRNA (Pisarev *et al*, 2007, 2010). Initiation factors eIF1 and eIF1A discriminate against non-initiator tRNA and thus promote the release of tRNA (Lomakin *et al*, 2006; Skabkin *et al*, 2013). Also, eIF3j is known to enhance the release of mRNA (Fraser *et al*, 2007).

Further, translation-machinery-associated factors eIF2D (ligatin), product of malignant T cell-amplified sequence 1 oncogene (MCT-1), and density regulated protein (DENR) (in mammals; Tma64, Tma20, and Tma22 in yeast) were identified to be involved in this process (Young *et al*, 2018; Skabkin *et al*, 2010). MCT-1 and DENR are homologs of eIF2D and structurally resemble the N- and C-terminus of eIF2D, respectively (Weisser *et al*, 2017). A ribosome profiling study in yeast, using tma-deletion strains, found 40S SSUs accumulating on stop codons, which points towards an active role of Tma proteins in 40S recycling. In the absence of these factors, the 40S persists on the mRNA and eventually starts scanning for a start codon in the 3'UTR. They further found that the Tma20/Tma22 heterodimer is mainly responsible for mRNA/tRNA recycling, whereas Tma64 probably takes in a more specialized role in this process (Young *et al*, 2021). A similar study further observed that tma-deletion leads to reduced rate of translation initiation and altered translation efficiency of specific mRNAs (Gaikwad *et al*, 2021). In contrast to these studies, these factors were reported to promote re-initiation in mammals (Schleich *et al*, 2014). In this process, the SSU stays bound to the mRNA after translating an upstream ORF and is then positioned at the start codon of the main ORF. Structures of the human eIF2D-bound re-initiation complex and the MCT-1/DENR re-initiation complex show how they monitor codon-anticodon interactions and position the initiator tRNA by binding to the intersubunit side of the SSU in a way similar to canonical IFs (Weisser *et al*, 2017). However, it is not clear when the 40S post-SC is subjected to recycling or re-initiation. Another hypothesis is, that the presence of eIF3 in the post-TC could decide on the fate of the 40S. If present, eIF3 would block the 40S for binding of MCT-1/DENR or eIF2D and thus promote re-initiation. Alternatively, features of the mRNA could regulate

the process (Lomakin *et al*, 2017). Future studies are needed to understand whether Tma proteins and their orthologues MCT-1/DENR and eIF2D promote or prevent re-initiation.

Ribosome recycling factor ABCE1

ATP binding cassette (ABC) proteins are a very abundant class of proteins that use the energy of nucleoside triphosphate and can be found in all kingdoms of life (Higgins, 1992; Hopfner, 2016; Locher, 2016). They are known to be involved in the transport of substances across membranes against a concentration gradient, DNA-associated organization of chromosomes, and DNA repair, as well as translation (Hopfner, 2016). In general, ABC proteins possess homodimeric or heterodimeric pairs of nucleotide binding domains (NBDs), which form nucleotide binding sites (NBS) at their interface. The binding and hydrolysis of ATP to the NBS results in conformational changes that generate mechanical force, or so-called “power stroke”. Associated domains with different functions are linked to the NBDs and thus movements can be propagated. This allows using the energy of ATP in many different ways (Hopfner, 2016; Locher *et al*, 2002; Locher, 2016).

The ABC proteins that play a role in protein translation are members of the ABCF and ABCE families, which lack the transmembrane domain that is present in most other ABC families (Kerr, 2004). The families contain soluble proteins that are made of a single polypeptide chain. Examples for eukaryotic ABCF proteins involved in translation are Gcn20, functioning in translational control by recognizing uncharged tRNAs and thus sensing starvation (Vazquez de Aldana *et al*, 1995), eEF3, a yeast specific elongation factor (Andersen *et al*, 2006; Murina *et al*, 2019; Ranjan *et al*, 2021), and yeast Arb1, a RQC factor (Su *et al*, 2019).

Translation-associated ABC proteins also include the ATP-binding cassette sub-family E member 1 (ABCE1), which was found to be highly conserved from archaea to eukaryotes (Kerr, 2004). ABCE1 in *S. cerevisiae* is RNase-L inhibitor (Rli1), which shares 68% and 43% sequence identity with its human and archaeal (*S. solfataricus*) orthologues, respectively (Barthelme *et al*, 2007; Kispal *et al*, 2005; Navarro-Quiles *et al*, 2018). Moreover, ABCE1 is essential (Coelho *et al*, 2005; Estévez *et al*, 2004; Winzeler *et al*, 1999) and depletion *in vivo* leads to cessation of growth and decreased polysome size (Dong *et al*, 2004).

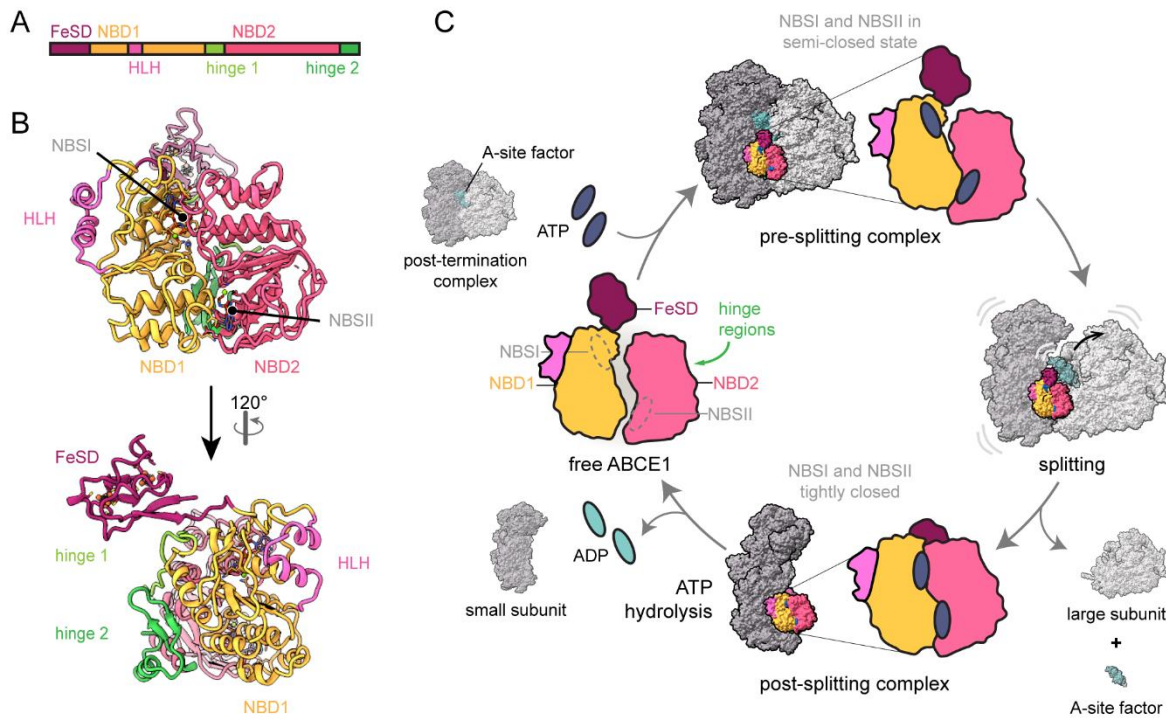


Figure 3: Structure of ABCE1 and conformational changes of ABCE1 during ribosome splitting. (A) Domain architecture of ABCE1: iron-sulfur cluster domain (FeSD), nucleotide-binding domains 1 and 2 (NBD1 and NBD2), helix-loop-helix domain (HLH), and hinge regions. (B) Cartoon representation of the molecular model of ABCE1 shown in the conformation as observed in the post-splitting complex with closed and occluded nucleotide binding sites (NBSI and NBSII) (PDB: 6TMF). (C) Schematic overview of ribosome recycling and different conformational states of ABCE1 during the process.

ABCE1 is composed of four domains (Figure 3). The two NBDs, NBD1 and NBD2, arrange in a head-to-tail orientation, and are linked by a so-called hinge region (hinge 1). Another part of the hinge region is located at the C-terminus trailed to NBD2 (hinge 2). Each NBD is formed by a bend β -sheet surrounded by α -helices. The third domain, a helix-loop-helix (HLH) motif, is an insertion of NBD1, and the fourth domain is the N-terminal twin 4Fe-4S cluster domain (Karcher *et al*, 2005, 2008). The FeSD does not exhibit any redox-activity but is essential for the protein's function (Kispal *et al*, 2005). The 4Fe-4S clusters are bound by conserved cysteine residues surrounded by a hydrophobic cocoon. The domain is linked to NBD1 by a hinged cantilever arm that allows moving the rigid FeSD (Barthelme *et al*, 2007, 2011; Karcher *et al*, 2008).

A tweezer-like motion of the NBDs is linked to ATP binding and hydrolysis (Chen *et al*, 2003; Hopfner & Tainer, 2003) and the hinge regions serve as a pivot point for this movement. Specific conformational states have been described for ABCE1 (Figure 3). In the crystal structures, ABCE1 takes an open conformation creating a roughly 10-14 Å wide interface cleft and the active sites contained Mg^{2+} -ADP (Karcher *et al*, 2005, 2008). This open ABCE1 conformation in solution was further confirmed by FRET studies (Gouridis *et al*, 2019). Bound to the 80S pre-SC, ABCE1 adopts a half open

conformation. ABCE1 binds to the translation factor-binding site of the 80S and contacts the SSU at rRNA junctions h5-h15 and h8-h14 via its HLH domain and the hinge region, respectively. NBD2 is in contact with LSU protein uL10. The FeSD contacts the C-domain of eRF1 (Becker *et al*, 2012; Brown *et al*, 2015; Preis *et al*, 2014). In the post-SC, ABCE1 was found in a closed nucleotide occluded state (Heuer *et al*, 2017; Kiosze-Becker *et al*, 2016). Upon domain closure, new interactions are formed with the 40S SSU and the few interactions to the LSU are lost. Hinge 1 and the HLH domain move upwards and interact with the rRNA in a different way. The contacts between hinge 2 and the ribosome do not change and thus this region represents an anchor point for ABCE1 when the ribosome is split. The FeSD undergoes a dramatic repositioning in respect to the NBDs. The FeSD as an entity does not change, but a rotation of 150° around the cantilever hinge moves it into a new interaction site. Closure of the NBDs creates a “power stroke” that drives these conformational changes. A short helix adjacent to the cantilever hinge unfolds and the interaction pattern of the cantilever arm changes from intramolecular interactions with NBD1 to intermolecular interactions with the rRNA backbone of h5. Eventually, the FeSD binds to a cleft formed by uS12 and rRNA helices h5-h15 and h44, a region previously occupied by the LSU (Heuer *et al*, 2017).

ABCE1, like all ABC proteins, forms two NBSs and contains the conserved sequence motifs which are important for ATP binding and hydrolysis. The Walker A (P-loop) and Walker B (D-loop) motifs, as well as the Q-loop and the His-switch (H-loop) of one NBD and the LSGGQ loop (signature motif or C loop) of the second NBD, coordinate the γ -phosphate of the ATP and the Mg^{2+} ion. The A-loop forms an aromatic stack with the adenine moiety and provides a hydrophobic interface for the ribose. A full range of interactions is achieved when the ATP molecules are sandwiched between the two NBDs. Then, the conserved Glu residue, following the Walker B motif, together with residues in other motifs like the D-, Q- and H-loop polarize a water molecule and thereby catalyze the nucleophilic attack at the γ -phosphate (Heuer *et al*, 2017; Karcher *et al*, 2005; Wilkens, 2015). Sequence analysis and structural comparison of the two sites showed an asymmetry, which suggested different functional roles of the two NBSs during the splitting process (Barthelme *et al*, 2011).

Although ribosome recycling has been studied extensively, the exact role of ATP hydrolysis by the two NBS and how they influence each other remains enigmatic. First, it was suggested that hydrolysis is required for splitting (Becker *et al*, 2012; Pisarev *et al*, 2010; Shoemaker & Green, 2011) or for dissociation of ABCE1 (Barthelme *et al*, 2011). Structural analysis of the pre-SC reported a half-open conformation, which is not competent for ATP hydrolysis. Further, it was concluded from the structures, that before closure of the NBSs, a movement of the FeSD is necessary (Becker *et al*, 2012; Karcher *et al*, 2008; Preis *et al*, 2014). Comparison of the pre-SC to the post-SC revealed that ATP binding and closure of the NBDs leads to splitting (Heuer *et al*, 2017; Kiosze-Becker *et al*, 2016). Later,

single-molecule FRET experiments confirmed that both ATP sites are in an asymmetric conformational equilibrium and only ATP binding is essential for splitting (Gouridis *et al*, 2019). Further, a mutational analysis showed that the NBSs have different turnover times with NBSI as the high-turnover site and NBSII as the low-turnover site. Based on these data the authors suggested a model, in which closure of NBSII is a prerequisite for pre-SC formation and triggers ATP hydrolysis in NBSI. Only closure of both NBSs leads to movement of the FeSD and splitting (Nürenberg-Goloub *et al*, 2018). Still, how the two sites communicate in the context of ribosome binding and splitting is not clear. Moreover, what events eventually trigger nucleotide hydrolysis and whether this directly leads to dissociation is not known.

Several studies reported retention of ABCE1 on the SSU until initiation phase. Due to the circularization of eukaryotic mRNA, ribosomes are released close to the 5' end after termination. Spatial proximity would allow the SSU to initiate on the same mRNA (Tarun & Sachs, 1996). The anti-association factor ABCE1 would inhibit unproductive subunit joining and could stimulate assembly of the pre-IC. Early studies found decreased rates of translation initiation with an ATPase deficient mutant of ABCE1 *in vivo*, as well as a role of ABCE1 in 43S PIC assembly *in vitro* (Andersen *et al*, 2006; Chen *et al*, 2006; Dong *et al*, 2004). Also, affinity purification of ABCE1 yielded a 40S SSU complex with eIF1A, eIF2, and eIF3 bound (Heuer *et al*, 2017). Moreover, ABCE1 was also visualized in a study reporting the structure of eukaryotic PIC, where it binds in the same conformation as in the post-SC (Simonetti *et al*, 2016; Mancera-Martínez *et al*, 2017; Schuller & Green, 2017). However, which role ABCE1 plays in translation initiation is not yet well-understood.

1.3 Ribosome rescue and ribosome-associated quality control pathways

Translation elongation can slow down or even stall when ribosomes face a functional problem. Causes for ribosomal stalling can be for example difficult to decode codons, damaged or truncated mRNA, strong secondary structure in the mRNA, or problematic amino acid sequences. When translation stops in the middle of an ORF and the problem cannot be resolved by the ribosome itself or specific translation factors, a so-called “no-go complex” is formed. Similarly, when a ribosome translates until the 3' end of an mRNA, translation is stalled and as a result a complex with an empty A-site is formed. As no stop codon is present, canonical termination cannot take place. Formation of this so-called “non-stop complex” can further be caused by stop codon readthrough or frameshifting. For a cell, it is crucial to detect and resolve such translational failures in order to avoid reduced capacity of protein production and to remove the problematic mRNA as well as the incompletely synthesized protein. A plethora of different factors orchestrates protein and mRNA surveillance by sensing the state of translation and acting in case of aberrant elongation (Brandman & Hegde, 2016; Joazeiro, 2019; Müller *et al*, 2021; Simms *et al*, 2017; Sitron & Brandman, 2020; Yan & Zaher, 2019). The following chapter describes the different pathways that recognize and recycle the translational machinery (ribosome rescue) and target the potentially defective incomplete protein as well as the mRNA for degradation (ribosome-associated quality control (RQC)).

1.3.1 Ribosome rescue and RQC in bacteria

Translation and mRNA decay are tightly intertwined processes (Pelechano *et al*, 2015; Radhakrishnan & Green, 2016). The translation process is aborted on a partially degraded mRNA and mRNA decay is initiated if translation fails. The degradation of mRNA can be carried out by two main types of RNases: endonucleases and exonucleases. While endonucleases cleave within the polynucleotide chain, exonucleases either digest RNA from the 3' or 5' end (Bechhofer & Deutscher, 2019). Translation of mRNAs truncated within an ORF can result in non-stop complexes. Likewise, no-go complexes can be transformed into a non-stop complex by exonuclease activity. In both cases, a ribosome with an empty A-site is the substrate for ribosome rescue systems (Figure 4) (Ivanova *et al*, 2004; Müller *et al*, 2021).

In bacteria, three independent ribosome rescue systems have been identified so far. The best characterized process that can resolve non-stop complexes is trans-translation (Giudice *et al*, 2014; Karzai *et al*, 1999; Keiler *et al*, 1996). It consists of a ribonucleoprotein complex formed by transfer messenger RNA (tmRNA) and the small protein B (SmpB) (Yamamoto *et al*, 2003). The tmRNA consists of two domains: the tRNA-like domain (TLD) and the mRNA-like domain (MLD) that are connected by several pseudoknots (Komine *et al*, 1994; Ushida *et al*, 1994). GTP-bound EF-Tu delivers the tmRNA-

SmpB complex to the A-site of the non-stop RNC (Barends *et al*, 2000; Rudinger-Thirion *et al*, 1999; Valle *et al*, 2003). The TLD mimics the structure of a tRNA^{Ala} and is charged with Ala at the CCA-3' end. However, it misses the anticodon stem loop structure. Instead, SmpB occupies this space and additionally binds to the empty part of the mRNA channel on the ribosome and stacks with the decoding bases A1493 and G530 using conserved aromatic residues. This decoding-like complex allows the Ala residue to enter the PTC and the aa is added to the nascent chain by peptide bond formation. Afterwards, EF-G binds and translocates the complex so that the TLD and SmpB are moved to the P-site with the C-terminal helix of SmpB occupying the E-site. At the same time, the MLD is loaded into the mRNA channel and is positioned in the A-site (Neubauer *et al*, 2012; Rae *et al*, 2019). With RNA in the A-site translation can continue the classical way. Translation of the tmRNA ORF adds a tag to the incompletely synthesized protein, which targets it for degradation. The last codon of the MLD is a stop codon so that the ribosome can enter the termination phase and afterwards will be recycled. Moreover, the trans-translation system recruits RNase R for degradation of the non-stop mRNA (Rae *et al*, 2019; Venkataraman *et al*, 2014a, 2014b).

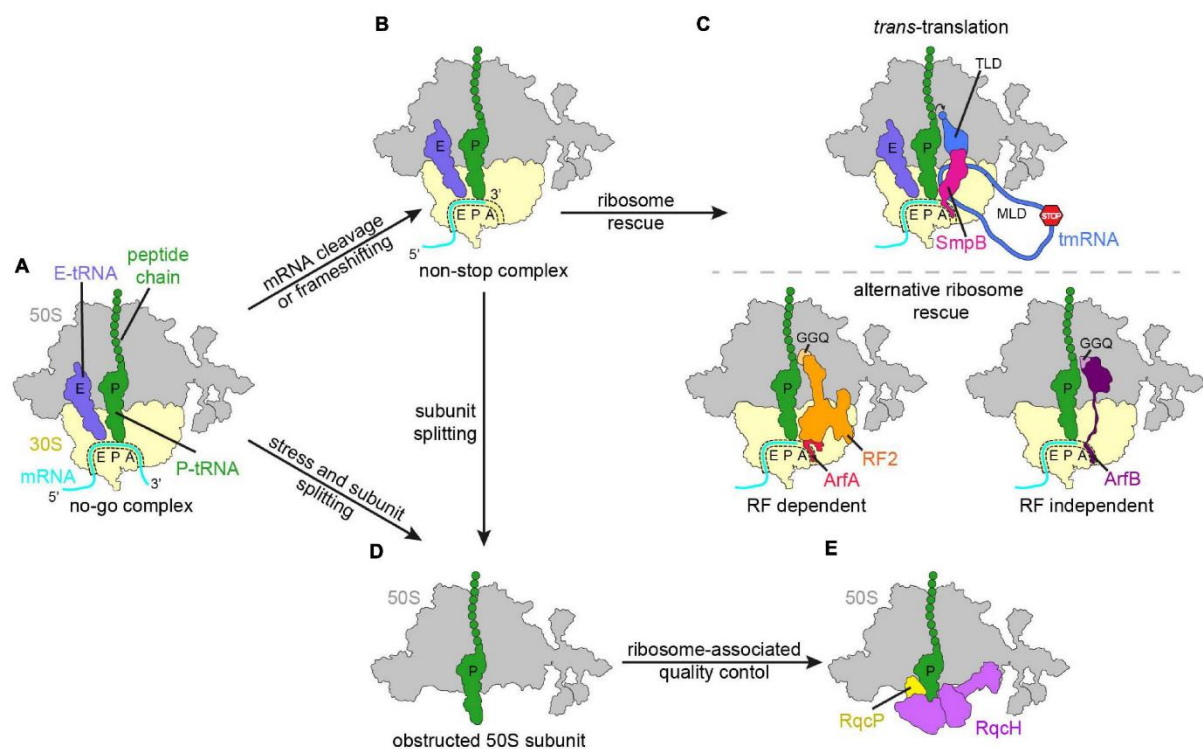


Figure 4: Schematic overview of ribosome rescue and ribosome-associated quality control. Translational stalling leads to formation of no-go complexes (A), which can be transformed into non-stop complex by mRNA cleavage or frameshifting (B). Non-stop complexes are rescued by the trans-translation system or alternative ribosome rescue (C). Subunit splitting of no-go complexes can result in obstructed 50S LSU (D), which are targeted by RQC (E). The figure was adapted from (Müller *et al*, 2021).

Depending on the species, the trans-translation system is often complemented by a protein based ribosome rescue system. This can be either dependent or independent of the release factors. In a screen in *E. coli*, in which the gene for tmRNA was deleted, the alternative ribosome rescue factor (Arf) A was identified (Chadani *et al*, 2010). Translation of the protein is regulated in such a way that it is only produced if trans-translation is defective or overwhelmed. (Chadani *et al*, 2010, 2011b, 2011a; Garza-Sánchez *et al*, 2011; Schaub *et al*, 2012). ArfA binds to non-stop complexes in the empty part of the mRNA channel and recruits RF2 (Huter *et al*, 2017b; James *et al*, 2016; Kurita *et al*, 2014; Ma *et al*, 2017; Zeng *et al*, 2017). While the C-terminus of ArfA probes the mRNA channel, the N-terminus is necessary to interact with RF2 and the decoding center. ArfA can stabilize the active open form of RF2 which reaches into the PTC and leads to hydrolysis of the nascent chain from the P-site tRNA by positioning of the GGQ motif. Analogous to termination, this leads to peptide release, and the ribosome can enter the recycling phase. In contrast to trans-translation, no degradation tag is added to the incompletely synthesized protein.

The RF-independent backup system for trans-translation is ArfB. Though deletion of the trans-translation system and ArfA are lethal in *E. coli*, overexpression of ArfB can rescue these cells (Chadani *et al*, 2011b; Handa *et al*, 2011). The protein consists of an NTD that is homologous to domain III of class I RFs, and a C-terminal tail. Upon binding to the ribosome the C-terminus of ArfB forms a helix that occupies the mRNA entry channel. Then the NTD accommodates in the A-site and analogous to termination the GGQ motif is inserted into the PTC so that the ester bond between tRNA and peptide can be hydrolyzed (Carbone *et al*, 2020; Chan *et al*, 2020; Gagnon *et al*, 2012). Further, it was shown that ArfB can rescue stalled ribosomes with downstream mRNA extending towards the A-site, but the efficiency of ribosome rescue decreases with longer mRNAs (Carbone *et al*, 2020; Chan *et al*, 2020; Handa *et al*, 2011). This selectivity arises from a two-step mechanism including a fast binding event and a slow mRNA-dependent engagement step during which the CTD is inserted into the mRNA channel. If the mRNA extension is more than 9 nucleotides, the binding of ArfB is decreased by over 10-fold (Chan *et al*, 2020). Moreover, it was found, that stalled RNCs with shorter mRNA are bound by ArfB as a monomer, but longer mRNAs can be bound by two ArfB molecules. The mRNA is then stabilized outside the mRNA channel (Carbone *et al*, 2020).

An evolutionarily distinct rescue factor in gram-positive bacteria is BrfA. Genetic analysis in *B. subtilis* shows that either BrfA or the trans-translation system is necessary for survival of the cell. It is RF2-dependent and uses a similar mechanism as ArfA to recognize non-stop complexes (Shimokawa-Chiba *et al*, 2019). Another RF-dependent system is employed in *Francisella tularensis* as the species also lacks both rescue systems ArfA and ArfB. The rescue factor is ArfT, which employs a distinct mechanism by recruiting either RF1 or RF2 to hydrolyze peptidyl tRNA on nonstop ribosomes (Goralski

et al, 2018). In general and compared to the trans-translation system, the mRNA and the incompletely synthesized protein are not targeted for degradation after the action of the alternative rescue factors. This adverse rescue explains why the expression of Arfs is only upregulated when the trans-translation system is overwhelmed.

Ribosome-associated quality control acting on 50S LSUs obstructed with peptidyl-tRNA was first discovered and characterized in eukaryotes. Recently, bacterial RQC was shown to exist as Rqc2 homologs are represented in all major bacterial phyla, except for gammaproteobacteria, to which *E. coli* belongs, and actinobacteria (Burroughs & Aravind, 2019; Lytvynenko *et al*, 2019). The obstructed 50S LSU are formed by ribosomal subunit dissociation without peptide release (Figure 4). It is not yet known from which process the unrecycled splitted subunits arise as there is no such pathway as the eukaryotic non-canonical recycling by Hbs1/Dom34 (HBS1L/Pelota) (see chapter 1.3.2 Ribosome rescue and RQC in eukaryotes). A bioinformatic analysis found the Rqc2 homolog in *B. subtilis* and renamed the protein YloA to RqcH (Rqc2 homolog) (Lytvynenko *et al*, 2019). In general, Rqc2 homologs have a high sequence homology and a similar domain architecture consisting of NFACT-N, coiled coils, helix-hairpin-helix, and NFACT-R domains (NFACT = domain found in NEMF, FbpA, Caliban, and Tae2). RqcH is a 570 aa residues long protein that binds to 50S LSU obstructed with nascent chain tRNA conjugates. It interacts with the tRNA via its NFACT-N and helix hairpin helix domain. The coiled coil domain reaches towards the translation factor binding site where it can contact L7/L12 stalk base. RqcH acts in concert with RqcP (ribosome quality control P-tRNA, formerly YabO), which was found in structural studies of the bacterial RQC (Crowe-McAuliffe *et al*, 2021; Filbeck *et al*, 2021). The protein interacts with the 23S rRNA of the LSU, the anticodon stem of the peptidyl-tRNA, and the NFACT-N domain of RqcH. The system allows several rounds of tRNA^{Ala} binding and thus adds a poly-Ala tag to the nascent chain that acts as degron and is recognized by the ClpXP protease (Lytvynenko *et al*, 2019). Peptide bond formation can occur by accurate positioning of the tRNA by RqcH and RqcP. Afterwards, RqcP must dissociate to allow the uncharged tRNA to relocate to the E-site. Dissociation of the E-site tRNA then leads to rebinding of RqcP and a conformational change that shifts the peptidyl tRNA into the P-site and frees the A-site, where another tRNA^{Ala} can bind. Alternatively, RqcH could dissociate and rebind together with the tRNA^{Ala} (Crowe-McAuliffe *et al*, 2021; Filbeck *et al*, 2021; Takada *et al*, 2021). Yet, how this process is terminated remains to be discovered (Müller *et al*, 2021).

1.3.2 Ribosome rescue and RQC in eukaryotes

In eukaryotes, non-canonical termination is initiated on stalled ribosomes and involves Dom34 (in yeast, Pelota in other eukaryotes) and Hbs1 (in yeast, HBS1L in mammals). These eRF1 and eRF3 homologs act in a similar way as eRF1 and eRF3 during termination. The GTPase Hbs1 delivers Dom34 to the stalled ribosome and nucleotide hydrolysis leads to Hbs1 dissociation and accommodation of Dom34 in the A-site (Becker *et al*, 2011; Hilal *et al*, 2016; Shoemaker & Green, 2011; Tsuboi *et al*, 2012). Dom34 does not contain the stop codon recognizing NIKS motif, but instead probes the mRNA channel and competes with mRNA for A-site binding by inserting a β -loop into the channel. It is able to bind to RNCs with empty or occupied A-site, but prefers an empty A-site as substrate (Guydosh & Green, 2014; Hilal *et al*, 2016; Pisareva *et al*, 2011). In contrast to the canonical RFs, Dom34 does not contain the GGQ motif and consequentially does not promote peptidyl hydrolysis. Dom34 and Hbs1 together with ABCE1 promote subunit dissociation (Becker *et al*, 2011, 2012; Pisareva *et al*, 2011; Shoemaker & Green, 2011). If the system splits a ribosome that was stalled on an mRNA ORF, the LSU is still bound to the peptidyl-tRNA. How this obstructed 60S LSU is recycled is described below.

During stress conditions, it is important for a cell to keep intact 80S as it is a very energy-consuming process to recycle and reproduce ribosomes (Ashe *et al*, 2000). The cell thus keeps a pool of inactive ribosomes. If environmental conditions change the Hbs1-Dom34 system together with ABCE1 can split these ribosomes and translation can be reinitiated. Lso2 and Stm1 associate with non-translating ribosomes after nutrient-starvation in rotated and non-rotated state, respectively (Balagopal & Parker, 2011; Ben-Shem *et al*, 2011; Wang *et al*, 2018b; Wells *et al*, 2020). Dom34-Hbs1 and ABCE1 was found to recycle Lso2-bound hibernating ribosomes, but not Stm1- bound hibernating ribosomes (Wells *et al*, 2020).

In the first step of RQC, stalled 80S ribosomes have to be identified. If a stalled complex lacks mRNA in the A-site, it can easily be recognized and split by Dom34-Hbs1 and ABCE1. But how does a cell differentiate between a stalled and an actively translating ribosome if the stalling event occurs in the middle of an ORF? If a stalling event cannot be resolved, it can trap multiple ribosomes as they simultaneously translate an mRNA molecule. This ultimately leads to collision of a trailing ribosome with the stalled ribosome. Collided ribosomes create a unique structural interface that can be recognized by a variety of factors to trigger downstream RQC processes (Ikeuchi *et al*, 2019b, 2019a; Juszkiwicz *et al*, 2018, 2020; Simms *et al*, 2017). One of these factors that were found to bind disomes at the 40S SSU mRNA entry near the collision interface is Mbf1 (in yeast, EDF1 in mammals) (Sinha *et al*, 2020; Juszkiwicz *et al*, 2020). Earlier, genetic studies had reported inhibition of frameshifting by Mbf1 on stalled ribosomes (Wang *et al*, 2018a). Structural studies then confirmed that Mbf1 clamps the mRNA at the entry channel of the collided ribosome. Further, EDF1 was shown to recruit

translational repressors to prevent translation initiation on the aberrant mRNAs (Sinha *et al*, 2020; Juszkiwicz *et al*, 2020). In addition, ubiquitin E3 ligase Hel2 (in yeast, Znf598 in mammals) was found to selectively bind to the collided disome structure (Garzia *et al*, 2017; Ikeuchi *et al*, 2019b; Juszkiwicz *et al*, 2018; Matsuo *et al*, 2017). Binding is enhanced by the presence of Mbf1 as a sign of a persistent stalling event (Juszkiwicz *et al*, 2020). Ligation of a polyubiquitin tag to ribosomal proteins of the SSU by Hel2 can then mediate downstream events like endonucleolytic cleavage of the mRNA in the vicinity of the stalled ribosome. The resulting mRNA fragments lack either a poly-A tail or the cap structure at the 5' end and thus are degraded by the exosome or the 5'-3' exonuclease Xrn1, respectively. This mRNA quality control pathway that targets mRNAs that inhibit translation is called no-go decay (NGD) (Doma & Parker, 2006; Schuller & Green, 2018). The order of action and the role of the different factors involved in ubiquitin-dependent ribosome subunit dissociations are incompletely understood and focus of current research.

An endonuclease that was found to be involved in stall-dependent mRNA cleavage is Cue2. It is recruited to the disome and supposedly cleaves the mRNA in the A-site of the collided ribosome (D'Orazio *et al*, 2019). The collided ribosome can then be rescued by the known ribosome rescue factors Dom34 and Hbs1 (Guydosh & Green, 2014; Hilal *et al*, 2016). The endonuclease Cue2 consists of two N-terminal CUE (coupling of ubiquitin to ER degradation) domains, two putative ubiquitin-binding domains (UBA – ubiquitin-associated domain), and a C-terminal SMR (small MutS-related) domain (D'Orazio *et al*, 2019). SMR domains are known to exhibit DNA and RNA nuclease activity and have a structural similarity to bacterial endonuclease RNase E (Fukui & Kuramitsu, 2011). Moreover, the domain was found to be structurally homologous to the CTD of the bacterial IF3, which binds close to the P- and A-site during translation initiation. Mutational analysis identified certain residues within the SMR domain, which are critical for endonuclease cleavage and which according to this structural homology would sit in close proximity to the mRNA (D'Orazio *et al*, 2019). Structural studies of Cue2-bound to collided ribosomes will be needed to understand the molecular mechanism of this process.

Another branch of this pathway is the Dom34/Pelota- and Hbs1- independent splitting (Matsuda *et al*, 2014). The RNA helicase Slh1 (in yeast, ASCC3 in mammals) together with ubiquitin-binding protein Cue3/Rqt3 and Ykr023w/Rqt4 forms the RQC trigger complex (RQT) (Matsuo *et al*, 2017; Sitron *et al*, 2017), which was found to specifically bind to polyubiquitinated collided ribosomes and split these into subunits in an ATP-dependent manner. It acts on the first stalled ribosome and splits it into 40S SSU and 60S LSU (Hashimoto *et al*, 2020; Matsuo *et al*, 2020). Future studies will be needed to understand the molecular mechanism of this splitting reaction.

After non-canonical splitting of the ribosome, the peptidyl-tRNA can still be attached to the 60S LSU. Before the 60S can be reused for translation this complex has to be recycled. Further, the incompletely synthesized protein has to be targeted for degradation as improper folding could lead to formation of toxic aggregates. An important discovery in how these complexes are recognized and the nascent chain is degraded was made by Bengtson and Joazeiro (Bengtson & Joazeiro, 2010). They identified Ltn1 (in yeast, Listerin in other eukaryotes), an E3 ubiquitin ligase that adds a polyubiquitin tag to the nascent chain and thus targets it for degradation. The large protein consists of conserved N-terminal and C-terminal domains that directly bind to the 60S and that are connected by a series of HEAT-type and ARM-type helical repeats. The NTD binds to the intersubunit side of the 60S LSU and the C-terminal RING domain is positioned at the exit tunnel (Lyumkis *et al*, 2014). Later, Rqc2 (in yeast, NEMF in eukaryotes) was found to be involved in this process (Brandman *et al*, 2012; Defenouillère *et al*, 2013; Lyumkis *et al*, 2014; Shao *et al*, 2015). Rqc2 also binds to the intersubunit side of the 60S LSU and interacts with the tRNA (Lyumkis *et al*, 2014). Consequently, Rqc2 could not bind to translating 80S and inhibits re-association of the 40S SSU. Rqc2 recruits Ltn1 to form the RQC complex (Lyumkis *et al*, 2014; Shao & Hegde, 2014; Shao *et al*, 2015). The architecture of the RQC complex allows to specifically recognize the substrate - obstructed 60S - and interact with the nascent chain. Ltn1 preferentially modifies lysine residues. If no lysine is present in the nascent chain, the system elongates the nascent peptide with alanine and threonine residues (CAT tail) by successive rounds of tRNA binding and peptide bond formation (Kostova *et al*, 2017; Osuna *et al*, 2017; Shen *et al*, 2015). This process is independent of mRNA and the 40S SSU. As a result, the nascent chain is pushed out of the tunnel and previously hidden lysine residues emerge from the exit tunnel. By adding the ubiquitin tag in the presence of the 60S LSU, Ltn1 can recognize a highly heterogeneous set of substrates. In case the RQC complex acts on a nascent chain without a lysine residue, the CAT tail itself can act as a degron (Sitron & Brandman, 2019). In mammalian cells it was found that an Ala tail is generated at the C-terminus. This can also act as a signal for degradation by the ubiquitin-proteasome system independent of Listerin (Thrun *et al*, 2021).

The process of CAT tailing is terminated by Vms1 (Zurita Rendón *et al*, 2018), which binds to the intersubunit side of the 60S LSU antagonizing Rqc2 (Su *et al*, 2019). Surprisingly, Vms1 was found to perform nucleolytic cleavage of the peptidyl-tRNA between nucleotide 73 and 74. This leaves a truncated tRNA and a nascent chain attached to the CCA end of the tRNA (Yip *et al*, 2019). The tRNA can be recycled by a CCA-adding enzyme that mediates tRNA biogenesis. Further, the ABCF-type ATPase Arb1 was found associated with Vms1-bound obstructed 60S LSU particles. It directly interacts with the peptidyl-tRNA and can stimulate the nuclease activity of Vms1 (Su *et al*, 2019). Eventually,

Rqc1 and the AAA-ATPase Cdc48 extract the polyubiquitinated nascent chain and target it to the proteasome.

2. AIMS AND OBJECTIVES

2.1 Structural analysis of ABCE1 in ribosome recycling and translation initiation

Several studies have characterized the role and structure of ABCE1 during the ribosome splitting process. Heuer and colleagues (Heuer *et al*, 2017) reported the *S. cerevisiae* structure of the ABCE1-bound post-SC at 3.9 Å. Comparison to the pre-SC (Becker *et al*, 2012; Brown *et al*, 2015; Preis *et al*, 2014), revealed a large rotation of the FeSD of ABCE1, which provided a plausible structural model for how the ribosome is split. Moreover, the movement is accompanied by closure of the NBDs and the change to a nucleotide-occluded conformation of the NBSs. The identity of the nucleotide in NBSI could certainly be assigned as AMP-PNP-Mg²⁺ and interaction to residues in the NBSI could be defined, whereas the local resolution of NBSII was lower and did not allow for analysis on side chain level. Given the asymmetry and the different roles of the two NBS in the splitting process (Barthelme *et al*, 2011; Nürenberg-Goloub *et al*, 2018), questions regarding the molecular basis of these differences remained. Moreover, how signals from the ribosome would be communicated into the NBSs was not understood. In publication 1 (Nürenberg-Goloub *et al*, 2020) we aimed to obtain a high-resolution cryo-EM structure and characterize the archaeal post-SC. Comparison to the yeast post-SC would then allow dissecting the structural relevance of evolutionarily conserved residues within ABCE1 and of residues participating in the interaction to the ribosome. Further, the structural data would be complemented with functional data by testing splitting efficiency and ribosome binding affinities of different ABCE1 mutants. We aimed to draw a more complete picture of ABCE1 and its functional sites during the splitting process.

The translation process is divided into four phases: initiation, elongation, termination, and recycling. Most of the translation factors can be mapped to one of these phases, but some exceptions exist. For example, eIF3, has been described to play a role in initiation, the first rounds of elongation as well as termination and recycling (Valášek *et al*, 2017). Another factor that links ribosome recycling to initiation is ABCE1. The splitting factor was found associated with initiation complexes (Andersen & Leever, 2007; Chen *et al*, 2006; Dong *et al*, 2004; Heuer *et al*, 2017) and it could be visualized in eukaryotic 43S PIC and partial 48S IC (Mancera-Martínez *et al*, 2017; Simonetti *et al*, 2016, 2020). However, these structures were obtained after adding non-hydrolysable nucleotide analogues, which would lock ABCE1 on the SSU, and thus the physiological relevance of these complexes was not clear. The question arose whether ABCE1 stayed bound after splitting to act only passively as an anti-association factor, or whether it plays a more active role in initiation. Further, it is important to understand which steps are influenced by ABCE1 and what eventually triggers its dissociation. Thus, the aim of publication 2 (Kratz *et al*, 2021) was to obtain native ABCE1-bound eukaryotic initiation

complexes representing different stages of initiation and analyse them by cryo-EM. This was complemented by quantitative mass spectrometry of elution fractions of ABCE1 affinity purification and crosslinking mass spectrometry of initiation complexes to validate structural findings. Furthermore, the structural analysis of the initiation complexes would allow dissecting the interaction network of other initiation factors such as eIF3.

2.2 Structural basis of ribosome rescue in bacteria

In prokaryotes, ribosome rescue systems for non-stop complexes have been investigated extensively. Most importantly, the trans-translation system, but also the backup systems ArfA and ArfB were described in great detail (Müller *et al*, 2021). These pathways require the mRNA to be degraded so that the A-site of the ribosome is empty. In eukaryotes, an additional mechanism was found to act as a sensor for translational failure. Stalling events lead to ribosome collisions, which form a unique structural interface that can be recognized by collision sensors to imitate ribosome rescue (Inada, 2020; Sitron & Brandman, 2020; Yan & Zaher, 2019). This mechanism allows recognition of ribosomes with occupied A-site and discrimination between actively translating and stalled RNCs. The aim of this work was to understand whether a similar mechanism exists in bacteria. Therefore, in publication 3 (Saito *et al*, 2021) bacterial disomes were isolated and structurally characterized. Subsequently, a structure of disomes with SmrB, a potential collision sensor resulting from a genetic screen in *E. coli*, was to be determined.

3. SUMMARY AND DISCUSSION OF PUBLICATIONS

Publication 1 | Molecular analysis of the ribosome recycling factor ABCE1 bound to the 30S post-splitting complex.

In the last step of protein translation, the ribosome is split into subunits. A key factor involved in this process is the recycling factor ABCE1. Previous structural studies of the ABCE1-bound pre- and post-SC laid the foundation of a principle understanding of this process. Still, how ABCE1 and its ATPase conformational cycle orchestrate ribosome recycling on a molecular level was enigmatic. In publication 1 (Nürenberg-Goloub *et al*, 2020), the cryo-EM reconstruction of ABCE1 bound within the archaeal 30S post-SC at 2.8 Å resolution is presented. The complex was obtained by performing an *in vitro* splitting reaction, in which the ATPase deficient mutant of ABCE1 was used. The reaction products were separated by sucrose density gradient centrifugation and the 30S SSU fractions were subjected to structural analysis. Cryo-EM data processing and focused refinements allowed to obtain a high-resolution structure for all regions of the post-SC. By analyzing the archaeal 30S SSU structure, a new archaeal ribosomal protein was discovered, located on the 30S platform and occupying an equivalent position as eS21 in eukaryotes. Moreover, the cryo-EM structure allowed to build the first molecular model of the *T. celer* 30S SSU.

The majority of the 30S SSU particles were bound by ABCE1 and the structure was in overall agreement with previous post-SC complexes. Yet, the structure of the post-SC contained important molecular details as the resolution for ABCE1 and its interaction sites with the SSU were significantly better resolved than previous structures. A comparison of the archaeal to the yeast post-SC (Heuer *et al*, 2017) revealed that most of the interactions to the ribosome are highly conserved and in some cases, a co-evolution of ABCE1 and the ribosome was observed. Based on the structure, ABCE1 mutants were generated and analyzed for cell viability.

ABCE1 is anchored on the SSU via its FeSD, HLH, and hinge regions. Mutation of most of the residues involved in the interactions showed a growth defect or were lethal and thus essential for ABCE1's function. Hinge 2 serves as a linchpin during ribosome splitting as its interactions to the ribosome are kept during the splitting process. The importance of specific residues in this domain could further be confirmed by directly testing the splitting efficiency or the ability to bind the ribosome of the respective ABCE1 mutants.

When analyzing NBSI and NBSII of ABCE1, the non-hydrolysable ATP-analogue AMP-PNP, complexed with an Mg²⁺ ion being bound, was identified. Furthermore, interactions within the NBSs could be described on side chain level. We thus asked whether the NBSs are in an ATP hydrolysis competent

state. In both NBSs, the γ -phosphate of AMP-PNP and the Mg^{2+} ion were coordinated by the canonical residues of Walker A, His-switch, signature motif and Q-loop. The nucleotide base is sandwiched between the A loop and the signature motif of the two opposing NBDs. Comparison of the NBS to other ABC proteins did not reveal any significant differences (Korkhov *et al*, 2012, 2014; Manolaridis *et al*, 2018). Although the local resolution of the NBSs allowed to identify the orientation of side chains, water molecules or small conformational changes could not be resolved. These changes could of course also influence the reaction process and thus the interpretation was limited by the local resolution of the NBSs. Moreover, ABCE1 mutated for the conserved glutamates adjacent to the Walker B motifs (E238A in NBSI, E485A in NBSII) was used and the non-hydrolysable nucleotide analogue AMP-PNP were added to the reaction. This may further limit the validity of this comparison. Still, it seemed likely that in the observed conformation hydrolysis would occur.

Asymmetry of the nucleotide binding sites of ABCE1

As many eukaryotic ABC transporters, ABCE1 consist of two asymmetric halves with a consensus and a degenerated NBS. Typically, the degenerated site shows decreased ATPase activity and this holds true for ABCE1. ABCE1 processes a functional and dynamic asymmetry of the two NBSs with the consensus NBSI and the degenerated NBSII (Barthelme *et al*, 2011; Gouridis *et al*, 2019; Nürenberg-Goloub *et al*, 2018). Hence, an important question to be addressed was the molecular basis for the asymmetry of the two NBSs. The resolution of our complex allowed to compare the two NBSs of ABCE1, showing that all residues are superimposable, except for the degenerated A-loop of NBSII. The conformation and the interactions of the nucleotide within the NBSs are indistinguishable. This structural analysis was in agreement with mutational studies showing that generating a consensus A-loop in NBSII did not affect its ATPase activity.

This led to the conclusion that ribosome binding might be rather allosterically than directly communicated into the NBSs. Therefore, potential communication pathways from the hinge regions into the NBS were analyzed. Here, the most striking observation was an opening of the hinge region. Detailed analysis of this movement allowed to formulate a model how the signal from ribosome binding may be transmitted to the NBSs.

Comparison between the pre- and post-splitting complex

ABC ATPases consist of two NBDs, and associated domains, which can serve very different functions. The NBSs are formed at the interface of the two NBDs and binding and hydrolysis is accompanied by conformational changes, which are propagated to the associated domains or interacting ligands. Further, the associated domains can activate ATP hydrolysis by allosteric signals. Together this drives

a conformational cycle and allows the protein to perform directional motion using the energy of ATP hydrolysis (power stroke) (Locher, 2016; Hopfner, 2016). In the case of ribosome splitting factor ABCE1, the associated domains are the FeSD, the HLH domain, and two hinge domains. These domains are responsible for nearly all interactions with the ribosome in the pre-SC and the post-SC (Brown *et al*, 2015; Heuer *et al*, 2017). The transition from the pre- to the post-SC leads to a rearrangement and conformational changes of these domains. But how are these movements are coupled to the ATPase cycle? The closure of the NBSs is accompanied by repositioning of the HLH domain and a large rotation of the FeSD, as well as a “hinge opening”. Here, hinge 2 acts as a linchpin that anchors ABCE1 on the SSU. The spatial separation of the two hinge domains alters the interface to the NBDs and this interface is in direct vicinity to the His-switches of NBSI and NBSII. This could create a direct link from the hinge region to the NBSs. As a matter of fact, ABCE1’s hinge domains are located in the same position as comparable, functionally important equivalents in other ABC proteins, like for example the coupling helices in ABC transporters (Locher, 2009). This further supports the hypothesis that the conformational changes in ABCE1’s hinge regions regulate nucleotide binding and hydrolysis

A refined model for ribosome splitting by ABCE1

In the pre-SC, interactions of ABCE1’s associated domains with the ribosome and the A-site factor (either eRF1 or Dom34/Pelota) together may enhance ATP binding affinity. The NBDs within this complex adopt a semi-closed state. The intrinsically slow closure of NBSII could then serve as a control step to ensure correct engagement with the post-termination complex. Structural analysis suggested that closure of NBSII prior to NBSI is possible as none of the mobile parts participates in ribosome binding. This is in agreement with earlier studies that reported NBSII as the control site and fast association of ABCE1 with the ribosome, but slow closure of NBSII (Gouridis *et al*, 2019; Nürenberg-Goloub *et al*, 2018). Complete closure of NBS II could then trigger an allosteric chain that leads to closure of NBSI, which displaces the FeSD and then splits the ribosome into SSU and LSU. Such a sequential hydrolysis has also been described for other ABC transporters (Aittoniemi *et al*, 2010; Stockner *et al*, 2020). Mutational analysis of the hinge regions focusing on residues that are important for ribosome binding as well as for the communication pathways to the NBSs could confirmed their important role in the splitting event.

In context of such model, the slow ATP turnover in NBSII could determine the dwell time of ABCE1 on the post-SC. After splitting, ABCE1 could act as anti-association factor or influence downstream events. Whether the ATPase activity of NBSII is the only parameter that determines the dwell time remains enigmatic. Our structure was derived from an *in vitro* splitting reaction and thus additional factor that could influence the process, would not be captured in this context.

3. SUMMARY AND DISCUSSION OF PUBLICATIONS

Future work will be needed to define the precise role of ABCE1 after splitting. Two important questions remain to be answered. First, does ABCE1 stay bound to the post-SC after splitting *in vivo*? And second, what triggers ATP hydrolysis and ABCE1 dissociation? Possibilities are an allosteric signal from the ribosome or other factors that are recruited to the split SSU. An experiment that could answer these questions would need to capture ABCE1 under native conditions.

Publication 2 | Structural inventory of native ribosomal ABCE1-43S pre-initiation complexes.

In publication 1, a thorough characterization of ABCE1's conformational changes during ribosome recycling was performed and linked to its ATPase cycle. However, open questions remained regarding the dissociation of ABCE1 from the SSU and its influence on downstream events. In publication 2 (Kratzat *et al*, 2021) the role of ABCE1 in translation initiation was investigated.

In general, in the first step of eukaryotic protein translation, the 40S SSU is bound by IFs to form the 43S PIC, which can bind and scan an mRNA until a start-codon is reached. Then the 60S LSU joins and translation of an ORF is initiated (see chapter Translation initiation in eukaryotes) (Hinnebusch, 2014, 2017; Merrick & Pavitt, 2018; Sokabe & Fraser, 2019). The 40S SSU within this process can originate from a splitting reaction, which is catalyzed by the ATPase ABCE1. Nucleotide binding and closure of the two NBSs of ABCE1 are necessary for the splitting reaction, whereas ATP hydrolysis is responsible for its dissociation from the SSU (Barthelme *et al*, 2011; Gouridis *et al*, 2019; Nürenberg-Goloub *et al*, 2018).

Notably, ABCE1 was previously found associated with 40S subunits and components of the 43S PIC, especially when Walker mutants of ABCE1 were analyzed or non-hydrolysable ATP or GTP analogues were added ((Heuer *et al*, 2017; Simonetti *et al*, 2016; Mancera-Martínez *et al*, 2017). Under these circumstances, ATP-hydrolysis dependent dissociation of ABCE1 from the SSUs was seemingly impaired. However, one important question was whether wild type ABCE1 can also stay associated with SSUs and even plays a *bona fide* role in initiation *in vivo*.

This study shows biochemically that wild type ABCE1 associates with 40S and 80S fractions. Quantitative mass spectrometry revealed that SSU ribosomal proteins, but also IFs, especially eIF3j, co-purified with ABCE1. As the sub-stoichiometric subunit of eIF3 was implicated with ABCE1-dependent ribosome recycling, its impact on ribosome splitting was tested. The *in vitro* splitting reactions with wild type ABCE1 showed that the addition of molar excess of eIF3j indeed increased the ratio of split subunits. Moreover, when analyzing the splitting products, ABCE1 as well as eIF3j were found associated with the 40S SSU.

In a second step, a structural analysis of PICs and ICs from human and yeast was performed using cryo-EM. All complexes were obtained without the addition of non-hydrolysable nucleotide analogues and large data sets were collected in order to dissect their complex composition *in silico*. Thus, a structural inventory of native initiation complexes could be obtained, in which ABCE1 was associated with 43S PIC as well as 48S IC. Focused classifications and multi-body refinements of the human 43S PIC allowed to obtain molecular resolution and thus to build a near-complete molecular model. In this complex,

ABCE1 was observed in a novel hybrid conformation. Different from previously observed structures, the NBSI of ABCE1 was in a new intermediate conformation with Mg^{2+} -ADP bound. NBSII was in a closed conformation with Mg^{2+} -ATP bound. This suggested that ATP-hydrolysis in NBSI had occurred, whereas NBSII was still inhibited. This conformation was also observed for the yeast ABCE1-bound complex. Moreover, this study revealed that the NBS conformation was stabilized by the N-terminus of eIF3j. Because the local resolution of this interaction was rather low, another data set of a yeast 43S PIC derived from a TAP-tagged eIF3c (Nip1) strain was collected. Crosslinking coupled with mass spectrometry of this complex confirmed that the N-terminus of eIF3j interacts with the NBDs of ABCE1 and thus could potentially modulate ATPase activity.

The role of recycling factor ABCE1 in translation initiation

Analysis of the cryo-EM data described above show that ABCE1 is present during all stages of initiation before subunit joining, leading to the hypothesis that it may be directly involved in initiation. But, why does ABCE1 stay associated with 43S PIC and 48S IC after ribosome recycling? Previously, it had been suggested that ABCE1 could act as an anti-association factor ensuring that the 40S would not engage in unproductive 80S formation directly after termination (Gerovac & Tampé, 2019; Heuer *et al*, 2017; Mancera-Martínez *et al*, 2017). However, this role cannot explain the presence of ABCE1 during all stages of initiation, especially because the initiation factors themselves can act as anti-association factors which would make ABCE1 dispensable. Early studies already brought ABCE1 in context with translation initiation as it co-purified with eukaryotic IFs (Dong *et al*, 2004; Chen *et al*, 2006), and associates with 40S SSU in an ATP-dependent manner (Andersen & Leever, 2007).

This study showed that ABCE1 directly interacts with eIF3j in the 43S PIC showing for the first time a direct physical link between the termination/recycling and the initiation machinery. These results were not only based on the cryo-EM structure but could also be confirmed by protein crosslinking coupled with mass spectrometry. The finding is further supported by earlier studies showing an interaction between ABCE1 and eIF3j by performing yeast two-hybrid assays (Khoshnevis *et al*, 2010; Kispal *et al*, 2005). The observed interaction is formed by the N-terminus of eIF3j protruding into the composite NBSs of ABCE1. This suggests that the function of eIF3j is to keep ABCE1 NBSI from fully opening up and thus to prevent dissociation of ABCE1 from the post-SC. The finding that ATP-hydrolysis in NBSI had occurred, whereas NBSII was still inhibited is consistent with earlier functional data showing that closure of NBSII allosterically activates NBSI (Nürnberg-Goloub *et al*, 2018). From the structural analysis, however, it is not clear why ATP hydrolysis has not happened in NBSII. Yet, the finding that the ATPase activity of ABCE1 is inhibited by the SSU but necessary for its dissociation (Nürnberg-Goloub *et al*, 2018) could explain why NBSII has not hydrolyzed the bound ATP. In general,

for most of the eukaryotic ABC transporters a degenerated NBS of functional importance has been reported (Stockner *et al*, 2020). It seems likely that a different factor after ribosome recycling is necessary to remove ABCE1. This could happen directly via an interaction and activation of NBSII or indirectly for example by competing for binding with eIF3j as its dissociation could allow further opening of NBSI.

Notably, in the yeast data set ABCE1 was not only observed associated with 43S but also with a 48S IC. This 48S IC, however, does not contain eIF3j, which suggested that eIF3j may stabilize ABCE1 in the PIC, but is not the trigger for its dissociation. This is in agreement with the fact that eIF3j is nonessential (Valásek *et al*, 1999), and ABCE1 was observed to be locked on the post-SC in the absence of eIF3j (Simonetti *et al*, 2016; Mancera-Martínez *et al*, 2017). Interestingly, in archaea the ribosomal stalk protein was found to interact with ABCE1 in the same region as eIF3j and modulate its ATPase activity (Imai *et al*, 2018). These data give rise to speculations, that eventually subunit joining is the final trigger for ABCE1 dissociation. Another possible explanation is a rearrangement of eIFs on the 48S IC. In this context, Llácer and colleagues (Llácer *et al*, 2015, 2021) reported a repositioning of the eIF3b-CTD/eIF3i/eIF3g-NTD module to the intersubunit side, which would sterically clash with ABCE1. However, as these structures were derived from *in vitro* reconstitution without ABCE1, it is difficult to assess whether this movement triggers ABCE1 dissociation or whether ABCE1 would block the relocation *in vivo*.

Taken together, this study establishes ABCE1 as an optional component of the 43S PIC. It describes the interplay with eIF3j and via this communication with other eIFs may be possible. Future studies will be necessary to further elucidate additional roles of ABCE1 during initiation.

The role of eIF3j in ribosome recycling and translation initiation

The role of eIF3j in ribosome recycling and translation initiation has been explored in several studies. Although the sub-stoichiometric subunit of eIF3 was initially only assigned to translation initiation, it was found that deletion of the eIF3j encoding Hcr1 gene leads to stop codon readthrough (Beznosková *et al*, 2013, 2015). A ribosome profiling study could confirm these results *in vivo* and further defined its role as accessory factor in 60S LSU recycling by ABCE1 after termination (Young & Guydosh, 2019). Moreover, a recent study reported that eIF3j already participates in recruitment and loading of eRFs to the ribosome, and stimulating peptidyl-tRNA hydrolysis (Egorova *et al*, 2021). In this study, the active role of eIF3j in ribosome recycling could be confirmed. The results of the *in vitro* splitting assays clearly showed a higher splitting rate for reactions that were performed with molar excess of eIF3j. For future experiments it would be interesting to investigate the structure of eIF3j-bound pre-SC.

When comparing the 43S PIC to an ABCE1-bound termination complex (Brown *et al*, 2015; Preis *et al*, 2014), the position of eIF3j would only sterically clash with the FeSD domain of ABCE1. One could imagine that eIF3j is recruited to the termination complex via an interaction with eRF3 and the ribosome (Egorova *et al*, 2021). Then, during recycling binding of eIF3j close to the A-site would enhance ribosome splitting as it facilitates displacement of the FeSD. Afterwards, both factors, ABCE1 and eIF3j, stay associated and eIF3j could help in recruitment of the MFC or eIF3 to form the 43SPIC (Aylett *et al*, 2015; Fraser *et al*, 2004).

Structural analysis of eIF3j using hydroxyl radical probing and cryo-EM mapped its binding site close to the A-site of the 40S SSU (Aylett *et al*, 2015; Erzberger *et al*, 2014; Fraser *et al*, 2007). However, the low resolution of these structures did not allow determination of the orientation or positioning of secondary structure elements of eIF3j. In this study, the high-resolution structure of the crosslinked yeast 43S PIC confirmed the binding site of eIF3j. Further, the structure allowed to build a molecular model and to describe interactions between eIF3j and the ribosome. Also in the cryo-EM structures of the human and yeast 43S PIC, eIF3j was well enough resolved to place secondary structure elements. The structure revealed that eIF3j folds into a dimer with the middle part of eIF3j forming a 6-helix bundle with the N-termini in close proximity and the C-termini facing into opposite directions. A crystal structure of the human eIF3j dimer had been described before, which matches these findings (PDB 3BPJ). The helix bundle is positioned near the A-site and might explain eIF3j's suggested role in start-site selection (Elantak *et al*, 2010). The N-termini could interact with ABCE1 and the RRM of eIF3b (Elantak *et al*, 2010). From the structure it remains unclear whether one N-terminus contacts both factors or whether both N-termini are involved.

Furthermore, the structure clearly showed the C-terminus of eIF3j elongating into the mRNA entry channel. This would clash with mRNA binding, which suggested that eIF3j would need to dissociate before 48S IC formation. This is in agreement with earlier studies, which found eIF3j and mRNA binding anti-cooperatively to the 40S SSU (Fraser *et al*, 2007; Mitchell *et al*, 2010). This suggests that eIF3j needs to dissociate after mRNA recruitment. However, as the factor was described to be involved in stringent AUG recognition (Elantak *et al*, 2010) and was found bound in a 48S IC (Querido *et al*, 2020), it seems more likely that the C-terminus is removed but eIF3j stays bound to the 48S IC.

Surprisingly, a comparison between the binding mode of eIF3j in yeast and human, revealed eIF3j bound in a similar overall position, yet rotated by 100°. An explanation for this could be that the binding mode differs between species or that eIF3j could take in multiple conformations. These conformations could be dependent on binding of other IFs or mRNA, and the state of translation

initiation. Here, future studies will likely shed light on the dynamic behavior of eIF3j from termination to initiation.

Different compositional states of the initiation complexes

The initiation pathway is usually presented as a sequence of defined steps, but in fact our understanding of the dwell time and the order of binding and release of all the different components during initiation is limited (Sokabe & Fraser, 2019). In this study, various compositional states were described and attempts were made to assign them to the distinct steps of initiation. For the human data set four different states were described (Figure 5). All of them represented 43S PICs as they lack density for mRNA. Particles were initially sorted on the presence of the TC, which yielded two equally populated classes. They were easy to distinguish not only by the presence or absence of the TC, but also by the different 40S head conformations as TC binding induces latch opening and thus allows for mRNA binding, as also previously described (Llácer *et al*, 2015). The TC-containing classes also showed density for eIF1A. In a second step, the particles were classified on the presence of ABCE1. ABCE1 was observed to be associated in approximately 30% of the 43S PIC particles, independent of the presence of the TC. Further classification could have yielded more different compositional states, but the particle number limited this procedure. A subpopulation containing ABCE1 and eIF3j was observed, which is in agreement with the native pullouts from yeast. Interestingly, presence of ABCE1 and eIF3j coincides with presence of the RRM of eIF3b in a defined position. The stabilization is probably achieved by an interaction with the N-terminus of eIF3j, which has been described before (Elantak *et al*, 2010; Valásek *et al*, 2001).

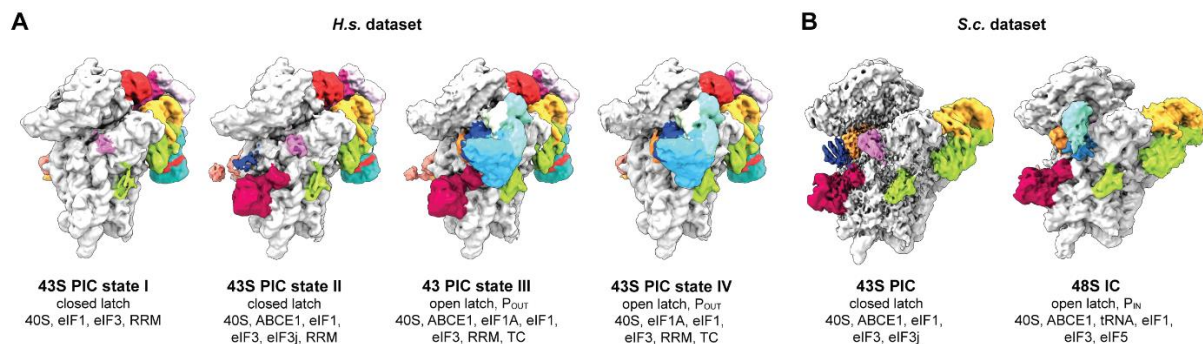


Figure 5: Overview of initiation complexes. (A) Different compositional states of the pre-initiation complexes (PICs) found in the human dataset. (B) ABCE1-bound 43S PIC and 48S initiation complex (IC) found in the yeast dataset. Figure adapted from Kratzat *et al*, 2021.

Another interesting aspect was the formation of the 43S PIC. It had been suggested that the MFC is formed by eIF1, TC, eIF3 and eIF5, which is then recruited to and embraces the 40S SSU. This is accompanied by large conformational changes (Zeman *et al*, 2019). The different compositional states in our study, led to the assumption that only after binding of eIF1 and eIF3, eIF1A and the TC are recruited to the 43S PIC. Still, whether these states exist because the factors dissociated during sample preparation or have not been bound yet, is not clear.

Apart from valuable insights into a potential regulation of ABCE1 dwell time on the 40S, the high-resolution structure of the human 43S PIC allowed to analyze its molecular architecture in unprecedented detail. For example the interaction network within the eIF2 $\alpha\beta\gamma$ -GTP-tRNA TC could be described, especially with respect to the eIF2 γ GTP-binding pocket and the positioning of the methionylated CCA-end of the tRNA. Moreover, the interaction between eIF3 and the ribosome as well as interactions in between the eIF3 subunits could be described on side chain level for most of the regions of the complex. This analysis revealed that the N-terminus of eIF3d is an integral part of the eIF3 PCI-MPN core. Further, a better resolution for the N-terminus of eIF3c allowed to precisely describe the position of its 4-helix bundle at the intersubunit space and its connection to the PCI-MPN core via an interaction with eIF1. Similarly, the structure provided insights into the linkage of the PCI-MPN core with the YLC via a long α -helix of the eIF3a C-terminus. In summary, the presented structures added important information on how the initiation factors entangle the 40S SSU during initiation.

Publication 3 | Ribosome collisions in bacteria promote ribosome rescue by triggering mRNA cleavage by SmrB.

Erroneous protein synthesis is highly detrimental to the cell. Recognition of translation failure and subsequent recycling of ribosomes are crucial to maintaining ribosome homeostasis in all domains of life. Moreover, the mRNA and the potentially toxic protein have to be degraded (Buskirk & Green, 2017; Joazeiro, 2019). In bacteria, two well-studied ribosome rescue systems distinguish stalled ribosomes from actively translating ribosomes by binding to the mRNA channel A-site (Müller *et al*, 2021). However, this cannot work when the stalling events occur in the middle of an ORF and the A-site is not accessible. Here, mRNA cleavage events were proposed to create substrates for the known rescue pathways. Though, the identity of the nucleases, as well as the mechanism of recognition of stalled complexes, had not been known.

In this work, a collision-dependent ribosome rescue system in *E. coli* that acts on no-go complexes is reported. This system was discovered by a genetic screen, which selected for mutants that allow ribosomes to translate through a stalling motif and a knock-out library of about 5 million colonies. The gene of *smrB* was identified as it was strongly enriched for transposon insertions. Afterwards a *smrB* deletion strain was created to confirm the phenotype. The SmrB protein contains an SMR domain, which was reported to possess endonucleolytic RNase activity (Bhandari *et al*, 2011; Wu *et al*, 2016; Zhou *et al*, 2017). Phylogenetic analysis showed that SMR domains are broadly conserved in bacteria and eukaryotes. Further, it revealed a conserved DxH motif associated with nuclease activity. Generation of an endogenous SmrB mutant strain (D₉₉LH₁₀₁ mutated to ALA) showed similar effects as deletion of *smrB*. In order to identify the mRNA cleavage site of SmrB in respect to a stalled ribosome, 5' and 3' Rapid Amplification of cDNA ends (RACE) experiments for a SecM reporter were conducted. The results revealed that SmrB cleaves upstream at the mRNA exit of the stalled ribosome. Moreover, the data suggested that in the absence of SmrB, other pathways lead to mRNA decay up to the A-site of the stalled ribosome. tmRNA tagging was monitored by LC-MS-MS and it was shown that SmrB cleavage generates substrates for tmRNA, but is not required for the activity of the pathway.

However, this could not explain how SmrB selectively recognizes stalled ribosomes. The 5'-RACE data showed that SmrB cleaves downstream mRNA at sites clustered with roughly 25 nts distance. This led to the speculation whether ribosome collisions could trigger SmrB cleavage. Therefore, nuclease-resistant disomes were created, and indeed an increased association of SmrB in these fractions was observed. Moreover, antibiotic treatment was used to increase the amount of collisions. Also here, sucrose gradients showed that after the treatment, SmrB was enriched in the polysome fractions. As collisions only occur when the mRNA exceeds a certain length, reporters with different lengths

upstream of the stalling site were created. The cleavage of mRNA by SmrB could only be observed for the reporters longer than 80 nts. This further supported the idea that SmrB activity is triggered by collisions.

To structurally characterize collided ribosomes, disomes in *E. coli* and *B. subtilis* were generated by *in vitro* translation of mRNAs encoding the arrest peptides VemP and MifM, respectively and subjected to structural analysis by cryo-EM. The 3D reconstruction of the *E. coli* disome revealed a tight interaction of the two ribosomes mostly via the 30S SSUs with the mRNA exit of the stalled ribosome facing the mRNA entry of the collided ribosome. Surprisingly, the L1 stalk of the stalled ribosome participates in this interaction network by forming a contact with its rRNA H78 to the 16S h16. Another bridge is formed by the protein bL9 of the stalled ribosome. Compared to bL9 in the collided ribosome it undergoes a large conformational change that flips out its C-terminal domain and allows the protein to reach over to the 30S SSU of the collided ribosome. Another important difference was that bS1 is missing in the stalled ribosome as it would sterically clash with the collided ribosome. Analysis of the *B. subtilis* disome structure revealed a very similar arrangement, which suggests that disome formation is conserved in bacteria.

Structural basis of bacterial ribosome collisions

The disome structure in eukaryotes is formed by extensive interactions between the 40S SSUs of the stalled and the collided ribosome. This study presents for the first time how ribosome collisions lead to a defined arrangement of the leading stalled ribosome and the trailing ribosome in bacteria. Although the ribosomes are oriented in a similar way, the disome interface is formed differently in bacteria and eukaryotes. In yeast, RACK1 and uS10, eS17 and uS2/eS21, eL27 and expansion segment 6b, expansion segment 31L and eS4 interact for the stalled and the collided ribosome, respectively (Ikeuchi *et al*, 2019b). So, many eukaryotic specific elements of the ribosome are involved in the interaction. In comparison in bacteria, uS10, uS9, uS2, uS4, uS11, bS6, bL9, and rRNA h16 and H78 are involved in formation of the disome interface. This difference and the fact that the overall architecture of a disome is conserved, implies that disome formation does not depend on the individual interactions between the rps. This is also supported by the finding that the conformational change of bL9 does not play an essential role in stabilization of the disome interactions. An important feature that could determine the disome structure is the force behind the motion of the trailing ribosome to move forward on the mRNA. As the stalled ribosome is trapped on the mRNA in a certain position that depends on the nature of the stalling motif or cause, the movement of the trailing ribosome is only stopped when the structure with the closest mRNA exit to mRNA entry distance is formed. In our cryo-EM reconstruction, we observed the density for the mRNA between the two ribosomes, which hints

towards a rather low flexibility as it would be the case for an mRNA that is stretched between the two ribosomes. The same is true for the disome structure in yeast (Ikeuchi *et al*, 2019b).

Upon ribosome collision, the ribosomal protein bS1 has to dissociate from the stalled ribosome as it would sterically clash with the 30S SSU of the collided ribosome. In general, bS1 is essential for translation, especially during initiation, where it helps to unwind secondary structure of the mRNA and to position the SD sequence (Boni *et al*, 1991; Duval *et al*, 2013; Gualerzi & Pon, 2015; Qu *et al*, 2012). The six domain protein is intrinsically flexible (Byrgazov *et al*, 2015; Sengupta *et al*, 2001) and loosely associated with the ribosome. On the ribosome it is located on the solvent side directly at the mRNA exit, where it interacts via its N-terminal helix in domain D1 with uS2 (Byrgazov *et al*, 2015). The domain D3- D6 interact with single stranded RNA (Lauber *et al*, 2012; Qu *et al*, 2012). In case of ribosome traffic jam on an mRNA, it seems likely that the movement of the trailing ribosome removes these domains if they interact with the mRNA. Moreover the disome structure is formed by an uS2-uS2 interaction. The site where uS2 of the collided ribosome interacts with uS2 of the stalled ribosome overlaps with the bS1 binding site. Therefore, bS1 would prevent premature formation of the disome structure in two ways. It interacts with the mRNA and could slow down translation of the trailing ribosome when approaching the leading ribosome. And additionally, it blocks the binding site on the stalled ribosome itself. Thereby bS1 acts as a molecular bumper allowing to discriminate between short lived translational stalls and long lasting stalling events that have to be rescued.

A study from 2019 investigated how the ribosome load of an mRNA influences frameshifting in bacteria and found that ribosome collisions alter frameshifting efficiencies. Especially in the collided ribosome, frameshifting is promoted upon collision. Further, the influence of bL9 was investigated and found that it can suppress frameshifting of its host ribosome. Collided ribosomes lacking bL9 can compact one codon closer (Smith *et al*, 2019). Also earlier studies had found that the absence of bL9 can cause increased frameshifting (Atkins *et al*, 2016; Herr *et al*, 2001; Seidman *et al*, 2011) and bL9 was proposed to function at the interface of collided ribosomes (Naganathan *et al*, 2015). This is in agreement with the observed structural data showing that bL9 of the stalled ribosome reaches towards the 30S SSU of the collided ribosome. Thereby it blocks the translation factor binding site and could act as molecular ruler between the two ribosomes. In this position bL9 could prevent the collided ribosome to move forward on the mRNA and frameshifting. Future work will be needed to further understand ribosome collisions in different species and the role of bS1 and bL9 in this process.

A new ribosome rescue pathway in bacteria

As a next step, SmrB, that was found in the above described genetic screen as a potential collision sensor was biochemically characterized and visualized on disomes. First, an *in vitro* cleavage experiment using the VemP-stalled *E. coli* disomes and SmrB was performed. The reaction products were analyzed by sucrose density gradient centrifugation and indeed, a dramatic decrease of the disome peak could be observed indicating endonucleolytic cleavage by SmrB. In a second experiment, “non-collided” disomes were created by *in vitro* translation of a twin staller mRNA containing two short ORFs that each only allow one ribosome to bind. The collided and non-collided disomes were incubated with SmrB and again analyzed by sucrose density gradient centrifugation. The results showed a much higher activity of SmrB on the collided disomes than on non-collided disomes.

Second, the structure of SmrB-bound disomes were solved using cryo-EM. The structure explained how SmrB is recruited to ribosomes and specifically recognizes the disome structure. SmrB binds with its SMR domain directly at the disome interface interacting with rps of both ribosomes. The 21 kDa protein consists of an N-terminal hook that wraps around uS2 of the collided ribosome, which allows SmrB to sample translating ribosomes. This part of the protein is important for recruitment to the ribosome. In the disome structure, the C-terminal SMR domain is clamped between the stalled and collided ribosome in close proximity to the mRNA and the suggested mRNA cleavage site. Thus, this part is important for recognition of the disome structure. The structural findings could be confirmed by further experiments showing that disruption of the SmrB binding pocket led to a reduced SmrB activity.

Positioning of the SMR domain of SmrB

So, how is the SMR domain positioned for cleavage? One way would be that SmrB is already positioned close to the mRNA entry on the trailing ribosome and upon collision interactions to the stalled ribosome activate it. The second possibility is that it only moves into the disome interface after a disome is formed. On one hand, one could speculate that it would be difficult to access the disome interface after it is formed. On the other hand, it seems unlikely that SmrB is bound to every ribosome before collisions happen and thus SmrB should be able to access the interface afterwards. This is further supported by our disome cleavage experiments that showed cleavage by SmrB upon addition to purified collided disomes. In general, nuclease activity often depends on the oligomerisation state, metal ions or allosteric signals (Bechhofer & Deutscher, 2019). From the cryo-EM structure, one could speculate that interactions to both ribosomes are necessary to activate its nuclease activity. However, the interpretation from the structural data are limited as the nuclease deficient mutant of SmrB was

used, and the cryo-EM map was not well enough resolved to determine the exact position of side chains. A high resolution structure of this complex will be difficult to obtain as the factor sits at the interface of two large and partially moving entities. Future work will be necessary to further dissect the exact mechanism of mRNA cleavage by SmrB.

Downstream events after mRNA cleavage by SmrB

Cleavage by SmrB then creates two entities. The upstream ribosome stalled on an mRNA with a truncated 5' end and the downstream ribosome on an mRNA with a truncated 3' end. The latter is not blocked by the stalled ribosome anymore and can translate up to the cleavage site. This results in an RNC with an empty A-site and thus can be rescued by trans-translation. Alternative rescue pathways could also recognize the complexes and recycle it. After splitting of the ribosome, the mRNA is susceptible to 3'-5' exonucleolytic decay. The upstream ribosome will not be split until the associated mRNA is degraded by 3'-5' exonucleases up to the 3'-boundary of the ribosome. Even though this is sufficient to recycle stalled RNCs, further factors could be involved in recognition and processing of the RNCs and the free 5'-end. Under nutrient starvation conditions, cleavage of the mRNA in the A-site by RelE could accelerate recycling of these ribosome complexes (Hwang & Buskirk, 2017; Neubauer *et al*, 2009; Pedersen *et al*, 2003).

Although our findings broaden our knowledge on how *E. coli* deals with translational failure, open questions remain regarding other species. As mentioned above the structural architecture of ribosome collisions are likely conserved and also SMR-domain proteins are evolutionarily conserved from bacteria to eukaryotes. Our results are in agreement with the reported function of other SMR domain-containing proteins. In *C. elegans* and *S. cerevisiae*, NONU-1 and Cue2 were described to cleave mRNA in the vicinity of stalled ribosomes (D'Orazio *et al*, 2019; Glover *et al*, 2020). However, the eukaryotic endonuclease Cue2 was found to cleave mRNA in the A-site of the collided ribosome. Moreover, loss of Cue2 can be compensated by 5'-3' nuclease activity of Xrn1, whereas *E. coli* does not possess a 5'-3' exonuclease and thus deletion of SmrB leads to increased sensitivity to conditions with increased ribosome stalling. It will be of great importance to dissect the rescue mechanism of other bacterial system. Many SMR domain-containing proteins possess additional domains, which could act differently in recognizing and processing translational failure.

4. REFERENCES

- Acker MG, Shin B-S, Dever TE & Lorsch JR (2006) Interaction between Eukaryotic Initiation Factors 1A and 5B Is Required for Efficient Ribosomal Subunit Joining. *J Biol Chem* 281: 8469–8475
- Acker MG, Shin B-S, Nanda JS, Saini AK, Dever TE & Lorsch JR (2009) Kinetic Analysis of Late Steps of Eukaryotic Translation Initiation. *Journal of Molecular Biology* 385: 491–506
- Adio S, Sharma H, Senyushkina T, Karki P, Maracci C, Wohlgemuth I, Holtkamp W, Peske F & Rodnina MV (2018) Dynamics of ribosomes and release factors during translation termination in *E. coli*. *eLife* 7: e34252
- Agrawal RK, Penczek P, Grassucci RA, Li Y, Leith A, Nierhaus KH & Frank J (1996) Direct Visualization of A-, P-, and E-Site Transfer RNAs in the *Escherichia coli* Ribosome. *Science* 271: 1000–1002
- Agrawal RK, Sharma MR, Kiel MC, Hirokawa G, Booth TM, Spahn CMT, Grassucci RA, Kaji A & Frank J (2004) Visualization of ribosome-recycling factor on the *Escherichia coli* 70S ribosome: functional implications. *Proc Natl Acad Sci U S A* 101: 8900–8905
- Aitken CE, Beznosková P, Vlčkova V, Chiu W-L, Zhou F, Valášek LS, Hinnebusch AG & Lorsch JR (2016) Eukaryotic translation initiation factor 3 plays distinct roles at the mRNA entry and exit channels of the ribosomal preinitiation complex. *eLife* 5: e20934
- Aittoniemi J, Wet H de, Ashcroft FM & Sansom MSP (2010) Asymmetric Switching in a Homodimeric ABC Transporter: A Simulation Study. *PLOS Computational Biology* 6: e1000762
- Algire MA, Maag D & Lorsch JR (2005) Pi Release from eIF2, Not GTP Hydrolysis, Is the Step Controlled by Start-Site Selection during Eukaryotic Translation Initiation. *Molecular Cell* 20: 251–262
- Alkalaeva EZ, Pisarev AV, Frolova LY, Kisselev LL & Pestova TV (2006) In vitro reconstitution of eukaryotic translation reveals cooperativity between release factors eRF1 and eRF3. *Cell* 125: 1125–1136
- Alone PV & Dever TE (2006) Direct binding of translation initiation factor eIF2gamma-G domain to its GTPase-activating and GDP-GTP exchange factors eIF5 and eIF2B epsilon. *J Biol Chem* 281: 12636–12644
- Andersen CBF, Becker T, Blau M, Anand M, Halic M, Balar B, Mielke T, Boesen T, Pedersen JS, Spahn CMT, *et al* (2006) Structure of eEF3 and the mechanism of transfer RNA release from the E-site. *Nature* 443: 663–668
- Andersen DS & Leevers SJ (2007) The Essential *Drosophila* ATP-binding Cassette Domain Protein, Pixie, Binds the 40 S Ribosome in an ATP-dependent Manner and Is Required for Translation Initiation*. *Journal of Biological Chemistry* 282: 14752–14760
- Anger AM, Armache J-P, Berninghausen O, Habeck M, Subklewe M, Wilson DN & Beckmann R (2013) Structures of the human and *Drosophila* 80S ribosome. *Nature* 497: 80–85
- Antoun A, Pavlov MY, Andersson K, Tenson T & Ehrenberg M (2003) The roles of initiation factor 2 and guanosine triphosphate in initiation of protein synthesis. *EMBO J* 22: 5593–5601
- Antoun A, Pavlov MY, Lovmar M & Ehrenberg M (2006) How initiation factors maximize the accuracy of tRNA selection in initiation of bacterial protein synthesis. *Mol Cell* 23: 183–193

- Archer SK, Shirokikh NE, Hallwirth CV, Beilharz TH & Preiss T (2015) Probing the closed-loop model of mRNA translation in living cells. *RNA Biol* 12: 248–254
- Armache J-P, Anger AM, Márquez V, Franckenberg S, Fröhlich T, Villa E, Berninghausen O, Thomm M, Arnold GJ, Beckmann R, *et al* (2013) Promiscuous behaviour of archaeal ribosomal proteins: Implications for eukaryotic ribosome evolution. *Nucleic Acids Res* 41: 1284–1293
- Asano K, Clayton J, Shalev A & Hinnebusch AG (2000) A multifactor complex of eukaryotic initiation factors, eIF1, eIF2, eIF3, eIF5, and initiator tRNA(Met) is an important translation initiation intermediate in vivo. *Genes Dev* 14: 2534–2546
- Ashe MP, De Long SK & Sachs AB (2000) Glucose depletion rapidly inhibits translation initiation in yeast. *Mol Biol Cell* 11: 833–848
- Atkins JF, Loughran G, Bhatt PR, Firth AE & Baranov PV (2016) Ribosomal frameshifting and transcriptional slippage: From genetic steganography and cryptography to adventitious use. *Nucleic Acids Res* 44: 7007–7078
- Atkinson GC, Baldauf SL & Hauryliuk V (2008) Evolution of nonstop, no-go and nonsense-mediated mRNA decay and their termination factor-derived components. *BMC Evol Biol* 8: 290
- Aylett CHS, Boehringer D, Erzberger JP, Schaefer T & Ban N (2015) Structure of a Yeast 40S–eIF1–eIF1A–eIF3–eIF3j initiation complex. *Nat Struct Mol Biol* 22: 269–271
- Balagopal V & Parker R (2011) Stm1 modulates translation after 80S formation in *Saccharomyces cerevisiae*. *RNA* 17: 835–842
- Ban N, Nissen P, Hansen J, Moore PB & Steitz TA (2000) The complete atomic structure of the large ribosomal subunit at 2.4 Å resolution. *Science* 289: 905–920
- Barends S, Wower J & Kraal B (2000) Kinetic parameters for tmRNA binding to alanyl-tRNA synthetase and elongation factor Tu from *Escherichia coli*. *Biochemistry* 39: 2652–2658
- Barthelme D, Dinkelaker S, Albers S-V, Londei P, Ermler U & Tampé R (2011) Ribosome recycling depends on a mechanistic link between the FeS cluster domain and a conformational switch of the twin-ATPase ABCE1. *PNAS* 108: 3228–3233
- Barthelme D, Scheele U, Dinkelaker S, Janoschka A, Macmillan F, Albers S-V, Driessen AJM, Stagni MS, Bill E, Meyer-Klaucke W, *et al* (2007) Structural organization of essential iron-sulfur clusters in the evolutionarily highly conserved ATP-binding cassette protein ABCE1. *J Biol Chem* 282: 14598–14607
- Battiste JL, Pestova TV, Hellen CU & Wagner G (2000) The eIF1A solution structure reveals a large RNA-binding surface important for scanning function. *Mol Cell* 5: 109–119
- Bechhofer DH & Deutscher MP (2019) Bacterial ribonucleases and their roles in RNA metabolism. *Crit Rev Biochem Mol Biol* 54: 242–300
- Becker T, Armache J-P, Jarasch A, Anger AM, Villa E, Sieber H, Motaal BA, Mielke T, Berninghausen O & Beckmann R (2011) Structure of the no-go mRNA decay complex Dom34–Hbs1 bound to a stalled 80S ribosome. *Nature Structural & Molecular Biology* 18: 715–720

- Becker T, Franckenberg S, Wickles S, Shoemaker CJ, Anger AM, Armache J-P, Sieber H, Ungewickell C, Berninghausen O, Daberkow I, *et al* (2012) Structural basis of highly conserved ribosome recycling in eukaryotes and archaea. *Nature* 482: 501–506
- Benelli D, Marzi S, Mancone C, Alonzi T, la Teana A & Londei P (2009) Function and ribosomal localization of aIF6, a translational regulator shared by archaea and eukarya. *Nucleic Acids Res* 37: 256–267
- Bengtson MH & Joazeiro CAP (2010) Role of a ribosome-associated E3 ubiquitin ligase in protein quality control. *Nature* 467: 470–473
- Ben-Shem A, Garreau de Loubresse N, Melnikov S, Jenner L, Yusupova G & Yusupov M (2011) The Structure of the Eukaryotic Ribosome at 3.0 Å Resolution. *Science* 334: 1524–1529
- Bertram G, Bell HA, Ritchie DW, Fullerton G & Stansfield I (2000) Terminating eukaryote translation: domain 1 of release factor eRF1 functions in stop codon recognition. *RNA* 6: 1236–1247
- Beznosková P, Cuchalová L, Wagner S, Shoemaker CJ, Gunišová S, Haar T von der & Valášek LS (2013) Translation Initiation Factors eIF3 and HCR1 Control Translation Termination and Stop Codon Read-Through in Yeast Cells. *PLOS Genetics* 9: e1003962
- Beznosková P, Wagner S, Jansen ME, von der Haar T & Valášek LS (2015) Translation initiation factor eIF3 promotes programmed stop codon readthrough. *Nucleic Acids Res* 43: 5099–5111
- Bhandari D, Guha K, Bhaduri N & Saha P (2011) Ubiquitination of mRNA cycling sequence binding protein from *Leishmania donovani* (LdCSBP) modulates the RNA endonuclease activity of its Smr domain. *FEBS Lett* 585: 809–813
- Bieniossek C, Schütz P, Bumann M, Limacher A, Uson I & Baumann U (2006) The crystal structure of the carboxy-terminal domain of human translation initiation factor eIF5. *J Mol Biol* 360: 457–465
- Blanchard SC, Kim HD, Gonzalez RL, Puglisi JD & Chu S (2004) tRNA dynamics on the ribosome during translation. *PNAS* 101: 12893–12898
- Boni IV, Isaeva DM, Musychenko ML & Tzareva NV (1991) Ribosome-messenger recognition: mRNA target sites for ribosomal protein S1. *Nucleic Acids Res* 19: 155–162
- Borg A, Pavlov M & Ehrenberg M (2016) Complete kinetic mechanism for recycling of the bacterial ribosome. *RNA* 22: 10–21
- Brandman O & Hegde RS (2016) Ribosome-associated protein quality control. *Nat Struct Mol Biol* 23: 7–15
- Brandman O, Stewart-Ornstein J, Wong D, Larson A, Williams CC, Li G-W, Zhou S, King D, Shen PS, Weibezahn J, *et al* (2012) A Ribosome-Bound Quality Control Complex Triggers Degradation of Nascent Peptides and Signals Translation Stress. *Cell* 151: 1042–1054
- Brown A & Shao S (2018) Ribosomes and cryo-EM: a duet. *Curr Opin Struct Biol* 52: 1–7
- Brown A, Shao S, Murray J, Hegde RS & Ramakrishnan V (2015) Structural basis for stop codon recognition in eukaryotes. *Nature* 524: 493–496

- Budkevich T, Giesebrecht J, Altman RB, Munro JB, Mielke T, Nierhaus KH, Blanchard SC & Spahn CMT (2011) Structure and dynamics of the mammalian ribosomal pretranslocation complex. *Mol Cell* 44: 214–224
- Burroughs AM & Aravind L (2019) The Origin and Evolution of Release Factors: Implications for Translation Termination, Ribosome Rescue, and Quality Control Pathways. *International Journal of Molecular Sciences* 20: 1981
- Buskirk AR & Green R (2017) Ribosome pausing, arrest and rescue in bacteria and eukaryotes. *Phil Trans R Soc B* 372: 20160183
- Byrgazov K, Grishkovskaya I, Arenz S, Coudeville N, Temmel H, Wilson DN, Djinovic-Carugo K & Moll I (2015) Structural basis for the interaction of protein S1 with the Escherichia coli ribosome. *Nucleic Acids Res* 43: 661–673
- Capecci MR (1967) Polypeptide chain termination in vitro: isolation of a release factor. *Proc Natl Acad Sci U S A* 58: 1144–1151
- Carbone CE, Demo G, Madireddy R, Svidritskiy E & Korostelev AA (2020) ArfB can displace mRNA to rescue stalled ribosomes. *Nat Commun* 11: 5552
- Carter AP, Clemons WM, Brodersen DE, Morgan-Warren RJ, Hartsch T, Wimberly BT & Ramakrishnan V (2001) Crystal structure of an initiation factor bound to the 30S ribosomal subunit. *Science* 291: 498–501
- Carter AP, Clemons WM, Brodersen DE, Morgan-Warren RJ, Wimberly BT & Ramakrishnan V (2000) Functional insights from the structure of the 30S ribosomal subunit and its interactions with antibiotics. *Nature* 407: 340–348
- Caskey CT, Tompkins R, Scolnick E, Caryk T & Nirenberg M (1968) Sequential translation of trinucleotide codons for the initiation and termination of protein synthesis. *Science* 162: 135–138
- Chadani Y, Matsumoto E, Aso H, Wada T, Kutsukake K, Sutou S & Abo T (2011a) trans-translation-mediated tight regulation of the expression of the alternative ribosome-rescue factor ArfA in Escherichia coli. *Genes Genet Syst* 86: 151–163
- Chadani Y, Ono K, Kutsukake K & Abo T (2011b) Escherichia coli YaeJ protein mediates a novel ribosome-rescue pathway distinct from SsrA- and ArfA-mediated pathways. *Mol Microbiol* 80: 772–785
- Chadani Y, Ono K, Ozawa S-I, Takahashi Y, Takai K, Nanamiya H, Tozawa Y, Kutsukake K & Abo T (2010) Ribosome rescue by Escherichia coli ArfA (YhdL) in the absence of trans-translation system. *Mol Microbiol* 78: 796–808
- Chan K-H, Petrychenko V, Mueller C, Maracci C, Holtkamp W, Wilson DN, Fischer N & Rodnina MV (2020) Mechanism of ribosome rescue by alternative ribosome-rescue factor B. *Nat Commun* 11: 4106
- Chang B, Halgamuge S & Tang S-L (2006) Analysis of SD sequences in completed microbial genomes: Non-SD-led genes are as common as SD-led genes. *Gene* 373: 90–99

- Chen J, Lu G, Lin J, Davidson AL & Quirocho FA (2003) A tweezers-like motion of the ATP-binding cassette dimer in an ABC transport cycle. *Mol Cell* 12: 651–661
- Chen Y, Kaji A, Kaji H & Cooperman BS (2017) The kinetic mechanism of bacterial ribosome recycling. *Nucleic Acids Res* 45: 10168–10177
- Chen Z, Dong J, Ishimura A, Daar I, Hinnebusch AG & Dean M (2006) The Essential Vertebrate ABCE1 Protein Interacts with Eukaryotic Initiation Factors. *J Biol Chem* 281: 7452–7457
- Cheng Z, Saito K, Pisarev AV, Wada M, Pisareva VP, Pestova TV, Gajda M, Round A, Kong C, Lim M, *et al* (2009) Structural insights into eRF3 and stop codon recognition by eRF1. *Genes & Development* 23: 1106–1118
- Cheung Y-N, Maag D, Mitchell SF, Fekete CA, Algire MA, Takacs JE, Shirokikh N, Pestova T, Lorsch JR & Hinnebusch AG (2007) Dissociation of eIF1 from the 40S ribosomal subunit is a key step in start codon selection in vivo. *Genes Dev* 21: 1217–1230
- Chiu W-L, Wagner S, Herrmannová A, Burela L, Zhang F, Saini AK, Valášek L & Hinnebusch AG (2010) The C-Terminal Region of Eukaryotic Translation Initiation Factor 3a (eIF3a) Promotes mRNA Recruitment, Scanning, and, Together with eIF3j and the eIF3b RNA Recognition Motif, Selection of AUG Start Codons. *MCB* 30: 4415–4434
- Coelho CMA, Kolevski B, Bunn C, Walker C, Dahanukar A & Leever SJ (2005) Growth and cell survival are unevenly impaired in pixie mutant wing discs. *Development* 132: 5411–5424
- Connell SR, Takemoto C, Wilson DN, Wang H, Murayama K, Terada T, Shirouzu M, Rost M, Schüler M, Giesebrecht J, *et al* (2007) Structural Basis for Interaction of the Ribosome with the Switch Regions of GTP-Bound Elongation Factors. *Molecular Cell* 25: 751–764
- Conte MR, Kelly G, Babon J, Sanfelice D, Youell J, Smerdon SJ & Proud CG (2006) Structure of the eukaryotic initiation factor (eIF) 5 reveals a fold common to several translation factors. *Biochemistry* 45: 4550–4558
- Cosson B, Berkova N, Couturier A, Chabelskaya S, Philippe M & Zhouravleva G (2002) Poly(A)-binding protein and eRF3 are associated in vivo in human and *Xenopus* cells. *Biol Cell* 94: 205–216
- Costello J, Castelli LM, Rowe W, Kershaw CJ, Talavera D, Mohammad-Qureshi SS, Sims PFG, Grant CM, Pavitt GD, Hubbard SJ, *et al* (2015) Global mRNA selection mechanisms for translation initiation. *Genome Biol* 16: 10
- Coureur P-D, Lazennec-Schurdevin C, Bourcier S, Mechulam Y & Schmitt E (2020) Cryo-EM study of an archaeal 30S initiation complex gives insights into evolution of translation initiation. *Commun Biol* 3: 58
- Coureur P-D, Lazennec-Schurdevin C, Monestier A, Larquet E, Cladière L, Klaholz BP, Schmitt E & Mechulam Y (2016) Cryo-EM study of start codon selection during archaeal translation initiation. *Nature Communications* 7: 13366
- Crick F (1958) On protein synthesis. *Symp Soc Exp Biol* 12: 138–163
- Crick F (1970) Central Dogma of Molecular Biology. *Nature* 227: 561–563

- Crick F, Barnett L, Brenner S & Watts-Tobin RJ (1961) General Nature of the Genetic Code for Proteins. *Nature* 192: 1227–1232
- Crick FH (1966) Codon--anticodon pairing: the wobble hypothesis. *J Mol Biol* 19: 548–555
- Crowe-McAuliffe C, Takada H, Murina V, Polte C, Kasvandik S, Tenson T, Ignatova Z, Atkinson GC, Wilson DN & Hauryliuk V (2021) Structural Basis for Bacterial Ribosome-Associated Quality Control by RqcH and RqcP. *Molecular Cell* 81: 115-126.e7
- Defenouillère Q, Yao Y, Mouaikel J, Namane A, Galopier A, Decourty L, Doyen A, Malabat C, Saveanu C, Jacquier A, *et al* (2013) Cdc48-associated complex bound to 60S particles is required for the clearance of aberrant translation products. *Proc Natl Acad Sci U S A* 110: 5046–5051
- Dennis MD, Person MD & Browning KS (2009) Phosphorylation of plant translation initiation factors by CK2 enhances the in vitro interaction of multifactor complex components. *J Biol Chem* 284: 20615–20628
- Dever TE, Dinman JD & Green R (2018) Translation Elongation and Recoding in Eukaryotes. *Cold Spring Harb Perspect Biol* 10: a032649
- Dever TE, Feng L, Wek RC, Cigan AM, Donahue TF & Hinnebusch AG (1992) Phosphorylation of initiation factor 2 alpha by protein kinase GCN2 mediates gene-specific translational control of GCN4 in yeast. *Cell* 68: 585–596
- Dever TE, Kinzy TG & Pavitt GD (2016) Mechanism and Regulation of Protein Synthesis in *Saccharomyces cerevisiae*. *Genetics* 203: 65–107
- Diaconu M, Kothe U, Schlünzen F, Fischer N, Harms JM, Tonevitsky AG, Stark H, Rodnina MV & Wahl MC (2005) Structural basis for the function of the ribosomal L7/12 stalk in factor binding and GTPase activation. *Cell* 121: 991–1004
- Doerfel LK, Wohlgemuth I, Kothe C, Peske F, Urlaub H & Rodnina MV (2013) EF-P is essential for rapid synthesis of proteins containing consecutive proline residues. *Science* 339: 85–88
- Doma MK & Parker R (2006) Endonucleolytic cleavage of eukaryotic mRNAs with stalls in translation elongation. *Nature* 440: 561–564
- Dong J, Lai R, Nielsen K, Fekete CA, Qiu H & Hinnebusch AG (2004) The Essential ATP-binding Cassette Protein RLI1 Functions in Translation by Promoting Preinitiation Complex Assembly. *J Biol Chem* 279: 42157–42168
- Dong Z, Qi J, Peng H, Liu J & Zhang J-T (2013) Spectrin domain of eukaryotic initiation factor 3a is the docking site for formation of the a:b:i:g subcomplex. *J Biol Chem* 288: 27951–27959
- Dontsova M, Frolova L, Vassilieva J, Piendl W, Kisselev L & Garber M (2000) Translation termination factor aRF1 from the archaeon *Methanococcus jannaschii* is active with eukaryotic ribosomes. *FEBS Lett* 472: 213–216
- D’Orazio KN, Wu CC-C, Sinha N, Loll-Krippelber R, Brown GW & Green R (2019) The endonuclease Cue2 cleaves mRNAs at stalled ribosomes during No Go Decay. *eLife* 8: e49117

- Dunkle JA, Wang L, Feldman MB, Pulk A, Chen VB, Kapral GJ, Noeske J, Richardson JS, Blanchard SC & Cate JHD (2011) Structures of the Bacterial Ribosome in Classical and Hybrid States of tRNA Binding. *Science* 332: 981–984
- Duval M, Korepanov A, Fuchsbauer O, Fechter P, Haller A, Fabbretti A, Choulier L, Micura R, Klaholz BP, Romby P, *et al* (2013) Escherichia coli ribosomal protein S1 unfolds structured mRNAs onto the ribosome for active translation initiation. *PLoS Biol* 11: e1001731
- Egorova T, Biziaev N, Shuvalov A, Sokolova E, Mukba S, Evmenov K, Zotova M, Kushchenko A, Shuvalova E & Alkalaeva E (2021) eIF3j facilitates loading of release factors into the ribosome. *Nucleic Acids Research*
- Elantak L, Tzakos AG, Locker N & Lukavsky PJ (2007) Structure of eIF3b RNA recognition motif and its interaction with eIF3j: structural insights into the recruitment of eIF3b to the 40 S ribosomal subunit. *J Biol Chem* 282: 8165–8174
- Elantak L, Wagner S, Herrmannová A, Karásková M, Rutkai E, Lukavsky PJ & Valásek L (2010) The indispensable N-terminal half of eIF3j/HCR1 cooperates with its structurally conserved binding partner eIF3b/PRT1-RRM and with eIF1A in stringent AUG selection. *J Mol Biol* 396: 1097–1116
- Enchev RI, Schreiber A, Beuron F & Morris EP (2010) Structural Insights into the COP9 Signalosome and Its Common Architecture with the 26S Proteasome Lid and eIF3. *Structure* 18: 518–527
- Ermolenko DN & Noller HF (2011) mRNA translocation occurs during the second step of ribosomal intersubunit rotation. *Nat Struct Mol Biol* 18: 457–462
- Erzberger JP, Stengel F, Pellarin R, Zhang S, Schaefer T, Aylett CHS, Cimermančič P, Boehringer D, Sali A, Aebersold R, *et al* (2014) Molecular Architecture of the 40S·eIF1·eIF3 Translation Initiation Complex. *Cell* 158: 1123–1135
- Estévez AM, Haile S, Steinbüchel M, Quijada L & Clayton C (2004) Effects of depletion and overexpression of the Trypanosoma brucei ribonuclease L inhibitor homologue. *Mol Biochem Parasitol* 133: 137–141
- Fekete CA, Mitchell SF, Cherkasova VA, Applefield D, Algire MA, Maag D, Saini AK, Lorsch JR & Hinnebusch AG (2007) N- and C-terminal residues of eIF1A have opposing effects on the fidelity of start codon selection. *EMBO J* 26: 1602–1614
- Ferguson A, Wang L, Altman RB, Terry DS, Juetz MF, Burnett BJ, Alejo JL, Dass RA, Parks MM, Vincent CT, *et al* (2015) Functional Dynamics within the Human Ribosome Regulate the Rate of Active Protein Synthesis. *Mol Cell* 60: 475–486
- Filbeck S, Cerullo F, Paternoga H, Tsaprailis G, Joazeiro CAP & Pfeffer S (2021) Mimicry of Canonical Translation Elongation Underlies Alanine Tail Synthesis in RQC. *Mol Cell* 81: 104-114.e6
- Fischer N, Neumann P, Konevega AL, Bock LV, Ficner R, Rodnina MV & Stark H (2015) Structure of the E. coli ribosome–EF-Tu complex at <3 Å resolution by Cs-corrected cryo-EM. *Nature* 520: 567–570
- Franckenberg S, Becker T & Beckmann R (2012) Structural view on recycling of archaeal and eukaryotic ribosomes after canonical termination and ribosome rescue. *Current Opinion in Structural Biology* 22: 786–796

- Frank J (2001) Cryo-electron microscopy as an investigative tool: the ribosome as an example. *BioEssays* 23: 725–732
- Frank J & Agrawal RK (2000) A ratchet-like inter-subunit reorganization of the ribosome during translocation. *Nature* 406: 318–322
- Frank J, Penczek P, Grassucci R & Srivastava S (1991) Three-dimensional reconstruction of the 70S *Escherichia coli* ribosome in ice: the distribution of ribosomal RNA. *Journal of Cell Biology* 115: 597–605
- Frank J, Zhu J, Penczek P, Li Y, Srivastava S, Verschoor A, Radermacher M, Grassucci R, Lata RK & Agrawal RK (1995) A model of protein synthesis based on cryo-electron microscopy of the *E. coli* ribosome. *Nature* 376: 441–444
- Fraser CS, Berry KE, Hershey JWB & Doudna JA (2007) eIF3j Is Located in the Decoding Center of the Human 40S Ribosomal Subunit. *Molecular Cell* 26: 811–819
- Fraser CS, Lee JY, Mayeur GL, Bushell M, Doudna JA & Hershey JWB (2004) The j-Subunit of Human Translation Initiation Factor eIF3 Is Required for the Stable Binding of eIF3 and Its Subcomplexes to 40 S Ribosomal Subunits in Vitro. *J Biol Chem* 279: 8946–8956
- Freistroffer DV, Pavlov MY, MacDougall J, Buckingham RH & Ehrenberg M (1997) Release factor RF3 in *E. coli* accelerates the dissociation of release factors RF1 and RF2 from the ribosome in a GTP-dependent manner. *EMBO J* 16: 4126–4133
- French SL, Santangelo TJ, Beyer AL & Reeve JN (2007) Transcription and translation are coupled in Archaea. *Mol Biol Evol* 24: 893–895
- Fringer JM, Acker MG, Fekete CA, Lorsch JR & Dever TE (2007) Coupled release of eukaryotic translation initiation factors 5B and 1A from 80S ribosomes following subunit joining. *Mol Cell Biol* 27: 2384–2397
- Frolova L, Le Goff X, Zhouravleva G, Davydova E, Philippe M & Kisselev L (1996) Eukaryotic polypeptide chain release factor eRF3 is an eRF1- and ribosome-dependent guanosine triphosphatase. *RNA* 2: 334–341
- Frolova LY, Tsivkovskii RY, Sivolobova GF, Oparina NY, Serpinsky OI, Blinov VM, Tatkov SI & Kisselev LL (1999) Mutations in the highly conserved GGQ motif of class 1 polypeptide release factors abolish ability of human eRF1 to trigger peptidyl-tRNA hydrolysis. *RNA* 5: 1014–1020
- Fu Z, Indrisiunaite G, Kaledhonkar S, Shah B, Sun M, Chen B, Grassucci RA, Ehrenberg M & Frank J (2019) The structural basis for release-factor activation during translation termination revealed by time-resolved cryogenic electron microscopy. *Nature Communications* 10: 2579
- Fu Z, Kaledhonkar S, Borg A, Sun M, Chen B, Grassucci RA, Ehrenberg M & Frank J (2016) Key Intermediates in Ribosome Recycling Visualized by Time-Resolved Cryoelectron Microscopy. *Structure* 24: 2092–2101
- Fukui K & Kuramitsu S (2011) Structure and Function of the Small MutS-Related Domain. *Mol Biol Int* 2011
- Gabashvili IS, Agrawal RK, Spahn CMT, Grassucci RA, Svergun DI, Frank J & Penczek P (2000) Solution Structure of the *E. coli* 70S Ribosome at 11.5 Å Resolution. *Cell* 100: 537–549

- Gäbel K, Schmitt J, Schulz S, Näther DJ & Soppa J (2013) A Comprehensive Analysis of the Importance of Translation Initiation Factors for *Haloferax volcanii* Applying Deletion and Conditional Depletion Mutants. *PLOS ONE* 8: e77188
- Gagnon MG, Seetharaman SV, Bulkley D & Steitz TA (2012) Structural basis for the rescue of stalled ribosomes: structure of YaeJ bound to the ribosome. *Science* 335: 1370–1372
- Gaikwad S, Ghobakhloo F, Young DJ, Visweswaraiiah J, Zhang H & Hinnebusch AG (2021) Reprogramming of translation in yeast cells impaired for ribosome recycling favors short, efficiently translated mRNAs. *eLife* 10: e64283
- Gao H, Zhou Z, Rawat U, Huang C, Bouakaz L, Wang C, Cheng Z, Liu Y, Zavialov A, Gursky R, *et al* (2007a) RF3 induces ribosomal conformational changes responsible for dissociation of class I release factors. *Cell* 129: 929–941
- Gao N, Zavialov AV, Ehrenberg M & Frank J (2007b) Specific interaction between EF-G and RRF and its implication for GTP-dependent ribosome splitting into subunits. *J Mol Biol* 374: 1345–1358
- Gao N, Zavialov AV, Li W, Sengupta J, Valle M, Gursky RP, Ehrenberg M & Frank J (2005) Mechanism for the Disassembly of the Posttermination Complex Inferred from Cryo-EM Studies. *Molecular Cell* 18: 663–674
- Gartmann M, Blau M, Armache J-P, Mielke T, Topf M & Beckmann R (2010) Mechanism of eIF6-mediated Inhibition of Ribosomal Subunit Joining. *J Biol Chem* 285: 14848–14851
- Garza-Sánchez F, Schaub RE, Janssen BD & Hayes CS (2011) tmRNA regulates synthesis of the ArfA ribosome rescue factor. *Mol Microbiol* 80: 1204–1219
- Garzia A, Jafarnejad SM, Meyer C, Chapat C, Gogakos T, Morozov P, Amiri M, Shapiro M, Molina H, Tuschl T, *et al* (2017) The E3 ubiquitin ligase and RNA-binding protein ZNF598 orchestrates ribosome quality control of premature polyadenylated mRNAs. *Nat Commun* 8: 16056
- Geggier P, Dave R, Feldman MB, Terry DS, Altman RB, Munro JB & Blanchard SC (2010) Conformational sampling of aminoacyl-tRNA during selection on the bacterial ribosome. *J Mol Biol* 399: 576–595
- Geissmann T, Marzi S & Romby P (2009) The role of mRNA structure in translational control in bacteria. *RNA Biology* 6: 153–160
- des Georges A, Dhote V, Kuhn L, Hellen CUT, Pestova TV, Frank J & Hashem Y (2015) Structure of mammalian eIF3 in the context of the 43S preinitiation complex. *Nature* 525: 491–495
- des Georges A, Hashem Y, Unbehaun A, Grassucci RA, Taylor D, Hellen CUT, Pestova TV & Frank J (2014) Structure of the mammalian ribosomal pre-termination complex associated with eRF1•eRF3•GDPNP. *Nucleic Acids Research* 42: 3409–3418
- Gerovac M & Tampé R (2019) Control of mRNA Translation by Versatile ATP-Driven Machines. *Trends in Biochemical Sciences* 44: 167–180
- Giudice E, Macé K & Gillet R (2014) Trans-translation exposed: understanding the structures and functions of tmRNA-SmpB. *Front Microbiol* 5: 113

- Glick BR & Ganoza MC (1975) Identification of a soluble protein that stimulates peptide bond synthesis. *Proc Natl Acad Sci U S A* 72: 4257–4260
- Glover ML, Burroughs AMax, Monem PC, Egelhofer TA, Pule MN, Aravind L & Arribere JA (2020) NONU-1 Encodes a Conserved Endonuclease Required for mRNA Translation Surveillance. *Cell Reports* 30: 4321–4331.e4
- Gomez MAR & Ibba M (2020) Aminoacyl-tRNA synthetases. *RNA* 26: 910–936
- Goralski TDP, Kirimanjeswara GS & Keiler KC (2018) A New Mechanism for Ribosome Rescue Can Recruit RF1 or RF2 to Nonstop Ribosomes. *mBio* 9: e02436-18
- Gouridis G, Hetzert B, Kiosze-Becker K, de Boer M, Heinemann H, Nürenberg-Goloub E, Cordes T & Tampé R (2019) ABCE1 Controls Ribosome Recycling by an Asymmetric Dynamic Conformational Equilibrium. *Cell Reports* 28: 723–734.e6
- Graf M, Huter P, Maracci C, Peterek M, Rodnina MV & Wilson DN (2018) Visualization of translation termination intermediates trapped by the Apidaecin 137 peptide during RF3-mediated recycling of RF1. *Nature Communications* 9: 3053
- Greber BJ, Boehringer D, Godinic-Mikulcic V, Crnkovic A, Ibba M, Weygand-Durasevic I & Ban N (2012) Cryo-EM Structure of the Archaeal 50S Ribosomal Subunit in Complex with Initiation Factor 6 and Implications for Ribosome Evolution. *J Mol Biol* 418: 10.1016/j.jmb.2012.01.018
- Gregio APB, Cano VPS, Avaca JS, Valentini SR & Zanelli CF (2009) eIF5A has a function in the elongation step of translation in yeast. *Biochem Biophys Res Commun* 380: 785–790
- Grifo JA, Abramson RD, Satler CA & Merrick WC (1984) RNA-stimulated ATPase activity of eukaryotic initiation factors. *J Biol Chem* 259: 8648–8654
- Gualerzi CO & Pon CL (2015) Initiation of mRNA translation in bacteria: structural and dynamic aspects. *Cell Mol Life Sci* 72: 4341–4367
- Gutierrez E, Shin B-S, Woolstenhulme CJ, Kim J-R, Saini P, Buskirk AR & Dever TE (2013) eIF5A promotes translation of polyproline motifs. *Mol Cell* 51: 35–45
- Guydosh NR & Green R (2014) Dom34 rescues ribosomes in 3' untranslated regions. *Cell* 156: 950–962
- Handa Y, Inaho N & Nameki N (2011) YaeJ is a novel ribosome-associated protein in Escherichia coli that can hydrolyze peptidyl-tRNA on stalled ribosomes. *Nucleic Acids Res* 39: 1739–1748
- Hannig EM, Cigan AM, Freeman BA & Kinzy TG (1993) GCD11, a negative regulator of GCN4 expression, encodes the gamma subunit of eIF-2 in Saccharomyces cerevisiae. *Mol Cell Biol* 13: 506–520
- Harms J, Schlutzenzen F, Zarivach R, Bashan A, Gat S, Agmon I, Bartels H, Franceschi F & Yonath A (2001) High Resolution Structure of the Large Ribosomal Subunit from a Mesophilic Eubacterium. *Cell* 107: 679–688
- Hasenöhrl D, Benelli D, Barbazza A, Londei P & Bläsi U (2006) Sulfolobus solfataricus translation initiation factor 1 stimulates translation initiation complex formation. *RNA* 12: 674–682
- Hasenöhrl D, Fabbretti A, Londei P, Gualerzi CO & Bläsi U (2009) Translation initiation complex formation in the crenarchaeon Sulfolobus solfataricus. *RNA* 15: 2288–2298

- Hashem Y, des Georges A, Dhote V, Langlois R, Liao HY, Grassucci RA, Hellen CUT, Pestova TV & Frank J (2013) Structure of the Mammalian Ribosomal 43S Preinitiation Complex Bound to the Scanning Factor DHX29. *Cell* 153: 1108–1119
- Hashimoto S, Sugiyama T, Yamazaki R, Nobuta R & Inada T (2020) Identification of a novel trigger complex that facilitates ribosome-associated quality control in mammalian cells. *Sci Rep* 10: 3422
- Hellen CUT (2018) Translation Termination and Ribosome Recycling in Eukaryotes. *Cold Spring Harb Perspect Biol* 10: a032656
- Henderson A & Hershey JW (2011) Eukaryotic translation initiation factor (eIF) 5A stimulates protein synthesis in *Saccharomyces cerevisiae*. *Proc Natl Acad Sci U S A* 108: 6415–6419
- Herr AJ, Nelson CC, Wills NM, Gesteland RF & Atkins JF (2001) Analysis of the roles of tRNA structure, ribosomal protein L9, and the bacteriophage T4 gene 60 bypassing signals during ribosome slippage on mRNA. *J Mol Biol* 309: 1029–1048
- Heuer A, Gerovac M, Schmidt C, Trowitzsch S, Preis A, Kötter P, Berninghausen O, Becker T, Beckmann R & Tampé R (2017) Structure of the 40S-ABCE1 post-splitting complex in ribosome recycling and translation initiation. *Nat Struct Mol Biol* advance online publication
- Higgins CF (1992) ABC transporters: from microorganisms to man. *Annu Rev Cell Biol* 8: 67–113
- Hilal T, Yamamoto H, Loerke J, Bürger J, Mielke T & Spahn CMT (2016) Structural insights into ribosomal rescue by Dom34 and Hbs1 at near-atomic resolution. *Nat Commun* 7: 13521
- Hinnebusch AG (2006) eIF3: a versatile scaffold for translation initiation complexes. *Trends in Biochemical Sciences* 31: 553–562
- Hinnebusch AG (2011) Molecular Mechanism of Scanning and Start Codon Selection in Eukaryotes. *Microbiology and Molecular Biology Reviews* 75: 434–467
- Hinnebusch AG (2014) The Scanning Mechanism of Eukaryotic Translation Initiation. *Annu Rev Biochem* 83: 779–812
- Hinnebusch AG (2017) Structural Insights into the Mechanism of Scanning and Start Codon Recognition in Eukaryotic Translation Initiation. *Trends in Biochemical Sciences* 42: 589–611
- Hinton TM, Coldwell MJ, Carpenter GA, Morley SJ & Pain VM (2007) Functional analysis of individual binding activities of the scaffold protein eIF4G. *J Biol Chem* 282: 1695–1708
- Hirashima A & Kaji A (1970) Factor dependent breakdown of polysomes. *Biochemical and Biophysical Research Communications* 41: 877–883
- Hirokawa G, Demeshkina N, Iwakura N, Kaji H & Kaji A (2006) The ribosome-recycling step: consensus or controversy? *Trends Biochem Sci* 31: 143–149
- Hoagland MB, Stephenson ML, Scott JF, Hecht LI & Zamecnik PC (1958) A soluble ribonucleic acid intermediate in protein synthesis. *Journal of Biological Chemistry* 231: 241–257
- Hopfner K-P (2016) Invited review: Architectures and mechanisms of ATP binding cassette proteins. *Biopolymers* 105: 492–504

- Hopfner K-P & Tainer JA (2003) Rad50/SMC proteins and ABC transporters: unifying concepts from high-resolution structures. *Current Opinion in Structural Biology* 13: 249–255
- Hoshino S, Imai M, Kobayashi T, Uchida N & Katada T (1999) The eukaryotic polypeptide chain releasing factor (eRF3/GSPT) carrying the translation termination signal to the 3'-Poly(A) tail of mRNA. Direct association of erf3/GSPT with polyadenylate-binding protein. *J Biol Chem* 274: 16677–16680
- Hussain T, Ll  cer JL, Fern  ndez IS, Munoz A, Martin-Marcos P, Savva CG, Lorsch JR, Hinnebusch AG & Ramakrishnan V (2014) Structural Changes Enable Start Codon Recognition by the Eukaryotic Translation Initiation Complex. *Cell* 159: 597–607
- Hussain T, Ll  cer JL, Wimberly BT, Kieft JS & Ramakrishnan V (2016) Large-Scale Movements of IF3 and tRNA during Bacterial Translation Initiation. *Cell* 167: 133-144.e13
- Huter P, Arenz S, Bock LV, Graf M, Frister JO, Heuer A, Peil L, Starosta AL, Wohlgemuth I, Peske F, *et al* (2017a) Structural Basis for Polyproline-Mediated Ribosome Stalling and Rescue by the Translation Elongation Factor EF-P. *Molecular Cell* 68: 515-527.e6
- Huter P, M  ller C, Beckert B, Arenz S, Berninghausen O, Beckmann R & Wilson DN (2017b) Structural basis for ArfA–RF2-mediated translation termination on mRNAs lacking stop codons. *Nature* 541: 546–549
- Hwang J-Y & Buskirk AR (2017) A ribosome profiling study of mRNA cleavage by the endonuclease RelE. *Nucleic Acids Res* 45: 327–336
- Ikeuchi K, Izawa T & Inada T (2019a) Recent Progress on the Molecular Mechanism of Quality Controls Induced by Ribosome Stalling. *Front Genet* 9
- Ikeuchi K, Tesina P, Matsuo Y, Sugiyama T, Cheng J, Saeki Y, Tanaka K, Becker T, Beckmann R & Inada T (2019b) Collided ribosomes form a unique structural interface to induce Hel2-driven quality control pathways. *The EMBO Journal* 38: e100276
- Imai H, Abe T, Miyoshi T, Nishikawa S, Ito K & Uchiumi T (2018) The ribosomal stalk protein is crucial for the action of the conserved ATPase ABCE1. *Nucleic Acids Research* 46: 7820–7830
- Inada T (2020) Quality controls induced by aberrant translation. *Nucleic Acids Res* 48: 1084–1096
- Ito K, Uno M & Nakamura Y (2000) A tripeptide ‘anticodon’ deciphers stop codons in messenger RNA. *Nature* 403: 680–684
- Ivanov PV, Gehring NH, Kunz JB, Hentze MW & Kulozik AE (2008) Interactions between UPF1, eRFs, PABP and the exon junction complex suggest an integrated model for mammalian NMD pathways. *EMBO J* 27: 736–747
- Ivanova N, Pavlov MY, Felden B & Ehrenberg M (2004) Ribosome rescue by tmRNA requires truncated mRNAs. *J Mol Biol* 338: 33–41
- Jackson RJ, Hellen CUT & Pestova TV (2010) The mechanism of eukaryotic translation initiation and principles of its regulation. *Nat Rev Mol Cell Biol* 11: 113–127
- James NR, Brown A, Gordiyenko Y & Ramakrishnan V (2016) Translational termination without a stop codon. *Science* 354: 1437–1440

- Janosi L, Hara H, Zhang S & Kaji A (1996) Ribosome recycling by ribosome recycling factor (RRF)--an important but overlooked step of protein biosynthesis. *Adv Biophys* 32: 121–201
- Jennings MD, Kershaw CJ, Adomavicius T & Pavitt GD (2017) Fail-safe control of translation initiation by dissociation of eIF2 α phosphorylated ternary complexes. *Elife* 6: e24542
- Jennings MD & Pavitt GD (2010) eIF5 is a dual function GAP and GDI for eukaryotic translational control. *Small GTPases* 1: 118–123
- Jennings MD, Zhou Y, Mohammad-Qureshi SS, Bennett D & Pavitt GD (2013) eIF2B promotes eIF5 dissociation from eIF2*GDP to facilitate guanine nucleotide exchange for translation initiation. *Genes & Development* 27: 2696–2707
- Jin H, Kelley AC, Loakes D & Ramakrishnan V (2010) Structure of the 70S ribosome bound to release factor 2 and a substrate analog provides insights into catalysis of peptide release. *Proc Natl Acad Sci U S A* 107: 8593–8598
- Jivotovskaya AV, Valásek L, Hinnebusch AG & Nielsen KH (2006) Eukaryotic translation initiation factor 3 (eIF3) and eIF2 can promote mRNA binding to 40S subunits independently of eIF4G in yeast. *Mol Cell Biol* 26: 1355–1372
- Joazeiro CAP (2019) Mechanisms and functions of ribosome-associated protein quality control. *Nat Rev Mol Cell Biol* 20: 368–383
- Juszkiewicz S, Chandrasekaran V, Lin Z, Kraatz S, Ramakrishnan V & Hegde RS (2018) ZNF598 Is a Quality Control Sensor of Collided Ribosomes. *Mol Cell* 72: 469-481.e7
- Juszkiewicz S, Slodkiewicz G, Lin Z, Freire-Pritchett P, Peak-Chew S-Y & Hegde RS (2020) Ribosome collisions trigger cis-acting feedback inhibition of translation initiation. *eLife* 9: e60038
- Kaledhonkar S, Fu Z, Caban K, Li W, Chen B, Sun M, Gonzalez RL & Frank J (2019) Late steps in bacterial translation initiation visualized using time-resolved cryo-EM. *Nature*: 1
- Kapp LD, Kolitz SE & Lorsch JR (2006) Yeast initiator tRNA identity elements cooperate to influence multiple steps of translation initiation. *RNA* 12: 751–764
- Kapp LD & Lorsch JR (2004) GTP-dependent recognition of the methionine moiety on initiator tRNA by translation factor eIF2. *J Mol Biol* 335: 923–936
- Karcher A, Bu \ddot{u} ttner K, Märtens B, Jansen R-P & Hopfner K-P (2005) X-Ray Structure of RLI, an Essential Twin Cassette ABC ATPase Involved in Ribosome Biogenesis and HIV Capsid Assembly. *Structure* 13: 649–659
- Karcher A, Schele A & Hopfner K-P (2008) X-ray Structure of the Complete ABC Enzyme ABCE1 from *Pyrococcus abyssi*. *J Biol Chem* 283: 7962–7971
- Karimi R, Pavlov MY, Buckingham RH & Ehrenberg M (1999) Novel roles for classical factors at the interface between translation termination and initiation. *Mol Cell* 3: 601–609
- Karzai AW, Susskind MM & Sauer RT (1999) SmpB, a unique RNA-binding protein essential for the peptide-tagging activity of SsrA (tmRNA). *EMBO J* 18: 3793–3799

- Keiler KC, Waller PR & Sauer RT (1996) Role of a peptide tagging system in degradation of proteins synthesized from damaged messenger RNA. *Science* 271: 990–993
- Kerr ID (2004) Sequence analysis of twin ATP binding cassette proteins involved in translational control, antibiotic resistance, and ribonuclease L inhibition. *Biochem Biophys Res Commun* 315: 166–173
- Khoshnevis S, Gross T, Rotte C, Baierlein C, Ficner R & Krebber H (2010) The iron-sulphur protein RNase L inhibitor functions in translation termination. *EMBO Rep* 11: 214–219
- Kiosze-Becker K, Ori A, Gerovac M, Heuer A, Nürenberg-Goloub E, Rashid UJ, Becker T, Beckmann R, Beck M & Tampé R (2016) Structure of the ribosome post-recycling complex probed by chemical cross-linking and mass spectrometry. *Nature Communications* 7: 13248
- Kispal G, Sipos K, Lange H, Fekete Z, Bedekovics T, Janáky T, Bassler J, Aguilar Netz DJ, Balk J, Rotte C, *et al* (2005) Biogenesis of cytosolic ribosomes requires the essential iron-sulphur protein Rli1p and mitochondria. *EMBO J* 24: 589–598
- Klinge S, Voigts-Hoffmann F, Leibundgut M, Arpagaus S & Ban N (2011) Crystal structure of the eukaryotic 60S ribosomal subunit in complex with initiation factor 6. *Science* 334: 941–948
- Kobayashi K, Saito K, Ishitani R, Ito K & Nureki O (2012) Structural basis for translation termination by archaeal RF1 and GTP-bound EF1 α complex. *Nucleic Acids Res* 40: 9319–9328
- Kohler R, Mooney RA, Mills DJ, Landick R & Cramer P (2017) Architecture of a transcribing-translating expressome. *Science* 356: 194–197
- Komine Y, Kitabatake M, Yokogawa T, Nishikawa K & Inokuchi H (1994) A tRNA-like structure is present in 10Sa RNA, a small stable RNA from *Escherichia coli*. *Proc Natl Acad Sci U S A* 91: 9223–9227
- Kong C, Ito K, Walsh MA, Wada M, Liu Y, Kumar S, Barford D, Nakamura Y & Song H (2004) Crystal Structure and Functional Analysis of the Eukaryotic Class II Release Factor eRF3 from *S. pombe*. *Molecular Cell* 14: 233–245
- Korkhov VM, Mireku SA & Locher KP (2012) Structure of AMP-PNP-bound vitamin B12 transporter BtuCD-F. *Nature* 490: 367–372
- Korkhov VM, Mireku SA, Veprintsev DB & Locher KP (2014) Structure of AMP-PNP-bound BtuCD and mechanism of ATP-powered vitamin B12 transport by BtuCD–F. *Nature Structural & Molecular Biology* 21: 1097–1099
- Korneeva NL, Lamphear BJ, Hennigan FL & Rhoads RE (2000) Mutually cooperative binding of eukaryotic translation initiation factor (eIF) 3 and eIF4A to human eIF4G-1. *J Biol Chem* 275: 41369–41376
- Korostelev A, Asahara H, Lancaster L, Laurberg M, Hirschi A, Zhu J, Trakhanov S, Scott WG & Noller HF (2008) Crystal structure of a translation termination complex formed with release factor RF2. *PNAS* 105: 19684–19689
- Korostelev A, Trakhanov S, Asahara H, Laurberg M, Lancaster L & Noller HF (2007) Interactions and dynamics of the Shine Dalgarno helix in the 70S ribosome. *Proceedings of the National Academy of Sciences* 104: 16840–16843

- Korostelev A, Zhu J, Asahara H & Noller HF (2010) Recognition of the amber UAG stop codon by release factor RF1. *EMBO J* 29: 2577–2585
- Kostova KK, Hickey KL, Osuna BA, Hussmann JA, Frost A, Weinberg DE & Weissman JS (2017) CAT-tailing as a fail-safe mechanism for efficient degradation of stalled nascent polypeptides. *Science* 357: 414–417
- Kothe U, Wieden H-J, Mohr D & Rodnina MV (2004) Interaction of helix D of elongation factor Tu with helices 4 and 5 of protein L7/12 on the ribosome. *J Mol Biol* 336: 1011–1021
- Kozak M (1986) Point mutations define a sequence flanking the AUG initiator codon that modulates translation by eukaryotic ribosomes. *Cell* 44: 283–292
- Kozak M (2005) Regulation of translation via mRNA structure in prokaryotes and eukaryotes. *Gene* 361: 13–37
- Kühlbrandt W (2014) Cryo-EM enters a new era. *Elife* 3: e03678
- Kurita D, Chadani Y, Muto A, Abo T & Himeno H (2014) ArfA recognizes the lack of mRNA in the mRNA channel after RF2 binding for ribosome rescue. *Nucleic Acids Res* 42: 13339–13352
- La Teana A, Gualerzi CO & Brimacombe R (1995) From stand-by to decoding site. Adjustment of the mRNA on the 30S ribosomal subunit under the influence of the initiation factors. *RNA* 1: 772–782
- Lamphear BJ, Kirchweyer R, Skern T & Rhoads RE (1995) Mapping of functional domains in eukaryotic protein synthesis initiation factor 4G (eIF4G) with picornaviral proteases. Implications for cap-dependent and cap-independent translational initiation. *J Biol Chem* 270: 21975–21983
- Lauber MA, Rappsilber J & Reilly JP (2012) Dynamics of ribosomal protein S1 on a bacterial ribosome with cross-linking and mass spectrometry. *Mol Cell Proteomics* 11: 1965–1976
- Laurberg M, Asahara H, Korostelev A, Zhu J, Trakhanov S & Noller HF (2008) Structural basis for translation termination on the 70S ribosome. *Nature* 454: 852–857
- Lecompte O, Ripp R, Thierry J-C, Moras D & Poch O (2002) Comparative analysis of ribosomal proteins in complete genomes: an example of reductive evolution at the domain scale. *Nucleic Acids Res* 30: 5382–5390
- Lee ASY, Kranzusch PJ, Doudna JA & Cate JHD (2016) eIF3d is an mRNA cap-binding protein that is required for specialized translation initiation. *Nature* 536: 96–99
- Linder P, Lasko PF, Ashburner M, Leroy P, Nielsen PJ, Nishi K, Schnier J & Slonimski PP (1989) Birth of the D-E-A-D box. *Nature* 337: 121–122
- Liu Y, Neumann P, Kuhle B, Monecke T, Schell S, Chari A & Ficner R (2014) Translation Initiation Factor eIF3b Contains a Nine-Bladed β -Propeller and Interacts with the 40S Ribosomal Subunit. *Structure* 22: 923–930
- Llácer JL, Hussain T, Dong J, Villamayor L, Gordiyenko Y & Hinnebusch AG (2021) Large-scale movement of eIF3 domains during translation initiation modulate start codon selection. *Nucleic Acids Research* 49: 11491–11511

- Llácer JL, Hussain T, Marler L, Aitken CE, Thakur A, Lorsch JR, Hinnebusch AG & Ramakrishnan V (2015) Conformational Differences between Open and Closed States of the Eukaryotic Translation Initiation Complex. *Molecular Cell* 59: 399–412
- Lo Gullo G, De Santis ML, Paiardini A, Rosignoli S, Romagnoli A, La Teana A, Londei P & Benelli D (2021) The Archaeal Elongation Factor EF-2 Induces the Release of aIF6 From 50S Ribosomal Subunit. *Frontiers in Microbiology* 12: 417
- Locher KP (2009) Review. Structure and mechanism of ATP-binding cassette transporters. *Philos Trans R Soc Lond B Biol Sci* 364: 239–245
- Locher KP (2016) Mechanistic diversity in ATP-binding cassette (ABC) transporters. *Nat Struct Mol Biol* 23: 487–493
- Locher KP, Lee AT & Rees DC (2002) The E. coli BtuCD structure: a framework for ABC transporter architecture and mechanism. *Science* 296: 1091–1098
- Lomakin IB, Kolupaeva VG, Marintchev A, Wagner G & Pestova TV (2003) Position of eukaryotic initiation factor eIF1 on the 40S ribosomal subunit determined by directed hydroxyl radical probing. *Genes Dev* 17: 2786–2797
- Lomakin IB, Shirokikh NE, Yusupov MM, Hellen CUT & Pestova TV (2006) The fidelity of translation initiation: reciprocal activities of eIF1, IF3 and YciH. *EMBO J* 25: 196–210
- Lomakin IB & Steitz TA (2013) The initiation of mammalian protein synthesis and mRNA scanning mechanism. *Nature* 500: 307–311
- Lomakin IB, Stolboushkina EA, Vaidya AT, Zhao C, Garber MB, Dmitriev SE & Steitz TA (2017) Crystal Structure of the Human Ribosome in Complex with DENR-MCT-1. *Cell Reports* 20: 521–528
- Lorsch JR & Dever TE (2010) Molecular view of 43 S complex formation and start site selection in eukaryotic translation initiation. *J Biol Chem* 285: 21203–21207
- Loveland AB, Demo G, Grigorieff N & Korostelev AA (2017) Ensemble cryo-EM elucidates the mechanism of translation fidelity. *Nature* 546: 113–117
- Loveland AB, Demo G & Korostelev AA (2020) Cryo-EM of elongating ribosome with EF-Tu•GTP elucidates tRNA proofreading. *Nature*: 1–6
- Luna RE, Arthanari H, Hiraishi H, Nanda J, Martin-Marcos P, Markus MA, Akabayov B, Milbradt AG, Luna LE, Seo H-C, *et al* (2012) The C-terminal domain of eukaryotic initiation factor 5 promotes start codon recognition by its dynamic interplay with eIF1 and eIF2β. *Cell Rep* 1: 689–702
- Lytvynenko I, Paternoga H, Thrün A, Balke A, Müller TA, Chiang CH, Nagler K, Tsaprilis G, Anders S, Bischofs I, *et al* (2019) Alanine Tails Signal Proteolysis in Bacterial Ribosome-Associated Quality Control. *Cell* 178: 76-90.e22
- Lyumkis D, Oliveira dos Passos D, Tahara EB, Webb K, Bennett EJ, Vinterbo S, Potter CS, Carragher B & Joazeiro CAP (2014) Structural basis for translational surveillance by the large ribosomal subunit-associated protein quality control complex. *Proc Natl Acad Sci U S A* 111: 15981–15986

- Ma C, Kurita D, Li N, Chen Y, Himeno H & Gao N (2017) Mechanistic insights into the alternative translation termination by ArfA and RF2. *Nature* 541: 550–553
- Maag D, Fekete CA, Gryczynski Z & Lorsch JR (2005) A conformational change in the eukaryotic translation preinitiation complex and release of eIF1 signal recognition of the start codon. *Mol Cell* 17: 265–275
- Majumdar R, Bandyopadhyay A & Maitra U (2003) Mammalian translation initiation factor eIF1 functions with eIF1A and eIF3 in the formation of a stable 40 S preinitiation complex. *J Biol Chem* 278: 6580–6587
- Majumdar R & Maitra U (2005) Regulation of GTP hydrolysis prior to ribosomal AUG selection during eukaryotic translation initiation. *EMBO J* 24: 3737–3746
- Malhotra A, Penczek P, Agrawal RK, Gabashvili IS, Grassucci RA, Jünemann R, Burkhardt N, Nierhaus KH & Frank J (1998) Escherichia coli 70 S ribosome at 15 Å resolution by cryo-electron microscopy: localization of fmet-tRNA^{fMet} and fitting of L1 protein¹¹Edited by D. Draper. *Journal of Molecular Biology* 280: 103–116
- Mancera-Martínez E, Brito Querido J, Valasek LS, Simonetti A & Hashem Y (2017) ABCE1: A special factor that orchestrates translation at the crossroad between recycling and initiation. *RNA Biology* 14: 1279–1285
- Manolaridis I, Jackson SM, Taylor NMI, Kowal J, Stahlberg H & Locher KP (2018) Cryo-EM structures of a human ABCG2 mutant trapped in ATP-bound and substrate-bound states. *Nature* 563: 426–430
- Maone E, Di Stefano M, Berardi A, Benelli D, Marzi S, La Teana A & Londei P (2007) Functional analysis of the translation factor aIF2/5B in the thermophilic archaeon *Sulfolobus solfataricus*. *Mol Microbiol* 65: 700–713
- Martin-Marcos P, Nanda J, Luna RE, Wagner G, Lorsch JR & Hinnebusch AG (2013) β -Hairpin loop of eukaryotic initiation factor 1 (eIF1) mediates 40 S ribosome binding to regulate initiator tRNA(Met) recruitment and accuracy of AUG selection in vivo. *J Biol Chem* 288: 27546–27562
- Masutani M, Sonenberg N, Yokoyama S & Imataka H (2007) Reconstitution reveals the functional core of mammalian eIF3. *EMBO J* 26: 3373–3383
- Matadeen R, Patwardhan A, Gowen B, Orlova EV, Pape T, Cuff M, Mueller F, Brimacombe R & van Heel M (1999) The Escherichia coli large ribosomal subunit at 7.5 Å resolution. *Structure* 7: 1575–1583
- Matheisl S, Berninghausen O, Becker T & Beckmann R (2015) Structure of a human translation termination complex. *Nucleic Acids Research* 43: 8615–8626
- Matsuda R, Ikeuchi K, Nomura S & Inada T (2014) Protein quality control systems associated with no-go and nonstop mRNA surveillance in yeast. *Genes Cells* 19: 1–12
- Matsuo Y, Ikeuchi K, Saeki Y, Iwasaki S, Schmidt C, Udagawa T, Sato F, Tsuchiya H, Becker T, Tanaka K, et al (2017) Ubiquitination of stalled ribosome triggers ribosome-associated quality control. *Nat Commun* 8: 159

- Matsuo Y, Tesina P, Nakajima S, Mizuno M, Endo A, Buschauer R, Cheng J, Shounai O, Ikeuchi K, Saeki Y, *et al* (2020) RQT complex dissociates ribosomes collided on endogenous RQC substrate SDD1. *Nature Structural & Molecular Biology* 27: 323–332
- Melnikov S, Ben-Shem A, Garreau de Loubresse N, Jenner L, Yusupova G & Yusupov M (2012) One core, two shells: bacterial and eukaryotic ribosomes. *Nature Structural & Molecular Biology* 19: 560–567
- Melnikov S, Mailliot J, Shin B-S, Rigger L, Yusupova G, Micura R, Dever TE & Yusupov M (2016) Crystal Structure of Hypusine-Containing Translation Factor eIF5A Bound to a Rotated Eukaryotic Ribosome. *Journal of Molecular Biology* 428: 3570–3576
- Merrick WC (2015) eIF4F: A Retrospective. *J Biol Chem* 290: 24091–24099
- Merrick WC & Pavitt GD (2018) Protein Synthesis Initiation in Eukaryotic Cells. *Cold Spring Harb Perspect Biol* 10: a033092
- Miller OL, Hamkalo BA & Thomas CA (1970) Visualization of Bacterial Genes in Action. *Science* 169: 392–395
- Mitchell SF, Walker SE, Algire MA, Park E-H, Hinnebusch AG & Lorsch JR (2010) The 5'-7-methylguanosine cap on eukaryotic mRNAs serves both to stimulate canonical translation initiation and to block an alternative pathway. *Mol Cell* 39: 950–962
- Moazed D & Noller HF (1989) Intermediate states in the movement of transfer RNA in the ribosome. *Nature* 342: 142–148
- Monestier A, Lazennec-Schurdevin C, Coureux P-D, Mechulam Y & Schmitt E (2018) Role of aIF1 in *Pyrococcus abyssi* translation initiation. *Nucleic Acids Res* 46: 11061–11074
- Morino S, Imataka H, Svitkin YV, Pestova TV & Sonenberg N (2000) Eukaryotic translation initiation factor 4E (eIF4E) binding site and the middle one-third of eIF4GI constitute the core domain for cap-dependent translation, and the C-terminal one-third functions as a modulatory region. *Mol Cell Biol* 20: 468–477
- Muhs M, Hilal T, Mielke T, Skabkin MA, Sanbonmatsu KY, Pestova TV & Spahn CMT (2015) Cryo-EM of Ribosomal 80S Complexes with Termination Factors Reveals the Translocated Cricket Paralysis Virus IRES. *Molecular Cell* 57: 422–432
- Müller C, Crowe-McAuliffe C & Wilson DN (2021) Ribosome Rescue Pathways in Bacteria. *Front Microbiol* 12
- Murina V, Kasari M, Takada H, Hinnu M, Saha CK, Grimshaw JW, Seki T, Reith M, Putrinš M, Tenson T, *et al* (2019) ABCF ATPases Involved in Protein Synthesis, Ribosome Assembly and Antibiotic Resistance: Structural and Functional Diversification across the Tree of Life. *Journal of Molecular Biology* 431: 3568–3590
- Myasnikov AG, Marzi S, Simonetti A, Giuliadori AM, Gualerzi CO, Yusupova G, Yusupov M & Klaholz BP (2005) Conformational transition of initiation factor 2 from the GTP- to GDP-bound state visualized on the ribosome. *Nat Struct Mol Biol* 12: 1145–1149
- Naganathan A, Wood MP & Moore SD (2015) The large ribosomal subunit protein L9 enables the growth of EF-P deficient cells and enhances small subunit maturation. *PLoS One* 10: e0120060

- Nakagawa S, Niimura Y, Miura K & Gojobori T (2010) Dynamic evolution of translation initiation mechanisms in prokaryotes. *PNAS* 107: 6382–6387
- Nanda JS, Cheung Y-N, Takacs JE, Martin-Marcos P, Saini AK, Hinnebusch AG & Lorsch JR (2009) eIF1 controls multiple steps in start codon recognition during eukaryotic translation initiation. *J Mol Biol* 394: 268–285
- Nanda JS, Saini AK, Muñoz AM, Hinnebusch AG & Lorsch JR (2013) Coordinated movements of eukaryotic translation initiation factors eIF1, eIF1A, and eIF5 trigger phosphate release from eIF2 in response to start codon recognition by the ribosomal preinitiation complex. *J Biol Chem* 288: 5316–5329
- Navarro-Quiles C, Mateo-Bonmatí E & Micol JL (2018) ABCE Proteins: From Molecules to Development. *Frontiers in Plant Science* 9
- Neubauer C, Gao Y-G, Andersen KR, Dunham CM, Kelley AC, Hentschel J, Gerdes K, Ramakrishnan V & Brodersen DE (2009) The Structural Basis for mRNA Recognition and Cleavage by the Ribosome-Dependent Endonuclease RelE. *Cell* 139: 1084–1095
- Neubauer C, Gillet R, Kelley AC & Ramakrishnan V (2012) Decoding in the absence of a codon by tmRNA and SmpB in the ribosome. *Science* 335: 1366–1369
- Nielsen KH, Valášek L, Sykes C, Jivotovskaya A & Hinnebusch AG (2006) Interaction of the RNP1 Motif in PRT1 with HCR1 Promotes 40S Binding of Eukaryotic Initiation Factor 3 in Yeast. *MCB* 26: 2984–2998
- Nissen P, Hansen J, Ban N, Moore PB & Steitz TA (2000) The Structural Basis of Ribosome Activity in Peptide Bond Synthesis. *Science* 289: 920–930
- Nürenberg-Goloub E, Heinemann H, Gerovac M & Tampé R (2018) Ribosome recycling is coordinated by processive events in two asymmetric ATP sites of ABCE1. *Life Science Alliance* 1: e201800095
- Obayashi E, Luna RE, Nagata T, Martin-Marcos P, Hiraishi H, Singh CR, Erzberger JP, Zhang F, Arthanari H, Morris J, *et al* (2017) Molecular Landscape of the Ribosome Pre-initiation Complex during mRNA Scanning: Structural Role for eIF3c and Its Control by eIF5. *Cell Reports* 18: 2651–2663
- Ogle JM, Brodersen DE, Clemons WM, Tarry MJ, Carter AP & Ramakrishnan V (2001) Recognition of Cognate Transfer RNA by the 30S Ribosomal Subunit. *Science* 292: 897–902
- Olsen DS, Savner EM, Mathew A, Zhang F, Krishnamoorthy T, Phan L & Hinnebusch AG (2003) Domains of eIF1A that mediate binding to eIF2, eIF3 and eIF5B and promote ternary complex recruitment in vivo. *EMBO J* 22: 193–204
- Osuna BA, Howard CJ, Kc S, Frost A & Weinberg DE (2017) In vitro analysis of RQC activities provides insights into the mechanism and function of CAT tailing. *Elife* 6: e27949
- Pang YLJ, Poruri K & Martinis SA (2014) tRNA synthetase: tRNA aminoacylation and beyond. *WIREs RNA* 5: 461–480
- Park MH, Nishimura K, Zanelli CF & Valentini SR (2010) Functional significance of eIF5A and its hypusine modification in eukaryotes. *Amino Acids* 38: 491–500

- Passmore LA, Schmeing TM, Maag D, Applefield DJ, Acker MG, Algire MA, Lorsch JR & Ramakrishnan V (2007) The Eukaryotic Translation Initiation Factors eIF1 and eIF1A Induce an Open Conformation of the 40S Ribosome. *Molecular Cell* 26: 41–50
- Pavitt GD, Ramaiah KV, Kimball SR & Hinnebusch AG (1998) eIF2 independently binds two distinct eIF2B subcomplexes that catalyze and regulate guanine-nucleotide exchange. *Genes Dev* 12: 514–526
- Pavlov MY, Freistroffer DV, MacDougall J, Buckingham RH & Ehrenberg M (1997) Fast recycling of *Escherichia coli* ribosomes requires both ribosome recycling factor (RRF) and release factor RF3. *EMBO J* 16: 4134–4141
- Pavlov MY, Watts RE, Tan Z, Cornish VW, Ehrenberg M & Forster AC (2009) Slow peptide bond formation by proline and other N-alkylamino acids in translation. *Proc Natl Acad Sci U S A* 106: 50–54
- Pedersen K, Zavialov AV, Pavlov MYu, Elf J, Gerdes K & Ehrenberg M (2003) The Bacterial Toxin RelE Displays Codon-Specific Cleavage of mRNAs in the Ribosomal A Site. *Cell* 112: 131–140
- Pedullà N, Palermo R, Hasenöhrl D, Bläsi U, Cammarano P & Londei P (2005) The archaeal eIF2 homologue: functional properties of an ancient translation initiation factor. *Nucleic Acids Res* 33: 1804–1812
- Pelechano V & Alepuz P (2017) eIF5A facilitates translation termination globally and promotes the elongation of many non polyproline-specific tripeptide sequences. *Nucleic Acids Res* 45: 7326–7338
- Pelechano V, Wei W & Steinmetz LM (2015) Widespread Co-translational RNA Decay Reveals Ribosome Dynamics. *Cell* 161: 1400–1412
- Peske F, Rodnina MV & Wintermeyer W (2005) Sequence of steps in ribosome recycling as defined by kinetic analysis. *Mol Cell* 18: 403–412
- Pestova TV, Borukhov SI & Hellen CU (1998) Eukaryotic ribosomes require initiation factors 1 and 1A to locate initiation codons. *Nature* 394: 854–859
- Pestova TV & Kolupaeva VG (2002) The roles of individual eukaryotic translation initiation factors in ribosomal scanning and initiation codon selection. *Genes Dev* 16: 2906–2922
- Pestova TV, Lomakin IB, Lee JH, Choi SK, Dever TE & Hellen CUT (2000) The joining of ribosomal subunits in eukaryotes requires eIF5B. *Nature* 403: 332–335
- Petry S, Brodersen DE, Murphy FV, Dunham CM, Selmer M, Tarry MJ, Kelley AC & Ramakrishnan V (2005) Crystal Structures of the Ribosome in Complex with Release Factors RF1 and RF2 Bound to a Cognate Stop Codon. *Cell* 123: 1255–1266
- Phan L, Zhang X, Asano K, Anderson J, Vornlocher HP, Greenberg JR, Qin J & Hinnebusch AG (1998) Identification of a translation initiation factor 3 (eIF3) core complex, conserved in yeast and mammals, that interacts with eIF5. *Mol Cell Biol* 18: 4935–4946
- Pierson WE, Hoffer ED, Keedy HE, Simms CL, Dunham CM & Zaher HS (2016) Uniformity of Peptide Release Is Maintained by Methylation of Release Factors. *Cell Rep* 17: 11–18

- Pisarev AV, Hellen CUT & Pestova TV (2007) Recycling of eukaryotic posttermination ribosomal complexes. *Cell* 131: 286–299
- Pisarev AV, Skabkin MA, Pisareva VP, Skabkina OV, Rakotondrafara AM, Hentze MW, Hellen CUT & Pestova TV (2010) The Role of ABCE1 in Eukaryotic Posttermination Ribosomal Recycling. *Molecular Cell* 37: 196–210
- Pisareva VP, Pisarev AV, Komar AA, Hellen CUT & Pestova TV (2008) Translation initiation on mammalian mRNAs with structured 5'UTRs requires DExH-box protein DHX29. *Cell* 135: 1237–1250
- Pisareva VP, Skabkin MA, Hellen CUT, Pestova TV & Pisarev AV (2011) Dissociation by Pelota, Hbs1 and ABCE1 of mammalian vacant 80S ribosomes and stalled elongation complexes: Ribosomal dissociation by Pelota/Hbs1/ABCE1. *The EMBO Journal* 30: 1804–1817
- Polacek N & Mankin AS (2005) The Ribosomal Peptidyl Transferase Center: Structure, Function, Evolution, Inhibition. *Critical Reviews in Biochemistry and Molecular Biology* 40: 285–311
- Prabhakar A, Capece MC, Petrov A, Choi J & Puglisi JD (2017) Post-termination Ribosome Intermediate Acts as the Gateway to Ribosome Recycling. *Cell Reports* 20: 161–172
- Preis A, Heuer A, Barrio-Garcia C, Hauser A, Eyler DE, Berninghausen O, Green R, Becker T & Beckmann R (2014) Cryoelectron Microscopic Structures of Eukaryotic Translation Termination Complexes Containing eRF1-eRF3 or eRF1-ABCE1. *Cell Reports* 8: 59–65
- Qu X, Lancaster L, Noller HF, Bustamante C & Tinoco I (2012) Ribosomal protein S1 unwinds double-stranded RNA in multiple steps. *Proc Natl Acad Sci U S A* 109: 14458–14463
- Querido JB, Sokabe M, Kraatz S, Gordiyenko Y, Skehel JM, Fraser CS & Ramakrishnan V (2020) Structure of a human 48S translational initiation complex. *Science* 369: 1220–1227
- Querol-Audi J, Sun C, Vogan JM, Smith MD, Gu Y, Cate JHD & Nogales E (2013) Architecture of Human Translation Initiation Factor 3. *Structure* 21: 920–928
- Rabl J, Leibundgut M, Ataide SF, Haag A & Ban N (2011) Crystal structure of the eukaryotic 40S ribosomal subunit in complex with initiation factor 1. *Science* 331: 730–736
- Radermacher M, Wagenknecht T, Verschoor A & Frank J (1987) Three-dimensional structure of the large ribosomal subunit from Escherichia coli. *The EMBO Journal* 6: 1107–1114
- Radhakrishnan A & Green R (2016) Connections Underlying Translation and mRNA Stability. *J Mol Biol* 428: 3558–3564
- Rae CD, Gordiyenko Y & Ramakrishnan V (2019) How a circularized tmRNA moves through the ribosome. *Science* 363: 740–744
- Ramrath DJF, Lancaster L, Sprink T, Mielke T, Loerke J, Noller HF & Spahn CMT (2013) Visualization of two transfer RNAs trapped in transit during elongation factor G-mediated translocation. *Proc Natl Acad Sci U S A* 110: 20964–20969
- Ranjan N, Pochopien AA, Chih-Chien Wu C, Beckert B, Blanchet S, Green R, V Rodnina M & Wilson DN (2021) Yeast translation elongation factor eEF3 promotes late stages of tRNA translocation. *EMBO J* 40: e106449

- Ratje AH, Loerke J, Mikolajka A, Br  nner M, Hildebrand PW, Starosta AL, D  nh  fer A, Connell SR, Fucini P, Mielke T, *et al* (2010) Head swivel on the ribosome facilitates translocation by means of intra-subunit tRNA hybrid sites. *Nature* 468: 713–716
- Reibarkh M, Yamamoto Y, Singh CR, del Rio F, Fahmy A, Lee B, Luna RE, Li M, Wagner G & Asano K (2008) Eukaryotic initiation factor (eIF) 1 carries two distinct eIF5-binding faces important for multifactor assembly and AUG selection. *J Biol Chem* 283: 1094–1103
- Ringquist S, Shinedling S, Barrick D, Green L, Binkley J, Stormo GD & Gold L (1992) Translation initiation in *Escherichia coli*: sequences within the ribosome-binding site. *Mol Microbiol* 6: 1219–1229
- Rodnina MV (2018) Translation in Prokaryotes. *Cold Spring Harb Perspect Biol* 10: a032664
- Rodnina MV, Beringer M & Wintermeyer W (2007) How ribosomes make peptide bonds. *Trends in Biochemical Sciences* 32: 20–26
- Rodnina MV, Fischer N, Maracci C & Stark H (2017) Ribosome dynamics during decoding. *Philosophical Transactions of the Royal Society B: Biological Sciences* 372: 20160182
- Roll-Mecak A, Alone P, Cao C, Dever TE & Burley SK (2004) X-ray structure of translation initiation factor eIF2gamma: implications for tRNA and eIF2alpha binding. *J Biol Chem* 279: 10634–10642
- Rowlands AG, Panniers R & Henshaw EC (1988) The catalytic mechanism of guanine nucleotide exchange factor action and competitive inhibition by phosphorylated eukaryotic initiation factor 2. *J Biol Chem* 263: 5526–5533
- Rudinger-Thirion J, Gieg   R & Felden B (1999) Aminoacylated tmRNA from *Escherichia coli* interacts with prokaryotic elongation factor Tu. *RNA* 5: 989–992
- Saini AK, Nanda JS, Lorsch JR & Hinnebusch AG (2010) Regulatory elements in eIF1A control the fidelity of start codon selection by modulating tRNA^{iMet} binding to the ribosome. *Genes Dev* 24: 97–110
- Saini AK, Nanda JS, Martin-Marcos P, Dong J, Zhang F, Bhardwaj M, Lorsch JR & Hinnebusch AG (2014) Eukaryotic translation initiation factor eIF5 promotes the accuracy of start codon recognition by regulating Pi release and conformational transitions of the preinitiation complex. *Nucleic Acids Res* 42: 9623–9640
- Saini P, Eyler DE, Green R & Dever TE (2009) Hypusine-containing protein eIF5A promotes translation elongation. *Nature* 459: 118–121
- Saito K, Kobayashi K, Wada M, Kikuno I, Takusagawa A, Mochizuki M, Uchiumi T, Ishitani R, Nureki O & Ito K (2010) Omnipotent role of archaeal elongation factor 1 alpha (EF1   in translational elongation and termination, and quality control of protein synthesis. *Proc Natl Acad Sci U S A* 107: 19242–19247
- Salas-Marco J & Bedwell DM (2004) GTP Hydrolysis by eRF3 Facilitates Stop Codon Decoding during Eukaryotic Translation Termination. *Molecular and Cellular Biology* 24: 7769–7778
- Salas-Marco J & Bedwell DM (2005) Discrimination Between Defects in Elongation Fidelity and Termination Efficiency Provides Mechanistic Insights into Translational Readthrough. *Journal of Molecular Biology* 348: 801–815

- Santos N, Zhu J, Donohue JP, Korostelev AA & Noller HF (2013) Crystal Structure of the 70S Ribosome Bound with the Q253P Mutant Form of Release Factor RF2. *Structure* 21: 1258–1263
- Saxena S, Myka KK, Washburn R, Costantino N, Court DL & Gottesman ME (2018) Escherichia coli transcription factor NusG binds to 70S ribosomes. *Mol Microbiol*
- Schaub RE, Poole SJ, Garza-Sánchez F, Benbow S & Hayes CS (2012) Proteobacterial ArfA peptides are synthesized from non-stop messenger RNAs. *J Biol Chem* 287: 29765–29775
- Schleich S, Strassburger K, Janiesch PC, Koledachkina T, Miller KK, Haneke K, Cheng Y-S, Kuechler K, Stoecklin G, Duncan KE, *et al* (2014) DENR-MCT-1 promotes translation re-initiation downstream of uORFs to control tissue growth. *Nature* 512: 208–212
- Schlessinger D, Mangiarotti G & Apirion D (1967) The formation and stabilization of 30S and 50S ribosome couples in Escherichia coli. *Proc Natl Acad Sci U S A* 58: 1782–1789
- Schlutzen F, Tocilj A, Zarivach R, Harms J, Gluehmann M, Janell D, Bashan A, Bartels H, Agmon I, Franceschi F, *et al* (2000) Structure of Functionally Activated Small Ribosomal Subunit at 3.3 Å Resolution. *Cell* 102: 615–623
- Schmeing TM, Seila AC, Hansen JL, Freeborn B, Soukup JK, Scaringe SA, Strobel SA, Moore PB & Steitz TA (2002) A pre-translocational intermediate in protein synthesis observed in crystals of enzymatically active 50S subunits. *Nat Struct Biol*
- Schmeing TM, Voorhees RM, Kelley AC, Gao Y-G, Murphy FV, Weir JR & Ramakrishnan V (2009) The crystal structure of the ribosome bound to EF-Tu and aminoacyl-tRNA. *Science* 326: 688–694
- Schmidt C, Becker T, Heuer A, Braunger K, Shanmuganathan V, Pech M, Berninghausen O, Wilson DN & Beckmann R (2016) Structure of the hypusinylated eukaryotic translation factor eIF-5A bound to the ribosome. *Nucleic Acids Research* 44: 1944–1951
- Schmitt E, Coureux P-D, Kazan R, Bourgeois G, Lazennec-Schurdevin C & Mechulam Y (2020) Recent Advances in Archaeal Translation Initiation. *Front Microbiol* 11
- Schmitt E, Coureux P-D, Monestier A, Dubiez E & Mechulam Y (2019) Start Codon Recognition in Eukaryotic and Archaeal Translation Initiation: A Common Structural Core. *IJMS* 20: 939
- Schmitt E, Naveau M & Mechulam Y (2010) Eukaryotic and archaeal translation initiation factor 2: a heterotrimeric tRNA carrier. *FEBS Lett* 584: 405–412
- Schmitt E, Panvert M, Lazennec-Schurdevin C, Coureux P-D, Perez J, Thompson A & Mechulam Y (2012) Structure of the ternary initiation complex aIF2–GDPNP–methionylated initiator tRNA. *Nature Structural & Molecular Biology* 19: 450–454
- Schuller AP & Green R (2017) The ABC(E1)s of Ribosome Recycling and Reinitiation. *Molecular Cell* 66: 578–580
- Schuller AP & Green R (2018) Roadblocks and resolutions in eukaryotic translation. *Nature Reviews Molecular Cell Biology* 19: 526–541
- Schuller AP, Wu CC-C, Dever TE, Buskirk AR & Green R (2017) eIF5A Functions Globally in Translation Elongation and Termination. *Molecular Cell* 66: 194–205.e5

- Schuwirth BS, Borovinskaya MA, Hau CW, Zhang W, Vila-Sanjurjo A, Holton JM & Cate JHD (2005) Structures of the Bacterial Ribosome at 3.5 Å Resolution. *Science* 310: 827–834
- Scolnick E, Tompkins R, Caskey T & Nirenberg M (1968) Release factors differing in specificity for terminator codons. *Proc Natl Acad Sci USA* 61: 768
- Seidman JS, Janssen BD & Hayes CS (2011) Alternative fates of paused ribosomes during translation termination. *J Biol Chem* 286: 31105–31112
- Selmer M, Dunham CM, Murphy FV, Weixlbaumer A, Petry S, Kelley AC, Weir JR & Ramakrishnan V (2006) Structure of the 70S Ribosome Complexed with mRNA and tRNA. *Science* 313: 1935–1942
- Semenkov YP, Rodnina MV & Wintermeyer W (1996) The ‘allosteric three-site model’ of elongation cannot be confirmed in a well-defined ribosome system from *Escherichia coli*. *Proc Natl Acad Sci U S A* 93: 12183–12188
- Sengupta J, Agrawal RK & Frank J (2001) Visualization of protein S1 within the 30S ribosomal subunit and its interaction with messenger RNA. *PNAS* 98: 11991–11996
- Shao S, Brown A, Santhanam B & Hegde RS (2015) Structure and assembly pathway of the ribosome quality control complex. *Mol Cell* 57: 433–444
- Shao S & Hegde RS (2014) Reconstitution of a minimal ribosome-associated ubiquitination pathway with purified factors. *Mol Cell* 55: 880–890
- Shao S, Murray J, Brown A, Taunton J, Ramakrishnan V & Hegde RS (2016) Decoding Mammalian Ribosome-mRNA States by Translational GTPase Complexes. *Cell* 167: 1229-1240.e15
- Sharma PK, Xiang Y, Kato M & Warshel A (2005) What are the roles of substrate-assisted catalysis and proximity effects in peptide bond formation by the ribosome? *Biochemistry* 44: 11307–11314
- Shen PS, Park J, Qin Y, Li X, Parsawar K, Larson MH, Cox J, Cheng Y, Lambowitz AM, Weissman JS, *et al* (2015) Protein synthesis. Rqc2p and 60S ribosomal subunits mediate mRNA-independent elongation of nascent chains. *Science* 347: 75–78
- Shimokawa-Chiba N, Müller C, Fujiwara K, Beckert B, Ito K, Wilson DN & Chiba S (2019) Release factor-dependent ribosome rescue by BrfA in the Gram-positive bacterium *Bacillus subtilis*. *Nat Commun* 10: 5397
- Shin DH, Brandsen J, Jancarik J, Yokota H, Kim R & Kim S-H (2004) Structural analyses of peptide release factor 1 from *Thermotoga maritima* reveal domain flexibility required for its interaction with the ribosome. *J Mol Biol* 341: 227–239
- Shine J & Dalgarno L (1974) The 3'-Terminal Sequence of *Escherichia coli* 16S Ribosomal RNA: Complementarity to Nonsense Triplets and Ribosome Binding Sites. *Proceedings of the National Academy of Sciences* 71: 1342–1346
- Shoemaker CJ & Green R (2011) Kinetic analysis reveals the ordered coupling of translation termination and ribosome recycling in yeast. *Proceedings of the National Academy of Sciences* 108: E1392–E1398

- Simms CL, Yan LL & Zaher HS (2017) Ribosome Collision Is Critical for Quality Control during No-Go Decay. *Molecular Cell* 68: 361-373.e5
- Simonetti A, Brito Querido J, Myasnikov AG, Mancera-Martinez E, Renaud A, Kuhn L & Hashem Y (2016) eIF3 Peripheral Subunits Rearrangement after mRNA Binding and Start-Codon Recognition. *Molecular Cell* 63: 206–217
- Simonetti A, Guca E, Bochler A, Kuhn L & Hashem Y (2020) Structural Insights into the Mammalian Late-Stage Initiation Complexes. *Cell Reports* 31: 107497
- Simonetti A, Marzi S, Billas IML, Tsai A, Fabbretti A, Myasnikov AG, Roblin P, Vaiana AC, Hazemann I, Eiler D, *et al* (2013a) Involvement of protein IF2 N domain in ribosomal subunit joining revealed from architecture and function of the full-length initiation factor. *Proc Natl Acad Sci U S A* 110: 15656–15661
- Simonetti A, Marzi S, Fabbretti A, Hazemann I, Jenner L, Urzhumtsev A, Gualerzi CO & Klaholz BP (2013b) Structure of the protein core of translation initiation factor 2 in apo, GTP-bound and GDP-bound forms. *Acta Cryst D* 69: 925–933
- Simonetti A, Marzi S, Myasnikov AG, Fabbretti A, Yusupov M, Gualerzi CO & Klaholz BP (2008) Structure of the 30S translation initiation complex. *Nature* 455: 416–420
- Simonović M & Steitz TA (2009) A structural view on the mechanism of the ribosome-catalyzed peptide bond formation. *Biochim Biophys Acta* 1789: 612–623
- Singh CR, Lee B, Udagawa T, Mohammad-Qureshi SS, Yamamoto Y, Pavitt GD & Asano K (2006) An eIF5/eIF2 complex antagonizes guanine nucleotide exchange by eIF2B during translation initiation. *EMBO J* 25: 4537–4546
- Sinha NK, Ordureau A, Best K, Saba JA, Zinshteyn B, Sundaramoorthy E, Fulzele A, Garshott DM, Denk T, Thoms M, *et al* (2020) EDF1 coordinates cellular responses to ribosome collisions. *eLife* 9: e58828
- Siridechadilok B, Fraser CS, Hall RJ, Doudna JA & Nogales E (2005) Structural roles for human translation factor eIF3 in initiation of protein synthesis. *Science* 310: 1513–1515
- Sitron CS & Brandman O (2019) CAT tails drive degradation of stalled polypeptides on and off the ribosome. *Nat Struct Mol Biol* 26: 450–459
- Sitron CS & Brandman O (2020) Detection and Degradation of Stalled Nascent Chains via Ribosome-Associated Quality Control. *Annu Rev Biochem* 89: 417–442
- Sitron CS, Park JH & Brandman O (2017) Asc1, Hel2, and Slh1 couple translation arrest to nascent chain degradation. *RNA* 23: 798–810
- Skabkin MA, Skabkina OV, Dhote V, Komar AA, Hellen CUT & Pestova TV (2010) Activities of Ligatin and MCT-1/DENR in eukaryotic translation initiation and ribosomal recycling. *Genes Dev* 24: 1787–1801
- Skabkin MA, Skabkina OV, Hellen CUT & Pestova TV (2013) Reinitiation and other unconventional posttermination events during eukaryotic translation. *Mol Cell* 51: 249–264

- Smith AM, Costello MS, Kettring AH, Wingo RJ & Moore SD (2019) Ribosome collisions alter frameshifting at translational reprogramming motifs in bacterial mRNAs. *PNAS* 116: 21769–21779
- Sokabe M & Fraser CS (2014) Human eukaryotic initiation factor 2 (eIF2)-GTP-Met-tRNAi ternary complex and eIF3 stabilize the 43 S preinitiation complex. *J Biol Chem* 289: 31827–31836
- Sokabe M & Fraser CS (2017) A helicase-independent activity of eIF4A in promoting mRNA recruitment to the human ribosome. *Proc Natl Acad Sci USA* 114: 6304–6309
- Sokabe M & Fraser CS (2019) Toward a Kinetic Understanding of Eukaryotic Translation. *Cold Spring Harb Perspect Biol* 11: a032706
- Sokabe M, Fraser CS & Hershey JWB (2012) The human translation initiation multi-factor complex promotes methionyl-tRNAi binding to the 40S ribosomal subunit. *Nucleic Acids Res* 40: 905–913
- Song H, Mugnier P, Das AK, Webb HM, Evans DR, Tuite MF, Hemmings BA & Barford D (2000) The Crystal Structure of Human Eukaryotic Release Factor eRF1—Mechanism of Stop Codon Recognition and Peptidyl-tRNA Hydrolysis. *Cell* 100: 311–321
- Spahn CMT, Gomez-Lorenzo MG, Grassucci RA, Jørgensen R, Andersen GR, Beckmann R, Penczek PA, Ballesta JPG & Frank J (2004) Domain movements of elongation factor eEF2 and the eukaryotic 80S ribosome facilitate tRNA translocation. *EMBO J* 23: 1008–1019
- Stansfield I, Jones KM, Kushnirov VV, Dagkesamanskaya AR, Poznyakovski AI, Paushkin SV, Nierras CR, Cox BS, Ter-Avanesyan MD & Tuite MF (1995) The products of the SUP45 (eRF1) and SUP35 genes interact to mediate translation termination in *Saccharomyces cerevisiae*. *EMBO J* 14: 4365–4373
- Stark H, Mueller F, Orlova EV, Schatz M, Dube P, Erdemir T, Zemlin F, Brimacombe R & Heel M van (1995) The 70S *Escherichia coli* ribosome at 23 Å resolution: fitting the ribosomal RNA. *Structure* 3: 815–821
- Steitz JA & Jakes K (1975) How ribosomes select initiator regions in mRNA: base pair formation between the 3' terminus of 16S rRNA and the mRNA during initiation of protein synthesis in *Escherichia coli*. *Proceedings of the National Academy of Sciences* 72: 4734–4738
- Steitz TA & Moore PB (2003) RNA, the first macromolecular catalyst: the ribosome is a ribozyme. *Trends in Biochemical Sciences* 28: 411–418
- Sternberg SH, Fei J, Prywes N, McGrath KA & Gonzalez RL (2009) Translation factors direct intrinsic ribosome dynamics during translation termination and ribosome recycling. *Nat Struct Mol Biol* 16: 861–868
- Stockner T, Gradisch R & Schmitt L (2020) The role of the degenerate nucleotide binding site in type I ABC exporters. *FEBS Lett* 594: 3815–3838
- Stolboushkina E, Nikonov S, Nikulin A, Bläsi U, Manstein DJ, Fedorov R, Garber M & Nikonov O (2008) Crystal structure of the intact archaeal translation initiation factor 2 demonstrates very high conformational flexibility in the alpha- and beta-subunits. *J Mol Biol* 382: 680–691

- Su T, Izawa T, Thoms M, Yamashita Y, Cheng J, Berninghausen O, Hartl FU, Inada T, Neupert W & Beckmann R (2019) Structure and function of Vms1 and Arb1 in RQC and mitochondrial proteome homeostasis. *Nature* 570: 538–542
- Sun C, Todorovic A, Querol-Audí J, Bai Y, Villa N, Snyder M, Ashchyan J, Lewis CS, Hartland A, Gradia S, *et al* (2011) Functional reconstitution of human eukaryotic translation initiation factor 3 (eIF3). *Proc Natl Acad Sci U S A* 108: 20473–20478
- Takada H, Crowe-McAuliffe C, Polte C, Sidorova ZY, Murina V, Atkinson GC, Konevega AL, Ignatova Z, Wilson DN & Haurlyuk V (2021) RqcH and RqcP catalyze processive poly-alanine synthesis in a reconstituted ribosome-associated quality control system. *Nucleic Acids Research* 49: 8355–8369
- Tarun SZ & Sachs AB (1996) Association of the yeast poly(A) tail binding protein with translation initiation factor eIF-4G. *EMBO J* 15: 7168–7177
- Tarun SZ, Wells SE, Deardorff JA & Sachs AB (1997) Translation initiation factor eIF4G mediates in vitro poly(A) tail-dependent translation. *Proc Natl Acad Sci U S A* 94: 9046–9051
- Taylor D, Unbehaun A, Li W, Das S, Lei J, Liao HY, Grassucci RA, Pestova TV & Frank J (2012) Cryo-EM structure of the mammalian eukaryotic release factor eRF1–eRF3-associated termination complex. *PNAS* 109: 18413–18418
- Taylor DJ, Nilsson J, Merrill AR, Andersen GR, Nissen P & Frank J (2007) Structures of modified eEF2-80S ribosome complexes reveal the role of GTP hydrolysis in translocation. *The EMBO Journal* 26: 2421–2431
- Thrun A, Garzia A, Kigoshi-Tansho Y, Patil PR, Umbaugh CS, Dallinger T, Liu J, Kreger S, Patrizi A, Cox GA, *et al* (2021) Convergence of mammalian RQC and C-end rule proteolytic pathways via alanine tailing. *Molecular Cell* 81: 2112-2122.e7
- Timsit Y, Sergeant-Perthuis G & Bennequin D (2021) Evolution of ribosomal protein network architectures. *Sci Rep* 11: 625
- Tsuboi T, Kuroha K, Kudo K, Makino S, Inoue E, Kashima I & Inada T (2012) Dom34:Hbs1 Plays a General Role in Quality-Control Systems by Dissociation of a Stalled Ribosome at the 3' End of Aberrant mRNA. *Molecular Cell* 46: 518–529
- Ude S, Lassak J, Starosta AL, Kraxenberger T, Wilson DN & Jung K (2013) Translation elongation factor EF-P alleviates ribosome stalling at polyproline stretches. *Science* 339: 82–85
- Uemura S, Aitken CE, Korlach J, Flusberg BA, Turner SW & Puglisi JD (2010) Real-time tRNA transit on single translating ribosomes at codon resolution. *Nature* 464: 1012–1017
- Unbehaun A, Borukhov SI, Hellen CUT & Pestova TV (2004) Release of initiation factors from 48S complexes during ribosomal subunit joining and the link between establishment of codon-anticodon base-pairing and hydrolysis of eIF2-bound GTP. *Genes Dev* 18: 3078–3093
- Ushida C, Himeno H, Watanabe T & Muto A (1994) tRNA-like structures in 10Sa RNAs of Mycoplasma capricolum and Bacillus subtilis. *Nucleic Acids Res* 22: 3392–3396
- Valášek L, Hasek J, Trachsel H, Imre EM & Ruis H (1999) The Saccharomyces cerevisiae HCR1 gene encoding a homologue of the p35 subunit of human translation initiation factor 3 (eIF3) is a

- high copy suppressor of a temperature-sensitive mutation in the Rpg1p subunit of yeast eIF3. *J Biol Chem* 274: 27567–27572
- Valášek L, Nielsen KH & Hinnebusch AG (2002) Direct eIF2-eIF3 contact in the multifactor complex is important for translation initiation in vivo. *EMBO J* 21: 5886–5898
- Valášek L, Phan L, Schoenfeld LW, Valásková V & Hinnebusch AG (2001) Related eIF3 subunits TIF32 and HCR1 interact with an RNA recognition motif in PRT1 required for eIF3 integrity and ribosome binding. *EMBO J* 20: 891–904
- Valášek LS (2012) 'Ribozoomin'--translation initiation from the perspective of the ribosome-bound eukaryotic initiation factors (eIFs). *Curr Protein Pept Sci* 13: 305–330
- Valášek LS, Zeman J, Wagner S, Beznosková P, Pavlíková Z, Mohammad MP, Hronová V, Herrmannová A, Hashem Y & Gunišová S (2017) Embraced by eIF3: structural and functional insights into the roles of eIF3 across the translation cycle. *Nucleic Acids Research* 45: 10948–10968
- Valle M, Gillet R, Kaur S, Henne A, Ramakrishnan V & Frank J (2003) Visualizing tmRNA Entry into a Stalled Ribosome. *Science* 300: 127–130
- VanLoock MS, Agrawal RK, Gabashvili IS, Qi L, Frank J & Harvey SC (2000) Movement of the Decoding Region of the 16S Ribosomal RNA Accompanies tRNA Translocation. *Journal of Molecular Biology* 304: 507–515
- Vassilenko KS, Alekhina OM, Dmitriev SE, Shatsky IN & Spirin AS (2011) Unidirectional constant rate motion of the ribosomal scanning particle during eukaryotic translation initiation. *Nucleic Acids Res* 39: 5555–5567
- Vazquez de Aldana CR, Marton MJ & Hinnebusch AG (1995) GCN20, a novel ATP binding cassette protein, and GCN1 reside in a complex that mediates activation of the eIF-2 alpha kinase GCN2 in amino acid-starved cells. *EMBO J* 14: 3184–3199
- Venkataraman K, Guja KE, Garcia-Diaz M & Karzai AW (2014a) Non-stop mRNA decay: a special attribute of trans-translation mediated ribosome rescue. *Front Microbiol* 5: 93
- Venkataraman K, Zafar H & Karzai AW (2014b) Distinct tmRNA sequence elements facilitate RNase R engagement on rescued ribosomes for selective nonstop mRNA decay. *Nucleic Acids Res* 42: 11192–11202
- Vestergaard B, Van LB, Andersen GR, Nyborg J, Buckingham RH & Kjeldgaard M (2001) Bacterial polypeptide release factor RF2 is structurally distinct from eukaryotic eRF1. *Mol Cell* 8: 1375–1382
- Villa N, Do A, Hershey JWB & Fraser CS (2013) Human Eukaryotic Initiation Factor 4G (eIF4G) Protein Binds to eIF3c, -d, and -e to Promote mRNA Recruitment to the Ribosome. *J Biol Chem* 288: 32932–32940
- Wada M & Ito K (2014) A genetic approach for analyzing the co-operative function of the tRNA mimicry complex, eRF1/eRF3, in translation termination on the ribosome. *Nucleic Acids Res* 42: 7851–7866

- Walker SE, Zhou F, Mitchell SF, Larson VS, Valasek L, Hinnebusch AG & Lorsch JR (2013) Yeast eIF4B binds to the head of the 40S ribosomal subunit and promotes mRNA recruitment through its N-terminal and internal repeat domains. *RNA* 19: 191–207
- Wallin G & Aqvist J (2010) The transition state for peptide bond formation reveals the ribosome as a water trap. *Proc Natl Acad Sci U S A* 107: 1888–1893
- Wang C, Molodtsov V, Firlar E, Kaelber JT, Blaha G, Su M & Ebright RH (2020) Structural basis of transcription-translation coupling. *Science* 369: 1359–1365
- Wang J, Johnson AG, Lapointe CP, Choi J, Prabhakar A, Chen D-H, Petrov AN & Puglisi JD (2019) eIF5B gates the transition from translation initiation to elongation. *Nature* 573: 605–608
- Wang J, Zhou J, Yang Q & Grayhack EJ (2018a) Multi-protein bridging factor 1(Mbf1), Rps3 and Asc1 prevent stalled ribosomes from frameshifting. *Elife* 7: e39637
- Wang YJ, Vaidyanathan PP, Rojas-Duran MF, Udeshi ND, Bartoli KM, Carr SA & Gilbert WV (2018b) Lso2 is a conserved ribosome-bound protein required for translational recovery in yeast. *PLOS Biology* 16: e2005903
- Washburn RS, Zuber PK, Sun M, Hashem Y, Shen B, Li W, Harvey S, Acosta Reyes FJ, Gottesman ME, Knauer SH, *et al* (2020) Escherichia coli NusG Links the Lead Ribosome with the Transcription Elongation Complex. *iScience* 23: 101352
- Watson ZL, Ward FR, Méheust R, Ad O, Schepartz A, Banfield JF & Cate JH (2020) Structure of the bacterial ribosome at 2 Å resolution. *eLife* 9: e60482
- Weis F, Giudice E, Churcher M, Jin L, Hilcenko C, Wong CC, Traynor D, Kay RR & Warren AJ (2015) Mechanism of eIF6 release from the nascent 60S ribosomal subunit. *Nat Struct Mol Biol* 22: 914–919
- Weisser M & Ban N (2019) Extensions, Extra Factors, and Extreme Complexity: Ribosomal Structures Provide Insights into Eukaryotic Translation. *Cold Spring Harb Perspect Biol* 11
- Weisser M, Schäfer T, Leibundgut M, Böhringer D, Aylett CHS & Ban N (2017) Structural and Functional Insights into Human Re-initiation Complexes. *Molecular Cell* 67: 447-456.e7
- Weisser M, Voigts-Hoffmann F, Rabl J, Leibundgut M & Ban N (2013) The crystal structure of the eukaryotic 40S ribosomal subunit in complex with eIF1 and eIF1A. *Nature Structural & Molecular Biology* 20: 1015–1017
- Weixlbaumer A, Jin H, Neubauer C, Voorhees RM, Petry S, Kelley AC & Ramakrishnan V (2008) Insights into translational termination from the structure of RF2 bound to the ribosome. *Science* 322: 953–956
- Weixlbaumer A, Petry S, Dunham CM, Selmer M, Kelley AC & Ramakrishnan V (2007) Crystal structure of the ribosome recycling factor bound to the ribosome. *Nat Struct Mol Biol* 14: 733–737
- Wells JN, Buschauer R, Mackens-Kiani T, Best K, Kratzat H, Berninghausen O, Becker T, Gilbert W, Cheng J & Beckmann R (2020) Structure and function of yeast Lso2 and human CCDC124 bound to hibernating ribosomes. *PLOS Biology* 18: e3000780

- Wells SE, Hillner PE, Vale RD & Sachs AB (1998) Circularization of mRNA by eukaryotic translation initiation factors. *Mol Cell* 2: 135–140
- Wilkins S (2015) Structure and mechanism of ABC transporters. *F1000Prime Rep* 7: 14
- Wilson DN & Cate JHD (2012) The Structure and Function of the Eukaryotic Ribosome. *Cold Spring Harb Perspect Biol* 4: a011536
- Wilson DN, Schlutzen F, Harms JM, Yoshida T, Ohkubo T, Albrecht R, Buerger J, Kobayashi Y & Fucini P (2005) X-ray crystallography study on ribosome recycling: the mechanism of binding and action of RRF on the 50S ribosomal subunit. *EMBO J* 24: 251–260
- Wimberly BT, Brodersen DE, Clemons WM, Morgan-Warren RJ, Carter AP, Vonnrhein C, Hartsch T & Ramakrishnan V (2000) Structure of the 30S ribosomal subunit. *Nature* 407: 327–339
- Winzler EA, Shoemaker DD, Astromoff A, Liang H, Anderson K, Andre B, Bangham R, Benito R, Boeke JD, Bussey H, *et al* (1999) Functional characterization of the *S. cerevisiae* genome by gene deletion and parallel analysis. *Science* 285: 901–906
- Woese CR, Kandler O & Wheelis ML (1990) Towards a natural system of organisms: proposal for the domains Archaea, Bacteria, and Eucarya. *Proceedings of the National Academy of Sciences* 87: 4576–4579
- Wu L, Zhou B, Oshiro-Rapley N, Li M, Paulo JA, Webster CM, Mou F, Kacergis MC, Talkowski ME, Carr CE, *et al* (2016) An Ancient, Unified Mechanism for Metformin Growth Inhibition in *C. elegans* and Cancer. *Cell* 167: 1705-1718.e13
- Yamamoto Y, Singh CR, Marintchev A, Hall NS, Hannig EM, Wagner G & Asano K (2005) The eukaryotic initiation factor (eIF) 5 HEAT domain mediates multifactor assembly and scanning with distinct interfaces to eIF1, eIF2, eIF3, and eIF4G. *Proc Natl Acad Sci U S A* 102: 16164–16169
- Yamamoto Y, Sunohara T, Jojima K, Inada T & Aiba H (2003) SsrA-mediated trans-translation plays a role in mRNA quality control by facilitating degradation of truncated mRNAs. *RNA* 9: 408–418
- Yan LL & Zaher HS (2019) How do cells cope with RNA damage and its consequences? *Journal of Biological Chemistry* 294: 15158–15171
- Yip MCJ, Keszei AFA, Feng Q, Chu V, McKenna MJ & Shao S (2019) Mechanism for recycling tRNAs on stalled ribosomes. *Nat Struct Mol Biol* 26: 343–349
- Yokoyama T, Shaikh TR, Iwakura N, Kaji H, Kaji A & Agrawal RK (2012) Structural insights into initial and intermediate steps of the ribosome-recycling process. *EMBO J* 31: 1836–1846
- Yoon HJ & Donahue TF (1992) The suil suppressor locus in *Saccharomyces cerevisiae* encodes a translation factor that functions during tRNA(iMet) recognition of the start codon. *Mol Cell Biol* 12: 248–260
- Young DJ & Gydosh NR (2019) Hcr1/eIF3j Is a 60S Ribosomal Subunit Recycling Accessory Factor In Vivo. *Cell Reports* 28: 39-50.e4
- Young DJ, Gydosh NR, Zhang F, Hinnebusch AG & Green R (2015) Rli1/ABCE1 Recycles Terminating Ribosomes and Controls Translation Reinitiation in 3'UTRs In Vivo. *Cell* 162: 872–884

- Young DJ, Makeeva DS, Zhang F, Anisimova AS, Stolboushkina EA, Ghobakhlou F, Shatsky IN, Dmitriev SE, Hinnebusch AG & Guydosh NR (2018) Tma64/eIF2D, Tma20/MCT-1, and Tma22/DENR Recycle Post-termination 40S Subunits In Vivo. *Molecular Cell* 71: 761-774.e5
- Young DJ, Meydan S & Guydosh NR (2021) 40S ribosome profiling reveals distinct roles for Tma20/Tma22 (MCT-1/DENR) and Tma64 (eIF2D) in 40S subunit recycling. *Nature Communications* 12: 2976
- Youngman EM, McDonald ME & Green R (2008) Peptide release on the ribosome: mechanism and implications for translational control. *Annu Rev Microbiol* 62: 353–373
- Yu Y, Marintchev A, Kolupaeva VG, Unbehauen A, Veryasova T, Lai S-C, Hong P, Wagner G, Hellen CUT & Pestova TV (2009) Position of eukaryotic translation initiation factor eIF1A on the 40S ribosomal subunit mapped by directed hydroxyl radical probing. *Nucleic Acids Res* 37: 5167–5182
- Yusupov MM, Yusupova GZh, Baucom A, Lieberman K, Earnest TN, Cate JHD & Noller HF (2001) Crystal Structure of the Ribosome at 5.5 Å Resolution. *Science* 292: 883–896
- Yusupova G, Jenner L, Rees B, Moras D & Yusupov M (2006) Structural basis for messenger RNA movement on the ribosome. *Nature* 444: 391–394
- Yusupova GZh, Yusupov MM, Cate JHD & Noller HF (2001) The Path of Messenger RNA through the Ribosome. *Cell* 106: 233–241
- Zavialov AV, Hauryliuk VV & Ehrenberg M (2005) Splitting of the posttermination ribosome into subunits by the concerted action of RRF and EF-G. *Mol Cell* 18: 675–686
- Zavialov AV, Mora L, Buckingham RH & Ehrenberg M (2002) Release of peptide promoted by the GGQ motif of class 1 release factors regulates the GTPase activity of RF3. *Mol Cell* 10: 789–798
- Zeman J, Itoh Y, Kukačka Z, Rosůlek M, Kavan D, Kouba T, Jansen ME, Mohammad MP, Novák P & Valášek LS (2019) Binding of eIF3 in complex with eIF5 and eIF1 to the 40S ribosomal subunit is accompanied by dramatic structural changes. *Nucleic Acids Research* 47: 8282–8300
- Zeng F, Chen Y, Remis J, Shekhar M, Phillips JC, Tajkhorshid E & Jin H (2017) Structural basis of co-translational quality control by ArfA and RF2 bound to ribosome. *Nature* 541: 554–557
- Zeng F & Jin H (2016) Peptide release promoted by methylated RF2 and ArfA in nonstop translation is achieved by an induced-fit mechanism. *RNA* 22: 49–60
- Zhou F, Walker SE, Mitchell SF, Lorsch JR & Hinnebusch AG (2014) Identification and characterization of functionally critical, conserved motifs in the internal repeats and N-terminal domain of yeast translation initiation factor 4B (yef4B). *J Biol Chem* 289: 1704–1722
- Zhou W, Lu Q, Li Q, Wang L, Ding S, Zhang A, Wen X, Zhang L & Lu C (2017) PPR-SMR protein SOT1 has RNA endonuclease activity. *Proc Natl Acad Sci U S A* 114: E1554–E1563
- Zhouravleva G, Frolova L, Le Goff X, Le Guellec R, Inge-Vechtomov S, Kisselev L & Philippe M (1995) Termination of translation in eukaryotes is governed by two interacting polypeptide chain release factors, eRF1 and eRF3. *EMBO J* 14: 4065–4072

Zurita Rendón O, Fredrickson EK, Howard CJ, Van Vranken J, Fogarty S, Tolley ND, Kalia R, Osuna BA, Shen PS, Hill CP, *et al* (2018) Vms1p is a release factor for the ribosome-associated quality control complex. *Nat Commun* 9: 2197

5. ACKNOWLEDGEMENTS

Everyone knows I like running. Only few people know I like running long straight roads. 5 years ago and a little naïve, I thought doing my PhD would be like this – doing a long run and seeing the goal at the end of the road, exactly knowing where to go from the start. I was right about the length, but it turned out to be everything else than a straight road! I started running in the wrong direction, climbed a few mountains, passed rough terrain, ran in circles, and found that the wrong road was not so wrong after all... It feels a bit unreal to be so close to the finish line now and I would like to thank the people who were part of this journey and kept me going.

First, I would like to thank Prof. Roland Beckmann for the opportunity to join his lab as a PhD student and start this journey. It has been a privilege to be part of his group and I am grateful that he let me work on so many different projects and pursue what I was interested in. He always managed to motivate me and gave me the feeling that my work is meaningful.

I want to thank the people who make sure I pass the finish line according to the rules. I would like to thank Prof. Karl-Peter Hopfner for taking the time to be part of my thesis committee and second thesis examiner. Further, I would like to thank all other members of my thesis committee: Prof. Gert Bange, Gregor Witte, Prof. Klaus Förstermann and Dietmar Martin.

It has been a pleasure to work with so many different great scientist during the last years.

I especially want to thank Prof. Gert Bange for many crazy ideas and the courage to view things differently. I would further like to thank the members of his lab that I worked with, Devid Mrusek, Patricia Bedrunka, Laura Czech and Vitan Blagotinsek for great collaborations. Moreover, I would like to thank our collaboration partners Prof. Robert Tampe and his group members Elina Nürenberg-Goloub and Holger Heinemann (Goethe University Frankfurt), Prof. Micheline Fromont-Racine and her group (Institut Pasteur, France), Prof. Franz Herzog and Mia Potocnjak (Gene Center Munich), Prof. Kurt Vermeire and Eva Pauwels (KU Leuven in Belgium), Prof. Rachel Green, Allen Buskirk and their group members Kazuki Saito and Annabelle Campbell.

I would like to thank the Graduate School Quantitative Bioscience Munich (QBM) and the Transregio TRR174 for providing a great start to my PhD, organizing retreats and courses, and funding.

I would like to thank the Beckmann lab technicians Joanna Musial, Andrea Gilmozzi, Susanne Rieder, Charlotte Ungewickel, and Heidemarie Sieber. Joanna, Andrea, and Heidi, thank you for keeping everything up and running in the lab and helping everyone with your open and caring nature.

Joanna, I can't thank you enough for helping me with all my *Bacillus* nightmares. Together we really transformed this into a successful project! You are just the best!

Charlotte and Susi, you are the cryo-queens and I am very thankful for all the samples you successfully plunged into liquid ethane and all the Spirit and Titan data sets you set up and collected! In this regard, I would of course also like to thank Dr. Otto Berninghausen, the master of microscopes! Thanks for caring about the health and well-being of our most precious equipment and making them collect so much nice data for my projects.

I would also like to thank Aleksandra Sarman-Grilc for help with contracts, paper work and travel reimbursements.

No good run without a good coach! I would like to thank our senior scientists Dr. Birgitta Beatrix and Dr. Thomas Becker. Gitti, you supported me with getting started in the lab and always helped with

words and deeds. Thomas, you rescued me when I was a PhD student running around lost and without a really successful project. It was a lot of fun for me to work on the ABCE1-projects with you and I love how excited you are about science. You thought me how to go from a structure to a beautifully written manuscript. You're really the master writer in the lab! Moreover, I am very grateful for all the valuable input to my thesis.

I would like to thank the amazing Beckmann IT team including Andre, Kathi, Lukas and Michi for keeping our infrastructure up and running and improving it constantly. As you know computers sometimes like to fade in my presence, so thank you for troubleshooting problems you have never seen before and providing me with new computers (also thanks to Roland, who probably paid for it).

I would like to thank my students: Olga, Michaela, Hanife, Fabian, and Hanna, you all contributed to my work and taught me how to teach.

I thank all the past and present Beckmann group members for running with me for a while and a great time together:

Andre & Kadda, you made the Beckmann lab and Munich to my new home. All this fun after work drinks, breakfasts, celebrations, and Flausch, I really miss this sometimes! Kadda, my secret twin, thank you so much for your friendship and support!

Kathi, Michi, Lukas or "the garlicks" as some people used to call us, I really enjoyed our amazing and long lunch breaks and/or the coffees on the roof terrace. If even the boss steals your food, it must be delicious! Thank you so much for the great time together. A special thanks to Kathi, you are the true and always faithful lunch partner and a really good friend!

Timur, I want to thank you for the great collaboration on initiation, eIF3j and ABCE1. We don't have so many things in common, but I just love to discuss with you, look at dimers and laugh about people who don't see them. Keep the dedication for your work and the people you work with!

Aga, even though you are a past Wilson group member, I am super happy you joined the dark side and stayed in Munich. It was a pleasure to sit next to you and talk about science, work or life.

Jen, thank you for brilliant haircuts and so many good conversations.

Robert, I want to thank you for your great help with the disome paper. More importantly, I always enjoyed talking to you at Beckmann lab parties about start-up ideas, cryptocurrency or coffee machines.

Jingdong, thanks for helping me with model building and answering all my model building questions.

Alex, Alexej, Anne, Bertrand, Christian, Cristian, Clara, Eli, Ivan, Jakub, Ken, Leona, Markus, Matthias, Petr, Shuang, Timo, Ting, Tsai, Vivek.... I could write so much more about each and every person! I am very thankful for everything I could learn from you scientifically but also personally!

Last but not least, I would like to thank all my friends, who believe in me and think of me as a brilliant scientist. Moreover, I would like to thank my family, who always supports me. My parents taught me early on how much fun it is to climb mountains and to work hard for your dreams. I would like to thank my sister for always being there for me!

Nico, you have become the most important person in my life! I always want to run next to you, no matter where the journey is going. Thank you for your support and love.

(Written on 17th of December, 2021 in Munich, Germany)

6. PUBLICATIONS OF THIS DISSERTATION

The following pages contain three publications:

Publication 1 - Molecular analysis of the ribosome recycling factor ABCE1 bound to the 30S post-splitting complex.

Nürnberg-Goloub E, **Kratzat H**, Heinemann H, Heuer A, Kötter P, Berninghausen O, Becker T, Tampé R, Beckmann R.

EMBO J. 2020 May 4;39(9):e103788. doi: 10.15252/embj.2019103788. Epub 2020 Feb 17. PMID: 32064661; PMCID: PMC7196836.

Publication 2 - A structural inventory of native ribosomal ABCE1-43S pre-initiation complexes.

Kratzat H, Mackens-Kiani T, Ameismeier M, Potocnjak M, Cheng J, Dacheux E, Namane A, Berninghausen O, Herzog F, Fromont-Racine M, Becker T, Beckmann R.





EMBO J. 2021 Jan 4;40(1):e105179. doi: 10.15252/embj.2020105179. Epub 2020 Dec 8. PMID: 33289941; PMCID: PMC7780240.

Publication 3 - Ribosome collisions in bacteria promote ribosome rescue by triggering mRNA cleavage by SmrB.

Saito K, **Kratzat H**, Campbell A, Buschauer R, Burroughs AM, Aravind L, Beckmann R, Green R, Buskirk AR.

bioRxiv 2021 Aug 16; doi: 10.1101/2021.08.16.456513.

Molecular analysis of the ribosome recycling factor ABCE1 bound to the 30S post-splitting complex

Elina Nürenberg-Goloub^{1,†}, Hanna Kratzat^{2,†}, Holger Heinemann^{1,†}, André Heuer², Peter Kötter³ , Otto Berninghausen², Thomas Becker² , Robert Tampé^{1,*}  & Roland Beckmann^{2,**} 

Abstract

Ribosome recycling by the twin-ATPase ABCE1 is a key regulatory process in mRNA translation and surveillance and in ribosome-associated protein quality control in Eukarya and Archaea. Here, we captured the archaeal 30S ribosome post-splitting complex at 2.8 Å resolution by cryo-electron microscopy. The structure reveals the dynamic behavior of structural motifs unique to ABCE1, which ultimately leads to ribosome splitting. More specifically, we provide molecular details on how conformational rearrangements of the iron-sulfur cluster domain and hinge regions of ABCE1 are linked to closure of its nucleotide-binding sites. The combination of mutational and functional analyses uncovers an intricate allosteric network between the ribosome, regulatory domains of ABCE1, and its two structurally and functionally asymmetric ATP-binding sites. Based on these data, we propose a refined model of how signals from the ribosome are integrated into the ATPase cycle of ABCE1 to orchestrate ribosome recycling.

Keywords ABC proteins, ribosome recycling; molecular machines; mRNA surveillance; ribosome-associated quality control

Subject Categories Structural Biology; Translation & Protein Quality

DOI 10.15252/emboj.2019103788 | Received 20 October 2019 | Revised 17

January 2020 | Accepted 21 January 2020 | Published online 17 February 2020

The EMBO Journal (2020) 39: e103788

Introduction

Protein biosynthesis via mRNA translation is a fundamental process in living cells. Strikingly, translation is interlaced in a complex network of cellular pathways including mRNA surveillance, ribosome-associated quality control, and ribosome biogenesis (Bassler & Hurt, 2019; Joazeiro, 2019; Nürenberg-Goloub & Tampé, 2019). These crucial pathways maintain protein, mRNA, and ribosome homeostasis (Young *et al.*, 2015; Mills *et al.*, 2016), induce organelle turnover (Wu *et al.*, 2018), assist embryonic development (Coelho *et al.*, 2005; Chen *et al.*, 2006), and are also linked to various

diseases including ribosomopathies and cancer (Tahmasebi *et al.*, 2018; Aspesi & Ellis, 2019). Accordingly, each of the four phases of translation—initiation, elongation, termination, and ribosome recycling—as well as the transitions between them must be under rigorous control. While the first three phases are directly involved in protein biosynthesis and have therefore been extensively studied, ribosome recycling has only recently been structurally and functionally characterized (Hellen, 2018). Herein, the conserved and essential ATP-binding cassette (ABC)-type twin-ATPase ABCE1 plays the key role for Archaea and Eukarya (Pisarev *et al.*, 2010; Barthelme *et al.*, 2011; Shoemaker & Green, 2011). ABCE1 recycles canonical 70S/80S post-termination complexes (post-TCs) after stop codon-dependent termination and non-canonical post-TCs during mRNA surveillance and resumption of translation after cellular stress. In both cases, a decoding A-site factor (archaeal/eukaryotic release factor 1 (a/eRF1) or its homologue a/ePelota, respectively) is delivered to the ribosomal A-site by a translational GTPase (aEF1/eRF3 or aEF1/Hbs1, respectively) and forms an interaction platform for ABCE1 to establish the 70S/80S pre-splitting complex (pre-SC; Becker *et al.*, 2012; Preis *et al.*, 2014; Brown *et al.*, 2015; Shao *et al.*, 2016). In concert with the A-site factor, ABCE1 splits the pre-SC into the small (SSU) and large (LSU) ribosomal subunit. In Eukarya, other components of the post-TC stay associated with the ribosomal subunits and are subsequently recycled by additional factors (Pisarev *et al.*, 2010; Skabkin *et al.*, 2010). Canonical termination, which includes peptide release by eRF1, yields 40S-mRNA-deacylated tRNA complexes and free 60S subunits whereas ribosome recycling of non-canonical post-TCs in the presence of Pelota results in 40S-mRNA and 60S-peptidyl-tRNA complexes due to Pelota's incapacity to release peptides. Moreover, Pelota/Hbs1/ABCE1 not only acts in the splitting of stalled (Shoemaker & Green, 2011), but also vacant (van den Elzen *et al.*, 2014), and newly synthesized ribosomes (Strunk *et al.*, 2012). Immediately after splitting, an ABCE1-bound 30S/40S post-splitting complex is formed (Kiosze-Becker *et al.*, 2016; Heuer *et al.*, 2017), in which ABCE1 may remain for a defined time span (Nürenberg-Goloub *et al.*, 2018; Gouridis *et al.*, 2019) to prevent re-association of the LSU (Heuer *et al.*, 2017). Additionally, ABCE1 has been shown to interact with initiation factors and is

¹ Institute of Biochemistry, Biocenter, Goethe University Frankfurt, Frankfurt a.M., Germany

² Department of Biochemistry, Gene Center, Ludwig-Maximilians University Munich, München, Germany

³ Institute for Molecular Biosciences, Biocenter, Goethe University Frankfurt, Frankfurt a.M., Germany

*Corresponding author. Tel: +49 069 798 29475; E-mail: tampe@em.uni-frankfurt.de

**Corresponding author. Tel: +49 089 218 076900; E-mail: beckmann@genzentrum.lmu.de

[†]These authors contributed equally to this work

assumed to promote their recruitment to the SSU (Dong *et al*, 2004; Chen *et al*, 2006), thus linking ribosome recycling to translation initiation.

A key question is which molecular mechanism is employed by ABCE1 as an ABC-type ATPase. All members of the ABC superfamily utilize the energy of ATP binding and hydrolysis generated in two conserved nucleotide-binding sites (NBS) and are ubiquitously found in numerous cellular processes. These include transport of a limitless range of substrates across membranes, chromatin remodeling, DNA repair, or modulation of ribosomal complexes. The NBSs are formed at the interface of two nucleotide-binding domains (NBDs), which are arranged reciprocally (Hopfner, 2016). ABCE1 additionally possesses an essential N-terminal iron-sulfur cluster domain (FeSD) (Barthelme *et al*, 2007) and a composite hinge region, which comprises a hinge 1 stretch between the NBDs and a hinge 2 stretch at the C terminus, and connects the two NBDs. A unique helix-loop-helix (HLH) insertion in NBD1 distinguishes it from the otherwise superimposable NBD2 (Karcher *et al*, 2008). The two functionally asymmetric NBSs have distinct roles during ribosome recycling (Nürenberg-Goloub *et al*, 2018) and can adopt multiple isoenergetic conformational states (Gouridis *et al*, 2019). We speculated that the state of the ribosome and the dynamic transitions during ribosome recycling (from pre-splitting to post-splitting states) can be precisely sensed by ABCE1 and are coupled to rearrangements in the NBSs (Nürenberg-Goloub *et al*, 2018).

To gain molecular information about the post-splitting complex, we solved the structure of the archaeal post-SC by cryogenic electron microscopy (cryo-EM) to an overall resolution of 2.8 Å. Our structure of ABCE1 bound to the 30S small ribosomal subunit allowed a thorough analysis of this asymmetric ABC protein in the nucleotide-occluded conformation at the level of individual residues. The NBSs of ABCE1 adopt the closed, nucleotide-occluded state with two ATP-mimicking Mg^{2+} -AMP-PNP molecules bound in both NBSs. In general, both catalytic sites superimpose well with marginal deviations. Comparison with the best-resolved structure of the pre-SC (Brown *et al*, 2015) reveals that the functionally important hinge region opens up in the post-SC, allowing ABCE1 to adopt the nucleotide-occluded state. Our high-resolution cryo-EM structure explains how this conformational change can induce an allosteric crosstalk from the SSU into the two functionally distinct NBSs, giving new insights into how the different stages of ribosome recycling are linked to ABCE1's ATPase cycle.

Results

Assembly of the post-splitting complex

To obtain archaeal post-SCs, we actively split isolated native *Thermococcus celer* (*T. celer*) 70S ribosomes using recombinant ABCE1, aRF1, and aPelota from the related archaeon *Saccharolobus solfataricus* (*S.s.*), thus ensuring to resemble the cellular recycling route for all ribosomes present in the native mixture: ribosomes with the A-site occupied by a stop codon (aRF1), a sense codon (e.g., in stalled ribosomes) or vacant ribosomes (aPelota). Thereby, we circumvented a low- Mg^{2+} and high K^+ treatment necessary for facilitated ribosome splitting as previously performed in yeast (Heuer *et al*,

2017). To stabilize the post-SC, a well-characterized, hydrolysis-deficient ABCE1 mutant was used. This mutant, with both catalytic glutamates being substituted by alanine (E238A/E485A, short IIEA), efficiently split 70S ribosomes and remained quantitatively bound to 30S subunits (Nürenberg-Goloub *et al*, 2018) (Fig 1A). Notably, 70S from *S. solfataricus* are intrinsically unstable (Barthelme *et al*, 2011) and thus unsuitable for our *in vitro* splitting approach.

The purified 30S-ABCE1^{IIEA} post-SC was subjected to single-particle cryo-EM analysis. 3D classification revealed that the vast majority (97%) of 30S particles were associated with ABCE1^{IIEA}. This class was refined to an average resolution of 2.8 Å (Fig 1B). Local resolution assessment showed that the body of the 30S formed a very rigid structure whereas the 30S head and ABCE1 showed flexibility and lower resolution (4–6 Å) (Fig EV1). However, using focused refinement, the local resolution was improved to 3.0 Å for ABCE1 and to 2.8 Å for the 30S head. This allowed to build a complete molecular model for the *T. celer* SSU associated with ABCE1 (Figs 1C and EV1).

Molecular model of the *Thermococcus celer* small ribosomal subunit

The *T. celer* 30S ribosome structure comprises 1,485 nucleic acid residues of 16S ribosomal RNA (rRNA) (Appendix Fig S1) and 28 ribosomal proteins (Fig EV2A). As an initial template, we used the structure of the closely related *Pyrococcus furiosus* (*P.fu.*) ribosome modeled at 6.6 Å resolution (Armache *et al*, 2013), to which *T. celer* rRNA shows 96% and ribosomal proteins 78–95% sequence identity, respectively. All residues were manually exchanged to the correct *T. celer* sequence and fitted into the electron density map. Several protein N and C termini as well as loop regions were built *de novo*. This was possible for the entire 30S subunit except for rRNA and proteins forming the beak (eL8, eS31, and parts of h33), which is known to be the most flexible moiety of the SSU (Fig EV1).

Interestingly, we discovered a previously unobserved density for a ribosomal protein on the 30S platform, which was identified as a so far uncharacterized protein and its structure was built *de novo* (Figs 1B and EV2). The 59 amino acid (aa) long protein (6.6 kDa) is located in a cleft between uS2, uS5, and uS8, close to helix (h) 36 and h26/h26a of 16S rRNA. There, it occupies the same position as eS21 in the *Saccharomyces cerevisiae* (*S.c.*) 40S ribosome, whereas in the 30S ribosome from *Escherichia coli* (*E.c.*), the equivalent position is not covered (Fig EV2B). The sequence matches UniProtKB: A0A218P055 (A0A218P055_THECE) and contains a zinc-binding zinc ribbon domain, for which we could assign density for two bound zinc ions. It is conserved in other archaeal species, yet sequence identity with eS21 is rather low (Fig EV2C) with 7% for the full-length protein, but 27% for residues 10–24 representing the zinc ribbon. In accordance with the universal nomenclature for ribosomal proteins (Ban *et al*, 2014), we will refer to the identified protein as eS21.

The architecture of the post-splitting complex is conserved among Eukarya and Archaea

Binding to 70S/80S ribosomes in pre-splitting and to 30S/40S ribosomes in post-splitting complexes is already known to be mainly mediated by the ABCE1-specific HLH motif and hinge region

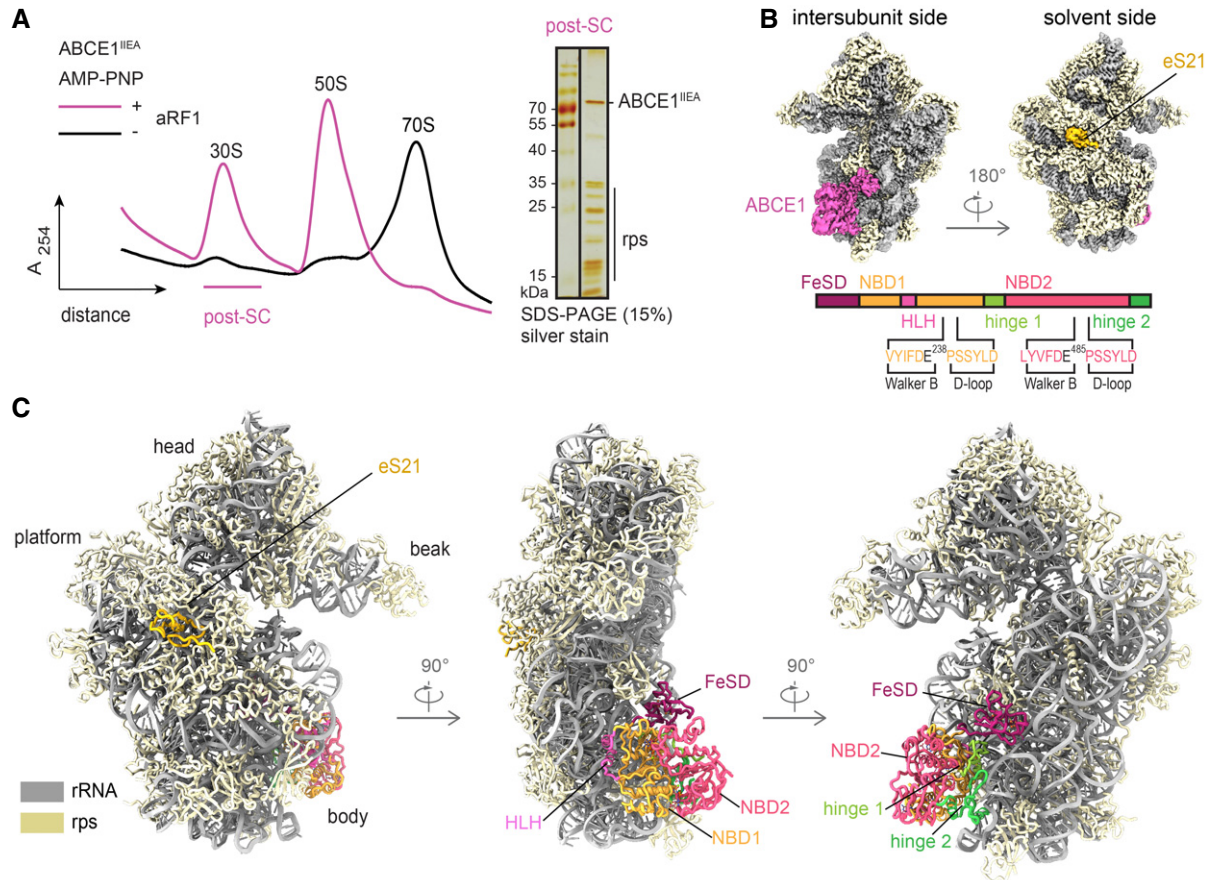


Figure 1. *In vitro* assembly and cryo-EM structure of the archaeal post-splitting complex.

- A ABCE1^{IEA} efficiently splits 70S ribosomes in the presence of AMP-PNP and aRF1/aPelota. The 30S population contains a stoichiometric ratio of ABCE1 and ribosomal proteins, forming the post-splitting complex. rps: small subunit ribosomal proteins.
- B Cryo-EM density of the post-SC highlights the archaeal ribosomal protein eS21 and ABCE1. Domain architecture of ABCE1 including the mutation sites is shown below.
- C Molecular model of the archaeal post-SC, domain colors as in (B).

Data information: In (A), the gradient profiles are representative for the respective nucleotide condition.

contacting the body of the SSU. Upon transition from the pre- to the post-splitting state, the NBSs move from a semi-open to a fully closed, nucleotide-occluded state. Concomitantly, the FeSD rotates around a cantilever toward the decoding site of the SSU close to rRNA helix h44 (Heuer *et al*, 2017).

The overall architecture of the archaeal post-SC is similar to the yeast 40S-ABCE1 complex (Heuer *et al*, 2017) showing the same hallmarks. The FeSD occupies a position close to rRNA h44, hinge region and HLH motif anchor the NBDs to the 30S body, and the two NBSs are in a closed conformation. Yet, the resolution of the archaeal post-SC (2.8 Å overall) is significantly higher than the one of the yeast post-SC (3.9 Å overall), especially in NBSII and the hinge region, thus allowing to describe interactions between ABCE1 and the SSU as well as interactions between the two NBSs on a molecular level. These molecular insights allowed us to draw conclusions and make predictions about the allosteric crosstalk between the two NBSs of ABCE1 as well as ABCE1 and the ribosome. Moreover, these insights guided the corresponding functional studies (see below).

The FeSD domain establishes inter- and intramolecular interactions specific for the post-SC

Based on the high-resolution data, we can delineate crucial interactions between the FeSD domain, NBD1, hinge 1, and the 30S ribosomal subunit. The FeSD is embedded in a pocket between rRNA h44, the h5-h15 junction, and the universally conserved ribosomal protein uS12 (Fig 2A). The majority of FeSD interactions with the ribosome are conserved, while the loop regions of the FeSD opposite of the ribosome (e.g., L36-K43) are variable in sequence and structure, underlining the significance of the interaction of the FeSD with the ribosome (Fig EV3A, Appendix Fig S2). The majority of interactions are formed by salt bridges and hydrogen bonds established between conserved residues in ABCE1 (R2, K15, N17, E19, K59) and the phosphate backbone as well as 2'OH groups of rRNA (Fig 2A). Similarly, also the interaction sites between ABCE1 and uS12 are conserved (P25, R28, and S29 of ABCE1 to Q76 and H100 of uS12) (Fig 2A). Interestingly, we observed a few cases where the ribosome and ABCE1 co-evolved to maintain the interaction pattern. For

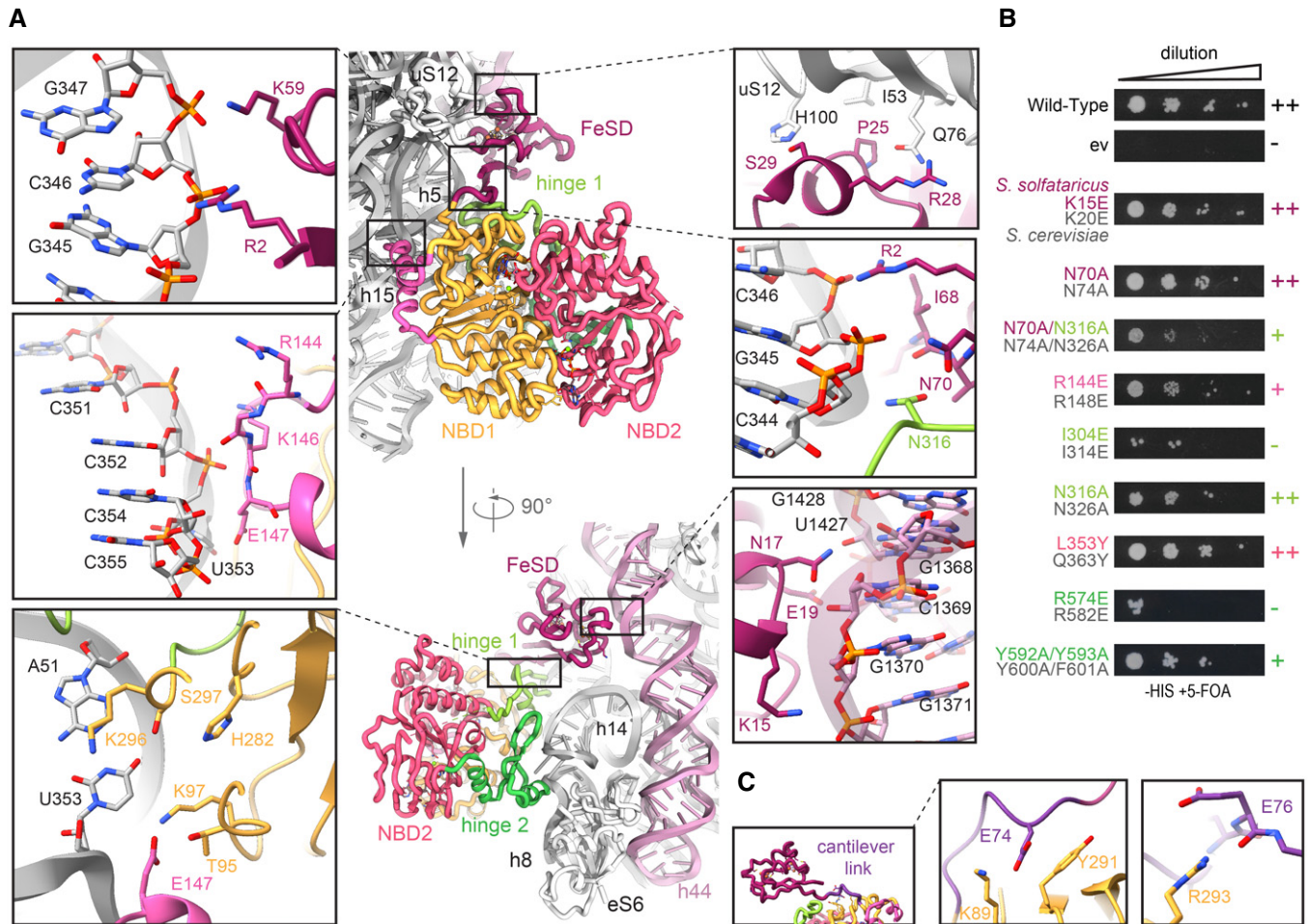


Figure 2. The conserved ABCE1-30S interface is formed by essential interactions.

A Zoom-ins into ABCE1-30S connections. Most interactions are salt bridges or H-bonds between ABCE1 residues and the rRNA phosphate backbone. The FeSD cluster domain contacts rRNA h5 via R2 and K59, interacts with uS12 via S29 and R28, and contacts h44 by N17 and K15. The helix-loop-helix motif connects to rRNA h15 via R144 and E147. The positioning of the cantilever is stabilized by an interaction network of R2, I68, and N70 with N316 of hinge 1 and rRNA h5.

B Yeast survival of ABCE1 variants (*S. solfataricus* colored, *S. cerevisiae* in gray). Most residues connecting to 30S in the post-SC show a growth defect when exchanged for a small one (alanine) or a negative charge (glutamate). ++ no effect, + growth defect, – lethal.

C The cantilever link forms salt bridges of E74 and E76 with NBD1 residues K89 and R293, respectively.

Data Information: In (B), data are representative for a set of two independent experiments.

example, the interaction between S29 of ABCE1 and H100 of uS12 is substituted by the contact of K36 (ABCE1) with N99 (uS12) in yeast (Fig EV3B), underlining the importance of an interaction at this position for re-orientation of the FeSD after ribosome splitting.

The FeSD is linked to the main twin-ATPase body via a flexible linker connecting the cantilever β -sheet β 4 with NBD1 (Fig 2C, Appendix Fig S2). This linker (D73-V79 in *S. solfataricus*) forms an α -helix in free ABCE1 and the pre-SC (Karcher *et al*, 2008; Brown *et al*, 2015), but unfolds into a loop in the post-SC. As in the yeast post-SC (Heuer *et al*, 2017), this cantilever helix is also unfolded in *S. solfataricus*. At high resolution, we deciphered a chain of inter- and intramolecular interactions that are a consequence of FeSD repositioning after splitting. We observed a similar stabilization of the cantilever loop by an interaction of Y291 in NBD1 (Y301 in *S.c.*) with the backbone of E74 (N78 in *S.c.*) (Fig 2C, Appendix Fig S2). In

our high-resolution structure, we identified additional stabilizing contacts for the cantilever loop. E74 also interacts with the side chain of K89 (NBD1) and the carbonyl group of E76 binds the guanine group of R293 (NBD1) (Fig 2C). Moreover, an interaction network is formed between R2 (R7 in *S.c.*) at the N terminus, I68 and N70 (N74 in *S.c.*) of the cantilever β -sheet β 4, and N316 (N326 in *S.c.*) in hinge 1, as well as the phosphate groups of G345 and G346 in rRNA h5 (Fig 2A). In yeast, the mutations Y301A and R7A impair the anti-association activity of ABCE1 *in vitro* and are synthetically lethal *in vivo* (Heuer *et al*, 2017). Additionally, we confirm synthetic lethality of N74A with N326A (Figs 2B and EV3C).

Taken together, closure of the NBSs displaces the FeSD, which leads to new interactions of the cantilever β -sheet and the cantilever loop with the ribosome, NBD1 and hinge 1. This allows for an allosteric communication of post-SC formation to the NBSs.

Hinge 2 serves as a linchpin during ribosome splitting

The NBDs of ABCE1 are located at the body of the 30S subunit with main anchor points contributed by the HLH motif (to h15) and the dipartite hinge region (to junction of h8 and h14) (Fig 2A). In stark contrast to the pre-splitting complex, the HLH is displaced from its contact point at h5 by 16 Å toward h15. In the post-SC, h15 is in contact with the loop containing two basic residues (R144-G145-K146-E147) between helices $\alpha 6$ and $\alpha 7$ (Fig 2A). A charge reversion of the respective arginine in yeast (R148E) leads to a substantial growth defect, confirming this important position (Figs 2B and EV3C). The other residues in the HLH loop rather stabilize an interaction formed by NBD1 with U353, which flips out of h15 and forms a Watson-Crick base pair with A51 in h5, establishing the h5-h15 junction. Multiple residues (T95, K97, E147, H282, K296, and S297) are facing this base pair, suggesting that this specific tertiary structure is precisely monitored by NBD1 and the HLH motif of ABCE1 (Fig 2A). In contrast to yeast, no contacts are observed between ABCE1 and eS24, which is also present but significantly shorter at its C terminus in *T. celer*.

The ABCE1-specific hinge region is subdivided into hinge 1 (*S. solfataricus* 298–325) and hinge 2 (*S. solfataricus* 547–594; Appendix Fig S2). Interactions with the ribosome are mainly established by hinge 2. Hinge 1 connects NBD1 and NBD2 via a flexible linker (*S. solfataricus* 326–338), which is—as in other structures—only partially visible. Similar to the HLH/NBD1 region, hinge 2 also recognizes a special tertiary structure of the rRNA. It binds at the junction between rRNA helices h8 and h14, where A329 flips out of h14 and stacks upon the ribose of A138 in h8. The geometry is read out by the conserved R565 forming a cation- π -stack with A138 (Fig 3A and D, Appendix Fig S2). Notably, this interaction is maintained during ribosome splitting (Fig 4), and exchange of the corresponding residue (R573E) leads to loss of function in yeast (Karcher *et al*, 2008). Hence, the *S. solfataricus* ABCE1^{R565E} mutant (Appendix Fig S3) was unable to bind 30S ribosomes (Figs 3E and EV4A) and failed to split 70S ribosomes (Figs 3F and EV4B), whereas the ATPase activity was similar to wild-type ABCE1 (Fig 3G).

The second main contact to the h8-h14 junction is formed by a salt bridge between R574 and the phosphate of U328 (Fig 3A and C). Moreover, R572 and N305 in hinge 1 stabilize the interaction network around this junction on the side of h14 (Fig 3C), while K577, S580, and R584 are in close contact to h8 (to G137 and A139) (Fig 3A and D). Further, hinge 2 forms an additional interaction site with eS6 by stacking Y581 against R69 (eS6) (Fig 3D). This interaction also occurs in yeast between Q589 and K58 (eS6), indicating a co-evolution of ABCE1 ribosome interactions as previously described for FeSD and uS12 (Fig EV3D).

While the hinge 2 region serves as a constant linchpin to the ribosome, the interaction pattern of hinge 1 is substantially altered compared to the pre-SC. In hinge 2, only R574 switches from U329 in the pre-SC to the adjacent U328 in the post-SC, while all other residues remain with their respective interaction partners (Fig 4A). In contrast, the entire hinge 1 region opens up relative to hinge 2, which results in a 5 Å shift of the hinge 2 β -sheets $\beta 25$ and $\beta 26$ (Fig 4A, Appendix Fig S2) and a 10 Å movement of hinge 1 helix $\alpha 15$. Together with the movement of the HLH (Fig 4B) and the FeSD, this conformational rearrangement, which we term “hinge opening”, leads to the formation of new ribosomal contacts specific

for the post-SC. Thus, $\alpha 15$ of hinge 1 binds U328 and the conserved N316 binds to A314 as well as the phosphates of G343 and G345 close to the h5-h15 junction (Fig 2A). As mentioned above, U328 also contacts R574 in hinge 2 (Fig 3C) while N316 is connected to the rearranged cantilever loop of the FeSD. Consequently, the FeSD, hinge 1, and hinge 2 form a post-SC state-specific intricate interaction network.

Functional analyses and lethality screens confirm the essential role of the hinge 2 region for ABCE1 function. As mentioned before, ABCE1^{S580E} (Appendix Fig S3) exhibits wild-type ATPase activity (Fig 3G) but neither binds to 30S ribosomes (Figs 3E and EV4A) nor splits 70S ribosomes (Figs 3F and EV4B). Additionally, the corresponding mutant is lethal in yeast (S588E) (Karcher *et al*, 2008). Interestingly, S580 is the N-terminal residue of helix $\alpha 25$ and does not directly interact with the ribosome but points toward $\alpha 25$ (Fig 3D). Thus, the mutation to glutamate at this position inhibits ribosome binding via destabilization of helix $\alpha 25$ rather than by direct repulsion. The importance of R574 for ribosome recognition is confirmed by our plasmid-rescue analysis in yeast, demonstrating that the respective R582E mutation is lethal (Figs 2B and EV3C).

Structural asymmetry of the nucleotide-binding sites

Apparently, ABCE1 can act as timer for ribosome recycling (Heuer *et al*, 2017; Nürenberg-Goloub *et al*, 2018). During this process, the NBSs receive and integrate signals about the state of the ribosome, e.g., discriminate between pre-splitting and post-splitting complexes. In the post-SC, both NBSs have mainly been observed in the closed state (Gouridis *et al*, 2019), coinciding with a movement of the FeSD (Kiosze-Becker *et al*, 2016; Heuer *et al*, 2017) as initially suggested (Becker *et al*, 2012). Yet, in all obtained cryo-EM structures of pre- and post-SCs, the identity of the bound nucleotides, especially in NBSII, remained unclear. Based on our high-resolution data, we can resolve both catalytic pockets and unambiguously identify the non-hydrolysable ATP-analogue AMP-PNP complexed with a Mg^{2+} ion in each NBS (Figs 3H–J and EV5). In agreement with the yeast post-SC and the structures of symmetric ABC-type NBD dimers (Lammens *et al*, 2011; Korkhov *et al*, 2012), AMP-PNP is sandwiched between the typical conserved motifs of ABC-type ATPases. In NBSI, the A-loop residue Y83 stacks on the purine base, which is contacted by the aliphatic part of D459 adjacent to the signature motif of the opposite NBD2. In addition, the ribose is stabilized by stacking with F88 (Fig 3I). The γ -phosphate is directly contacted by N108 (Walker A), H269 (His-switch), S461-G463 (signature motif), and Q167 (Q-loop), while T113 (Walker A) and D237 (Walker B) coordinate the Mg^{2+} ion. Analogous residues are superimposable in NBSII, i.e., we find that N377 (Walker A), S214, G216 (signature motif), and H518 (His-switch) coordinate the γ -phosphate while Q411 (Q-loop), T382 (Walker A), and D484 (Walker B) contact the Mg^{2+} ion (Fig 3J). Notably, the characteristic A-loop is degenerated in NBSII of most (but not all) organisms, featuring aliphatic or even polar residues (Gerovac & Tampé, 2019). Despite the degenerated A-loop (L353 instead of the aromatic residue), the accommodation of the purine base is similar to the one observed in NBSI (Fig 3H). The base is sandwiched between L353 and I212 adjacent to the signature motif of NBD1. Yet, we hypothesized that higher flexibility of the nucleotide in NBSII due to the degenerated A-loop might explain (i) the reduced intrinsic ATPase activity in

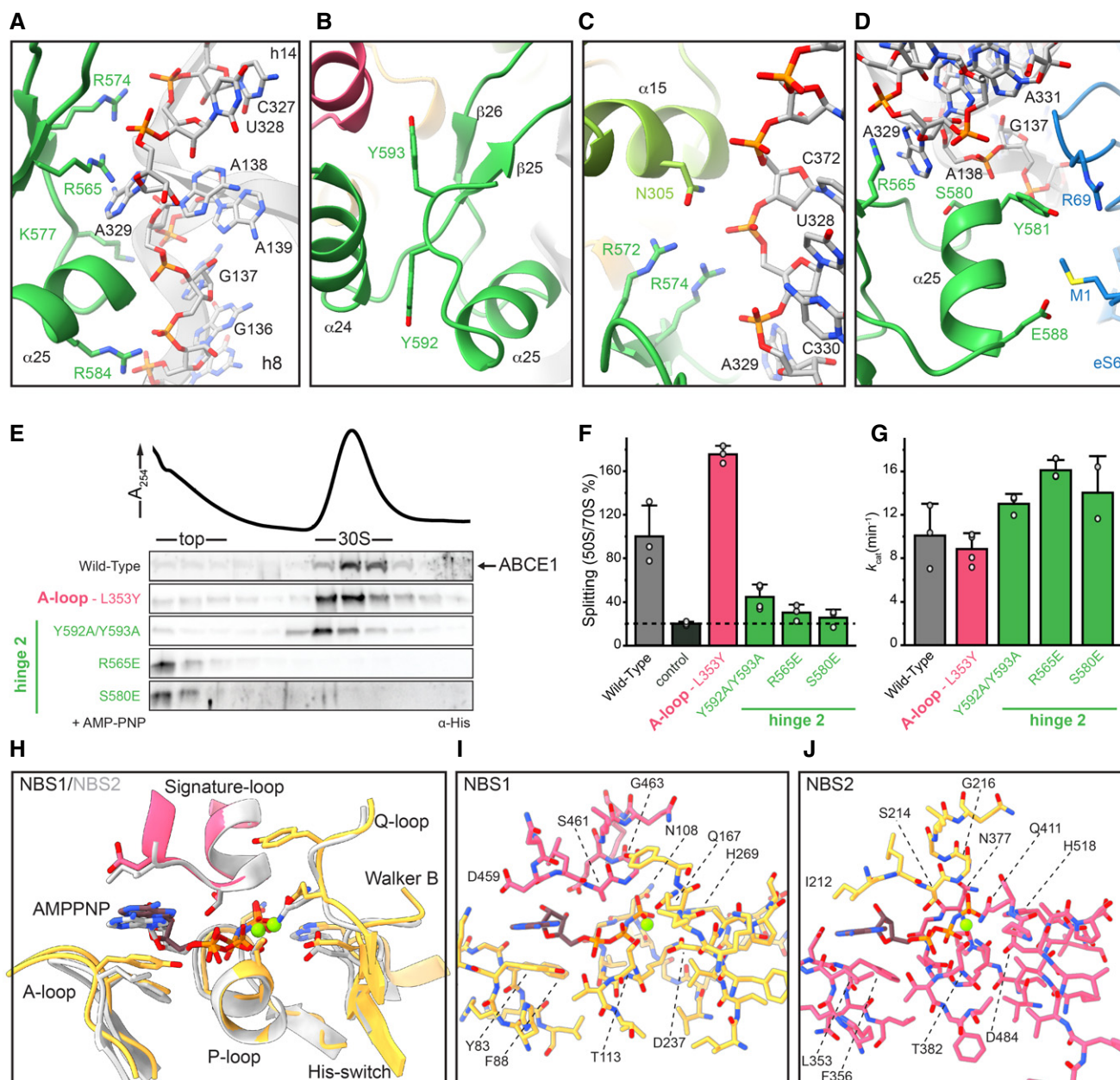


Figure 3. Structural and functional analysis of the hinge regions and NBSs.

A–D Hinge 2 (emerald) residues interacting with the ribosome. R565E forms a conserved cation- π -stacking with A329 of h8; R574 forms a salt bridge with the phosphate backbone of U328 in h14. Aromatic C-terminal residues Y592 and Y593 adopt a parallel coordination. R572 of hinge 2 and N305 of hinge 1 (light green) form an interaction that might be important for sensing. Essential S580 does not contact the ribosome, whereas Y581 and E588 form H-bonds to R69 and M1 of eS6 (blue), respectively.

E Mutations in the α -helices of hinge 2 prevent 30S binding while the Y592A/Y593A (C terminus) and L353Y (A-loop in NBSII) exchanges do not influence ribosome binding.

F 70S splitting efficiency normalized to wild type. Hinge 2 mutations Y592A/Y593A, R565E, and S580E display strongly impaired splitting activity. Unspecific ribosome dissociation level as determined in control experiments in the absence of ABCE1 is marked by the dotted line.

G ATP turnover per ABCE1 is not affected in all tested mutants.

H–J Overview of ATP coordination in both NBSs and overlay of the two NBSs reveals only slight differences, which cannot elucidate the functional asymmetry. Residues of NBD1 and NBD2 involved in coordination are shown in gold and punch, respectively.

Data Information: In (F) and (G), the mean \pm SD of assay triplicates and duplicates are plotted. Source data are available online for this figure.

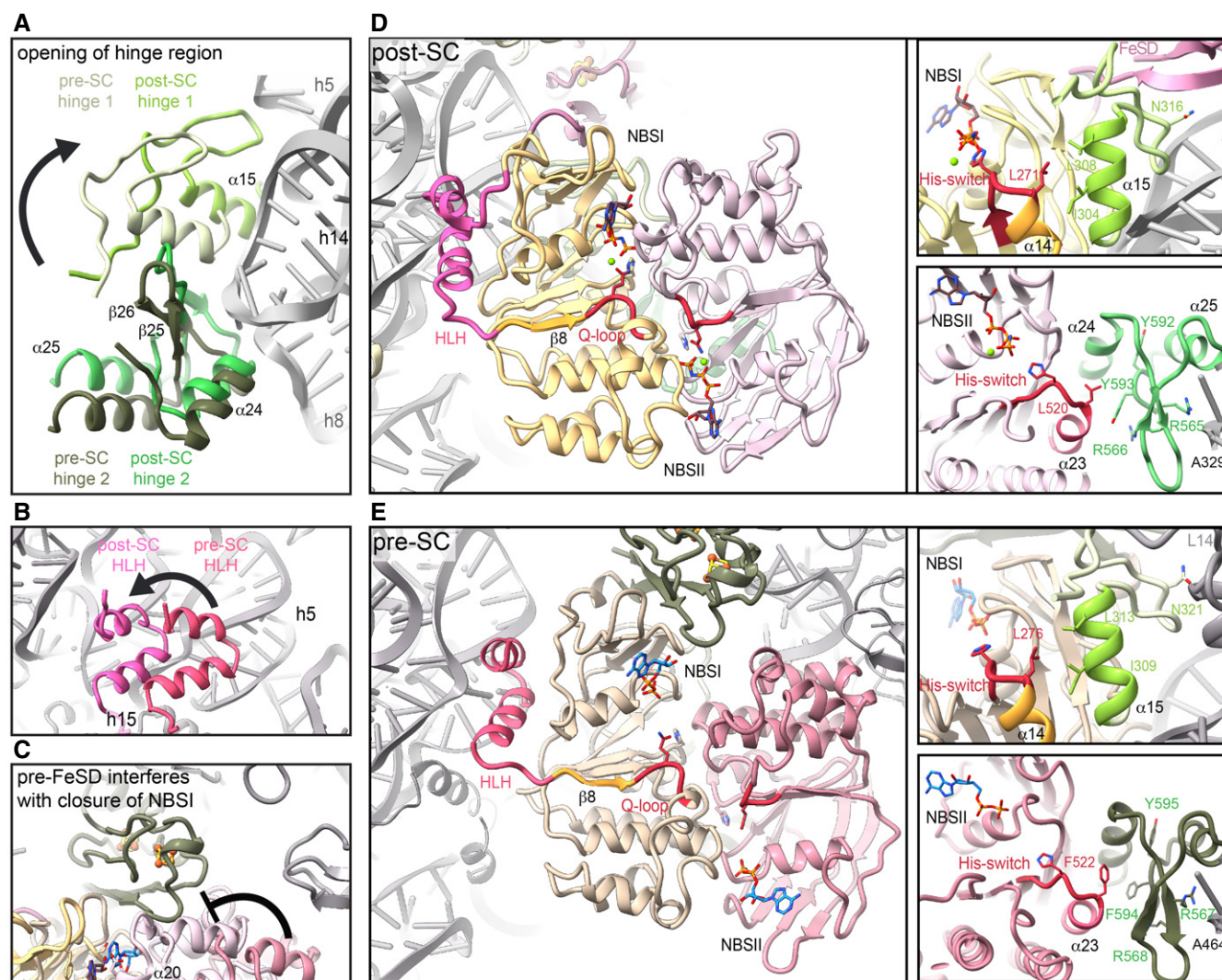


Figure 4. Hinge regions and HLH sense the ribosome splitting event and allosterically communicate with the NBSs.

- A** Hinge 1 moves away from hinge 2 during transition from pre-SC (cotton) to post-SC (lime), thereby forming new interactions with the ribosome. In contrast, hinge 2 movement from pre- (moss) to post-SC (emerald) does not change the interaction with the ribosome.
- B** The HLH motif is displaced from h5 in the pre- (watermelon) to h15 in the post-SC (pink).
- C** Positioning of the FeSD (sage) interferes with the closure of NBD2 (blush) in the pre-SC (rose).
- D** Possible communication pathways from ribosome binding sites to the NBSs in the post-SC. HLH is connected to the Q-loop of NBSI via $\beta 8$. I304 of hinge 1 connects to $\alpha 14$ which is adjacent to the His-switch in NBSI. Analogously, hinge 2 binding to the SSU might be communicated via Y593 and R566 to $\alpha 23$ next to the His-switch of NBSII.
- E** Interaction pattern of the communication pathways between HLH and hinge 1 to NBSI as well as hinge 2 to NBSII is different in the pre-SC compared to the post-SC.

NBSII (Nürenberg-Goloub *et al*, 2018) and (ii) the lower resolution of this site in cryo-EM studies (Heuer *et al*, 2017). To test this hypothesis, we substituted L353 by a tyrosine, thereby generating a consensus A-loop in NBSII. However, 30S binding, 70S splitting efficiency, and ATPase activity of ABCE1^{L353Y} (Appendix Fig S3) were comparable to wild type (Figs 3E–G and EV4). Consequently, the respective yeast mutation Q363Y had no effect on growth and survival (Figs 2B and EV3C). Thus, the functional asymmetry of ABCE1 may originate from the connection of each NBS to an allosteric regulatory element on the ABCE1 surface, i.e., the FeSD, HLH motif, and hinge regions, rather than from single residues within the ATP-binding pockets.

Ribosome binding is allosterically communicated to conserved motifs in the NBSs

Ribosome splitting completely alters the interaction pattern of ABCE1 with the ribosome at all contact points excluding the hinge 2 region. Based on the high-resolution structure, we elaborated allosteric communication pathways between the ribosome-ABCE1 interface and the NBSs. In the pre-splitting complex, the FeSD does not interfere with the NBSI semi-open state (Brown *et al*, 2015). However, upon closure, the loop K12-P13-D14 of the FeSD would clash into NBDII, in particular into residues preceding the NBSI signature motif and $\alpha 20$, involving the L453-E454-S455 stretch

(Fig 4C). The movement of NBSI is thus coupled to rearrangements of the FeSD and *vice versa*. Moreover, the flexible HLH motif via $\beta 8$ is linked to the Q-loop of NBSI (Fig 4D and E). Mutations in the Q-loops strongly affect the ATPase activity of ABCE1 and compromise its function in yeast (Karcher *et al*, 2008; Barthelme *et al*, 2011). As stated above, we observed clear density for Q167 sensing the presence of the γ -phosphate. Additionally, we envision that hinge opening is directly transmitted to the H-loops in both NBSs, which are key motifs in controlling ATPase activity of ABCE1 and other ABC proteins (Zaitseva *et al*, 2005; Barthelme *et al*, 2011; Hurlimann *et al*, 2017). In the post-SC, hinge 1 forms a specific contact to the h5-h15 junction where N316 interacts with G345. Compared to the pre-SC, hinge 1 $\alpha 15$ moves closer toward NBSI and forms a contact with $\alpha 14$, directly adjacent to the H-loop of NBSI (Fig 4D and E). The conserved I304 in $\alpha 15$ points toward $\alpha 14$, allowing a communication between hinge 1 and NBSI. Consistent with this essential function, the corresponding mutation I314E is lethal in yeast (Figs 2B and 4D and E, and EV3C). Similarly, a conserved series of residues communicates ribosome binding from hinge 2 to the H-loop of NBSII. Herein, R565 in hinge 2 senses the h8-h14 junction while R566 and Y593 contact helix $\alpha 23$. Analogously to $\alpha 14$ in NBD1, helix $\alpha 23$ occupies the position adjacent to the H-loop in NBSII (Fig 4D and E). We substituted the conserved Y592 and Y593 by alanine and probed for ABCE1 function. Consistent with the role of Y593 in ribosome sensing without direct contact to rRNA or ribosomal proteins, the 70S splitting ability of ABCE1^{Y592A/Y593A} (Appendix Fig S3) is substantially inhibited (Figs 3F and EV4B) while the 30S binding efficiency and ATPase activity are similar to wild type (Figs 3D and E, and EV4A). Additionally, the respective double-mutant Y600A/F601A exhibits a growth defect in yeast (Figs 2B and EV3C). The five-stranded β -sheet harboring the degenerated A-loop in NBSII is in close proximity of hinge 2. Comparing the pre-SC with the post-SC, we observed a conformational change in this region which contributes to ATP occlusion by allowing the hydrophobic stacking of L353 and the adenine base (Fig 3J).

We finally inspected the Walker B/D-loops, which are known to assure transport directionality in the ABC transporter associated with antigen processing (TAP) (Grossmann *et al*, 2014). Notably, the D-loops are, together with the H-loops, already part of the contact interface between the NBDs in the pre-splitting state. This interface drastically alters upon closure of the NBSs, ribosome splitting, and post-SC formation, allowing a multilayered communication network between both sites in addition to the allosteric regulation by the ribosome (Fig 4D and E).

Discussion

By using an ATPase-deficient mutant of ABCE1 in an *in vitro* ribosome recycling assay, we were able to capture the archaeal post-splitting complex comprising the 30S subunit and ABCE1. Our structure reveals this essential, asymmetric ABC-type protein in a fully nucleotide-occluded state at atomic resolution. Furthermore, the cryo-EM structure allows a prediction of the communication pathways within the post-splitting complex, which we functionally and genetically assessed. Ribosome binding is sensed by the HLH motif and hinge region that opens up during ribosome splitting. This

“hinge opening” modulates the His-switches in both NBSs by altering the contact interface to adjacent α -helices. We observed that NBSI is in an active conformation with all residues needed for catalytic activity in place, i.e., activation of a water molecule for nucleophilic attack on the γ -phosphate (Chen *et al*, 2003; Lammens *et al*, 2011; Hofmann *et al*, 2019). The functional and dynamic asymmetry of the two NBSs (Barthelme *et al*, 2011; Nürenberg-Goloub *et al*, 2018; Gouridis *et al*, 2019) does not arise from incomplete ATP alignment due to a non-canonical A-loop in NBSII, as we confirmed by biochemical and yeast viability studies. In the ABC transporter TAP and its homolog TmrAB, the position of the non-canonical site cannot be switched without compromising the transport function, indicating that additional signals from outside the binding pocket are integrated into the ATPase cycle (Chen *et al*, 2003; Procko *et al*, 2006; Zutz *et al*, 2011). Consistently, we envision an allosteric regulatory network that extends from the ABCE1-ribosome interface into the NBSs. The spatial separation of hinge 1 from hinge 2 is linked to both NBSs and in addition might be a prerequisite for closure of NBSII (Fig 4 and Movie EV1). In agreement, the introduction of mutations disrupting ribosome binding in hinge 1 (R311A in *S.c.*; R301 in *S. solfataricus*) or hinge 2 (R573E, R582E, and S588E in *S.c.*; R565, R574, and S580, in *S. solfataricus*, respectively) compromise ABCE1 function (Karcher *et al*, 2008) (Figs 2B and 3B–D, and EV3C, and EV4). The exchange of G303 in hinge 1 (Appendix Fig S2), located at the contact interface to NBD1, leads to a reduced wing size in *Drosophila melanogaster* (G316D in the *pixie* gene), further highlighting the role of the hinge region for ABCE1 function (Coelho *et al*, 2005). Notably, hinge 1 and hinge 2 occupy a position analogous to the regulatory elements of bacterial ABC importers (Newstead *et al*, 2009; Johnson *et al*, 2012; Chen *et al*, 2013) (Appendix Fig S4), showing that a regulation from this site can be exploited by ABC-type proteins.

Closure of NBSII allosterically activates NBSI, which is consistent with the increased ATPase activity of ABCE1 in the presence of 70S/80S ribosomes and release factors (Pisarev *et al*, 2010; Shoemaker & Green, 2011; Nürenberg-Goloub *et al*, 2018). On a structural level, we assume that NBSII can close prior to NBSI to prime ribosome splitting at the pre-SC (Fig 5). In more detail, the movement of the signature motif toward NBSII is possible when still bound to the 70S/80S ribosomes, since ABCE1 anchors via the hinge 2 region and HLH motif, and none of the mobile parts participate in ribosome binding. Furthermore, 70S/80S are split as soon as both sites occlude Mg^{2+} -ATP and switch to the closed conformation (Fig 5), as found within the post-SC (Heuer *et al*, 2017; Nürenberg-Goloub *et al*, 2018; Gouridis *et al*, 2019). During the closing movement, the FeSD is pushed away by NBD2 and, concomitantly, interactions between NBD1, the HLH motif, and the ribosome must be temporarily broken, allowing hinge 1 to move away from hinge 2 (Fig 5). Structurally, separation of the two hinge regions occurs concomitantly with FeSD movement and adoption of the fully closed state of the ABCE1 NBDs. These structural rearrangements may well determine the ribosome splitting rate. Consistently, in the presence of Mg^{2+} -AMP-PNP, ABCE1 transiently associates with 30S ribosomes within 5 s, while closure of NBSII takes app. 7 min and stabilizes the post-SC (Gouridis *et al*, 2019).

Remarkably, translation termination is a slow event. Several ribosome profiling studies showed a high enrichment of reads

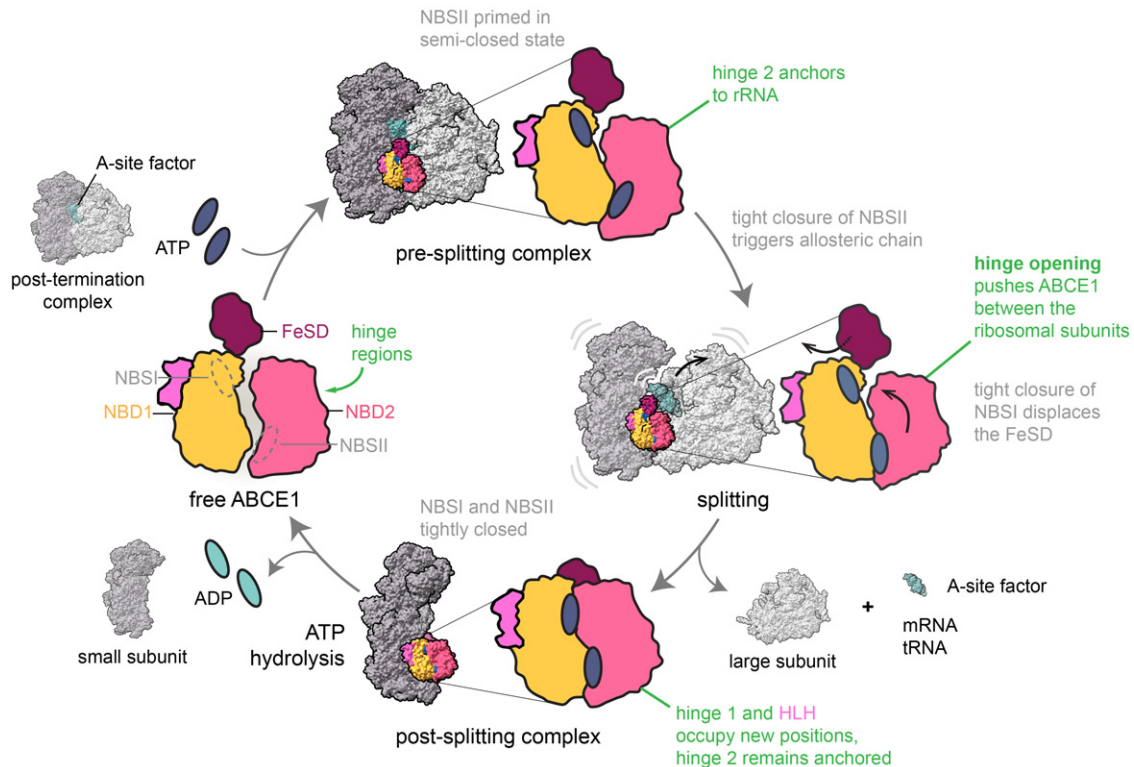


Figure 5. Model for ribosome splitting by ABCE1.

ABCE1 binds to 70S/80S ribosomes containing mRNA, tRNA in the P-site (not shown), and an A-site factor (a/eRF1 after canonical termination; a/e Pelota during stalled ribosome recognition) to form pre-splitting complexes. Here, NBSII is primed in a semi-closed state and anchored to ribosomal RNA via hinge 2. ATP occlusion and tight closure of NBSII triggers an allosteric chain within ABCE1 leading to a tight closure of NBSI. Consequently, the FeSD is displaced and the parallel hinge opening rearranges ABCE1 in the ribosomal subunit cleft. Thereby, the subunits are split apart and the FeSD is repositioned at h44. During and/or after the splitting process, the A-site factor dissociates and mRNA and tRNA are recycled (not shown). At the post-SC, ABCE1 occludes two ATP molecules in the NBSs. ATP hydrolysis is a prerequisite for NBS opening and dissociation of ABCE1 from the SSU. Black arrows indicate domain movements within ABCE1.

indicating a high occupancy of ribosomes on stop codons (Andreev *et al*, 2017). Moreover, a significant population of ABCE1-containing termination complexes was found in native polysomes, along with translating ribosomes (Behrmann *et al*, 2015). Similarly, the half-life of ribosomes stalled during translation and rescued by the Pelota/Hbs1/ABCE1 system is supposedly long. In light of this, it makes sense that ribosome splitting is regulated and coordinated by the action of the intrinsically slow NBSII. Slow closure of NBSII could ensure correct engagement within the pre-splitting complex, and slow ATP hydrolysis could determine the dwell time of ABCE1 after splitting to prevent premature re-association with large ribosomal subunits, or coordinate downstream events such as translation initiation and/or tRNA/mRNA recycling. In this context, the question remains open as to how ATPase activity and thus the 30S/40S dissociation is modulated (Fig 5). Here, external factors, e.g., components of the initiation machinery, might play a direct or indirect role in communicating conformational rearrangements during pre-initiation complex formation into the NBSs of ABCE1 to trigger its release. In particular, and possibly by modulating its ATPase activity, the non-essential eukaryotic eIF3j subunit (Hcr1 in *S.c.*) assists ABCE1 in ribosome recycling, and thereby may also promote post-SC disassembly (Young & Guydosh, 2019). In the

future, the precise role of ABCE1 in initiation will need to be elucidated to complete the translation cycle for Eukarya and Archaea.

Material and Methods

Protein purification

Construction of the pSA4 plasmids for recombinant expression of ABCE1, aRF1, aPelota, and aIF6 from *S. solfataricus* in *E. coli* was described previously (Barthelme *et al*, 2007, 2011). All proteins were expressed, purified, and stored as previously described (Nürenberg-Goloub *et al*, 2018). Protein quality was assured by SDS-PAGE and size exclusion chromatography (Superdex 200 Increase 3.2/300, GE Healthcare) in SEC buffer (20 mM Tris-HCl pH 7.5, 150 mM NaCl, 2 mM β -mercaptoethanol) at 4°C recording absorption at 280 and 410 nm to monitor FeSD cluster integrity.

Ribosome purification

Frozen cell pellets from *T. celer* were purchased from the Centre of Microbiology and Archaea, University of Regensburg, Germany.

Cell pellets were resuspended in 2.5× volume S30 buffer (10 mM Tris–HCl pH 7.5, 60 mM KOAc, 14 mM MgCl₂, 1 mM dithiothreitol (DTT)) and lysed using a Branson Sonifier. Cell debris was removed by centrifugation 2 × 30 min at 34,000 g and 4°C. The supernatant was loaded on a high-salt sucrose cushion (10 mM Hepes-KOH pH 7.5, 1.1 M sucrose, 1 M NH₄Cl, 10.5 mM Mg(OAc)₂, 0.1 mM EDTA, 4 mM β-mercaptoethanol), and ribosomes were pelleted at 200,000 g for 15 h at 4°C. For 70S preparation, pelleted ribosomes were resuspended in S30 buffer and gradient purified (10–40% (w/v) sucrose, S30 buffer) for 14 h at 68,000 g. Fractions were collected using a Piston Gradient Fractionator (Bio-comp) recording the A₂₅₄ profile. The buffer of 70S containing fractions was exchanged to TrB25 (56 mM Tris–HCl pH 8.0, 250 mM KOAc, 80 mM NH₄OAc, 25 mM MgCl₂, 1 mM DTT) via Econo-Pac 10DG Desalting Columns (Bio-Rad), and 70S were concentrated using a 100K Amicon Ultra (Merck). For 30S purification (for 30S binding assays), high-salt sucrose cushion pelleted ribosomes were resuspended in buffer A30 (10 mM Hepes-KOH pH 7.5, 100 mM NH₄Cl, 10.5 mM Mg(OAc)₂, 0.1 mM EDTA, 4 mM β-mercaptoethanol) and loaded onto a HiPrep 16/60 Sephacryl S-400 HR size exclusion chromatography column (GE Healthcare). Ribosome fractions were collected and again pelleted through a low magnesium sucrose cushion in buffer A30 (2.5 mM Mg(OAc)₂) for subunit dissociation. Ribosomes were resuspended in S30 buffer (with 2.5 mM Mg(OAc)₂ instead of MgCl₂) and gradient purified. 30S fractions were pooled, the buffer exchanged to S30 and concentrated as before.

Assembly of the post-splitting complex for cryo-EM

To mimic the physiological translation cycle, post-splitting complexes were generated by splitting of 1 nmol purified 70S ribosomes from *T. celer* by ABCE1^{HIEA} (8 μM), aPelota, and aRF1 (5 μM each) in the presence of 0.5 mM AMP-PNP in 50 mM HEPES-KOH pH 7.5, 30 mM KCl, 10 mM MgCl₂, and 2 mM DTT at 65 °C for 15 min. Samples were chilled on ice and cross-linked with 1% (v/v) formaldehyde for 30 min on ice. Higher molecular weight aggregates were removed for 15 min at 16,100 g and 4 °C. Samples were loaded onto 10–30% (w/v) sucrose density gradient in 50 mM HEPES-KOH pH 7.5, 30 mM KCl, 0.5 mM MgCl₂, and 2 mM DTT, and ribosomal particles were separated by centrifugation for 13.5 h at 78,000 g and 4°C in a SW40 rotor (Beckman Coulter Life Sciences). Gradients were fractionated into 0.3 ml using Piston Gradient Fractionator (Biocomp Instruments) while recording A₂₅₄. Fractions containing 30S were pooled, and the sucrose was removed by Sephadex G-25 gravity flow size exclusion columns (GE Healthcare). Ribosomes were diluted to concentrations of 50–70 nM (based on OD₂₆₀) for quality control by negative stain EM. Samples were vitrified immediately.

70S splitting assay

7.5 pmol *T. celer* 70S were split using ABCE1, aRF1, aPelota, and aIF6 (75 pmol each) in the presence of 22.5 nmol AMP-PNP in S30 buffer at 65°C for 15 min. Higher molecular weight aggregates were removed for 10 min at 16,100 g and 4°C. Samples were analyzed via 10–40% (w/v) sucrose density gradient in S30 buffer as described. Splitting efficiency was calculated as the ratio of 50S peak

area to 70S peak area of the A₂₅₄ gradient profile using OriginPro 2018 (OriginLab) and normalized to the mean value of wild-type ABCE1. Splitting experiments were performed at least three times per ABCE1 variant; bars show mean ± SD value.

30S binding assay

17.5 pmol *T. celer* 30S were incubated with 8.5 pmol ABCE1 in the presence of AMP-PNP, or ADP (8.5 nmol each), or in the absence of any nucleotide in S30 buffer for 10 min at 65°C. Higher molecular weight aggregates were removed for 10 min at 16,100 g and 4°C. Samples were loaded onto a 10–40% (w/v) sucrose density gradient in S30 buffer, as described. 0.5-ml fractions were collected, precipitated overnight at –20°C in 2× volume acetone, and pelleted for 1 h at 16,100 g and 4 °C. The pellet was resuspended in SDS loading dye and analyzed by SDS–PAGE and immunoblotting. All ABCE1 variants contained a C-terminal His₆ tag and were detected using rabbit anti-His (ab1187, Abcam) and goat anti-rabbit (AP307P, Merck) antibodies. Binding assays were performed once per ABCE1^{variant}. The gradient profiles shown are representative for the respective nucleotide condition.

ATPase assay

ATPase activity was measured using a Malachite Green-based assay (adapted from Baykov *et al*, 1988). Samples were measured at least in duplicates. 1–2 μM ABCE1 was incubated with 2 mM ATP in ATPase buffer (10 mM Hepes pH 7.5, 150 mM NaCl, 2.5 mM MgCl₂) for 8 min at 80°C in a total volume of 25 μl. The reaction was stopped by addition of 175 μl ice-cold 20 mM H₂SO₄. 50 μl Malachite Green working solution (2 ml conc. Malachite Green solution (60 ml H₂SO₄ in 300 ml H₂O with 0.44 g Malachite Green), 40 μl Tween-20 (10% v/v) and 550 μl Na₂MoO₄) was added per sample and incubated for 2–5 min at room temperature. A₆₂₀ was recorded in a CLARIOstar plate reader (BMG Labtech). Bar diagrams represent mean ± SD of two (ABCE1^{S580E}), four (ABCE1^{L353Y}) or three (all other ABCE1 variants) independent experiments.

Yeast plasmid shuffling assay

In vivo function of ABCE1 mutants was checked as previously described (Heuer *et al*, 2017). The haploid yeast strain CEN.MG1-9B (*MATa his3Δ1 leu2-3,112 trp1-289 MAL2-8^C SUC2 ura3-52 rli1::KanMX4* + pRS426-ABCE1) was generated in which the essential *ABCE1* gene (*RLI1*) was deleted by *KanMX4* and substituted by pRS426-ABCE1 [*URA3*] expressing wild-type *ABCE1* under the control of the endogenous promoter. CEN.MG1-9B strain was transformed with pRS423-ABCE1 [*HIS3*] plasmid coding for wt and mutated *ABCE1* and with empty vector pRS423 as negative control and selected on -HIS. If such a strain harboring both plasmids was grown on medium containing 5-FOA, the pRS426-ABCE1 [*URA3*] plasmid is lost by counter-selection as the *URA3* gene product converts 5-FOA to a toxic compound. Consequently, the strain was prone to survive only in the presence of pRS423-ABCE1. Growth and survival were checked by growth studies in a serial dilution assay over 2–3 days. Data in Figs 2B and EV4C are representative for a set of two independent experiments.

Cryo-EM analysis

For the archaeal post-SC, the sample was applied to 2-nm pre-coated Quantifoil R3/3 holey carbon-supported grids and vitrified using a Vitrobot mark IV (FEI). Data were collected on a TITAN KRIOS[™] cryo-TEM (Thermo Fisher) equipped with a Falcon III chip enhanced Falcon II direct detector at 300 keV under low-dose conditions of approximately 25 e⁻/Å² for 10 frames in total, and a defocus range of −1.1 to −2.3 μm. Magnification settings resulted in a pixel size of 1.084 Å per pixel. Original image stacks were summed and corrected for drift and beam-induced motion at the micrograph level by using MotionCor2 (Zheng *et al*, 2017). The contrast transfer function (CTF) estimation of each micrograph was performed with Gctf (Zhang, 2016).

Data processing

The ABCE1-30S data set was processed, unless otherwise stated, following the standard workflow using RELION 2 and 3 (Kimanius *et al*, 2016; Zivanov *et al*, 2018). After particle picking with GAUTO-MATCH (<http://www.mrc-lmb.cam.ac.uk/kzhang/>) and 2D classification, particles were subjected to a thorough 3D classification regimen. About 97% of all particles contained ABCE1 stably bound to the small ribosomal subunit. Different conformational states of the ribosome 30S head were separated and a homogeneous class with 293.010 particles was selected for further refinement. First, the particles of this class were CTF-corrected and refined to an overall resolution of 2.8 Å after post-processing. A focused refinement on the head and ABCE1 could improve the local resolution of the structure.

Model building

The molecular model of the small ribosomal subunit was built using the 70S model of *P.fu*. [4V6U (Armache *et al*, 2013), 5JBH (Coureux *et al*, 2016)]. After rigid-body fitting of the 30S into the density, the sequence was manually changed to *T. celer* and modeled into the cryo-EM density using Coot (version 0.8.9.1) (Emsley & Cowtan, 2004). The sequences were taken from the *T. celer* Vu 13 = JCM 8558A genome, available at NCBI. A previously unidentified protein could be modeled by building the sequence *de novo* into the density. The *T. celer* genome was searched for characteristic sequence motifs of the protein taking the approximate size of the protein into consideration. An initial model of ABCE1 was generated using Phyre2 (Kelley *et al*, 2015). The model of *S.c.* ABCE1 (Heuer *et al*, 2017) was used as a template, and the resulting model was manually refined in Coot. After Phenix refinement (Adams *et al*, 2010), the models and maps of 30S head, body, and ABCE1 were combined and refined again. Cryo-EM structures and models were displayed using UCSF Chimera (Pettersen *et al*, 2004) and ChimeraX (version 0.8; Goddard *et al*, 2018).

Data availability

The cryo-EM density maps of the archaeal 30S ribosome and ABCE1 have been deposited in the Electron Microscopy Data Bank under accession number EMD-10519 (<https://www.ebi.ac.uk/pdbe/entry/emdb/EMD-10519>) (see Table 1). Atomic coordinates for the

Table 1. Data collection, refinement, and validation statistics.

	30S-ABCE1 (EMD-10519, PDB ID 6TMF)
Data collection	
Voltage (kV)	300
Electron exposure (e ⁻ /Å ²)	25
Defocus range (μm)	−1.1 to −2.3
Pixel size (Å)	1.084
Symmetry imposed	C1
Refinement	
Particle images (no.)	293 010
Map resolution (Å) (overall/30S head/ABCE1)	2.8/2.8/3.0
FSC threshold	0.143
Map sharpening B factor (Å ²) (overall/30S head/ABCE1)	−117.8/−128.8/−151.9
Model composition	
Correlation coefficient (%; Phenix)	0.85
Initial model used (PDB codes)	5JBH, ABCE1: 5LL6 (chain h)
Non-hydrogen atoms	65 449
Protein residues	4 172
RNA bases	1 485
R.m.s. deviations	
Bond lengths (Å)	0.017 (30)
Bond angles (°)	1.208 (44)
Validation	
MolProbity score	1.79
Clash score	4.66
Rotamer outliers (%)	0.73
Ramachandran plot	
Favored (%)	89.98
Allowed (%)	9.51
Disallowed (%)	0.51
Validation RNA	
Correct sugar pucker (%)	98
Good backbone conf. (%)	80

atomic models have been deposited in the Protein Data Bank under accession number PDB ID 6TMF (<https://doi.org/10.2210/pdb/6TMF/pdb>). Correspondence and requests for materials should be addressed to R.T. (tampe@em.uni-frankfurt.de) or R.B. (beckmann@genzentrum.lmu.de).

Expanded View for this article is available online.

Acknowledgements

The authors thank Simon Trowitzsch, Lukas Susac, Jingdong Cheng, and Michael Ameisemeier for discussions; Charlotte Ungewickell and Susanne Riederer for technical assistance; Lukas Kater for support with processing and the pre-processing pipeline of the cryo-EM data; and Petr Tesina for help with final model refinements in Phenix. E.N.G. was supported by the Christiane Nüsslein-

Volhard Foundation, L'Oréal, and the United Nations Educational, Scientific and Cultural Organization (UNESCO). H.K. is supported by a DFG fellowship through the Graduate School of Quantitative Bioscience Munich (QBM). The German Research Foundation (DFG) SFB 902 "Molecular mechanisms of RNA-based regulation" (to R.T.), TRR174 "Spatiotemporal dynamics of bacterial cells" (to R.B.) and FOR 1805 (to R.B.) funded this work.

Author contributions

EN-G, HK, HH, TB, RB, and RT designed the study. EN-G and HH developed the preparation of the post-splitting complex. EN-G, HK, HH, and AH optimized the sample preparation for cryo-EM. EN-G, HK, HH, and AH prepared the EM samples. HK and OB collected and HK processed the cryo-EM data. HK built and refined the model. HK, TB, EN-G, HH, RT and RB analyzed and interpreted the structures. HH and EN-G performed all functional assays. EN-G and PK conducted the genetic analysis in yeast. EN-G, HK, TB, HH, RB, and RT wrote the manuscript with contributions from all authors. RT initiated the project.

Conflict of Interest

The authors declare that they have no conflict of interest.

References

- Adams PD, Afonine PV, Bunkoczi G, Chen VB, Davis IW, Echols N, Headd JJ, Hung LW, Kapral GJ, Grosse-Kunstleve RW *et al* (2010) PHENIX: a comprehensive Python-based system for macromolecular structure solution. *Acta Crystallogr D Biol Crystallogr* 66: 213–221
- Andreev DE, O'Connor PB, Loughran G, Dmitriev SE, Baranov PV, Shatsky IN (2017) Insights into the mechanisms of eukaryotic translation gained with ribosome profiling. *Nucleic Acids Res* 45: 513–526
- Armache JP, Anger AM, Marquez V, Franckenberg S, Frohlich T, Villa E, Berninghausen O, Thomm M, Arnold GJ, Beckmann R *et al* (2013) Promiscuous behaviour of archaeal ribosomal proteins: implications for eukaryotic ribosome evolution. *Nucleic Acids Res* 41: 1284–1293
- Aspesi A, Ellis SR (2019) Rare ribosomopathies: insights into mechanisms of cancer. *Nat Rev Cancer* 19: 228–238
- Ban N, Beckmann R, Cate JH, Dinman JD, Dragon F, Ellis SR, Lafontaine DL, Lindahl L, Liljas A, Lipton JM *et al* (2014) A new system for naming ribosomal proteins. *Curr Opin Struct Biol* 24: 165–169
- Barthelme D, Scheele U, Dinkelaker S, Janoschka A, Macmillan F, Albers SV, Driessen AJ, Stagni MS, Bill E, Meyer-Klaucke W *et al* (2007) Structural organization of essential iron-sulfur clusters in the evolutionarily highly conserved ATP-binding cassette protein ABCE1. *J Biol Chem* 282: 14598–14607
- Barthelme D, Dinkelaker S, Albers SV, Londei P, Ermiler U, Tampé R (2011) Ribosome recycling depends on a mechanistic link between the FeS cluster domain and a conformational switch of the twin-ATPase ABCE1. *Proc Natl Acad Sci USA* 108: 3228–3233
- Bassler J, Hurt E (2019) Eukaryotic ribosome assembly. *Annu Rev Biochem* 88: 281–306
- Baykov AA, Evtushenko OA, Awaeva SM (1988) A malachite green procedure for orthophosphate determination and its use in alkaline phosphatase-based enzyme immunoassay. *Anal Biochem* 171: 266–270
- Becker T, Franckenberg S, Wickles S, Shoemaker CJ, Anger AM, Armache JP, Sieber H, Ungewickell C, Berninghausen O, Daberkow I *et al* (2012) Structural basis of highly conserved ribosome recycling in eukaryotes and archaea. *Nature* 482: 501–506
- Behrmann E, Loerke J, Budkevich TV, Yamamoto K, Schmidt A, Penczek PA, Vos MR, Burger J, Mielke T, Scheerer P *et al* (2015) Structural snapshots of actively translating human ribosomes. *Cell* 161: 845–857
- Brown A, Shao S, Murray J, Hegde RS, Ramakrishnan V (2015) Structural basis for stop codon recognition in eukaryotes. *Nature* 524: 493–496
- Chen J, Lu G, Lin J, Davidson AL, Quirocho FA (2003) A tweezers-like motion of the ATP-binding cassette dimer in an ABC transport cycle. *Mol Cell* 12: 651–661
- Chen ZQ, Dong J, Ishimura A, Daar I, Hinnebusch AG, Dean M (2006) The essential vertebrate ABCE1 protein interacts with eukaryotic initiation factors. *J Biol Chem* 281: 7452–7457
- Chen S, Oldham ML, Davidson AL, Chen J (2013) Carbon catabolite repression of the maltose transporter revealed by X-ray crystallography. *Nature* 499: 364–368
- Coelho CM, Kolevski B, Bunn C, Walker C, Dahanukar A, Leever SJ (2005) Growth and cell survival are unevenly impaired in pixie mutant wing discs. *Development* 132: 5411–5424
- Coureaux PD, Lazennec-Schurdevin C, Monestier A, Larquet E, Cladiere L, Klaholz BP, Schmitt E, Mechulam Y (2016) Cryo-EM study of start codon selection during archaeal translation initiation. *Nat Commun* 7: 13366
- Dong J, Lai R, Nielsen K, Fekete CA, Qiu H, Hinnebusch AG (2004) The essential ATP-binding cassette protein RLI1 functions in translation by promoting preinitiation complex assembly. *J Biol Chem* 279: 42157–42168
- van den Elzen AM, Schuller A, Green R, Seraphin B (2014) Dom34-Hbs1 mediated dissociation of inactive 80S ribosomes promotes restart of translation after stress. *EMBO J* 33: 265–276
- Emsley P, Cowtan K (2004) Coot: model-building tools for molecular graphics. *Acta Crystallogr D Biol Crystallogr* 60: 2126–2132
- Gerovac M, Tampé R (2019) Control of mRNA translation by versatile ATP-driven machines. *Trends Biochem Sci* 44: 167–180
- Goddard TD, Huang CC, Meng EC, Pettersen EF, Couch GS, Morris JH, Ferrin TE (2018) UCSF ChimeraX: meeting modern challenges in visualization and analysis. *Protein Sci* 27: 14–25
- Gouridis G, Hetzert B, Kiosze-Becker K, de Boer M, Heinemann H, Nürenberg-Goloub E, Cordes T, Tampé R (2019) ABCE1 controls ribosome recycling by an asymmetric dynamic conformational equilibrium. *Cell Rep* 28: 723–734.e6
- Grossmann N, Vakkasoglu AS, Hulpke S, Abele R, Gaudet R, Tampé R (2014) Mechanistic determinants of the directionality and energetics of active export by a heterodimeric ABC transporter. *Nat Commun* 5: 5419
- Hellen CUT (2018) Translation termination and ribosome recycling in eukaryotes. *Cold Spring Harb Perspect Biol* 10: a032656
- Heuer A, Gerovac M, Schmidt C, Trowitzsch S, Preis A, Kötter P, Berninghausen O, Becker T, Beckmann R, Tampé R (2017) Structure of the 40S-ABCE1 post-splitting complex in ribosome recycling and translation initiation. *Nat Struct Mol Biol* 24: 453–460
- Hofmann S, Janulien D, Mehdipour AR, Thomas C, Stefan E, Bruchert S, Kuhn BT, Geertsma ER, Hummer G, Tampé R *et al* (2019) Conformation space of a heterodimeric ABC exporter under turnover conditions. *Nature* 571: 580–583
- Hopfner KP (2016) Invited review: architectures and mechanisms of ATP binding cassette proteins. *Biopolymers* 105: 492–504
- Hurlimann LM, Hohl M, Seeger MA (2017) Split tasks of asymmetric nucleotide-binding sites in the heterodimeric ABC exporter EfrCD. *FEBS J* 284: 1672–1687
- Joazeiro CAP (2019) Mechanisms and functions of ribosome-associated protein quality control. *Nat Rev Mol Cell Biol* 20: 368–383

- Johnson E, Nguyen PT, Yeates TO, Rees DC (2012) Inward facing conformations of the MetNI methionine ABC transporter: implications for the mechanism of transinhibition. *Protein Sci* 21: 84–96
- Karcher A, Schele A, Hopfner KP (2008) X-ray structure of the complete ABC enzyme ABCE1 from *Pyrococcus abyssi*. *J Biol Chem* 283: 7962–7971
- Kelley LA, Mezulis S, Yates CM, Wass MN, Sternberg MJ (2015) The Phyre2 web portal for protein modeling, prediction and analysis. *Nat Protoc* 10: 845–858
- Kimanius D, Forsberg BO, Scheres SH, Lindahl E (2016) Accelerated cryo-EM structure determination with parallelisation using GPUs in RELION-2. *Elife* 5: e18722
- Kiosze-Becker K, Ori A, Gerovac M, Heuer A, Nürenberg-Goloub E, Rashid UJ, Becker T, Beckmann R, Beck M, Tampé R (2016) Structure of the ribosome post-recycling complex probed by chemical cross-linking and mass spectrometry. *Nat Commun* 7: 13248
- Korkhov VM, Mireku SA, Locher KP (2012) Structure of AMP-PNP-bound vitamin B12 transporter BtuCD-F. *Nature* 490: 367–372
- Lammens K, Bemeleit DJ, Möckel C, Clausing E, Schele A, Hartung S, Schiller CB, Lucas M, Angermüller C, Söding J et al (2011) The Mre11:Rad50 structure shows an ATP-dependent molecular clamp in DNA double-strand break repair. *Cell* 145: 54–66
- Mills EW, Wangen J, Green R, Ingolia NT (2016) Dynamic regulation of a ribosome rescue pathway in erythroid cells and platelets. *Cell Rep* 17: 1–10
- Newstead S, Fowler PW, Bilton P, Carpenter EP, Sadler PJ, Campopiano DJ, Sansom MS, Iwata S (2009) Insights into how nucleotide-binding domains power ABC transport. *Structure* 17: 1213–1222
- Nürenberg-Goloub E, Heinemann H, Gerovac M, Tampé R (2018) Ribosome recycling is coordinated by processive events in two asymmetric ATP sites of ABCE1. *Life Sci Alliance* 1: e201800095
- Nürenberg-Goloub E, Tampé R (2019) Ribosome recycling in mRNA translation, quality control, and homeostasis. *Biol Chem* 401: 47–61
- Pettersen EF, Goddard TD, Huang CC, Couch GS, Greenblatt DM, Meng EC, Ferrin TE (2004) UCSF Chimera—a visualization system for exploratory research and analysis. *J Comput Chem* 25: 1605–1612
- Pisarev AV, Skabkin MA, Pisareva VP, Skabkina OV, Rakotondrafara AM, Hentze MW, Hellen CU, Pestova TV (2010) The role of ABCE1 in eukaryotic posttermination ribosomal recycling. *Mol Cell* 37: 196–210
- Preis A, Heuer A, Barrio-Garcia C, Hauser A, Eyler DE, Berninghausen O, Green R, Becker T, Beckmann R (2014) Cryoelectron microscopic structures of eukaryotic translation termination complexes containing eRF1-eRF3 or eRF1-ABCE1. *Cell Rep* 8: 59–65
- Procko E, Ferrin-O'Connell I, Ng SL, Gaudet R (2006) Distinct structural and functional properties of the ATPase sites in an asymmetric ABC transporter. *Mol Cell* 24: 51–62
- Shao S, Murray J, Brown A, Taunton J, Ramakrishnan V, Hegde RS (2016) Decoding Mammalian Ribosome-mRNA States by Translational GTPase Complexes. *Cell* 167: 1229–1240.e15
- Shoemaker CJ, Green R (2011) Kinetic analysis reveals the ordered coupling of translation termination and ribosome recycling in yeast. *Proc Natl Acad Sci USA* 108: E1392–E1398
- Skabkin MA, Skabkina OV, Dhote V, Komar AA, Hellen CU, Pestova TV (2010) Activities of Ligatin and MCT-1/DENR in eukaryotic translation initiation and ribosomal recycling. *Genes Dev* 24: 1787–1801
- Strunk BS, Novak MN, Young CL, Karbstein K (2012) A translation-like cycle is a quality control checkpoint for maturing 40S ribosome subunits. *Cell* 150: 111–121
- Tahmasebi S, Khoutorsky A, Mathews MB, Sonenberg N (2018) Translation deregulation in human disease. *Nat Rev Mol Cell Biol* 19: 791–807
- Wu Z, Wang Y, Lim J, Liu B, Li Y, Vartak R, Stankiewicz T, Montgomery S, Lu B (2018) Ubiquitination of ABCE1 by NOT4 in response to mitochondrial damage links co-translational quality control to PINK1-directed mitophagy. *Cell Metab* 28: 130–144.e7
- Young DJ, Guydosh NR, Zhang F, Hinnebusch AG, Green R (2015) Rli1/ABCE1 recycles terminating ribosomes and controls translation reinitiation in 3'UTRs *in vivo*. *Cell* 162: 872–884
- Young DJ, Guydosh NR (2019) Hcr1/eIF3j Is a 60S ribosomal subunit recycling accessory factor *in vivo*. *Cell Rep* 28: 39–50.e4
- Zaitseva J, Jenewein S, Jumpertz T, Holland IB, Schmitt L (2005) H662 is the linchpin of ATP hydrolysis in the nucleotide-binding domain of the ABC transporter HlyB. *EMBO J* 24: 1901–1910
- Zhang K (2016) Gctf: real-time CTF determination and correction. *J Struct Biol* 193: 1–12
- Zheng SQ, Palovcak E, Armache JP, Verba KA, Cheng Y, Agard DA (2017) MotionCor2: anisotropic correction of beam-induced motion for improved cryo-electron microscopy. *Nat Methods* 14: 331–332
- Zivanov J, Nakane T, Forsberg BO, Kimanius D, Hagen WJ, Lindahl E, Scheres SH (2018) New tools for automated high-resolution cryo-EM structure determination in RELION-3. *Elife* 7: e42166
- Zutz A, Hoffmann J, Hellmich UA, Glaubitz C, Ludwig B, Brutschy B, Tampé R (2011) Asymmetric ATP hydrolysis cycle of the heterodimeric multidrug ABC transport complex TmrAB from *Thermus thermophilus*. *J Biol Chem* 286: 7104–7115



License: This is an open access article under the terms of the Creative Commons Attribution 4.0 License, which permits use, distribution and reproduction in any medium, provided the original work is properly cited.

Expanded View Figures

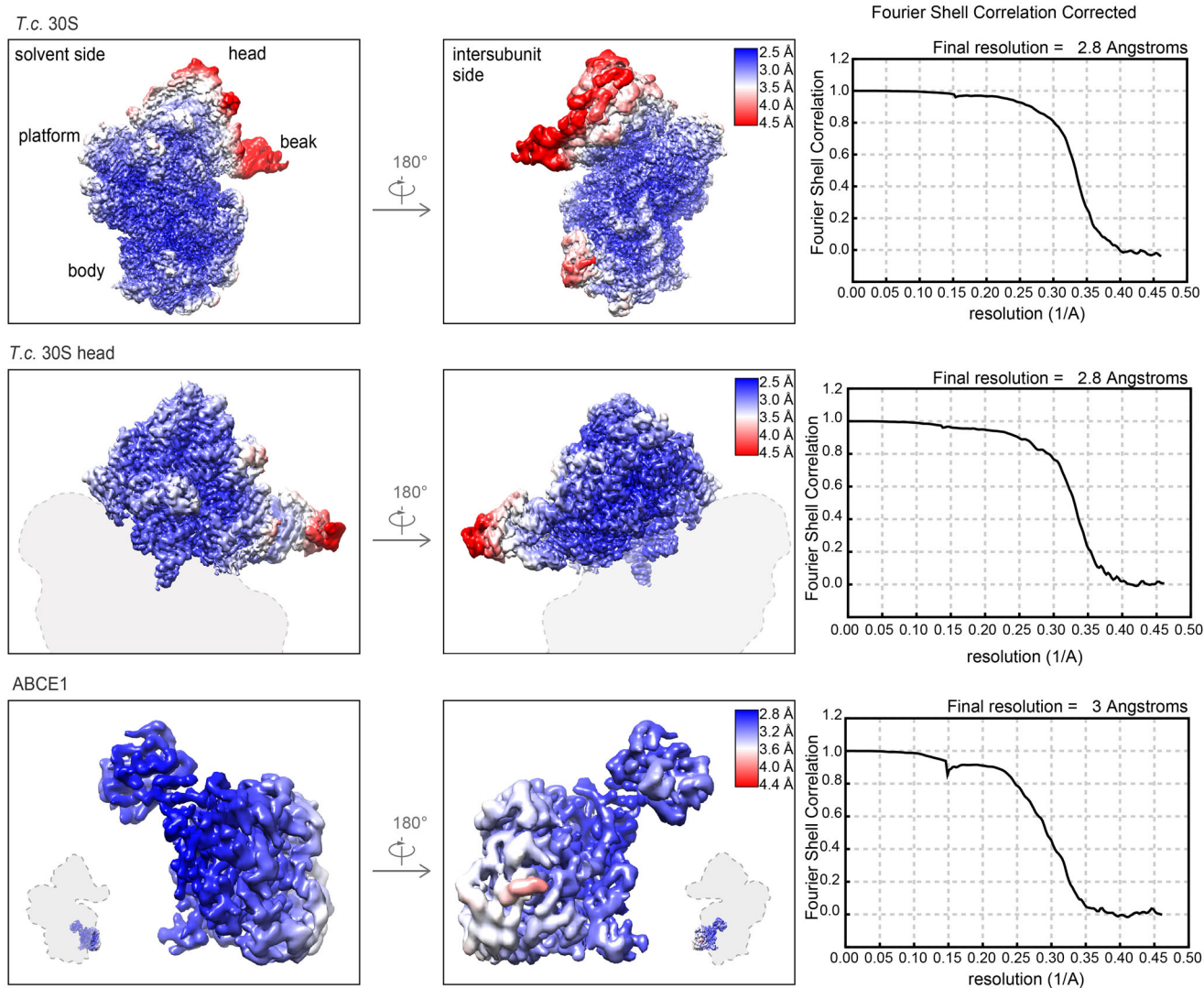


Figure EV1. Local resolution of the post-SC.

Cryo-EM maps of the overall 30S-ABCE1 post-SC (top) and locally refined 30S head (middle) and ABCE1 (bottom) moieties. Maps are colored and filtered according to local resolution, and corresponding gold standard FSC curves are shown. Using focused refinement, local resolution of the 30S head and ABCE1 was improved from approx. 4–6 Å to 3.0 Å and 2.8 Å, respectively.

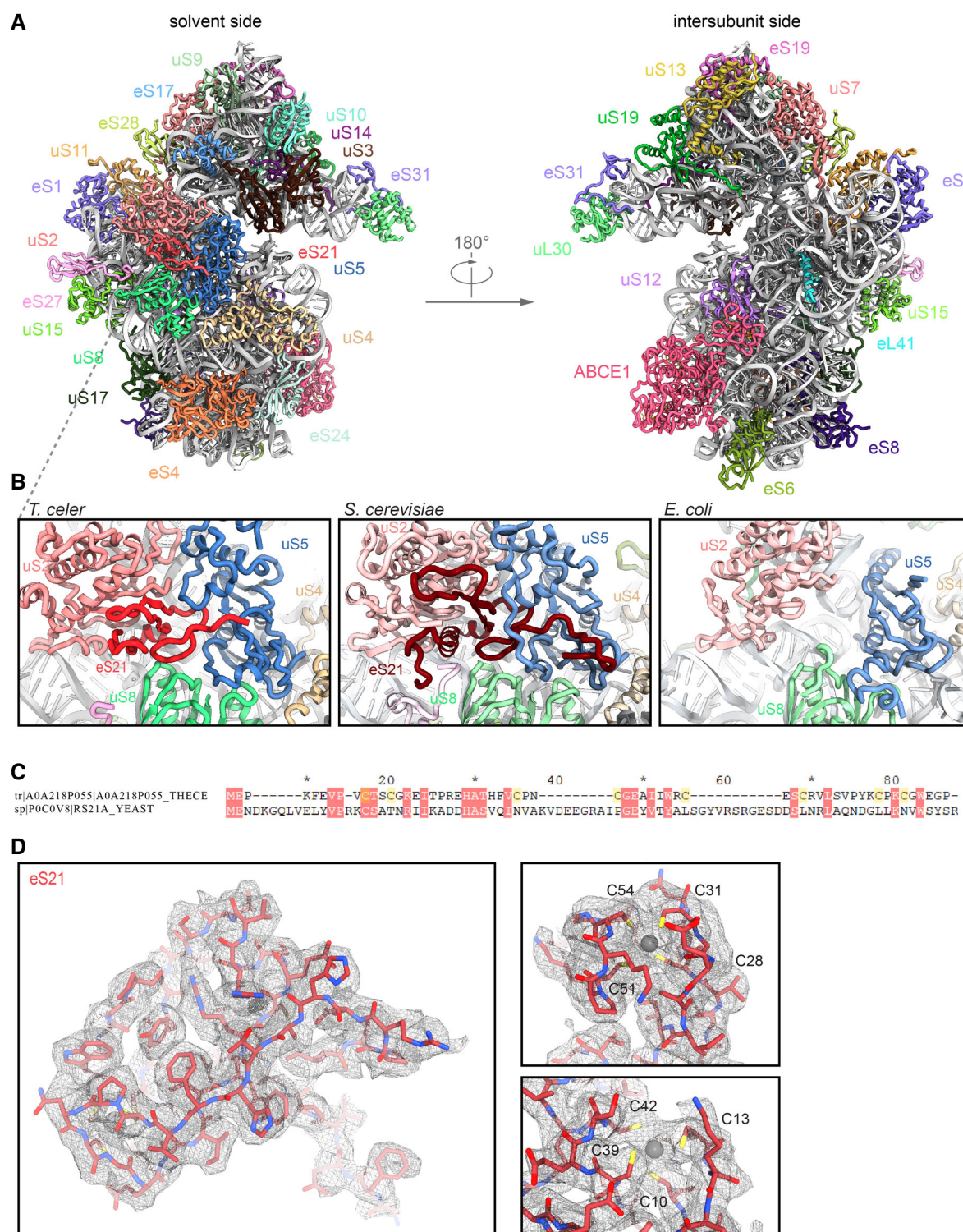


Figure EV2. Location of eS21 and molecular model of the *T. celer* 30S subunit.

A *T. celer* 30S subunit contains 28 ribosomal proteins, including the large subunit protein eL41.

B Close-up view on eS21 located at the solvent side between uS2, uS5, and uS8. Comparison with other species reveals that the respective position at the ribosome is not occupied in *E. coli*, but by eS21 in *S. cerevisiae*.

C Sequence alignment of *T. celer* eS21 and *S. cerevisiae* eS21a shows low homology, indicating that the two proteins are only weakly related.

D Cryo-EM density for e21 and fit of the *de novo* model. The protein forms two zinc-binding pockets, each coordinated by four cysteines.

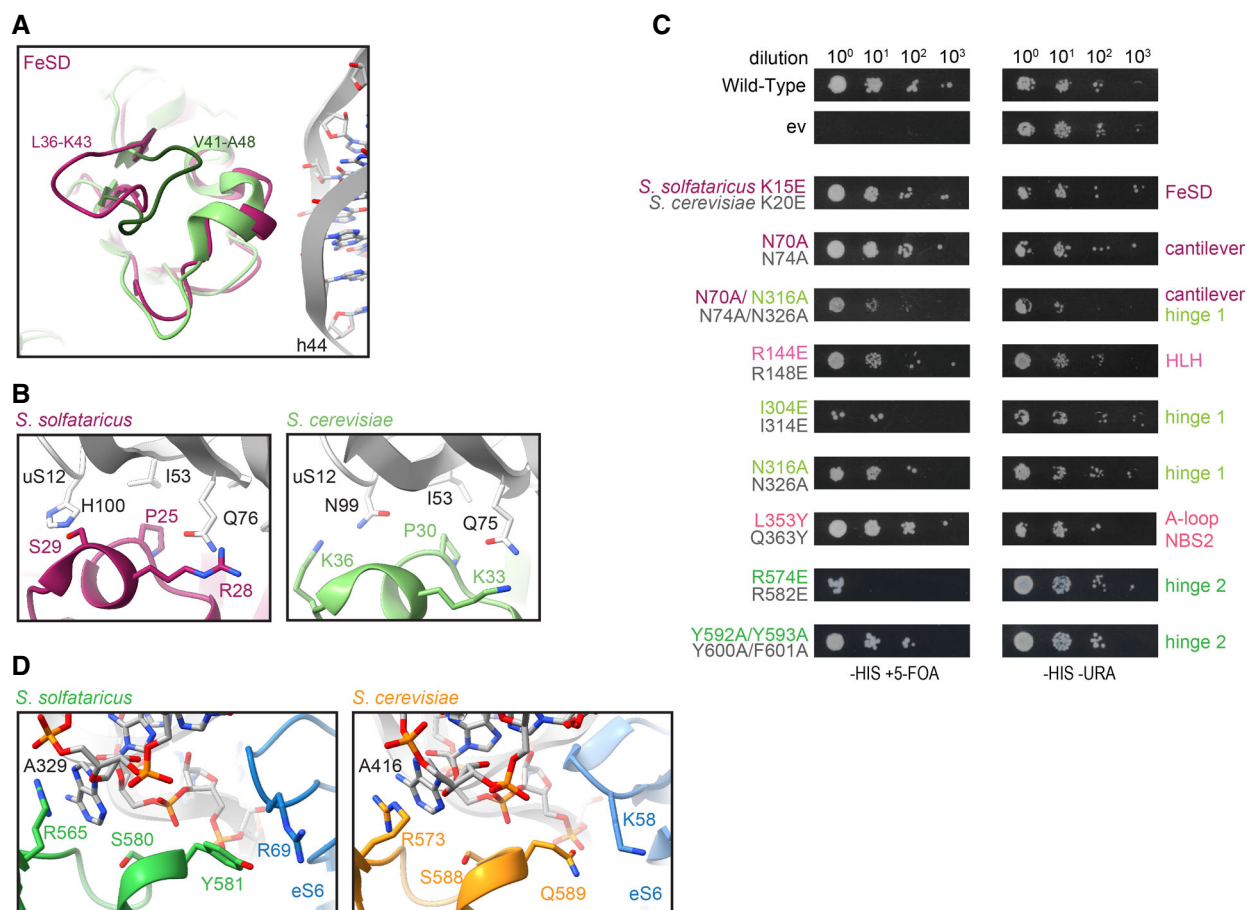


Figure EV3. Conserved interactions of ABCE1 with 30S are essential for ABCE1 function.

- A FeSD interactions are conserved between *S. solfataricus* and *S. cerevisiae*, except for the loops L36–K43 (*S. solfataricus*) and V41–A48 (*S.c.*), which face away from the ribosome and vary in sequence and structure.
- B The interaction between S29 and H100 (uS12) is substituted by K36 and N99 (uS6) in yeast, indicating co-evolution of ABCE1 and the ribosome.
- C Yeast plasmid shuffling assay illustrates cell viability and growth either dependent or independent on the plasmid with mutant ABCE1 in the presence or absence of 5-FOA, respectively.
- D Stacking of Y581 with R69 (eS6) occurs in yeast as Q589 with K58 (eS6), giving another hint for ABCE1-ribosome co-evolution in order to maintain essential interactions.

Data Information: In (C), data are representative for a set of two independent experiments.

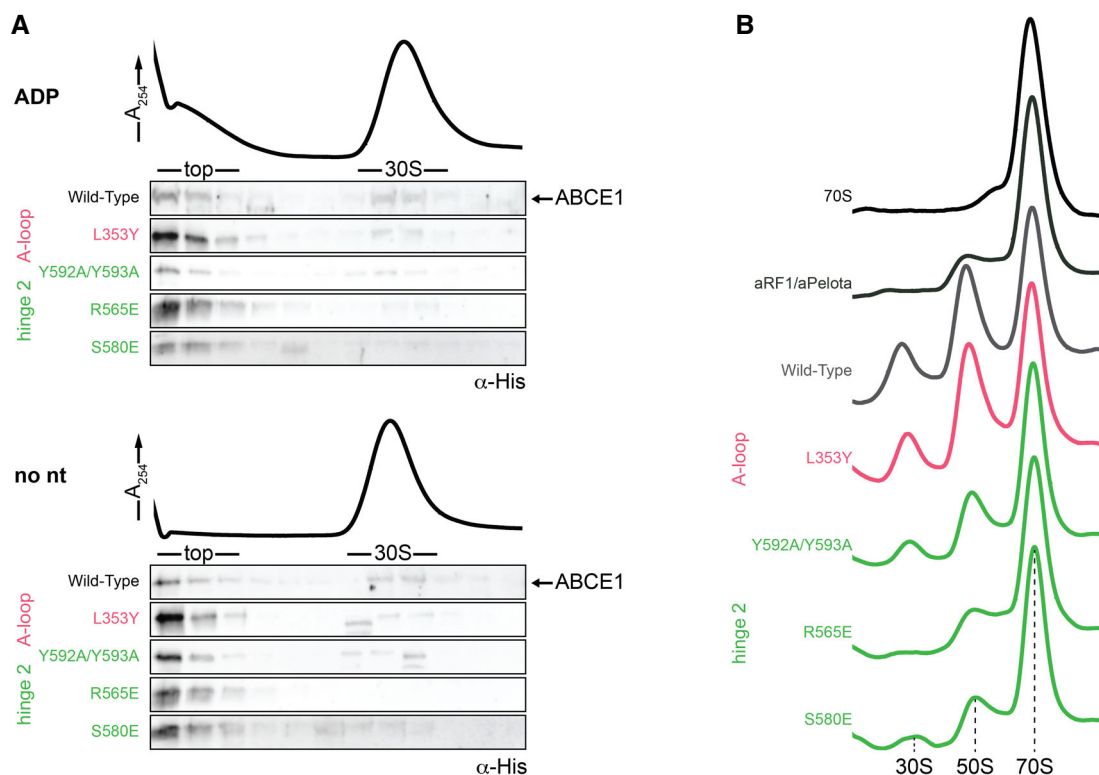


Figure EV4. Detailed *in vitro* biochemical characterization of ABCE1 variants.

A As wild-type ABCE1, all variants are unable to bind 30S ribosomes in the presence of ADP or in the absence of nucleotide (no nt), thereby excluding that the respective mutation does not lead to unspecific binding to the ribosome.

B Examples of sucrose density gradient profiles of 70S splitting reactions illustrate reduced splitting efficiencies of hinge 2 mutants compared to wild-type ABCE1. SDG profile of the background control (aRF1/aPelota) is similar to R565E, highlighting its essential anchoring function (see Fig 3C).

Source data are available online for this figure.

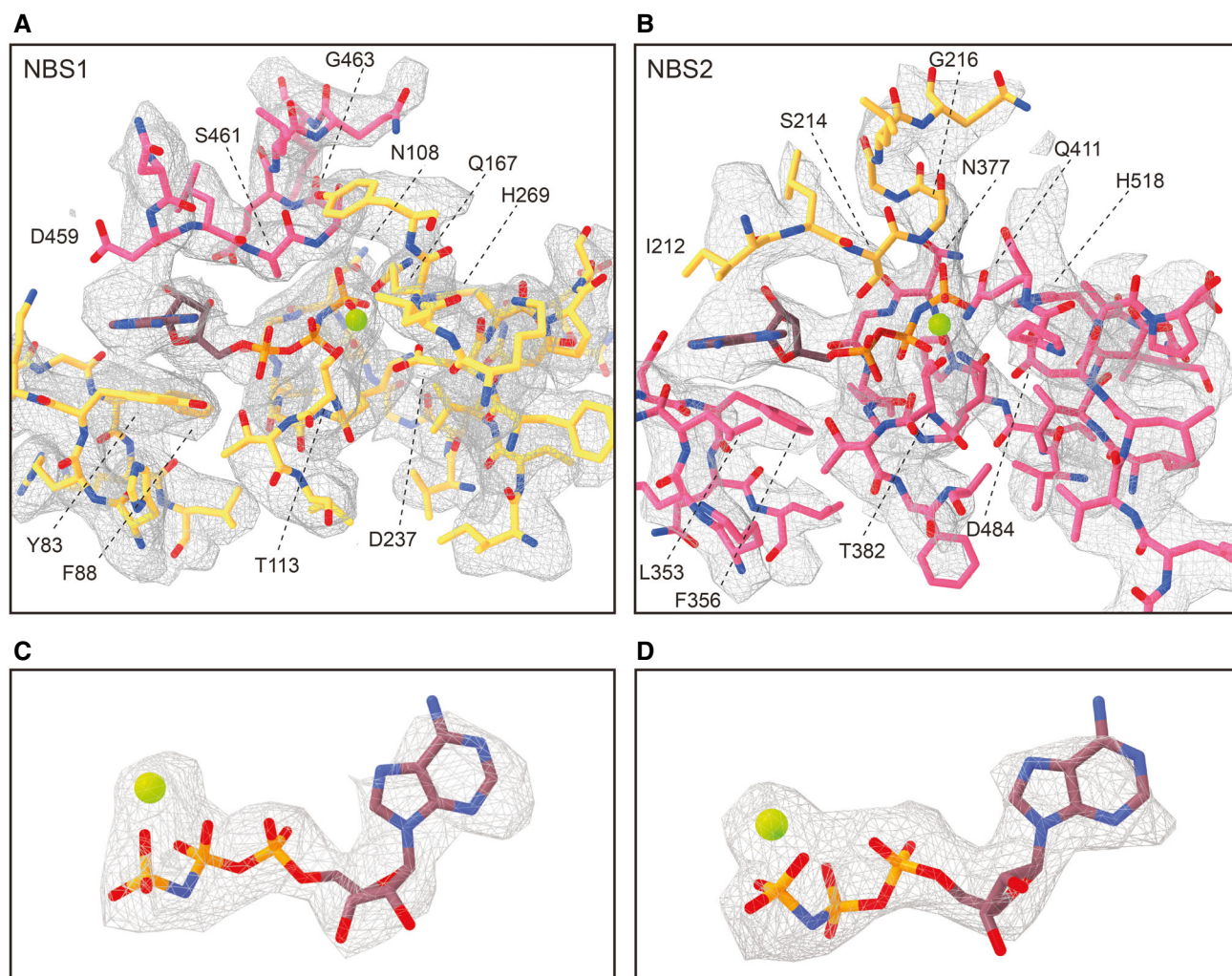


Figure EV5. Fitting of NBSI and NBSII in the cryo-EM density.

- A Zoomed view on the model for NBSI fit into the electron density map shown in the same view as in Fig 3I. Residues from NBD1 and NBD2 are shown in gold and punch, respectively, and residues contributing to Mg^{2+} -AMP-PNP binding are labeled.
- B Same as in (A) but for NBSII, corresponding to Fig 3J.
- C, D Electron density and fit model for isolated Mg^{2+} -AMP-PNP from both NBSI (C) and NBSII (D). We clearly observe density for the Mg^{2+} -ion coordinated by the γ - and β -phosphates of the trinucleotide in both NBSs.

Appendix

Table of content

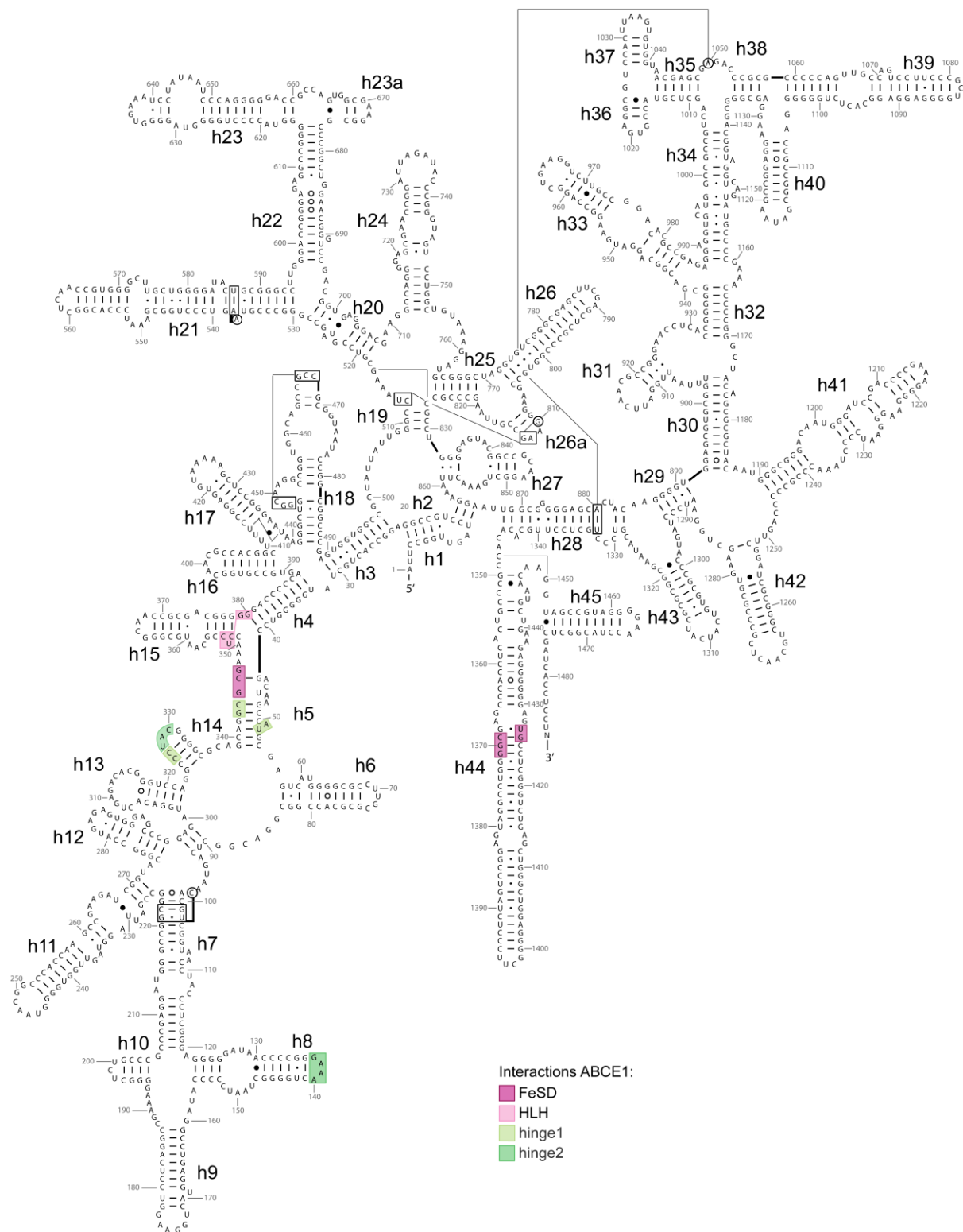
Appendix Figure S1 - Secondary structure of *T. celer* 16S rRNA

Appendix Figure S2 - Sequence alignment of ABCE1 from different species

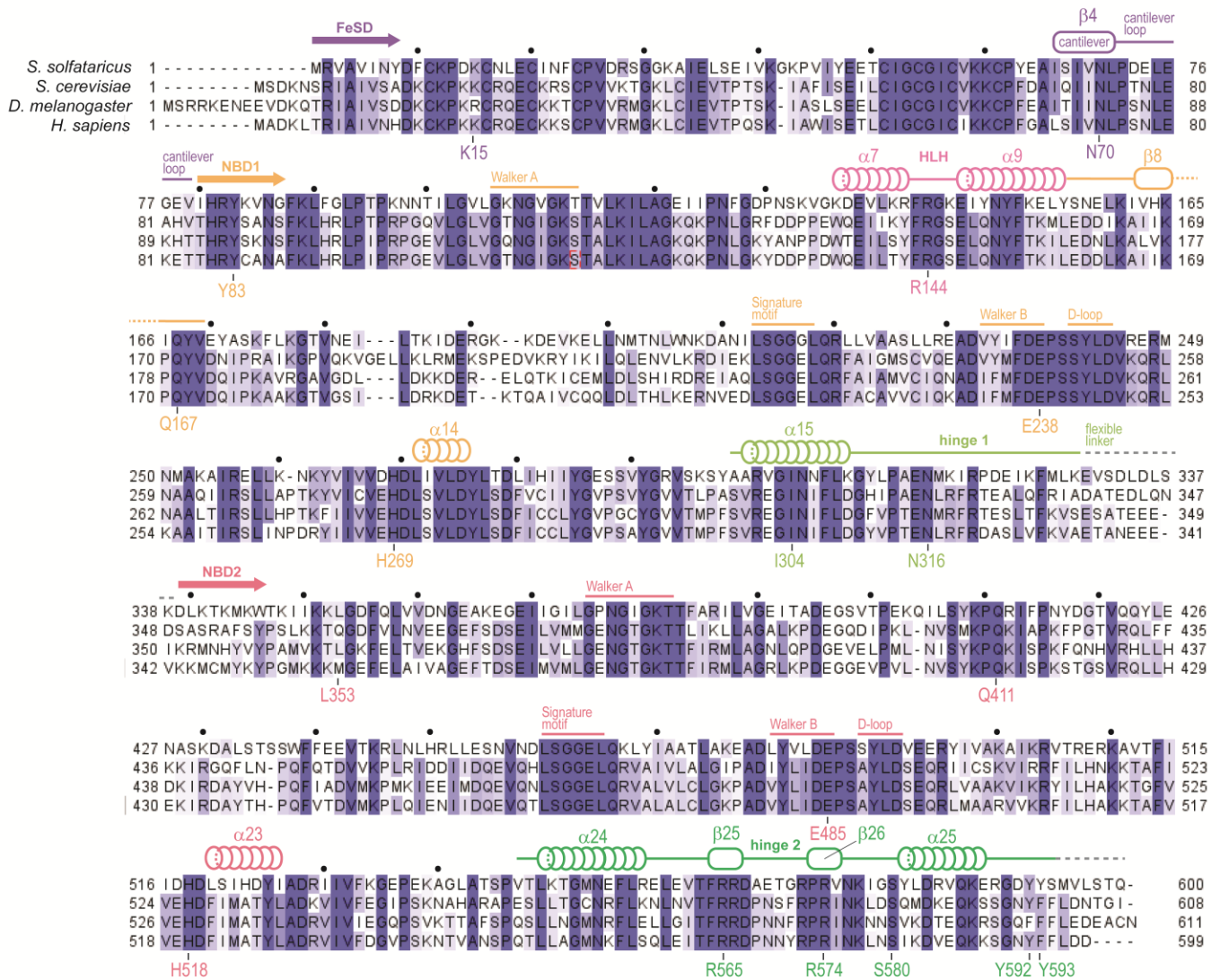
Appendix Figure S3 - Quality control of *S. solfataricus* ABCE1 variants

Appendix Figure S4 - Structural alignment of ABCE1 with bacterial ABC-importers

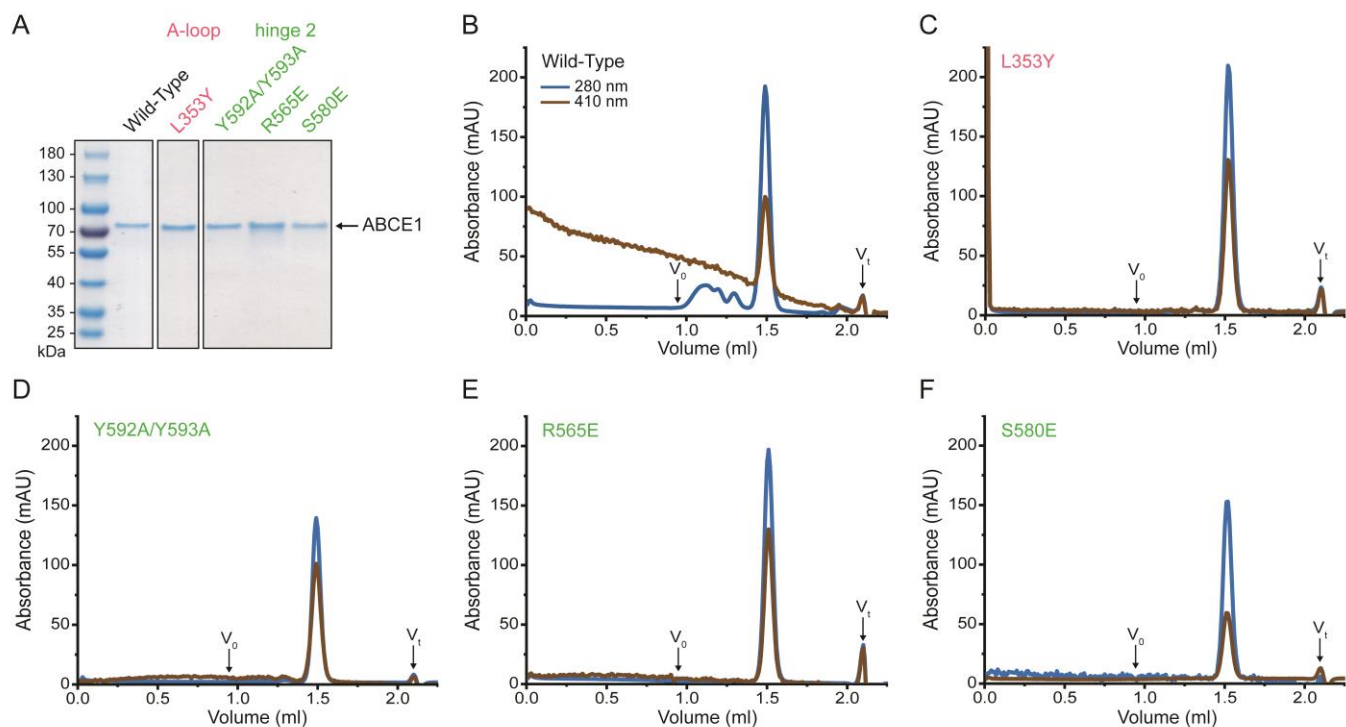
Appendix References



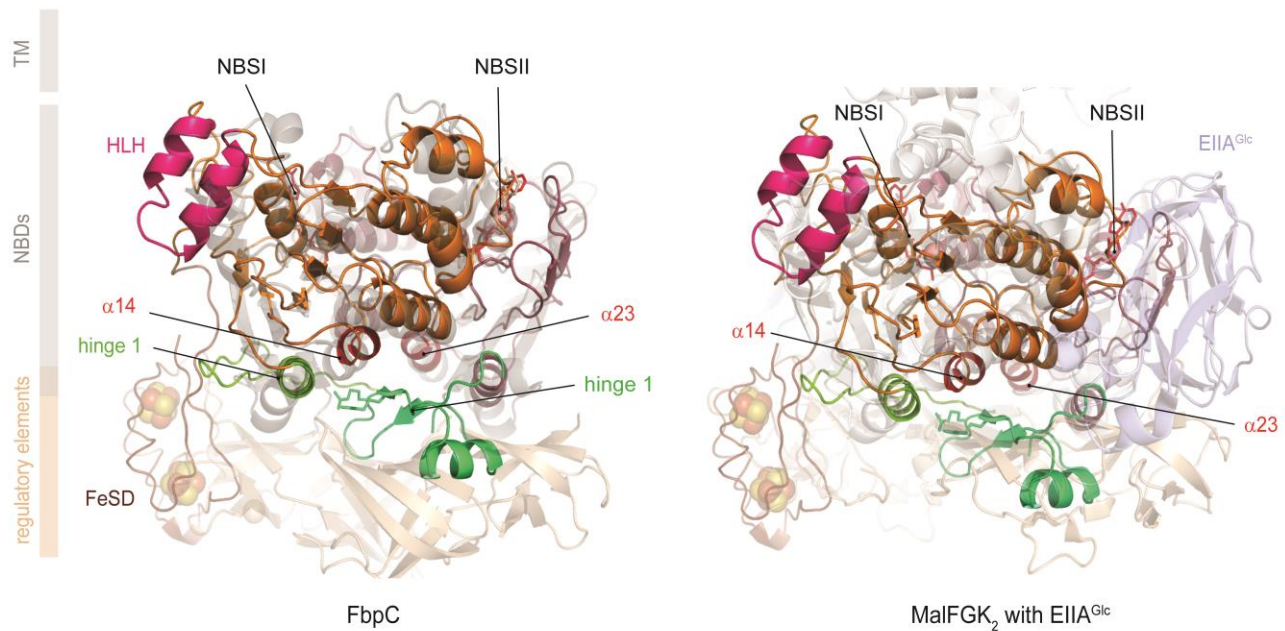
Appendix Figure S1. Secondary structure of *T. celer* 16S rRNA. 1487 nucleic acid residues form the *T. celer* 16S rRNA (Cannone *et al*, 2002). ABCE1-domain interactions with the 16S rRNA are colored according to the domain architecture of ABCE1 in Figure 1. FeSD contacts G345, C346 and G347 of h5, and C1369, G1370, G1371, G1426 and U1427 of h44. HLH motif binds to C352, U253, C354 and G379 of h15, and G380 of h4. Hinge 1 contacts h5 at A51, U52, G343 and C344, and h14 at C326 and C327. Hinge 2 anchors to the ribosome at G137, A138, A139 and A140 of h8, and U328, A329 and C330 of h14.



Appendix Figure S2. Sequence alignment of ABCE1 from different species. *S. solfataricus*, *S. cerevisiae*, *D. melanogaster* and *H. sapiens* ABCE1 display strong sequence conservation, illustrated by the shades of blue. Numbering according to *S.s.* ABCE1. Domains are indicated by arrows. Loops are represented by lines, α-helices by tubes and β-sheets by boxes. Conserved motifs, important secondary structure elements (numbered according to (Karcher *et al*, 2008) and colored according to Figure 1) and residues are indicated.



Appendix Figure S3: Quality control of *S. solfataricus* ABCE1 variants. **A**, Quality of purified ABCE1 variants is assured by single protein bands at the expected molecular weight in SDS-PAGE. **B-F**, All ABCE1 variants elute in single symmetric peaks in size-exclusion-chromatography confirming monodisperse protein samples. Absorbance at 410 nm attests correct assembly of the iron-sulfur clusters.









Appendix Figure S4. Structural alignment of ABCE1 with bacterial ABC-importers. Superposition of the NBDs from ABCE1, the iron uptake transporter FbpC (left) of *Neisseria gonorrhoeae* (3FVQ) (Newstead *et al*, 2009), and the maltose transporter MalFGK₂ (right) in complex with the glucose-specific phosphotransferase enzyme EIIA^{Glc} from *E. coli* (4JBW) (Chen *et al*, 2013). The hinge regions of ABCE1 are located at the same position as the regulatory elements of the ABC-importers. Thus, hinge 1 and hinge 2 may fulfill regulatory functions in ribosome sensing and communication to the NBSs via $\alpha 14$ and $\alpha 23$, in accordance with the evolution of the ubiquitous ABC-protein system.

Appendix References

- Cannone JJ, Subramanian S, Schnare MN, Collett JR, D'Souza LM, Du Y, Feng B, Lin N, Madabusi LV, Muller KM, Pande N, Shang Z, Yu N, Gutell RR (2002) The comparative RNA web (CRW) site: an online database of comparative sequence and structure information for ribosomal, intron, and other RNAs. *BMC bioinformatics* 3: 2
- Chen S, Oldham ML, Davidson AL, Chen J (2013) Carbon catabolite repression of the maltose transporter revealed by X-ray crystallography. *Nature* 499: 364-8
- Karcher A, Schele A, Hopfner KP (2008) X-ray structure of the complete ABC enzyme ABCE1 from *Pyrococcus abyssi*. *J Biol Chem* 283: 7962-71
- Newstead S, Fowler PW, Bilton P, Carpenter EP, Sadler PJ, Campopiano DJ, Sansom MS, Iwata S (2009) Insights into how nucleotide-binding domains power ABC transport. *Structure* 17: 1213-22

A structural inventory of native ribosomal ABCE1-43S pre-initiation complexes

Hanna Kratzat^{1,†}, Timur Mackens-Kiani^{1,†}, Michael Ameismeier¹ , Mia Potocnjak¹, Jingdong Cheng¹ , Estelle Dacheux², Abdelkader Namane² , Otto Berninghausen¹, Franz Herzog¹, Micheline Fromont-Racine² , Thomas Becker^{1,*}  & Roland Beckmann^{1,**} 

Abstract

In eukaryotic translation, termination and ribosome recycling phases are linked to subsequent initiation of a new round of translation by persistence of several factors at ribosomal sub-complexes. These comprise/include the large eIF3 complex, eIF3j (Hcr1 in yeast) and the ATP-binding cassette protein ABCE1 (Rli1 in yeast). The ATPase is mainly active as a recycling factor, but it can remain bound to the dissociated 40S subunit until formation of the next 43S pre-initiation complexes. However, its functional role and native architectural context remains largely enigmatic. Here, we present an architectural inventory of native yeast and human ABCE1-containing pre-initiation complexes by cryo-EM. We found that ABCE1 was mostly associated with early 43S, but also with later 48S phases of initiation. It adopted a novel hybrid conformation of its nucleotide-binding domains, while interacting with the N-terminus of eIF3j. Further, eIF3j occupied the mRNA entry channel via its ultimate C-terminus providing a structural explanation for its antagonistic role with respect to mRNA binding. Overall, the native human samples provide a near-complete molecular picture of the architecture and sophisticated interaction network of the 43S-bound eIF3 complex and the eIF2 ternary complex containing the initiator tRNA.

Keywords ABCE1; eIF3; cryo-EM; translation initiation; ribosome recycling

Subject Categories Structural Biology; Translation & Protein Quality

DOI 10.15252/embj.2020105179 | Received 3 April 2020 | Revised 21 September 2020 | Accepted 29 September 2020 | Published online 8 December 2020

The EMBO Journal (2021) 40: e105179

Introduction

Translation of an mRNA into a polypeptide sequence is a central cellular process, which is highly regulated and linked to other cellular processes like ribosome biogenesis, mRNA turnover, and ribosome quality control. Most decisive for translational efficiency and

regulation is the initiation phase; however, in eukaryotes the individual phases of translation were found to be coupled, especially termination with ribosome recycling and a new round of initiation. Two prominent examples are the conserved multisubunit complex eIF3, which has been described as a factor functioning across the translation cycle (Valasek *et al*, 2017), as well as the ATP-binding cassette (ABC) ATPase ABCE1 (Rli1 in *Saccharomyces cerevisiae*), which was shown to enhance termination activity of the eRF1 release factor and which represents the key enzyme for ATP-dependent ribosome recycling (Pisarev *et al*, 2010; Shoemaker & Green, 2011). Moreover, ABCE1 was found associated with initiation factors (Chen *et al*, 2006; Dong *et al*, 2004) and as a part of eIF3-containing 43S or 48S pre-initiation complexes (Andersen & Leever, 2007; Preis *et al*, 2014; Mancera-Martinez *et al*, 2017).

The ABCE1 ATPase consists of two nucleotide-binding domains (NBDs) that are forming two nucleotide-binding sites (NBSs) at their interface, as well as an essential iron-sulfur cluster domain (FeSD) at its N-terminus (Barthelme *et al*, 2007; Hopfner, 2016). ABCE1 binds the 80S ribosome during canonical stop codon-dependent termination or during rescue of stalled ribosomes and splits the 80S ribosomes into 40S and 60S small (SSU) and large (LSU) subunits, respectively. This recycling reaction requires an A site factor in the ribosome, either release factor eRF1 (after termination) or its homologue Pelota (Dom34 in *S.c.*; for ribosome rescue), in order to form part of the interaction network for ABCE1 (Becker *et al*, 2012; Brown *et al*, 2015; Preis *et al*, 2014). ABCE1 binds these pre-splitting complexes in a semi-open state with respect to its NBSs. Splitting requires binding of ATP and site-occlusion to both NBS (Barthelme *et al*, 2011; Gouridis *et al*, 2019; Nurenberg-Goloub *et al*, 2018). According to current models, the conformational change occurring during site-occlusion would be transmitted *via* the FeSD of ABCE1 to the bound A site factor (eRF1 or Dom34), whereby the FeSD exerts a force on the A site factor which ultimately leads to ribosome splitting (Becker *et al*, 2012; Heuer *et al*, 2017; Nurenberg-Goloub *et al*, 2020). The splitting reaction can be recapitulated *in vitro* (Becker *et al*, 2012; Nurenberg-Goloub & Tampe, 2019; Pisareva *et al*, 2011; Shao *et al*, 2015;

¹ Gene Center and Center for Integrated Protein Science Munich, Department of Biochemistry, University of Munich, Munich, Germany

² Génétique des Interactions Macromoléculaires, UMR3525 CNRS, Institut Pasteur, Paris, France

*Corresponding author. Tel: +49 89 2180 76915; E-mail: becker@genzentrum.lmu.de

**Corresponding author. Tel: +49 89 2180 76900; E-mail: beckmann@genzentrum.lmu.de

[†]These authors contributed equally to this work

[Correction added on 5 February 2021 after first online publication: Publishing license has been changed]

Shoemaker & Green, 2011), where ABCE1 was observed to remain bound to the 40S small subunit to form a post-splitting complex (PSC), in which the two NBDs are present in a closed, nucleotide-occluding state (Heuer *et al.*, 2017; Kiosze-Becker *et al.*, 2016; Nürenberg-Goloub *et al.*, 2020). Therefore, it was assumed that *in vivo* as well, ABCE1 may remain bound to the 40S for a defined time span (Gerovac & Tampe, 2019) to prevent re-association of the LSU (Heuer *et al.*, 2017) or to coordinate assembly of initiation factors on the 40S subunit. However, a direct physical involvement of ABCE1 in the translation initiation process has not been shown to date.

In eukaryotes, the start of translation initiation requires the assembly of the 43S pre-initiation complex (PIC). It consists of the 40S subunit, eIF3, eIF1, eIF1A, eIF5, and the ternary complex (TC) formed by the trimeric eIF2 $\alpha\beta\gamma$, initiator methionyl tRNA (tRNA_i), and GTP. After 43S PIC assembly, the mRNA—in collaboration with the eIF4F complex (the cap-binding protein eIF4E, the helicase eIF4A, and the scaffolding protein eIF4G)—can be recruited to the 43S PIC, forming the 48S initiation complex (IC). This event is coordinated by interactions between eIF3 and eIF4F as well as eIF4B, a single-stranded RNA-binding protein that attaches to the 40S subunit (Walker *et al.*, 2013) and stimulates the helicase activity of eIF4A. The 48S complex then scans the mRNA for the first cognate AUG codon. After start-codon recognition, inorganic phosphate (P_i) is released from the eIF2 complex, which is stimulated by eIF5 acting as a GTPase-activating protein, likely *via* an arginine-finger mechanism (Algire *et al.*, 2005; Das *et al.*, 2001; Paulin *et al.*, 2001). Subsequently, initiation factors apart from eIF1A and eIF3 dissociate (Mohammad *et al.*, 2017; Sha *et al.*, 2009) and subunit joining with the 60S LSU is then mediated by the GTPase eIF5B (Acker *et al.*, 2006; Acker *et al.*, 2009; Lee *et al.*, 2002; Pestova *et al.*, 2000).

An important regulatory and scaffolding role in these processes is taken on by the multisubunit complex eIF3 (Cate, 2017; Hinnebusch, 2006), which can be structurally divided into the so-called PCI-MPN core and the peripheral subunits. In yeast, the PCI-MPN core consists of the two subunits eIF3a (Rpg1/Tif32) and eIF3c (Nip1), whereas in mammals, it is formed by an octamer of eIFs 3a, 3c, 3e, 3f, 3h, 3i, 3k, and 3l (Valasek *et al.*, 2017). The peripheral subunits consist of the so-called yeast-like core (YLC) module, containing eIF3b (Prt1), eIF3g (Tif35), and eIF3i (Tif34), as well as the C-terminus of eIF3a, the N-terminal domain of eIF3c that interacts with eIF1 and eIF5 (Valasek *et al.*, 2003; Valasek *et al.*, 2004; Yamamoto *et al.*, 2005; Zeman *et al.*, 2019), and in mammals eIF3d. In addition, eIF3j is associated with eIF3 but does not belong to its core, and plays a special role (Block *et al.*, 1998; Valasek *et al.*, 1999). It was shown that eIF3j participates during termination by recycling eRF3 (Beznoskova *et al.*, 2013) and during ribosome recycling by assisting ABCE1 in subunit splitting (Young & Guydosh, 2019). Furthermore, it is involved in dissociation of mRNA from the 40S subunit (Pisarev *et al.*, 2007; Pisarev *et al.*, 2010). In the context of initiation, eIF3j is believed to participate in the recruitment of eIF3 to the 40S (Elantak *et al.*, 2010; Fraser *et al.*, 2004; Nielsen *et al.*, 2006), to antagonize premature mRNA recruitment (Fraser *et al.*, 2007), and to regulate start-site selection (Elantak *et al.*, 2010).

For a better mechanistic understanding of this complicated interplay, a number of cryo-EM structures of 43S PICs and partial 48S ICs gave first insights into the architectural variety of initiation complexes (Aylett *et al.*, 2015; des Georges *et al.*, 2015; Eliseev *et al.*, 2018; Erzberger *et al.*, 2014; Hashem *et al.*, 2013; Hussain *et al.*, 2014;

Llacer *et al.*, 2015; Llacer *et al.*, 2018; Mancera-Martinez *et al.*, 2017). During 43S assembly, the 40S subunit gets prepared to thread the mRNA into the mRNA-binding channel between the 40S body and the head. The main constriction for mRNA is at the so-called “latch”, a structural element formed between ribosomal RNA (rRNA) helix h18 and ribosomal protein (r-protein) uS12 on the 40S body, and h34 and uS3 on the head (Schlunzen *et al.*, 2000). Empty or only ABCE1-bound 40S usually does not adopt a defined head conformation, and the latch is rather closed (Heuer *et al.*, 2017; Passmore *et al.*, 2007). Binding of eIF1 and especially eIF1A, which bridges the body with the head, seems to prime and confine the 40S by inducing a small rotation of the 40S head (Llacer *et al.*, 2015; Passmore *et al.*, 2007), but the latch still remains in a closed position (Llacer *et al.*, 2015). Latch opening was only observed in *in vitro* reconstituted partial 48S ICs containing mRNA and both eIF3 and the eIF2 TC in addition to eIF1 and eIF1A (Llacer *et al.*, 2015; Llacer *et al.*, 2018). Here, two conformations of the 48S IC can be distinguished: the open P_{OUT} and the closed P_{IN} conformation, which differ in the orientation of the 40S head and the TC. Compared to the empty and eIF1/1A-bound structures, the head is moved upwards away from the body in the P_{OUT} conformation. This leads to widening of the latch and the P site tRNA_i in the TC is only bound *via* the anticodon loop (AL) to the 40S head but not the body. In the P_{IN} conformation, the AL moves down and engages in stable codon–anticodon interactions with the cognate start codon in the P site, accompanied by a downward movement of the 40S head.

In all eIF3-containing structures, the PCI-MPN core was located on the back of the 40S subunit, from where peripheral subunits stretch out. In 43S PICs, the YLC was found close to the mRNA entry site of the 40S (Aylett *et al.*, 2015; des Georges *et al.*, 2015; Eliseev *et al.*, 2018; Erzberger *et al.*, 2014), however only at low resolution. Moreover, the YLC module has been shown to relocate to the intersubunit space (ISS), as observed in *in vitro* reconstituted partial 48S complexes (Llacer *et al.*, 2015), thereby occupying the position of ABCE1. The other peripheral subunits eIF3d and the eIF3c N-terminal domain have been localized near the mRNA exit site (eIF3d: Eliseev *et al.*, 2018) and in the ISS (eIF3c-NTD: Llacer *et al.*, 2015; Obayashi *et al.*, 2017). Interestingly, two structures of partial native 43S/48S complexes exist in which ABCE1 could be visualized in substantial quantities (Simonetti *et al.*, 2016, re-interpreted in Mancera-Martinez *et al.*, 2017; Heuer *et al.*, 2017). Notably, both samples were obtained after adding non-hydrolyzable AMP-PNP and/or GMP-PNP to either yeast (Heuer *et al.*, 2017) or rabbit reticulocyte (Simonetti *et al.*, 2016) lysates and subsequent isolation of the 43S peak from a sucrose gradient. This may have led to non-physiological locking of ABCE1 on the 40S subunit, thereby limiting any conclusions about a putative role of ABCE1 during the phase connecting recycling with initiation. Furthermore, apart from a low-resolution cryo-EM map (Aylett *et al.*, 2015) no structural data exist on eIF3j in the context of the native 43S PIC. Therefore, the native structural landscape enabling the transition from translation termination *via* recycling to initiation is not yet well-understood.

Results

In this work, we set out to provide a structural inventory of ABCE1-containing 43S or 48S initiation complexes from native small

ribosomal subunits (SSU). We first asked if substantial amounts of ABCE1 are associated with initiation factor-bound 40S under native conditions. To that end, lysates from a yeast strain (*S.c.*) containing TAP-tagged ABCE1 (Rli1) were subjected to density gradient centrifugation followed by Western blotting of fractions (Fig EV1A). In agreement with previous studies (Andersen & Leever, 2007; Pisarev *et al*, 2010; Pisareva *et al*, 2011), we observed that ABCE1 was especially enriched on 40S and 80S ribosomes. We further performed affinity purification from the lysates under varying buffer conditions but without any stabilizing non-hydrolyzable ATP or GTP analogs, and analyzed the elution fractions by quantitative mass spectrometry (LC-MS/MS) (Figs 1A and EV1B and C). We found that the expected SSU proteins but also eIF3 core components and especially eIF3j (Hcr1) were enriched by ABCE1 affinity purification, indicating that both proteins were indeed integral components of native pre-initiation complexes. Because of this finding and since eIF3j was implicated in ABCE1-dependent ribosome splitting *in vivo* (Young & Guydosh, 2019), we tested if eIF3j together with ABCE1 had a direct impact on ribosome splitting in a reconstituted system. To this end, we performed *in vitro* splitting assays in yeast and tested if eIF3j can play a stimulatory role. Purified 80S ribosomes were incubated with the purified splitting factors Dom34, Hbs1, Rli1 (ABCE1), eIF6 to prevent re-association of ribosomal subunits, ATP and GTP as well as different amounts of eIF3j. Splitting efficiency was assessed from sucrose density gradient UV profiles by monitoring 80S versus ribosomal subunit amounts (Figs 1B and C, and EV1D). Indeed, we observed that an addition of eIF3j in molar excess increased the ratio of split subunits to 80S when compared to a reaction containing the splitting factors only (Fig 1C). Increasing amounts of eIF3j resulted in higher splitting activity. However, eIF3j alone did not exhibit any activity (Fig EV1E). In addition, we found that eIF3j and substoichiometric amounts of ABCE1 remained bound to the 40S after splitting (Fig EV1F). To further confirm that eIF3j can still be associated with the 40S-ABCE1 complex after splitting, we employed the “facilitated splitting” assay as described before (Heuer *et al*, 2017). In this assay, ribosomes are allowed to dissociate under splitting-promoting conditions (low Mg^{2+} and high salt) and in the presence of putative subunit-binding factors (see Materials and Methods). Indeed, in this assay we observed that eIF3j remained on the 40S SSU together with ABCE1, confirming that the two factors remain together on the 40S for downstream events such as initiation after collaborating during splitting (Fig EV1G and H).

To gain further insights into the composition of native small subunits in yeast and human cells, we adopted a shotgun cryo-EM approach. Yeast SSU complexes were obtained after harvesting the crude 43S/48S peak from a preparative sucrose density gradient of yeast cell lysate that was not further treated or stabilized with a non-hydrolyzable nucleotide analog. Similarly, human native 40S was obtained from untreated lysates of HEK Flp-In 293 T-Rex cells after serendipitous non-specific enrichment on sepharose material during unrelated affinity pullouts (see Materials and Methods). Of these samples, large enough cryo-EM data sets were collected in order to analyze their complex composition by extensive 3D classification (Appendix Figs S1 and S2).

In the yeast data set, as expected, the selected particles contained pre-initiation complexes, which could be further classified into defined states varying in composition and conformation of eIF-

associated 40S subunits. The majority of these complexes (62%) contained ABCE1, and the most interesting classes consisted of 43S particles containing ABCE1, eIF3, eIF1, eIF1A, and eIF3j on the 40S (Aylett *et al*, 2015; Heuer *et al*, 2017). The mRNA path (latch) was in the closed conformation (Passmore *et al*, 2007), and at the mRNA entry, we found a density for a typical RNA recognition motif (RRM) (see below). Importantly, in these classes we observed an interaction between the FeSD of ABCE1 and eIF3j (Fig 1D). Moreover, we found one class of particles with mRNA bound, apparently representing a partial 48S IC complex. It contained eIF3, eIF1, tRNA_i in the P_{IN} conformation, as well as the N-terminal domain (NTD) of eIF5 as observed before (Llacer *et al*, 2018), and, to our surprise, also ABCE1 (Fig 1E). The classes representing 43S PIC and 48S IC were refined to a resolution of 5.3 and 6.2 Å, respectively, allowing us to fit molecular models of existing structures as rigid bodies (Fig 1D and E, Appendix Fig S3, Appendix Table S1).

In the human sample, we also found 40S subunits associated with initiation factors, similar to the yeast sample. After classification, four major stable eIF3-containing classes could be obtained (Fig 2A). The 40S in State I resembled the state of an empty 40S subunit with a closed latch (Heuer *et al*, 2017; Passmore *et al*, 2007), and only the core eIF3 subunits and weakly bound eIF1 were found. State II had a similar conformation, and we found extra densities in the ISS for eIF1, eIF3j, and ABCE1. State III additionally contained eIF1A and the ternary eIF2-GTP-tRNA_i complex (TC) in the open P_{OUT} conformation (Llacer *et al*, 2015), whereas State IV was similar to State III but lacked ABCE1. Notably, in contrast to the yeast sample, we did not find any 48S classes containing mRNA. Thus, our human sample mainly represented 43S post-splitting or pre-initiation complexes prior to mRNA recruitment.

Independent focused classification and multi-body refinements focusing on individual sub-complexes (Fig EV2 and Appendix Fig S2) enabled us to obtain molecular resolution for large parts of the human 43S sub-complexes. Therefore, we were able to build models for the octameric eIF3 PCI-MPN core at the backside of the 40S, parts of the YLC at the mRNA entry site and most factors located in the ISS, including ABCE1, eIF3j, eIF1 (including the N-terminal tail), eIF1A, the full eIF2 TC, and the eIF3c N-terminal domain, thus resulting in a near-complete molecular model of the human 43S particle bound to ABCE1 (Fig 2B and C, Appendix Table S2).

Conformation of ABCE1-bound 40S-initiation complexes

Strikingly, we observed ABCE1 associated with 40S subunits during all stages of 43S PIC assembly in humans and even with 48S IC complexes in the yeast sample. In all complexes, the FeSD of ABCE1 was in the extended conformation packed against h44, and the ATPase body occupied the universal translation factor binding site on the 40S, which is highly similar to previous observations of non-native complexes (h8-h14 junction; h5-h15 junction) (Heuer *et al*, 2017; Mancera-Martinez *et al*, 2017; Nürenberg-Goloub *et al*, 2020) (Fig 3A). Here, the 40S subunit is engaged in a very similar way as in the archaeal 30S-ABCE1 structure (Nürenberg-Goloub *et al*, 2020) *via* the ABCE1-specific helix-loop-helix (HLH) domain and the open conformation with respect to the composite hinge regions (h1 and h2). Surprisingly, however, in all structures we observed the ATPase in a novel state that has not yet been described for ABC-type ATPases (Figs 3B, C and D, and EV3A): Compared to the closed

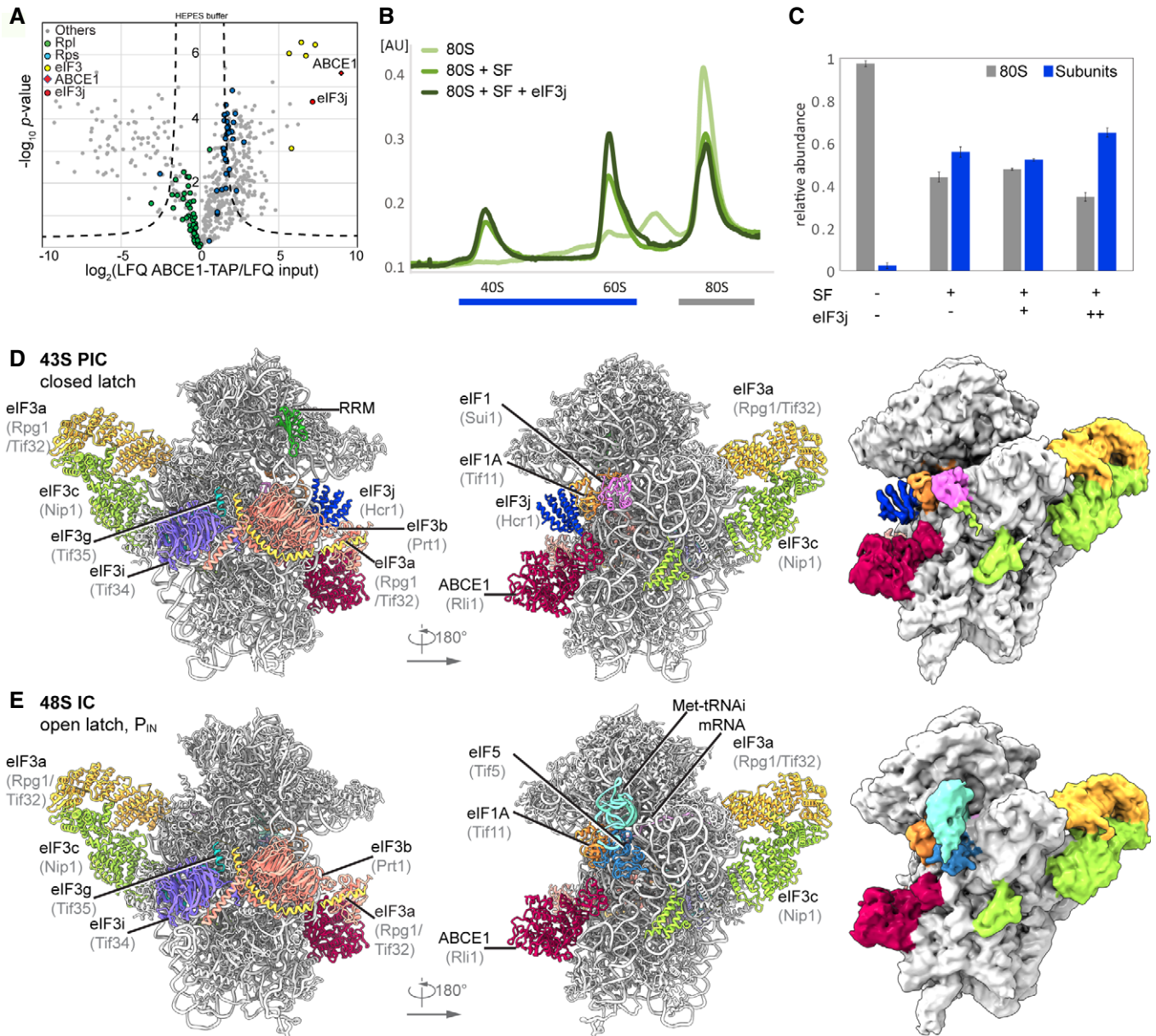


Figure 1. Biochemical analysis and cryo-EM structures of yeast ABCE1-containing initiation complexes.

A Volcano plot representing the statistical analysis of the fold enrichment of proteins after affinity purification in HEPES buffer of ABCE1-TAP followed by label-free quantification (LFQ) using liquid chromatography–tandem mass spectrometry (LC-MS/MS). Proteins above the curved lines show a statistically significant enrichment according to the t-test value.

B, C Sucrose density gradient UV profile after *in vitro* splitting assays (**B**) and relative abundance of 80S and subunits as calculated from triplicates and displayed as mean \pm SD. (**C**): SF = splitting factors including Dom34, Hbs1, ABCE1, and eIF6; (+) = 4-fold molar excess of eIF3j; (++) = 20-fold molar excess of eIF3j.

D, E Cryo-EM maps low-pass filtered at 6 Å and models of the yeast subclasses representing an ABCE1- and eIF3j-containing 43S PIC (**D**) and an ABCE1- and eIF5-containing partial 48S IC (**E**).

Source data are available online for this figure.

conformation as observed in *in vitro* reconstituted 30S and 40S PSCs (Heuer *et al*, 2017; Nürenberg-Goloub *et al*, 2020), we found that only NBSII is closed whereas NBSI adopts a half-open conformation comparable to the one observed in several 80S pre-splitting complexes (Fig 3B) (Becker *et al*, 2012; Brown *et al*, 2015; Preis *et al*, 2014). When analyzing our best-resolved human map, which

was obtained after focused classification on ABCE1, we unambiguously identified an Mg^{2+} -ATP (Fig 3E) occluded in NBSII, similar to the archaeal 30S-ABCE1 structure with Mg^{2+} -AMP-PNP (Nürenberg-Goloub *et al*, 2020). In the human structure, residues of the typical conserved motifs of ABC-type ATPases are involved: Lys386 of the Walker A, Gly220 of the NBD1-Signature loop, and His521 of H-loop

contact the γ -phosphate, and the Mg^{2+} ion is coordinated by Thr387 (Walker A) and Gln415 (Q-loop). In contrast, for NBSI we observed Mg^{2+} -ADP bound exactly as observed in the crystal structures of open archaeal ABCE1 (Barthelme *et al*, 2011; Karcher *et al*, 2008): Y87 of the A-loop stacks on the adenine base, F92 on the ribose, the Walker A-loop (Asn112-Ser117) binds the α - and β -phosphates, and the Mg^{2+} ion is coordinated by the β -phosphate, Ser117, Gln171 (Q-loop) and Asp241, Glu242 (Walker B). Importantly, the signature loop of NBD2 (Leu463-Glu467), which occludes ATP in the catalytically active closed state, is moved by 3.5 Å away from NBD1. In conclusion, our data suggest that—in contrast to the nucleotide-occluded state observed *in vitro*—in native SSU-ABCE1 complexes, ATP hydrolysis in NBSI has already occurred, whereas NBSII is still inhibited.

As an additional difference to previous structures, we observed a rod-like extra density (ED) after low-pass filtering in all native 43S PIC structures, protruding from h17 of the 40S body via the HLH motif into the cleft between NBD1 and NBD2 of ABCE1 (Fig 3F). However, local resolution in both human and yeast samples was too low to identify this factor. To stabilize this assembly, we generated a chemically crosslinked yeast initiation complex sample derived from a strain harboring TAP-tagged eIF3c (Nip1) and performed a cryo-EM analysis focused on the ABCE1 and the adjacent eIF3j (Appendix Figs S1B and S4). Indeed, in this reconstruction, we clearly observed an extra density protruding from eIF3j into the composite NBSs of ABCE1. At a resolution of 3.0 Å, we built the model for yeast eIF3j (Fig 3G and 4, Appendix Fig S4) based on the human eIF3j dimer (unpublished; PDB 3BPJ; lacking 137 residues at the N-terminus and 28 residues at the C-terminus). In brief, this dimer folds into a stable entangled 6-helix bundle that is arranged such that the N-termini are in close vicinity. Yet, the C-termini face into opposite directions, whereby the C-terminal tail of one protomer reaches into the mRNA entry channel (see below). On this basis, we could assign the extra density in ABCE1 as a part of the eIF3j N-terminus. This assignment was further confirmed by protein crosslinking coupled with mass spectrometry (XL-MS) using a lysine-specific BS2G crosslinker (Appendix Fig S5, Appendix Table S3). Two crosslinks between the Lys118 of eIF3j with Lys121 and Lys181 of ABCE1, both located near the ATP-binding site of NBD1, were identified (Fig 3G). In this position, the eIF3j N-terminus may easily modulate the ATPase activity of ABCE1 by restricting further movements of the HLH or the two NBDs with respect to each other. Interestingly, the position of the eIF3j-NTD on ABCE1 is similar to the one observed in a recent structure of archaeal ABCE1 co-crystallized with an 18-mer fragment from the C-terminus of the archaeal 50S stalk protein aP1 (Imai *et al*, 2018). This suggests that ABCE1 possesses a multivalent interaction patch in this region, which would allow for regulation of its ATPase activity. The observed stabilization of ABCE1 in the half-open conformation with one ADP still bound in NBS1 may indicate an inhibition of ADP release, which would explain its rather stable association with the 40S subunit.

Conformation of eIF3j in human and yeast 40S-initiation complexes

As described above, we found yeast and human 43S PIC sub-populations concomitantly bound to ABCE1 and eIF3j. The eIF3j subunit was positioned on the intersubunit side, roughly resembling the

location previously described in low-resolution maps (Aylett *et al*, 2015) (Fig 4). The main difference between the maps was the absence (human) or presence (yeast) of eIF1A. However, apart from a small rotation around the neck (approx. 3°), we did not observe significant conformational changes in the 40S when comparing the two structures.

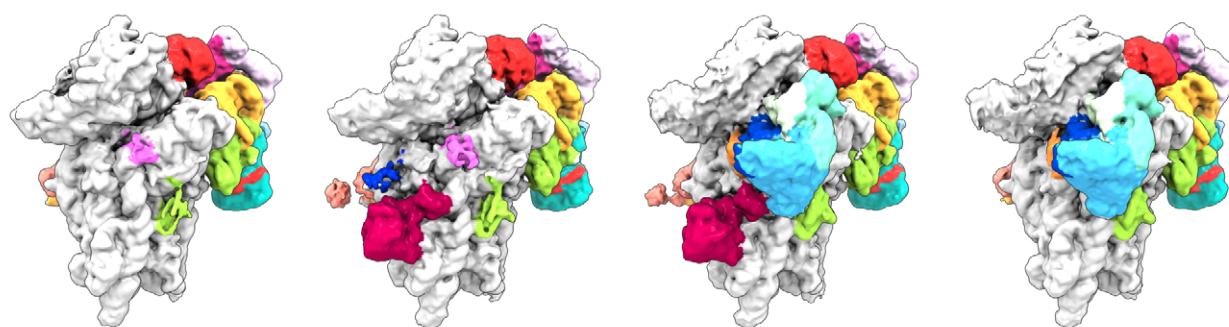
In the low-pass-filtered human State II, which lacks eIF1A, we identified the eIF3j 6-helix bundle located above the ABCE1 ATPase body and in close vicinity to NBD1 (Fig 4A and B), but no direct contacts were formed with ABCE1. On the 40S, eIF3j contacted the N-terminal tail of eS30 (protomer 1) and the C-terminus of uS12 (protomer 2). The C-terminal helix of protomer 2 further projects toward the three-way junction formed by h32, h33, and h34 at the 40S head, whereas in protomer 1 it points toward h17 and the HLH of ABCE1 (Figs 4B and EV3E). In this position, the N-termini of eIF3j are located above the ABCE1 ATPase body close to the NBD1-NBD2 cleft.

In the yeast 43S PIC, in which eIF1A was present, we found eIF3j in a similar position, but different conformation compared to the human structure (Fig 4C and D). Here, the 6-helix bundle is stably anchored between the 40S beak at rRNA h33 on one side and the 40S body near the ABCE1 FeSD and eIF1A on the other side. The two sides of the anchor are formed again by the C-terminal helices of eIF3j: protomer 2 contacts eS30 at a similar site as in the human structure but now the entire helix bundle was rotated by approximately 100 degrees (Fig EV3B, C, and D). Consequently, the tip of the protomer 2 C-terminal helix now pointed toward the 40S head, whereas the C-terminal helix of protomer 1 projected toward the ABCE1-FeSD, thereby passing along eIF1A (Figs 4D and EV3F). Molecular details of the eIF3j-40S interaction were derived from the high-resolution structure of the crosslinked 43S-PIC (Fig 4E). In brief, the 6-helix bundle accommodates between the 40S body and head *via* interactions of both protomers. The body is contacted by the first and third helix of protomer 2 (to the h17-h18 junction and eS30) mainly by basic residues. The third helix projects toward the beak to contact the phosphate backbone of h33 (G1264). Following this helix, the ultimate eIF3j C-terminus forms a loop inside a pocket formed by h33, h34, and eS10 and from there runs along h18 and uS3, parallel to the latch, to position the ultimate C-terminal tail inside the mRNA entry channel (Figs 4F, EV3G, and H; for a detailed description of molecular contacts see Appendix Text 1). In this position, eIF3j directly overlaps with the mRNA path and would possibly interfere with mRNA loading during 48S-IC formation (Fig 4G).

Taken together, our structural data explain how eIF3j could exert its functions during key steps of translation initiation in conjunction with eIF1A.

Molecular architecture of the PCI-MPN core and its interactions with 40S

State I of the human sample represented a stable class with mainly eIF3 and weak density for eIF1 bound to the 40S SSU. This appears plausible when considering that eIF3 activity during termination and ribosome recycling has been proposed (Beznoskova *et al*, 2013; Pisarev *et al*, 2007; Valasek *et al*, 2017), which further indicates that eIF3 can already bind the 40S before eIF1A comes into play. The lack of ABCE1 in this complex may be a result of fast dissociation after splitting or of an alternative splitting mechanism. In any case,

A *H.s.* 43S PIC

43S state I
closed latch
40S, eIF1, eIF3, RRM

43S state II
closed latch
40S, ABCE1, eIF1, eIF3, eIF3j, RRM

43 state III
open latch, P_{OUT}
40S, ABCE1, eIF1A, eIF1,
eIF3, RRM, TC

43S state IV
open latch, P_{OUT}
40S, eIF1A, eIF1, eIF3, RRM, TC

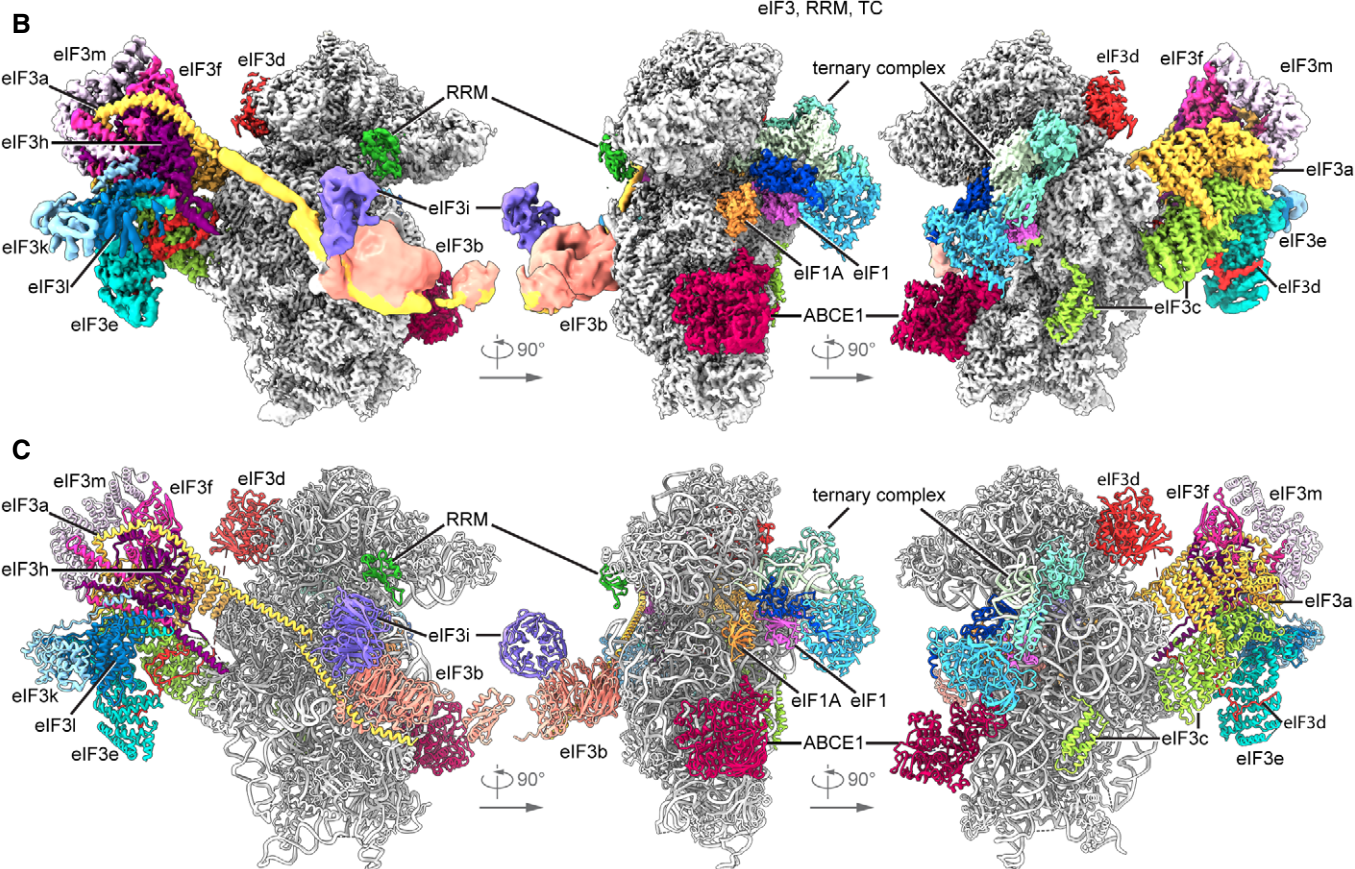


Figure 2. Cryo-EM structures of human 43S PICs in different assembly states.

A Overview of four selected compositional states present in the human 43S PIC data set.

B Composite map of the complete human 43S PIC after focused and multi-body refinements on individual sub-complexes, filtered at local resolution.

C Composite model of the complete human 43S PIC, as represented by state III.

after accommodation of eIF1 and eIF1A, the eIF2 TC binds to the 43S to induce the P_{OUT} conformation (State III-IV). Here, the improved resolution allowed us to describe the interaction network of these factors at unprecedented molecular detail.

The PCI-MPN core is located at the backside of the 40S as observed before (des Georges *et al.*, 2015; Hashem *et al.*, 2013; Srivastava *et al.*, 1992), and high resolution of the core was obtained

by multi-body refinement of State I and State II particles. The structure assembles into β -sheets with the shape of an arc formed by PCI domains of eIF3 subunits a, c, e, i, k, and m. The arc wraps around a seven-helix bundle formed by the C-terminal helices of subunits c, e, f, h, k, and l (Figs 5A and EV4A), resulting in the typical five-lobed structure (left and right arm, left and right leg and head), which was visualized at a local resolution of 3.4 Å (left arm, head

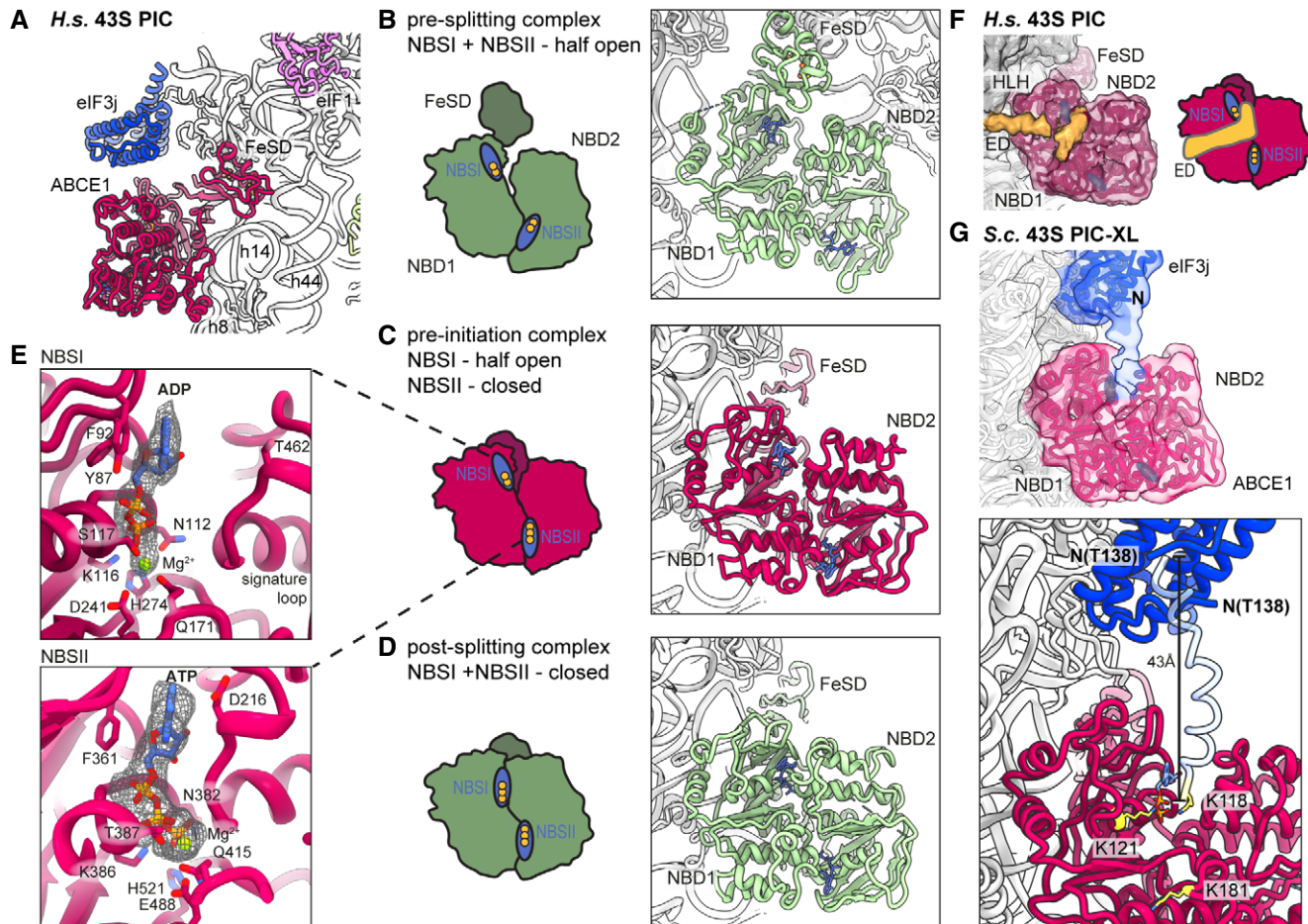


Figure 3. Conformation of ABCE1 in native 40S initiation complexes.

- A Overall position of ABCE1 in 40S initiation complexes, here representatively shown for the human State II with eIF3j.
- B–D Schematic representation and structure of semi-open ABCE1 as in 80S-pre-splitting complexes (Brown *et al*, 2015, PDB 3JAH) (B), hybrid semi-open/closed ABCE1 as in native 40S initiation complexes (C) and fully closed ABCE1 as in *in vitro* reconstituted post-splitting complexes (Nürenberg-Goloub *et al*, 2020, PDB 6TMF) (D). Nucleotide-binding sites colored in blue and bound nucleotide indicated with yellow circles (one circle per phosphate group).
- E Zoom into NBSI and NBSII showing bound Mg^{2+} -ADP (in NBSI) and Mg^{2+} -ATP (in NBSII) fit in density as obtained after focused classification on ABCE1 and refinement.
- F View focusing on the NBDs and the unassigned extra density (ED) reaching from the 40S *via* the HLH into NBSI. The ABCE1 map was low-pass filtered at 6 Å. Schematic representation highlighting the position of the ED with respect to the NBSs.
- G Upper panel: Position of eIF3j and ABCE1 in the crosslinked yeast 43S-PIC (43S-PIC-XL) sample. View focusing on the ABCE1-eIF3j interaction (same view as (F)): An extra density attributing to the eIF3j N-terminal region is connecting the eIF3j 6-helix bundle with NBSI of ABCE1. The map was low-pass filtered at 8 Å. Lower panel: N-terminally extended model of eIF3j (transparent blue) highlighting the position of K118, which was found crosslinked to K121 and K181 of ABCE1 (atoms colored in yellow).

and right arm) and 3.8 Å (left and right leg) (Fig EV2C). This allowed for an almost complete molecular interpretation (Fig EV4A, Appendix Table S4), thus refining previous low-resolution models (des Georges *et al*, 2015; Eliseev *et al*, 2018; Erzberger *et al*, 2014), for example, by correcting the register of helices and extending molecular models (Appendix Fig S6).

The main anchor of the eIF3 PCI-MPN core to the 40S is provided by the eIF3a and eIF3c subunits, which form the “head” and the “right arm” of the PCI-MPN core, respectively. eIF3a contacts eS1 *via* its N-terminal PCI helix H1 and the loop between H1 and H2. Here, Arg14 forms salt bridges to Glu78 and Asp77 of eS1 (Fig 5B and C, see Appendix Table S4 for an inventory of observed molecular

interactions). A second contact site was established between Glu17, Phe18, and Val21 of eIF3a and the eS1 Pro190 as well as adjacent residues. The loop H1-H2 of eIF3c (residues 340–345) interacts with rRNA h22 (G929, C930) and multiple sites at the Zn-knuckle domain of eS27 (Figs 5C and EV4B). Furthermore, the β -sheet insert between PCI helices 4 and 5 (residues 417–441) of eIF3c forms interactions with uS15, and basic residues in the PCI loops of both eIF3a and eIF3c are positioned to interact with the flexible tip of rRNA ES7 (Fig 5B).

An additional anchor of the eIF3 PCI-MPN to the 40S is provided by the N-terminus of eIF3d (from A2 to D84) (Figs 5C and D, and EV4C). Interestingly, we found that it meanders along the PCI helices 1 to 3, 7, 9, 10, and 12 of eIF3e (left arm) and bridges eIF3e with

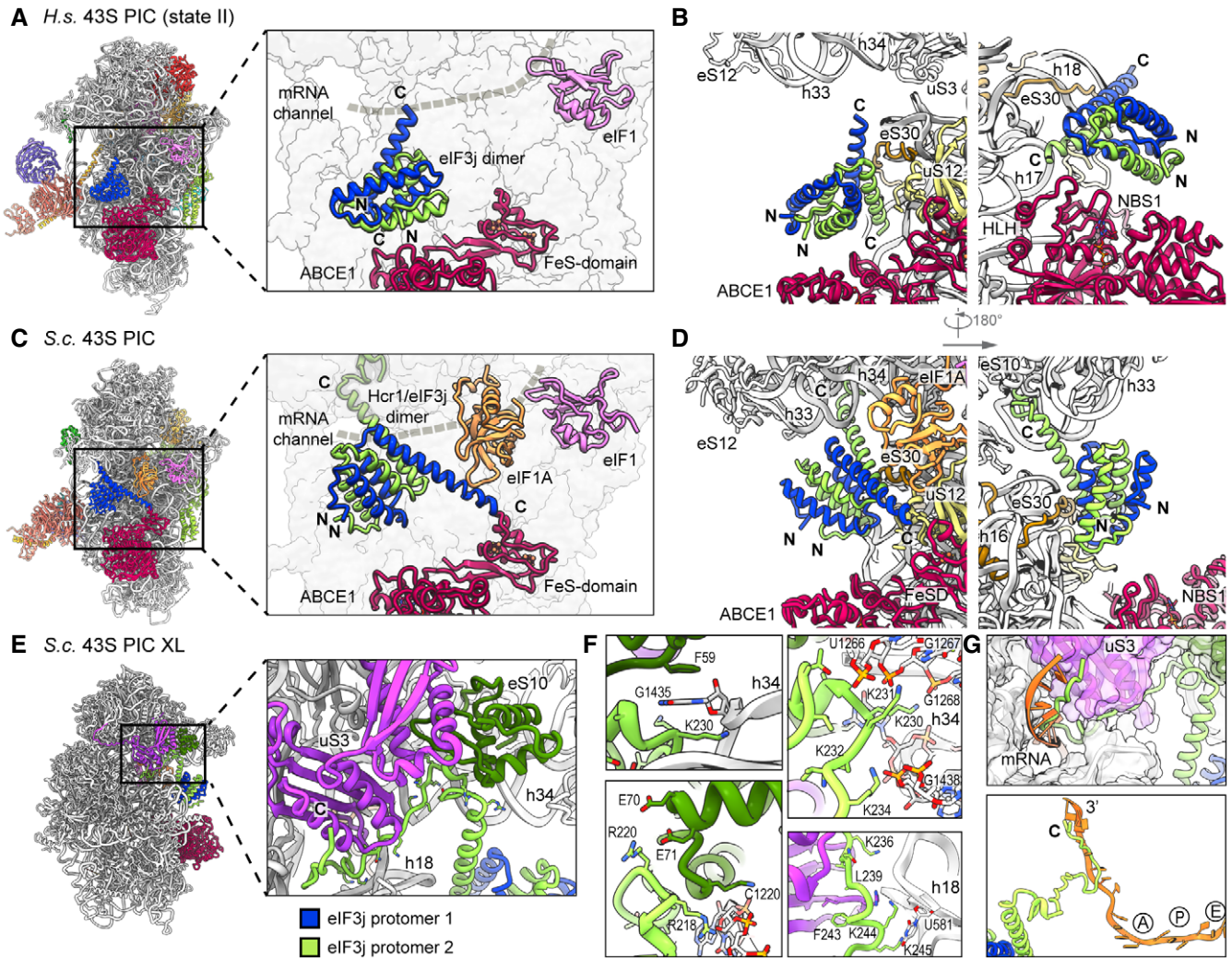


Figure 4. Two conformations of eIF3j in human and yeast 43S PICs.

- A** Overview and zoomed view on the model of human 43S PIC II (lacking eIF1A), focusing on the two protomers of the dimeric eIF3j 6-helix bundle in the ISS. eIF3j is in close vicinity to NBD1 of ABCE1 but only forms contacts to the 40S. The mRNA channel is indicated by a dashed gray line.
- B** Two different views showing the interaction of the two *Homo sapiens* (*H.s.*) eIF3j protomers with the 40S.
- C** Same views as in (A) on the model of the yeast 43S PIC. Here, eIF3j (Hcr1) is turned approximately 100 degrees around a pivot formed by the C-terminal helices contacting eS30 and uS12. Protomer 1 thereby contacts eIF1A and the FeSD of ABCE1 and protomer 2 contacts h33.
- D** Two different views showing the interaction of the two *S.c.* eIF3j protomers with the 40S and ABCE1.
- E** Overview and zoomed view highlighting the position of the eIF3j C-terminus in the yeast 43S-PIC-XL structure.
- F** Zoomed views focusing on interactions of the eIF3j C-terminus with the 40S. The loop following the third helix of eIF3j protomer 2 is in a pocket formed by the 40S h33, h34, and eS10. Lys230 of eIF3j C-terminus (protomer 2) and Phe59 of eS10 are sandwiching the flipped-out G1435 base of h34 (upper left); Lys231 and Lys234 interact with h33 (U1266 and G1267) and h34 (G1438) (upper right); salt bridges between Arg220 and Glu70-Glu71 of eS10 further stabilize the loop (lower left). Following the loop, the eIF3j C-terminus bridges the 40S body and head in the latch and contacts are formed with h18 (*via* Lys236) and *via* hydrophobic interactions with uS3 (lower right). See Appendix Text 1 for more molecular details.
- G** Position of the ultimate eIF3j C-terminus in the mRNA entry tunnel (upper panel) and steric clash with mRNA as positioned in an 80S ribosome stalled during translation (PDB 5MC6); for clarity, in the lower panel only eIF3j and mRNA are shown, A/P/E, respectively indicate the positions of aminoacyl, peptidyl, and exit site in the 80S ribosome.

eIF3c (head) by interacting with PCI helices 12, 14, and 16 (eIF3e) and PCI helix 11 (eIF3c). Another specific contact between eIF3c and eIF3e is formed by stacking of Y286 (eIF3e) to Y583 (eIF3c). Moreover, eIF3d also interacts with PCI helices 10, 13, and 14 of eIF3c by forming a large loop, which is anchored by the conserved Trp45 (interactions to Pro603, Ile607, and Glu666 of eIF3c). The interaction to

eS27 is established *via* its Zn knuckle, where Phe80 of eIF3d is sandwiched between the side chains R80 and K36 of eS27.

Taken together, the PCI-MPN core of eIF3 establishes a multi-modal molecular interaction pattern with the 40S involving the eIF3a, c, and d subunits, which display an unexpected degree of inter-connectivity.

Structure and location of the peripheral subunits

The peripheral subunits, which consist of the YLC, the eIF3c-NTD, and in humans the eIF3d cap-binding protein domain, are connected to the PCI-MPN scaffold *via* flexible linkers. While eIF3a connects *via* its CTD to the YLC module located close to the mRNA entry site, the N-terminus of eIF3c protrudes from the mRNA exit toward the ISS, where it interacts directly with eIF1. While the N-terminus of eIF3d as an integral part of the PCI-MPN core is anchored to the 40S body, the cap-binding protein domain of eIF3d is located on the 40S head close to the mRNA exit site as observed before (Eliseev *et al*, 2018). Here, it contacts the 40S SSU *via* its highly conserved helix $\alpha 10$ (Lee *et al*, 2016) that packs upon eS28 *via* Gln416, Thr423, and Lys426 and reaches into the interface between eS28 and uS7, where Gln416 stacks on Arg51 (eS28), which in turn stacks on Phe61 (uS7). The eIF3d helix $\alpha 12$ lies on top of uS7 and forms contacts *via* Lys472, Glu475, Ser478, and Gln479. Notably, since eIF3d is bridging the 40S head with the eIF3 PCI-MPN core anchored to the 40S body, it could serve to relay conformational rearrangements of the 40S head—as occurring during the assembly of 43S and 48S complexes—to the PCI-MPN core or, vice versa, allow the eIF3 complex to directly control the conformational state of the 40S head (Figs 5D and EV4C and D).

For eIF3c, only a part of its NTD could be located on the ISS of the 40S so far, where it forms a helix bundle (Llacer *et al*, 2015). We found a particularly stable arrangement of the eIF3c NTD in classes containing the eIF2 TC and, after multi-body refinement, local resolution of 3 to 4 Å (Figs EV2B, EV5A and B) allowed us to determine the register of the four eIF3c-NTD helices (Val47 to Y149) (Fig 6). A stretch preceding the first helix (47–51) contacts h24 and h27 *via* R47 to the backbone phosphate of C1039 and the 2'-OH of A1181. The peptide bond of Val49 of eIF3c stacks on base C1180, which is also contacted by the first helix (52–74) of the bundle. Here, the two charged residues K55 and R56 interact with the backbone of rRNA G1179 and C1180. Backbone-phosphate interactions were also formed by the second helix (76–92) to rRNA h11 (A364) and h27 (U1178), by the fourth helix (136–143) to rRNA h11 *via* K136 (to U367), and finally by the peptide bond of Thr140 stacking upon the U367 base, as well as Gln143 hydrogen bonding to U367. Additional but less rigid contacts were established by the K-rich loop between helix 3 and helix 4 of eIF3c (Figs 6E and F, and EV5A and B, Appendix Table S4).

Notably, when low-pass filtered, a rod-like extra density for the eIF3c N-terminus became apparent, bridging the 4-helix bundle with eIF1 near rRNA h23 and h24. This density was neither present in our nor in other (Llacer *et al*, 2015) yeast 43S/48S reconstructions, where the four-helix bundle was directly connected to the eIF3c core moiety, and a site N-terminal of this region interacted with eIF1 (Fig 6A and B). Sequence alignments of the yeast and human eIF3c N-termini revealed an insertion on the C-terminal side of the conserved four-helix bundle in humans (Figs 6C and D, EV5C). This insertion from residue 165 to 213 displays 32.0% sequence identity and 56.0% sequence similarity with a stretch at the N-terminus of yeast (42–92), which was previously shown to be involved in the interaction of eIF3c with eIF1 by NMR studies (Obayashi *et al*, 2017). Here, chemical shift perturbation after eIF1 binding is observed for Glu51, Ala67, and a stretch between Lys68 and Lys77. Moreover, in our human complex one stretch of well-resolved

density for the eIF3c-NTD was present at the eIF1 loop between helix $\alpha 1$ and helix $\alpha 2$ (Asp53–Lys58) as well as Ile100 and Gly101 of $\alpha 2$ (Fig EV5D). This observation is highly consistent with the NMR study, in which the same interacting region on eIF1 is identified for the eIF3c-NTD of yeast. Together, these observations lead us to the conclusion that the density observed near eIF1 in the human structure corresponds to this insertion C-terminal of the helix bundle, fulfilling an analogous role to the previously characterized N-terminal stretch of eIF3c in yeast.

From local classification, we also obtained one class with strong density for the YLC module including the eIF3a-linker that connects it to the PCI-MPN core (Appendix Fig S7). In brief, the YLC module contains two β -propellers: the 7-bladed WD40 repeat of eIF3i and the 9-bladed WD40 repeat near the C-terminus of eIF3b. The two propellers are held together by the C-terminal helical domain of eIF3b, which is formed by 3 α -helices: the most C-terminal one binds to eIF3i, while the two preceding α -helices are bracketing the eIF3a C-terminus against the eIF3b β -propeller (des Georges *et al*, 2015; Herrmannova *et al*, 2012). N-terminal of its β -propeller, eIF3b contains a noncanonical RNA recognition motif (RRM) (Elantak *et al*, 2007) that can form further interactions with the eIF3a-CTD (Dong *et al*, 2013; Khoshnevis *et al*, 2014; Valasek *et al*, 2002; Valasek *et al*, 2001) as well as the N-terminus of eIF3j (Elantak *et al*, 2010; Valasek *et al*, 2001).

For the CTD of eIF3a, we could build a long α -helix (residues 602–743) into the elongated rod-like density protruding from the PCI-MPN core to contact uS2 and eS21 (Appendix Fig S7A). This helix extends further toward the YLC where it forms a hinge-like structure and then connects to the stretch of the eIF3a helix that is bound to the eIF3b β -propeller. It thereby contacts the tip of the otherwise flexible rRNA expansion segment ES6C, which in turn contacts the loop between the first two helices of the eIF3b helical domain. In this arrangement, the eIF3b WD40 is rigidly confined between rRNA h16 and uS4 on one side, and ES6C on the other side, and is thus well resolved in the proximity of the 40S (Appendix Fig S7B, Appendix Table S4). The eIF3i-eIF3g complex and the eIF3b-RRM, however, remained rather flexible as observed before (Erzberger *et al*, 2014). Nonetheless, we observed a stabilization of the eIF3b-RRM in ABCE1- and eIF3j-containing classes, possibly due to an interaction of the eIF3b-RRM with the eIF3j N-terminus (Elantak *et al*, 2010; Valasek *et al*, 2001).

In yeast, the positioning of the YLC module at the mRNA exit was the same, because here it was also held in place by ES6C (Appendix Fig S7C). However, in the majority of particles in the yeast dataset (approximately 85%), we could observe a conformational change in the eIF3i-eIF3g module relative to the ES6 anchor point. Especially in the eIF3j-containing 43S class, the eIF3i-eIF3g entity rotates by approximately 120 degrees away from the mRNA entry toward ES6C and ES6B. The loop preceding the eIF3i-contacting helix of eIF3b (Thr697–Asp701) appears to serve as a hinge for this rotation (Appendix Fig S7D).

Apart from the YLC, we observed an additional density near the mRNA entry at the tip of h16 in all of our 43S structures, which was previously assigned to the RRM of eIF4B (Eliseev *et al*, 2018) (Appendix Fig S8). This density is especially prominent in subclasses of the human dataset lacking the TC, in which we could unambiguously identify the typical RRM fold at a local resolution around 4 Å (Appendix Figs S8C and D). Notably, besides eIF4B, the

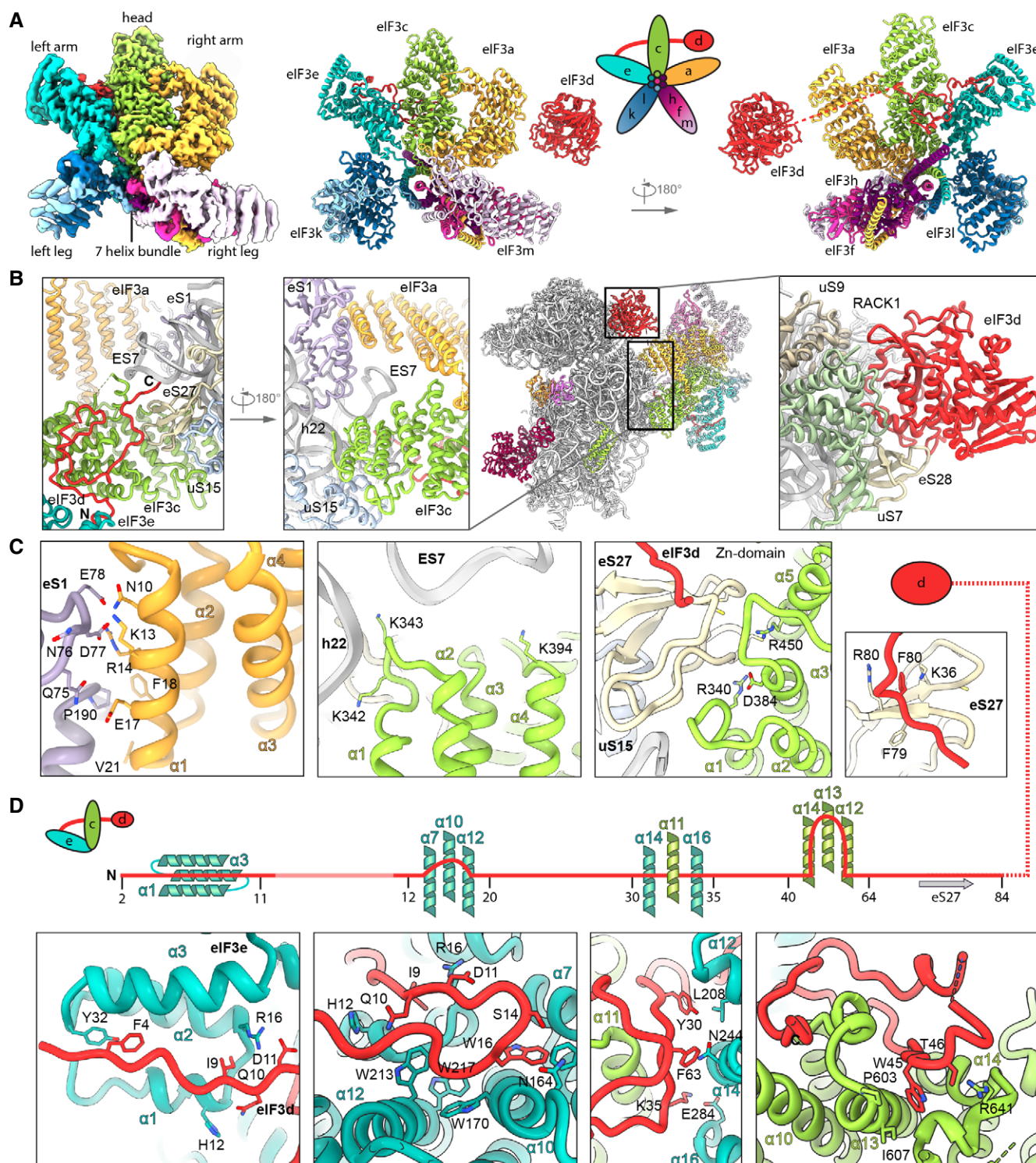


Figure 5. Molecular interactions of the human PCI-MPN core of eIF3 in the 43S PIC.

- A** Isolated map and molecular model of the eIF3 PCI-MPN core color coded as in Fig 2. Structural hallmarks are indicated, and a scheme shows the composition of the lobes.
- B, C** Interactions of eIF3a, eIF3c, and eIF3d with the ribosome: (B) shows an overview of the structure and zoomed views highlighting the interactions of eIF3a, eIF3c, the eIF3d N-terminal tail and the eIF3d cap-binding domain with the 40S, (C) shows molecular details of eIF3a interacting with eS1; eIF3c interacting with rRNA h22 and eIF3c and the N-terminal tail of eIF3d with the Zn-knuckle domain of eS27.
- D** Interactions of the eIF3d N-terminal tail with the PCI-MPN core.

largely flexible eIF3g subunit is a potential candidate for this density because it also contains an RRM, which shares very high structural and sequence similarity (50.0%) to eIF4B (Appendix Fig S8D and E), and it was crosslinked to the nearby proteins uS10 and uS3 (Cuchalova *et al*, 2010). Unfortunately, at the current resolution we cannot unambiguously distinguish these two RRM in our maps and it is possible that both compete for the same binding site. Next to this domain, we observed density reaching from the RRM into the mRNA channel in all human early 43S PIC structures with a closed latch (Appendix Fig S8A and B). Close to the RRM, this density forms a loop that shows multiple contacts to uS3 before winding along uS3 toward the mRNA channel. Within the channel, one side chain can clearly be identified as a tryptophan facing toward uS3 (contacting Lys148 and Met150) and further interacting with uS3 Leu142 and Val115. The stretch also contacts 18S rRNA G626, A628, and U630 of h18 as well as C1698 of h28, C1331, and A1489 of h34 (all in the A site). Thereby, this peptide stretch blocks the entire mRNA channel down to the P site where it contacts the flipped-out base C1701 at the tip of h44. Unfortunately, local resolution in this region is insufficient to provide further molecular detail and clearly identify this entity, yet considerable candidates may be

further missing parts of eIF3g, eIF4B, the C-terminus of eIF3j as observed in yeast maps, the CTD of eIF3a, or the ribosome hibernation factor SERBP1 (Stm1 in yeast) (Anger *et al*, 2013; Ben-Shem *et al*, 2011; Brown *et al*, 2018). In any case, it is apparent that accommodation of mRNA in the 48S IC complex would require its relocation, which may allow for allosteric communication between the different eIFs.

Conformation of the ternary complex

After analyzing the eIF3 complex, we also gained molecular information on the human eIF2 TC by focused classification. The TC as well as eIF1 and eIF1A were observed on the intersubunit side in a similar overall position and conformation as described before for other ICs in P_{OUT} conformation at low resolution (PDB 6GSM, PDB 3J4Q (Llacer *et al*, 2015)) (Appendix Fig S2). Briefly, eIF2 consists of three subunits, α , β , and γ . The eIF2 γ subunit shares structural homology to EF-Tu-like translational GTPases (e.g., Schmitt *et al*, 2002) and consists of a G-domain (domain I), including the regulatory switch loops (swI and swII), followed by two β -barrel domains. eIF2 α consists of an N-terminal OB-fold domain, a central helical

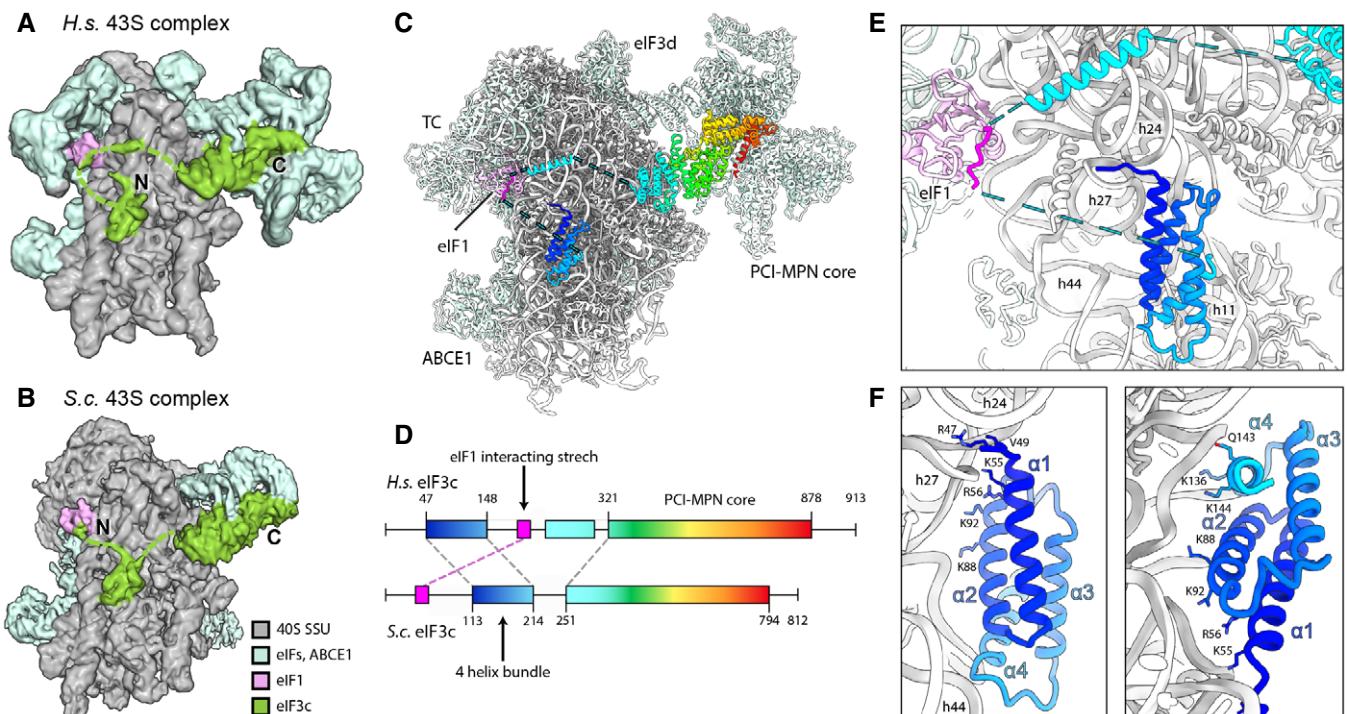


Figure 6. Arrangement of the eIF3c-NTD in human and yeast 43S PICs.

- A Cryo-EM map obtained after focused sorting of the human 43S PIC on the TC: when low-pass filtered at 6 Å, it shows the density of almost complete eIF3c-NTD in the ISS.
- B Cryo-EM map of the yeast 43S PIC low-pass filtered at 6 Å.
- C Model for human eIF3c in the TC-containing 43S colored in rainbow (C) and scheme of the alignment between human and yeast eIF3c sequences, colored accordingly (D). The eIF1-interacting stretch present in the N-terminus of *S.c.* eIF3c shows 32.0/56.0% sequence identity/similarity with an insert C-terminal of the conserved 4-helix bundle conserved in mammals.
- D Zoomed view highlighting the position of the eIF3c NTD and eIF1 in the 40S ISS.
- E Molecular model for the 4-helix bundle interacting with 40S rRNA and r-proteins.
- F Molecular model for the 4-helix bundle interacting with 40S rRNA and r-proteins.

domain, and a C-terminal α - β domain. The eIF2 β subunit has an unstructured N-terminal domain, followed by a central helix-turn-helix (HTH) domain and C-terminal zinc binding domain (ZBD). In solution, tRNA_i was shown to be bound to the TC in a distinct way different to canonical tRNA-bound EF-Tu/eEF1A by employing additional composite interactions with both eIF2 α and eIF2 γ (Schmitt *et al*, 2012). The eIF2 β subunit, however, has never been sufficiently resolved to elucidate its molecular contribution to tRNA_i binding and 43S PIC formation.

In our structure, we found the tRNA_i embraced by all three eIF2 subunits (Fig 7A and B). Similar to the 5 Å resolution crystal structure (3V11 Schmitt *et al*, 2012), the methionylated CCA-end is sandwiched between the GTPase domain and domain II of eIF2 γ . The terminal adenine base A76 is accommodated in a pocket formed by the β -sheets of the eIF2 γ domain II including Val278, Phe322, Gly340, and Arg260 (Fig 7C, Appendix Fig S9C). The 2'-OH group of the ribose moiety interacts with the carbonyl group of Ala323 and the methionyl side chain stacks on Tyr83 of eIF2 γ G-domain. The CCA-end is further stabilized by contacts including a cation- π stack of Lys266 on tRNA_i C75 and Asn71 of the eIF2 γ swI loop with tRNA_i C74. Moreover, Arg296 of the eIF2 β ZBD intercalates into the major groove of the acceptor-stem helix (G70; supported by Lys293 contacting the phosphate backbone of U69) (Fig 7D, Appendix Fig S9C). eIF2 α contacts the T- and D-loops mainly *via* its central helical domain whereas the N-terminal OB-fold domain intercalates between anticodon stem and uS7 in the E site on the head of the 40S. The central eIF2 β HTH domain contacts the anticodon from the A site and thereby forms multiple contacts to eIF1, also involving residues of the newly built C-terminus (I314-R329), which stretches below the tRNA_i anticodon stem toward the E site and contacts C1057 of rRNA h24 (*via* N327).

Notably, in the GTP binding pocket of eIF2 γ we clearly identified a Mg²⁺-GTP (Fig 7D). Ser55 of the conserved P-loop and Thr78 of swI coordinate the Mg²⁺-ion, whereas Asp134 and Pro135 of swII likely contact the γ -phosphate. Compared to the crystal structure of the archaeal TC (Schmitt *et al*, 2012), the 2012 so that this citation matches the Reference List. Please confirm that this is correct."--> e guanine base is rotated by 90° and accommodated in a pocket between Asn190 and Ala226 of eIF2 γ and Cys305 of the eIF2 β ZBD, which is tightly packed upon the nucleotide-binding pocket.

Interestingly, both switch loops were embedded in a tight interaction network involving interactions with tRNA_i, eIF2 β , and the eIF1 N-terminal tail, which we built *de novo*. The N-terminal tail of eIF1 protrudes from the 5-stranded β -sheet and binds to Arg446 of eIF2 γ domain III, where it forms a loop and projects toward Arg75 of eIF2 γ swI, forming a cation- π stack with Phe13 (Fig 7D, Appendix Fig S9C and D). Furthermore, the conformation of the swI loop was stabilized by the tRNA_i *via* Asn71 (see above) and an interaction between conserved Ser310 of the ZBD of eIF2 β with Glu74.

In close vicinity to the guanosine binding pocket, we find eIF2 β Ser307, the equivalent of yeast eIF2 β Ser264. In yeast, a Ser264Tyr mutation causes the Sui⁻ (suppressor of initiation codon) phenotype, leading to increased utilization of UUG start codons (Huang *et al*, 1997). This mutation was shown to increase GTP hydrolysis rates and stabilize the closed P_{IN} conformation of the 43S PIC (Martin-Marcos *et al*, 2014). In the observed position, the tyrosine mutation of Ser307 could easily interfere with the bound nucleotide, for example, by stacking on the guanine base, and thus alter the geometry of the nucleotide-binding pocket.

Taken together, we found the TC in a stable state within the 43S PIC, in an open conformation in the absence of mRNA. An intricate interaction framework is established by the 40S and eIF1 to accommodate the GTP-bound eIF2-tRNA_i in a rigid position. The switch loops are kept in a rigid conformation stabilized by tRNA_i, eIF2 β , and the eIF1 N-terminal tail, and the GTPase pocket of eIF2 γ is closed by eIF2 β . This may prevent premature release of the bound nucleotide and, at the same time, may restrict access for eIF5-NTD to avoid premature GAP activity.

Following TC assembly on 43S PIC and opening of the latch, mRNA can be threaded into the mRNA binding site, followed by scanning for the first AUG codon by the 48S particle. While we do not find scanning intermediates in either yeast or human datasets, in our yeast native 40S population we find one state containing eIF1A, tRNA_i in the P_{IN} state, and the eIF5-NTD instead of eIF1 (yeast 43S PIC). Apart from weaker density for eIF2, this state is similar to one observed before (Llacer *et al*, 2018), where it was interpreted as a late state after start-codon recognition. However, to our surprise we still find ABCE1 in this complex. This suggests that ABCE1 may play further roles even in later stages of initiation, or that its dissociation is not required at this stage.

Discussion

While the role of highly conserved ABCE1 during ribosome recycling has been studied in mechanistic details (Becker *et al*, 2012; Nürenberg-Goloub *et al*, 2018; Nürenberg-Goloub *et al*, 2020), its role after 60S dissociation remained largely elusive. However, when first characterized biochemically, ABCE1 was found associated with 43S/48S pre-initiation complexes in yeast, humans, and *Drosophila* (Andersen & Leivers, 2007; Chen *et al*, 2006; Dong *et al*, 2004). Since then, it is a long-standing question what the function of ABCE1 in these complexes is. Our extensive single particle analysis of native small subunits from yeast and human cells captured a variety of states throughout the assembly of the 43S PIC prior to mRNA loading, in which ABCE1 can stay associated with the 40S. Surprisingly, in yeast we even find ABCE1-48S complexes beyond the stage of mRNA engagement and start-codon recognition as indicated by the presence of the eIF5-NTD (Fig 8).

We further observe that in all ABCE1-containing 43S structures its NBDs are in an unusual hybrid conformation, where NBS2 is closed and NBS1 is semi-open. This is contrary to previous *in vitro* studies showing SSU-associated ABCE1 in the ATP-occluded fully closed state. Notably, the two NBSs in ABCE1 were shown to be highly asymmetric and NBSII has a low ATP-turnover rate compared to NBSI (Gouridis *et al*, 2019; Nürenberg-Goloub *et al*, 2018). Consistent with this behavior, we find Mg²⁺-ATP still bound in the closed NBSII, whereas Mg²⁺-ADP is present in NBSI. This is in agreement with the most recent model for the ABCE1 ATPase cycle, in which closure of the NBSII was discussed to be the decisive step for disassembly of 80S pre-splitting complexes, a process that is then triggered by subsequent closure and ATP hydrolysis in NBSI. Subsequently, re-opening of NBSI would be expected on the small subunit. But if ATP hydrolysis is prevented either by usage of a non-hydrolyzable ATP analog or by hydrolysis-deficient Walker B mutants, ABCE1 can be trapped in the fully closed state on the small subunit under facilitated splitting conditions (Heuer *et al*, 2017;

Kiosze-Becker *et al*, 2016; Nürenberg-Goloub *et al*, 2020). In native ABCE1-associated complexes, however, NBSI is already in a more open conformation and additionally obstructed by a part of the eIF3j N-terminal domain, which intercalates between the two NBDs close to NBSI. Thus, eIF3j may keep NBSI from closing (after putative binding of another ATP), or alternatively, prevents further opening into a state as observed in free ABCE1. This brings up the question of why ATP hydrolysis in NBSII, which would lead to dissociation from the 40S SSU, is inhibited. We find NBSII in a very similar conformation as in the fully closed archaeal structure (Nürenberg-Goloub *et al*, 2020), and the structure reveals no clues to explain why ATP hydrolysis is slowed down. Thus, we speculate that a further and likely only small-scale allosteric signal into NBSII may be necessary for its activation. This may occur after dissociation of the eIF3j N-terminus upon further opening of NBSI and be accompanied by changes in the ABCE1-specific HLH and hinge regions.

The observation that ABCE1 dissociation can apparently be actively prevented points toward a direct role in 43S PIC and even 48S IC assembly, most likely in concert with eIF3j. We could corroborate the finding that eIF3j assists in ABCE1-dependent splitting by *in vitro* dissociation assays, and furthermore, we established that eIF3j remains bound to the 40S together with ABCE1 after the splitting cycle. A high-resolution structure of a crosslinked yeast 43S-PIC revealed that dimeric eIF3j is highly stabilized in the presence of ABCE1, positioning the ultimate C-terminus of one protomer in the

mRNA channel near the entry site. This position explains, how eIF3j could exert its roles as an antagonist of mRNA binding, for example by recycling of mRNA from the 40S subunit (Pisarev *et al*, 2007; Pisarev *et al*, 2010), or during initiation by preventing premature mRNA recruitment (Fraser *et al*, 2007). Notably, its position close to eIF1A and thus near the A site may also explain its suggested role in regulating start-site selection (Elantak *et al*, 2010). Moreover, the comparison of yeast with the human structures of early 43S PICs suggests that eIF3j and ABCE1 may be beneficial for binding of eIF1A. In the yeast conformation, eIF3j appears like a molecular ruler reading out the exact distance between the post-splitting-specific FeSD conformation of ABCE1 and the 40S head and beak conformation as adopted after eIF1A binding. Thus, it is tempting to speculate that the observed conformational change in eIF3j may play a role in priming the 40S for eIF1A binding and/or stabilizing the early closed-latch conformation of the 43S PIC when eIF1A is bound. Notably, eIF1A is the only factor that was not found to be pre-assembled in a 40S-free multi-factor complex (MFC) consisting of eIF1, eIF2-tRNA_i-GTP, eIF3, and eIF5 in yeast (Asano *et al*, 2000; Zeman *et al*, 2019), plants, and mammals (Sokabe *et al*, 2012). While eIF1A is capable of binding 40S SSU independently and adopting a similar conformation as within the context of initiation (Yu *et al*, 2009), it is possible that after binding of the MFC eIF3j binding between the 40S head and body in concert with rigidifying the latch structure may be constructive for its productive integration into the 43S complex.

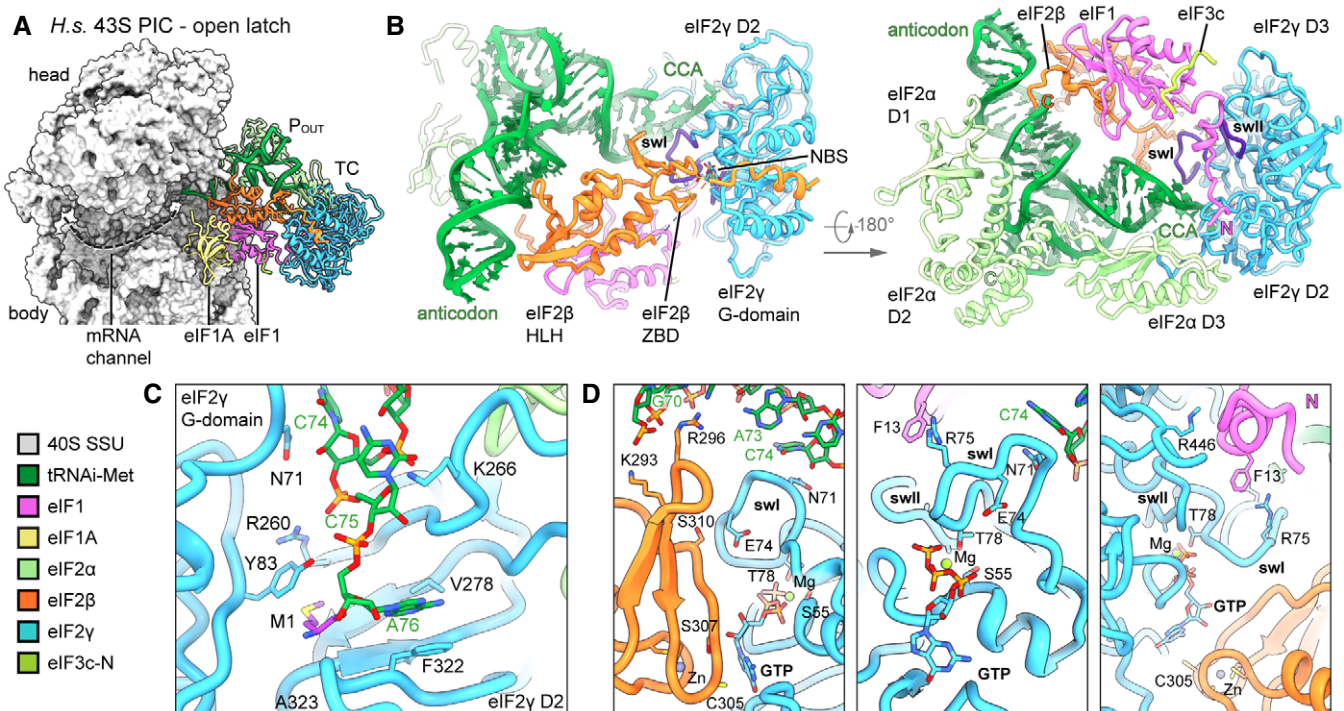


Figure 7. Conformation of the TC in the complete human 43S PIC.

A Overview highlighting the positions of TC, eIF1, and eIF1A in the complete human 43S PIC.

B Interactions of eIF2 subunits and domains and eIF1 with methionylated tRNA_i; switch loops (sw) of eIF2y are labeled and colored in purple; nucleotide-binding site (NBS) with Mg-GTP bound; the *de novo* built N-terminal tail of eIF1; and the C-terminus of eIF2α and eIF2β are labeled with N and C, respectively.

C Molecular interactions of the methionylated CCA-end of tRNA_i and eIF2y.

D Molecular interactions within the nucleotide-binding pocket and conformation of sw loops stabilized by the eIF1 N-terminal tail, the eIF2β ZBD, and tRNA_i.

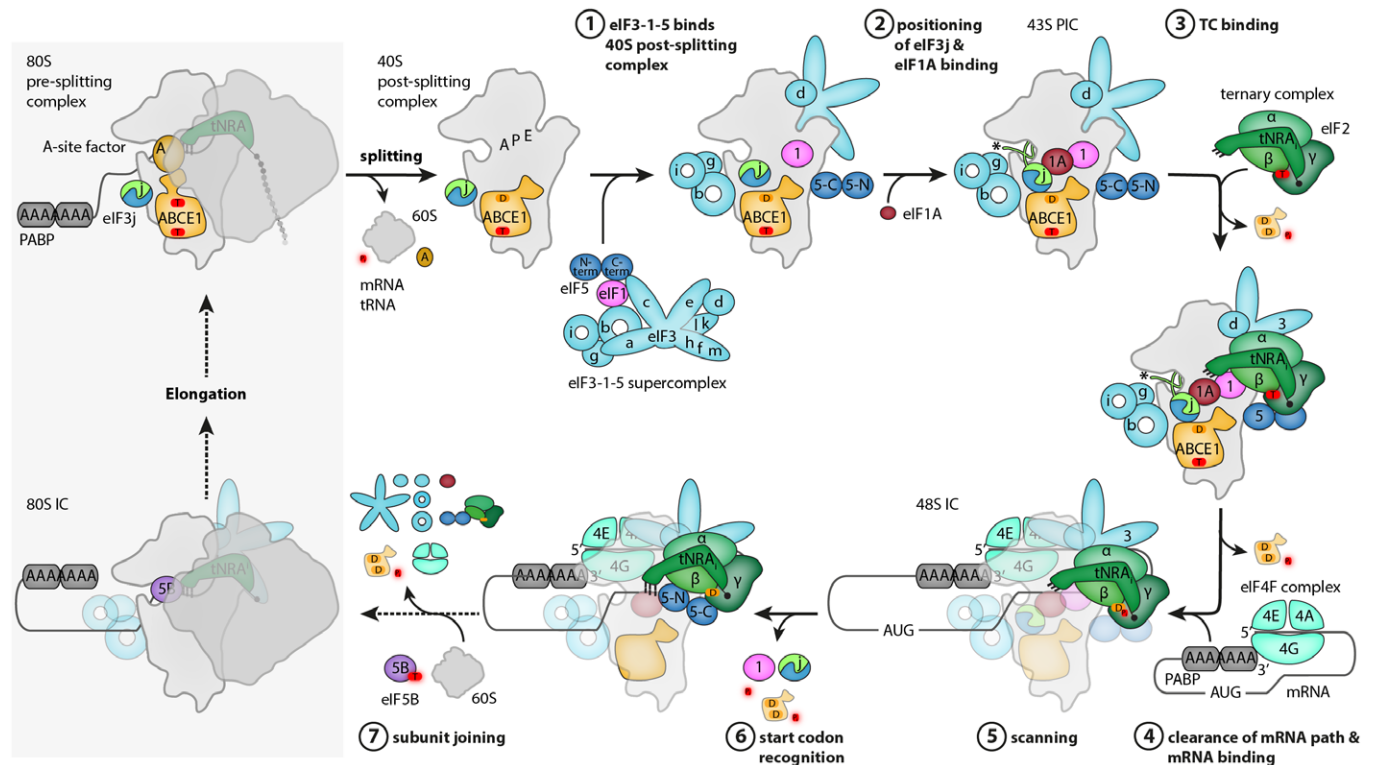


Figure 8. Role of ABCE1 in eukaryotic translation initiation.

Schematic representation of eukaryotic translation initiation. ABCE1 is shown in orange, nucleotide states are symbolized with "T" for ATP bound and "D" for ADP bound; the two protomers of eIF3j are shown in blue and green, the eIF3j C-terminus of protomer 2 in mRNA entry channel is marked with an asterisk. For details, see main text (discussion).

Concluding our cryo-EM analysis of native initiation complexes, we can deduce a putative order of events during 43S PIC and 48S IC assembly by formation of several structural hallmarks (Fig 8). 80S ribosomes are recycled by ABCE1 after canonical or noncanonical termination. eIF3j may assist the recycling by actively aiding ABCE1 during splitting or by destabilizing mRNA while inserting with its C-terminus into the mRNA channel. As a first step during initiation, the MFC binds to the recycled 40S as indicated by the highly populated eIF3-eIF1 bound classes. While the PCI-MPN core is stably anchored at the solvent side of the 40S, the eIF3c-NTD locates into the ISS via the 4-helix bundle, positioning eIF1 in the process. The YLC module is guided to the mRNA entry by stable positioning of the eIF3b β -propeller between h16 and of rRNA expansion segment ES6c. Here, the eIF3i-eIF3g complex can adopt variable positions that may be important for the role of eIF3g-eIF3i during scanning (Cuchalova *et al*, 2010). Concomitantly, the RRM of either eIF3g or eIF4B accommodates on the mRNA entry, and in the human 43S complexes, the mRNA entry channel is blocked by a yet unidentified density. After eIF1A accommodation, the TC can be stably integrated to form the complete mRNA-free P_{OUT} state 43S. This opens up the latch and leads to clearance of the mRNA path, since in P_{OUT} complexes no density in the mRNA path is visible.

With respect to a fully accommodated TC, our structure reveals for the first time a network of interactions between the tRNA_i and all subunits of eIF2 as well as eIF1 at molecular

resolution. The eIF2 γ switch loops are highly confined, and the GTPase pocket is closed by the ZBD of eIF2 β , thus restricting the access for the eIF5-NTD to exert its GAP activity. Notably, GTP hydrolysis in eIF2 γ may already occur during scanning. This would require that the eIF5 N-terminal tail could reach into the eIF2 γ GTPase pocket and, thus, result in a rearrangement of the eIF2 β ZBD. A structure of a scanning 48S, however, is still lacking. Yet, large structural rearrangements have been observed after start-codon recognition, during which the 48S IC adopts the closed P_{IN} state. Here, the entire TC rearranges, and especially, eIF2 β alters its location on the 40S head and relative to eIF1 and eIF1A. It is likely that this conformational switch could already partially occur during scanning and that this would also affect the position of the eIF2 β ZBD, which was too flexible to be resolved in all previous cryo-EM structures (Llacer *et al*, 2015; Llacer *et al*, 2018; Simonetti *et al*, 2016; Eliseev *et al*, 2018). After eIF5-dependent GTP hydrolysis, release of inorganic phosphate (P_i) would still be inhibited until start-codon recognition. During or after this process, the eIF5 NTD replaces the gatekeeper eIF1 and leads to a further stabilization and compaction of the P_{IN} state, which may be a prerequisite for the following step of eIF5B-mediated subunit joining (Llacer *et al*, 2018).

Our analysis shows that ABCE1 can still be associated with initiating 40S. Yet, which role might ABCE1 play during formation of the full 43S and—as observed in yeast—even in context of the eIF5-

accommodated partial 48S? Currently, ABCE1 is assumed to act as an anti-association factor, ensuring that premature 60S interaction is prevented after termination and ribosome splitting. However, in this function it would likely become redundant after the formation of the 43S PIC, failing to explain its presence in later stages of initiation. Another possibility is that its observed interplay with eIF3j as early as during the splitting reaction supports the timely recruitment of the remaining eIFs to the vacant 40S. Furthermore, we speculate that the inhibiting peptide close to NBSI would need to be ejected to facilitate ATP-hydrolysis in NBSII. Here, it is possible that dynamics of the rather flexible YLC module could play a role. In fact, this module is able to relocate into the ISS to occupy the position of ABCE1 (Llacer *et al*, 2015). With this steric competition in mind, it would be plausible that it contributes to ABCE1 dissociation, although it is not entirely clear at which stage this relocation happens. In addition, eIF3j, which is still present at least as fuzzy density in the fully assembled 43S, may also contribute in coordinating such events, for example, *via* its known interaction with eIF1A and the eIF3b-RRM (Elantak *et al*, 2010). Finally, since ABCE1 is even present on 48S IC complexes after start-codon recognition, events during subunit joining may be the final trigger for ABCE1 dissociation. In this context, the P proteins of the 60S subunit may not only play a role during ribosome splitting as suggested before (Imai *et al*, 2018), but also for ABCE1 removal after initiation. Yet to reveal exact timing of these events and the mechanistic interplay of these factors, future work will be needed.

Materials and Methods

Yeast strains

Saccharomyces cerevisiae ribosomes for biochemical assays were purified from a wild-type BY4741 strain, which was grown on YPD medium.

Samples for LC-MS/MS analyses were purified from a BY4741 (*MATa*, *ura3Δ0*, *his3Δ1*, *leu2Δ0*, *met15Δ0*), Rli1-TAP:HIS3MX6 strain (Ghaemmaghami *et al*, 2003).

For the preparation of native yeast 40S initiation complexes, a BY4741 strain containing genomic TAP-tagged SKI3 and a plasmid overexpressing SKA1 (pCM190) (Zhang *et al*, 2019) were used; the crosslinked yeast 43S pre-initiation complex was derived from a *S.c.* W303 strain (*MATa*, *ade2Δ1*, *trp1Δ1*, *can1Δ100*, *leo2Δ3,112*, *his3Δ11*, *ura3*, *GAL*) expressing genomically TAP-tagged Nip1 (eIF3c).

ABCE1-TAP polysome profile and sucrose density gradient fractionation

Yeast (*Saccharomyces cerevisiae*; *S.c.*) cells from the BY4741 strain expressing C-terminally TAP-tagged ABCE1 (Rli1) were grown in 200 ml YPD to an OD₆₀₀ of 0.8. The cells were then treated with 50 μg ml⁻¹ cycloheximide on ice for 5 min. and collected by centrifugation. The cells were lysed in lysis buffer (20 mM Tris-HCl, pH 7.4, 50 mM KCl, 10 mM MgCl₂, 50 μg ml⁻¹ cycloheximide, and EDTA-free protease inhibitors (Roche)) by vortexing them with glass beads (12 cycles of 30 sec. vortex/30 sec. on ice). The lysate was cleared by centrifugation for 10 min. at

16,000 g, 4 °C and stored at -80 °C. Ten A₂₆₀ units were loaded on a 10–50% sucrose gradient and centrifuged at 187,813 g for 2.75 h at 4 °C in a SW41Ti rotor (Beckman Coulter). The fractions of the gradient were collected, and proteins were precipitated with trichloroacetic acid and separated on a 10% acrylamide gel. The proteins were detected with antibodies after Western blotting: ABCE1-TAP with peroxidase anti-peroxidase (PAP) complex (Sigma-Aldrich) at 1:2,000, and Nog1 with a rabbit anti-Nog1 antibody at 1:5,000 dilution.

ABCE1-TAP tandem affinity purifications

Cells expressing C-terminally TAP-tagged ABCE1 (Rli1) were cultivated in rich medium (YPD) until OD₆₀₀ of 2, and cultures were centrifuged at 4 °C, rinsed in cold water, and frozen at -80 °C. Cells were thawed on ice, resuspended in lysis buffer (50 mM Tris-HCl pH 8.0, 100 mM NaCl, 10 mM MgCl₂, complete EDTA-free protease inhibitor mix or: 20 mM HEPES/KOAc pH 7.4, 100 mM KOAc, 10 mM MgCl₂, complete EDTA-free protease inhibitor mix), and lysed with glass beads using a Magnalyser. The lysates were clarified by centrifugation at 16,000 g for 10 min. at 4 °C. Supernatants were collected, and triton (0.5% final) or NP-40 (0.1% final) was added to the lysate. Binding to magnetic beads coupled with IgG was performed on a wheel at 4 °C overnight. Beads were collected on a magnet, flow-through was discarded, and beads were washed in lysis buffer. Elution was performed by resuspension in 2% SDS, 1× Tris-EDTA buffer and incubation at 65 °C for 10 min. Eluted beads were discarded on a magnet, and eluate was purified on HiPPR Detergent Removal Resin (Thermo Scientific, 88305). Purified proteins were eluted in PBS. The rest of the eluates was precipitated by the methanol/chloroform technique (Wessel & Flugge, 1984) and analyzed by mass spectrometry.

To control the quality of the affinity purification, a sample of eluates (3%) was separated on acrylamide NuPAGE Novex 4–12% Bis-Tris gels (Life Technologies) and analyzed by silver staining.

Mass spectrometry: data acquisition and analysis

After reduction and alkylation, protein samples were treated with endoprotease Lys-C (Wako) and trypsin (Trypsin Gold Mass Spec Grade; Promega). Peptide samples were desalted by OMIX C18 pipette tips (Agilent Technologies) and then analyzed by LC-MS/MS on an LTQ-Orbitrap velos instrument (Thermo Fisher Scientific) connected online to an E17ASY-nLC system (Thermo Fisher Scientific). Raw mass spectrometry (MS) data from the LTQ-Orbitrap were analyzed using MaxQuant software (Cox & Mann, 2008) version 1.6.10.43, which uses Andromeda search engine (Cox *et al*, 2011). Bioinformatic analysis of the MaxQuant/Andromeda workflow output and the analysis of the abundances of the identified proteins were performed with the Perseus module (Tyanova *et al*, 2016) version 1.6.10.43. Only protein identifications based on a minimum of two peptides were selected for further quantitative studies. After data processing, label-free quantification (LFQ) values from the “proteinGroups.txt” output file of MaxQuant were further analyzed. To distinguish specifically enriched proteins from the background, protein abundances were compared between sample and control groups using Student’s t-test statistic, and results were visualized as volcano plots (Hubner & Mann, 2011).

Preparation of puromycin-treated 80S ribosomes from yeast

S.c. BY4741 wild-type cells were grown in YP medium with 2% glucose to an OD₆₀₀ of 2.5, then harvested by spinning at 4,400 g for 10 min. Cells were washed first with water, then 1% KCl, then resuspended in 30 ml lysis buffer (20 mM HEPES/KOH pH 7.4, 100 mM KOAc, 7.5 mM Mg(OAc)₂, 1 mM DTT, 0.5 mM PMSF, complete EDTA-free protease inhibitor mix). Lysis was performed using a Microfluidics M-110L microfluidizer at 15k psi.

The lysate was cleared by centrifugation first at 26,892 g for 15 min., then at 140,531 g for 30 min. 15 ml of cleared lysate was loaded on a layered sucrose cushion consisting of 4 ml 2 M sucrose and 4 ml 1.5 M sucrose (buffer: 20 mM HEPES/KOH pH 7.4, 500 mM KOAc, 5 mM Mg(OAc)₂, 1 mM DTT, 0.5 mM PMSF) and centrifuged at 246,468 g for 21 h and 15 min.

The pellet containing ribosomal components was resuspended in water and mixed with 2× puromycin buffer (40 mM HEPES pH 7.5, 1 M KOAc, 25 mM Mg(OAc)₂, 2 mM puromycin, 2 mM DTT, 1 U/ml SUPERase-In RNase Inhibitor (Invitrogen)). The mixture was incubated for 30 min at room temperature and then loaded on 10–40% sucrose density gradients (20 mM HEPES/KOH pH 7.4, 500 mM KOAc, 5 mM Mg(OAc)₂, 1 mM DTT, 0.5 mM PMSF). Gradients were centrifuged at 20,755 g in an SW 32 Ti rotor (Beckman Coulter) for 20 h. 80S ribosomal fractions were identified using a Biocomp Gradient station *ip* and a Triax Flow cell and were manually collected. Fractions were then pelleted in a TLA110 rotor at 417,200 g for 45 min and resuspended in storage buffer (20 mM HEPES/KOH pH 7.5, 100 mM KOAc, 5 mM Mg(OAc)₂, 1 mM DTT). Aliquots were frozen in liquid nitrogen and stored at -80 °C until use.

Protein expression and purification

eIF3j (*Hcr1*) purification

Escherichia coli (*E. coli*) BL21(DE3) cells were transformed with the pTYB2 plasmid containing full-length *HCR1* and selected on LB plates containing ampicillin. Cells from a pre-culture were inoculated into 1.5 l of LB medium with ampicillin, and cell growth was monitored at 37 °C. At an OD₆₀₀ of 0.6, the cultures were transferred to an ice-water bath and incubated for 20 min. 0.1 mM IPTG was added to induce protein expression, and cells were incubated for 15 h at 16 °C while shaking. Cells were harvested by centrifugation at 3,500 g for 10 min and washed with 1% KCl, then resuspended in lysis buffer (20 mM HEPES pH 7.5, 500 mM NaCl). Cells were then pelleted again at 2,600 g, frozen in liquid nitrogen, and stored at -80 °C until further use.

Frozen cell pellets were thawed, resuspended in lysis buffer, and lysed using a Microfluidics M-110L microfluidizer at 15k psi. The lysate was cleared by centrifugation at 20,000 g for 30 min. Clear lysate fraction was added to 1.5 ml magnetic chitin beads (NEB E8036S) equilibrated in lysis buffer. Binding was performed for 1.5 h at 4 °C on a wheel. Beads were harvested on a magnet and washed once using 5 ml lysis buffer, twice using washing buffer (20 mM HEPES pH 7.4, 1 M NaCl, 1 mM EDTA) and once again using lysis buffer. The protein was then eluted from the beads using 5 ml elution buffer (20 mM HEPES pH 7.4, 500 mM KCl, 50 mM DTT) by incubating on a wheel at 4 °C overnight. A second elution step was performed using the same buffer for one hour after

removal of the first elution fraction. Both elution volumes were combined and concentrated using an Amicon Ultra 10k MWCO concentrator. Aliquots of pure eIF3j were flash-frozen in liquid nitrogen and stored at -80 °C.

ABCE1 (*Rli1*) purification

ABCE1 (*Rli1*) was overexpressed in *S. cerevisiae* strain WCGα using the pYes2-ABCE1-His₆ plasmid (kindly provided by R. Green, Department of Molecular Biology and Genetics, Johns Hopkins University School of Medicine) (Shoemaker & Green, 2011). Cells were grown in YP medium lacking uracil and containing 2% galactose, 1% raffinose at 30 °C to mid-log phase and were harvested at a final OD₆₀₀ of 1.0 by centrifugation at 3,500 g for 10 min. Cells were washed once with 1% KCl, pelleted again, and resuspended in lysis buffer (75 mM HEPES pH 8.0, 300 mM NaCl, 5 mM beta-mercaptoethanol (β-ME), 1% Tween, 20 mM imidazole, 2 mM MgCl₂, 10% glycerol). Excess buffer was removed by centrifugation at 2,600 g, and the cells were frozen in liquid nitrogen. Frozen cells were ground using a Spex SamplePrep Freezer Mill and the powder stored at -80 °C until further use. The cell powder was thawed and resuspended in lysis buffer. Cell debris was removed by centrifugation at 47,807.6 g for 30 min and filtered using a 1.6-μm membrane.

ABCE1 was purified first by metal affinity chromatography. Cleared lysate was applied to a HisTrap HP column (GE 5 ml column). The column was washed with 15 column volumes (CV) wash buffer (50 mM HEPES pH 8.0, 500 mM NaCl, 5 mM β-ME, 20 mM imidazole, 2 mM MgCl₂, 10% glycerol), and the protein was eluted with 4 CV over a gradient from 20 mM to 300 mM imidazole. Fractions containing ABCE1 were combined and dialyzed against Buffer A (20 mM HEPES pH 7.6, 100 mM KCl, 5 mM β-ME, 0.1 mM EDTA, 10% glycerol, 0.1 mM PMSF) overnight. The sample was diluted to 50 ml and loaded onto a cation exchange column (HiTrap SP 5 ml, GE). The column was washed with 6 CV Buffer A, and ABCE1 was eluted over gradient from 100 mM to 1 M KCl over 8 CV. ABCE1-containing fractions were concentrated using Amicon® 50k MWCO concentrator before loading onto a gel filtration column (Superdex200) for size-exclusion chromatography. The fractions containing ABCE1 were concentrated, and aliquots of pure ABCE1 in 20 mM HEPES pH 7.5, 200 mM KCl, 1.5 mM MgCl₂, 2 mM β-ME, and 5% glycerol were flash-frozen and stored at -80 °C.

eIF6 purification

E. coli BL21 (DE3) cells were transformed with a p7XC3GH plasmid expressing eIF6 fused to 3C protease cleavage site, GFP, and 10-His. Cells were grown on LB medium to mid-log phase (OD₆₀₀ = 0.7–0.8) at 37 °C and induced with 1 mM IPTG at 16 °C for 20 h. Cells were harvested by centrifugation at 4,400 g and 4 °C for 8 min, washed with PBS, and resuspended in lysis buffer (20 mM Tris-HCl pH 8.0, 300 mM NaCl, 2 mM β-ME) with 10% glycerol. Resuspended cells were flash-frozen in liquid nitrogen and stored at -80 °C until further use. For purification, frozen cells were thawed and resuspended in lysis buffer without glycerol. Lysis was performed using a Microfluidics M-100L microfluidizer at 15k psi. Crude lysate was cleared by centrifugation at 30,596 g for 20 min. TALON metal affinity resin was equilibrated in lysis buffer and added to the cleared lysate, then incubated at 4 °C for 40 min on a wheel. After collection of the flow-through, the column was washed using lysis buffer with 10 mM

imidazole. Elution was performed by incubating the resin with lysis buffer with 10 mM imidazole and 0.25 mg ml⁻¹ 3C protease for 30 min at 4 °C on a wheel. The elution fraction was concentrated using an Amicon 10k MWCO concentrator and loaded onto a Superdex200 column for size-exclusion chromatography using storage buffer (50 mM HEPES/KOH pH 7.5, 500 mM KCl, 2 mM MgCl₂, 2 mM β-ME). The purified protein in storage buffer was flash-frozen in liquid nitrogen and stored at -80 °C.

Dom34 and Hbs1 were purified as described before (Lee *et al*, 2007).

Splitting assays

In vitro splitting assays

Ribosome splitting assays were carried out to test the influence of eIF3j (Hcr1) on the canonical splitting reaction mediated by Dom34, Hbs1, and ABCE1 in yeast. For each reaction, 5 pmol of yeast 80S ribosomes (see above) was mixed with fivefold molar excess of splitting factors Dom34, Hbs1, and ABCE1 as well as the anti-association factor eIF6 under physiological buffer conditions (20 mM HEPES/KOH pH 7.5, 100 mM KOAc, 4 mM Mg(OAc)₂, 5 mM β-ME, 1 mM ATP, 1 mM GTP). Varying amounts of eIF3j were added to the reactions, ranging from twofold to twentyfold molar excess over the 80S ribosomes.

The samples were incubated on ice for 30 min and then loaded on 10-50% sucrose density gradients (20 mM HEPES/KOH pH 7.5, 100 mM KOAc, 5 mM Mg(OAc)₂, 1 mM DTT, 10-50% (w/v) sucrose). Gradients were spun in an SW 40 Ti rotor (Beckman Coulter) at 202,048 g for 4 h and fractionated at a BioComp Gradient Station *ip* using a Triax Flow Cell for UV measurement.

Ribosomal peak fractions were collected manually, and from each fraction, proteins were precipitated using 0.015% sodium deoxycholate and 7.2% trichloroacetic acid at 4 °C.

Proteins were separated on a 15% SDS-PAGE gel and visualized using SimplyBlue staining reagent.

“Facilitated” splitting assays

“Facilitated” splitting assays were performed to test the association of yeast ABCE1 and eIF3j to ribosomal particles under non-physiological high-salt conditions and in the presence of ATP or the non-hydrolyzable ATP analog AMP-PNP. To induce splitting, purified 80S ribosomes were mixed with tenfold molar excess of ABCE1 in splitting facilitating buffer (20 mM HEPES/KOH pH 7.4, 500 mM KCl, 1.5 mM MgCl₂, 1 mM DTT). Depending on the experiment, 0.5 mM AMP-PNP or ATP and 10-fold molar excess of eIF3j were added. For the experiments described here, approx. 50 pmol ribosomes in a total reaction volume of 250 μl were used. The samples were incubated for 20 min at 25°C and then cooled down to 4 °C on ice and loaded on 10-50% sucrose density gradients (20 mM HEPES/KOH pH 7.5, 100 mM KOAc, 5 mM Mg(OAc)₂, 1 mM DTT, 10-50% (w/v) sucrose). All following procedures were carried out as described above for splitting assays.

Cryo-EM sample preparation

Preparation of native yeast 40S complexes

A BY4741 strain containing genomic TAP-tagged SKI3 and a plasmid overexpressing SKA1 (pCM190) (Zhang *et al*, 2019) was used for generation of the cryo-EM sample.

Yeast cells were grown in synthetic medium lacking uracil (SL-Ura) with 2% glucose at 30 °C to an OD₆₀₀ of 3.0, whereupon the cultures were chilled in ice water. The cells were harvested by centrifugation at 4,422 g for 10 min in a Sorvall SLC-6000 rotor, washed with water, and resuspended in lysis buffer (20 mM HEPES/KOH pH 7.4, 100 mM KOAc, 5 mM Mg(OAc)₂, 1 mM DTT, 0.5 mM PMSF, complete EDTA-free protease inhibitor mix). Cells were frozen in liquid nitrogen and ground using a Spex SamplePrep Freezer/Mill.

Frozen cell powder was resuspended in lysis buffer (1:3 w/v), and the lysate was cleared by centrifugation in an SS-34 rotor (Thermo Scientific) at 26,891.8 g for 15 min.

Approximately 150 A₂₆₀ absorption units were loaded on a 10-50% sucrose density gradient (buffer composition identical to lysis buffer). Gradients were spun in an SW40 Ti rotor (Beckman Coulter) at 202,048 g for 3 h, and the 40S peak was harvested manually using a Triax Flow Cell.

Total A₂₆₀ of the collected 40S fraction from yeast lysate was measured, and the buffer was exchanged to cryo-EM grid buffer (20 mM HEPES/KOH pH 7.4, 100 mM KOAc, 5 mM Mg(OAc)₂, 1 mM DTT, 0.5 mM PMSF, complete EDTA-free protease inhibitor mix, 0.05% Nikkol) by three successive rounds of concentration and dilution by a factor of approx. 1:5 using an Amicon Ultra Centrifugal Filter (MWCO 100k) (total dilution factor approx. 1:125). The sample was then concentrated again. The A₂₆₀ was measured as A₂₆₀/ml = 6.3.

Freshly prepared sample was diluted to approx. 1.25 A₂₆₀ / ml, and 3.5 μl was applied to 2 nm pre-coated Quantifoil R3/3 holey carbon support grids and vitrified in liquid ethane using a Vitrobot mark IV (FEI Company, Netherlands). (wait time 45 s, blotting time 2 s).

Preparation of crosslinked yeast 43S pre-initiation complexes

S.c. W303 cells expressing genomically TAP-tagged Nip1 (eIF3c) were grown in YP medium with 2% glucose at 30 °C to an OD₆₀₀ of 2.0 and harvested by centrifugation at 4,422 g for 10 min in a Sorvall SLC-6000 rotor, washed with water, and resuspended in lysis buffer (50 mM HEPES/KOH pH 7.4, 100 mM KOAc, 1.5 mM Mg(OAc)₂, 1 mM DTT, 0.5 mM PMSF, complete EDTA-free protease inhibitor mix). Cells were frozen in liquid nitrogen and ground using a Spex SamplePrep Freezer/Mill.

Frozen powder was resuspended in lysis buffer with 0.15% (v/v) NP-40, and the lysate was cleared by centrifugation first at 20,000 g for 30 min in an SS-34 rotor and then at 26,891.8 g for 15 min in the same rotor.

The cleared lysate was applied to IgG Sepharose (GE17-0969-01) equilibrated in lysis buffer and incubated for 1 h at 4 °C on a rotating wheel. After binding, the supernatant was removed by centrifugation at 1,383 g for 3 min and the sepharose was transferred to a Bio-Rad Micro Bio-Spin Chromatography Column. The sepharose was sequentially washed with 10 column volumes each of lysis buffer containing 0.15% NP-40 and elution buffer (50 mM HEPES/KOH pH 7.4, 100 mM KOAc, 1.5 mM Mg(OAc)₂, 1 mM DTT).

Elution was performed by incubating the sepharose with elution buffer and approx. 2.4 U/μl AcTEV (Invitrogen) for 90 min at 20 °C. The eluted sample was harvested by spinning the columns at 380 g for 2 min.

The eluted sample was transferred onto a 10-50% sucrose density gradient (50 mM HEPES/KOH pH 7.4, 100 mM KOAc, 5 mM

Mg(OAc)₂, 1 mM DTT). Gradients were spun in an SW40 Ti rotor (Beckman Coulter) at 202,048 g for 3 h, and the 40S peak was harvested manually using a Triax Flow Cell for UV absorption measurement.

The 40S fraction was concentrated and the buffer exchanged to elution buffer using an Amicon Ultra Centrifugal Filter (MWCO 100k). The sample was crosslinked by shaking with 0.5 mM BS3 at 10 °C, 1,200 rpm for 10 min and then further incubated at 4 °C for approx. 10 min. The reaction was quenched by addition of 40 mM Tris-HCl. To the sample, 0.05% β -OG was added and cryogenic freezing was performed.

Preparation of native human 40S complexes

Human 40S initiation complexes were found as byproducts in an affinity purification using internally tagged RIOK1 and mutant RIOK1-D324A as bait. In brief, HEK Flp-In 293 T-Rex (Invitrogen) was grown in a 10-cm cell-culture dish to approximately 70% confluency and transfected with 0.5 μ g of a pcDNA5/FRT/TO vector containing RIOK1 or RIOK1-D324A and 4.5 μ g pOG44 (Invitrogen), using 20 μ g polyethylenimine (PEI). Cells were selected using 150 μ g ml⁻¹ hygromycin B (Thermo Scientific) and maintained in DMEM (Thermo Scientific) containing 10% fetal calf serum, 100 μ g ml⁻¹ hygromycin B, 10 μ g ml⁻¹ blasticidin and 1 \times penicillin/streptomycin and GlutaMAX (Thermo Scientific). Stable cell lines were subsequently grown in multiple 15-cm cell-culture dishes, protein expression induced with 1.6 μ g ml⁻¹ tetracycline and harvested in 0.025% trypsin/EDTA (Thermo Scientific) after 24 h. Cells were washed one in 1 \times phosphate-buffered saline (PBS) and subsequently pelleted at 1,600 g at 4 °C. Cells were then resuspended in lysis buffer (20 mM HEPES pH 7.6, 150 mM potassium acetate, 5 mM MgCl₂, 1 mM DTT, 0.5 mM NaF, 0.1 mM Na₃VO₄, 1 \times protease inhibitor (Sigma-Aldrich), 0.5% NP-40 substitute) and incubated for 30 min in an overhead rotator at 4 °C, before centrifugation at 4,000 g for 15 min at 4 °C. The cleared lysate was then added to 100 μ l of anti-Flag affinity beads (Sigma-Aldrich) and rotated for 2 h at 4 °C. Beads were harvested and 4 times washed with 1 ml wash buffer (20 mM HEPES pH 7.6, 150 mM potassium acetate, 5 mM MgCl₂, 1 mM DTT, 0.5 mM NaF, 0.1 mM Na₃VO₄, 1 \times protease inhibitor (Sigma-Aldrich)), before bound complexes were eluted 6 times with 100 μ l of 20 mM HEPES pH 7.6, 150 mM potassium acetate, 5 mM MgCl₂, 1 mM DTT, 0.05% Nikkol, and 0.2 mg ml⁻¹ 3 \times Flag peptide (Sigma-Aldrich). All eluate fractions were combined and concentrated on 300 kDa molecular mass cut-off filters (Sartorius).

3.5 μ l of the concentrated sample was applied to glow discharged copper grids with holey carbon support and a 2 nm continuous carbon layer (R3/3, Quantifoil). Grids were blotted in a Vitrobot Mark IV (FEI Company) for 2 s after incubation for 45 s at 4 °C and frozen in liquid ethane.

Cryo-EM data collection and processing

Data collection and processing of the yeast 40S complex sample

Cryo-EM data were collected on a Titan Krios TEM, using a Falcon II DED at 300 kV, with an electron dose of approx. 2.5 e⁻/Å² per frame for 10 frames (defocus range of 1.1 to 2.3 μ m). The magnified pixel size was 1.084 Å/pixel.

Micrograph stacks collected at the TEM were summed and corrected using MotionCor2 (Zheng *et al*, 2017). Micrograph quality was assessed individually, and CTF parameters were estimated using GCTF (Zhang, 2016). Particle picking was performed using Gautomatch (<http://www.mrc-lmb.cam.ac.uk/kzhang/>), and all further processing was performed using RELION 3.0 (Scheres, 2012; Zivanov *et al*, 2018).

Data collection and processing of the crosslinked yeast 43S PIC sample

For the crosslinked yeast sample, 5126 micrograph movies were collected at a Titan Krios at 300 kV, at a nominal pixel size of 1.059 Å, and a defocus range from 0.5 to 2.5 μ m. Movies were recorded on a K2 Summit direct electron detector using low-dose conditions with 40 frames at approximately 1.12 e⁻/Å² each. All frames were gain corrected and subsequently aligned and summed using MotionCor2 (Zheng *et al*, 2017), and CTF parameters were determined using CTFFIND (Rohou & Grigorieff, 2015) and Gctf (Zhang, 2016). Particles were picked using Gautomatch (<http://www.mrc-lmb.cam.ac.uk/kzhang/>), and particle images were extracted in RELION 3.1 (Zivanov *et al*, 2018). 2D classification was performed using a previously generated cryo-EM map of an idle 40S subunit as reference, and all particles with recognizable features of the small subunit were selected and subjected to an initial 3D refinement using the same reference, followed by 3D classification. All classes with density corresponding to ABCE1 were selected, grouped, and classified again using an ellipsoid mask around ABCE1. Particles with ABCE1 in the semi-open conformation as observed in the native yeast sample were selected, refined, and subjected to one round of CTF refinement and Bayesian polishing. Thereupon, these particles were further sub-classified using an ellipsoid mask around eIF3j, and all particles containing eIF3j were selected as the final class containing both semi-open ABCE1 and eIF3j. This class represented 4.8% of the total dataset. Particles in this class were subjected to one more round of CTF refinement and Bayesian polishing, before 3D refinement and post-processing as well as local resolution estimation (all within RELION 3.1) yielded the final reconstructions at 3.0 Å average resolution, as shown in (Appendix Fig S1).

Data collection and processing of the human 40S complex sample

Data collection was performed on a Titan Krios at 300 kV, where 7,365 and 4,499 movies were collected for RIOK1-D324A and RIOK1, respectively, at a nominal pixel size of 1.059 Å and at a defocus range from 0.5 to 2.5 μ m. Movies were recorded on a K2 Summit direct electron detector using low-dose conditions with 48 frames at approximately 1 e⁻/Å². All frames were gain corrected and subsequently aligned and summed using MotionCor2 (Zheng *et al*, 2017), and CTF parameters were determined using CTFFIND (Rohou & Grigorieff, 2015) and Gctf (Zhang, 2016). Particles were then picked using Gautomatch (<http://www.mrc-lmb.cam.ac.uk/kzhang/>). Particle images were extracted in RELION 3.0 (Zivanov *et al*, 2018) and subjected to reference-free 2D classification. Good particles were selected, 3D refined, and classified. Besides the expected pre-40S classes (unpublished), one class containing the initiation complex was obtained in both datasets, comprising approximately 2% (RIOK1-D324A data set) and 8.7% (RIOK1 data set) of the total particle number. The two datasets were subsequently subjected to Bayesian polishing and CTF refinement, combined and further classified extensively as shown in Appendix Fig S2. Final reconstructions were

then B-factor sharpened with RELION and the local resolution estimated. Where indicated (Appendix Fig S2), local or multi-body refinement was performed.

Model building and refinement

For rigid body fits and figures, Chimera version 1.13.1 (Pettersen *et al*, 2004) and ChimeraX version 0.91 (Goddard *et al*, 2018) were used. Homology models were created using SWISS-MODEL Repository (Bienert *et al*, 2017; Waterhouse *et al*, 2018).

Yeast 43S PIC and 48S IC model

The atomic models PDB 5NDG (Prokhorova *et al*, 2017), 6FYY, 6FYX (Llacer *et al*, 2018), and 6TB3 (Buschauer *et al*, 2020) containing the models for *S.c.* 40S rRNA, r-proteins, and eIFs were fitted as rigid bodies into the cryo-EM maps of the *S.c.* 43S PIC and 48S IC. For the 43S PIC, the 40S rRNA and ribosomal proteins were fitted from PDB 5NDG and eIFs were fitted from PDB 6FYY. For the 48S IC, the 40S rRNA and ribosomal proteins were fitted from PDB 6TB3 and eIFs were fitted from PDB 6FYX. For ABCE1, the hybrid semi-open/closed model derived from the human 43S PIC (see below) was fitted into the density. For Hcr1, a homology model was created based on the structure of the human eIF3j dimer (PDB 3BPJ). The C-terminus of protomer 1 was extended by 3 amino acids, and the C-terminus of protomer 2 was extended by 19 amino acids based on a comparison with the data from the yeast 43S PIC-XL sample with the density observed for the native sample.

Models for the “mRNA entry position” of the YLC were obtained by fitting the crystal structure of eIF3i/g (PDB 4U1E, Erzberger *et al*, 2014) to the observed density as a rigid body and matching it to the structure of eIF3b CTD from PDB 6FYY; to obtain the “ES6 position”, the eIF3i-eIF3g moiety bound to the C-terminal helix of eIF3b was rotated by 120 degrees around the Thr697-Asp701 hinge in the CTD of eIF3b as a rigid body.

Yeast 43S PIC-XL model

The atomic model 6TB3 (Buschauer *et al*, 2020) containing the models for *S.c.* 40S rRNA and r-proteins was split into 40S head and body and fitted as rigid bodies into the best-resolved cryo-EM map of the complex using ChimeraX version 1.0 (Goddard *et al*, 2018). The homology models for eIF3j and ABCE1 previously generated for the native 43S complex were also fitted, and the entire model was adjusted in WinCoot 0.8.9.2 (Emsley & Cowtan, 2004). The C-terminus of eIF3j protomer 2 was built *de novo*. A focused refined cryo-EM map for the NBD2 of ABCE1 was consulted to improve accuracy in the model for this domain during initial model building. The model was real space refined using Phenix 1.18 (Afonine *et al*, 2018; Liebschner *et al*, 2019).

Human 43S PIC

To obtain the atomic model, the best-resolved maps as obtained after local focused refinement or multi-body refinement (Fig EV2, Appendix Fig S2) were used to build the different parts of the *H.s.* 43S PIC. The 40S subunit was fit into maps of 40S body and 40S head obtained from multi-body refinement III (Appendix Fig S2) starting with the 40S model (PDB 6G5H, Ameismeier *et al*, 2018). After rigid body fitting, side chains of ribosomal proteins and rRNA

were adjusted using Coot (version 0.8.9.2) (Emsley & Cowtan, 2004). Further, the 60S ribosomal protein eL41 was added to the model using PDB 6EK0 (chain h, Natchiar *et al*, 2017). For eIF1A, the homology model based on PDB 3J81 (Hussain *et al*, 2014) was fitted and adjusted using the 40S body map. The N-terminal helix bundle of eIF3c (47-149) was built *de novo* into the same map.

The homology model of the crystal structure of the C-terminal part of eIF3d (162-527; PDB 5K4B, Lee *et al*, 2016) was fitted into the map for the 40S head obtained from multi-body refinement III (Appendix Fig S2). The atomic model was only modified in the regions interacting with the 40S head. Similarly, the model for eIF3b (PDB 5K1H, Simonetti *et al*, 2016) was only adjusted in blades 5 and 6, which contact the 40S body. Here, the best-resolved cryo-EM map, obtained by focused classification on the YLC, could be used (Appendix Fig S2). Also, the homology model of eIF3i (PDB 5K0Y, Simonetti *et al*, 2016) and an α -helix corresponding to the C-terminal part of eIF3a were fitted into this map.

The eIF3-PCI-MPN core (including eIF3a, c, e, f, h, k, l, m) was modeled into the two maps of multi-body refinement II (Appendix Fig S2) using the human homology model based on PDB 5A5T (des Georges *et al*, 2015) as starting model. eIF3d-N (2-84) was built *de novo* into the density.

For eIF3j, the unpublished crystal structure of the human eIF3j dimer (PDB 3BPJ) was fitted as rigid body into the density of 43S PIC state II.

Classification of the entire 43S dataset focusing on ABCE1 followed by focused refinement yielded a well-resolved map, which could be used for model building. A homology model based on the closed-state yeast ABCE1 bound to the 40S (PDB 5LL6, Heuer *et al*, 2017) was used as starting model. ATP and ADP were added to the NBSs.

One class obtained by focused classification on the YLC represents a very stable 43S complex in P_{OUT} state and yielded a well-resolved map of the TC after focused refinement. The models of tRNA_i (PDB 6FEC, Eliseev *et al*, 2018), eIF2 α , and eIF2 γ (PDB 6O85, Kenner *et al*, 2019) and the homology models of eIF2 β and eIF1 (based on PDB 6GSM) were fitted into the map and adjusted using Coot. Further, a stretch of 8 amino acids was modeled into the density adjacent to eIF1, which corresponds to eIF3c. For the unassigned RRM on top of 18S rRNA h16, we generated a poly-alanine model.

All models were real space refined using Phenix (version 1.17 and 1.18) (Afonine *et al*, 2018; Liebschner *et al*, 2019). In order to model the interfaces between the different parts of the structure, maps before and after multi-body refinement were used. Furthermore, neighboring parts were included in the real space refinement using focused cryo-EM maps. The final composite model was subjected to a final refinement using the overall cryo-EM map of state II and state III (Appendix Fig S2, Appendix Table S2). In regions with local resolution lower than 4 Å, side chains were not modeled.

Chemical crosslinking and mass spectrometry

For the crosslinking analysis followed by mass spectrometry of the ABCE1 43S pre-initiation complex, the sample was prepared as described above (see section Preparation of crosslinked yeast 43S pre-initiation complexes). After the sucrose density gradient, the buffer was exchanged to 50 mM HEPES/KOH pH 7.4, 50 mM KCl, 5 mM MgCl₂, 1 mM DTT, and crosslinking was performed using an equimolar mixture of isotopically labeled BS2G (H6/D6)

(bis(sulfosuccinimidyl) 2,2,4,4-glutarate, Creative molecules) for 30 min at 1,200 rpm and 10°C. The reaction was quenched with 100 mM ammonium bicarbonate for 10 min. Digestion and peptide clean-up were performed using the EasyPep Mini MS Sample Prep Kit (Thermo Scientific), according to the manufacturer's protocol. Crosslinks were further enriched on a Superdex Peptide PC 3.2/30 column (300 × 3.2 mm), and the fractions were analyzed by liquid chromatography coupled to tandem mass spectrometry with an LTQ-Orbitrap Elite (Thermo Scientific) instrument (Herzog *et al*, 2012). Identification of the crosslinked peptides was done using xQuest (Walzthoeni *et al*, 2012). The results were filtered with an MS1 tolerance window of −4 to 4 ppm and score ≥ 22 followed by manual validation.

Sequence alignments

In order to quantify the conservation of protein sequences between human and yeast proteins of interest, pairwise alignments were conducted using the T-Coffee implementation at <https://toolkit.tuebingen.mpg.de> (Notredame *et al*, 2000; Zimmermann *et al*, 2018) and visualized using JalView (Waterhouse *et al*, 2009). Multiple sequence alignments of the conserved elements of the eIF3c N-terminus were created using MAFFT (Katoh *et al*, 2019).

Data availability

Cryo-EM density map of the yeast 43S PIC: Electron Microscopy Data Bank 11160 (<https://www.ebi.ac.uk/pdbe/entry/emdb/EMD-11160>).

Atomic model of the yeast 43S PIC: Protein Data Bank 6ZCE (<http://www.rcsb.org/structure/6ZCE>).

Cryo-EM density map of the yeast 48S IC: Electron Microscopy Data Bank 11439 (<https://www.ebi.ac.uk/pdbe/entry/emdb/EMD-11439>).

Atomic model of the yeast 48S IC: Protein Data Bank 6ZU9 (<http://www.rcsb.org/structure/6ZU9>).

Cryo-EM density map of the yeast 43S PIC-XL: Electron Microscopy Data Bank 11608 (<https://www.ebi.ac.uk/pdbe/entry/emdb/EMD-11608>).

Atomic model of the yeast 43S PIC: Protein Data Bank 7A1G (<http://www.rcsb.org/structure/7A1G>).

Cryo-EM density map of the human 43S PIC—state II: Electron Microscopy Data Bank 11458 (<https://www.ebi.ac.uk/pdbe/entry/emdb/EMD-11458>).

Atomic model of the human 43S PIC—state II: Protein Data Bank 6ZVJ (<http://www.rcsb.org/structure/6ZVJ>).

Cryo-EM density map of the human 43S PIC—state III: Electron Microscopy Data Bank 11602 (<https://www.ebi.ac.uk/pdbe/entry/emdb/EMD-11602>).

Atomic model of the human 43S PIC—state III: Protein Data Bank 7A09 (<http://www.rcsb.org/structure/7A09>).

Mass spectrometry proteomics data of the yeast 43S PIC: ProteomeXchange Consortium PXD020849 (<http://proteomecentral.proteomexchange.org/cgi/GetDataset?ID=PX020849>).

The cryo-EM density maps of the yeast 43S PIC, the yeast 48S IC, the yeast 43S PIC-XL, the human 43S-PIC state II, and the human 43S-PIC state III have been deposited in the Electron Microscopy

Data Bank under accession numbers EMD-11160, EMD-11429, EMD-11608, EMD-11458, and EMD-11602, respectively (<https://www.emdataresource.org/>). Atomic coordinates for the atomic models have been deposited in the Protein Data Bank under accession number PDB ID 6ZCE, 6ZU9, 7A1G, 6ZVJ, and 7A09, respectively. (<https://www.wwpdb.org/>) (see Appendix Table S1 and S2). The mass spectrometry proteomics data have been deposited to the ProteomeXchange Consortium via the PRIDE (Perez-Riverol *et al*, 2019) partner repository with the dataset identifier PXD020849. Correspondence and requests for materials should be addressed to T.B. (becker@genzentrum.lmu.de) or R.B. (beckmann@genzentrum.lmu.de).

Expanded View for this article is available online.

Acknowledgements

The authors thank H. Sieber, J. Musial, C. Ungewickell, and S. Rieder for technical assistance, L. Kater and K. Best for support with the pre-processing pipeline of cryo-EM data, R. Buschauer for assistance in model building, L. Valášek and A. Jacquier for critical reading of the manuscript, J. Wells for support during the setup of splitting assays and J. Zeman for support with the XL-MS experiments. This work was supported by German Research Council (BE1814/15-1 and TRR174), the Center for Integrated Protein Science Munich (CiPS-M), the ANR-17-CE11-0049-01 and the ANR-17-CE12-0024-02 grants, the Pasteur Institute and the Centre National de la Recherche Scientifique. H.K., M.A., and M.P. are supported by a DFG fellowship through the Graduate School of Quantitative Bioscience Munich (QBM). Open Access funding enabled and organized by ProjektDEAL.

Author contributions

HK, T M-K, TB, and RB designed the study. MA prepared the sample for the human and TM-K for the yeast native 40S complexes. TM-K and HK prepared components for *in vitro* splitting assays and TM-K performed splitting assays. MA, TM-K, and OB collected and MA and TM-K processed the cryo-EM data. HK, JC, and TM-K built and refined the model. HK, TM-K, TB, and RB analyzed and interpreted the structures. ED, AN, and MF-R performed ABCE1-TAP purification and quantitative label-free MS. MP and FH performed crosslinking mass spectrometry. TB, HK, TM-K, and RB wrote the manuscript with contributions from all authors.

Conflict of interest

The authors declare that they have no conflict of interest.

References

- Algire MA, Maag D, Lorsch JR (2005) Pi release from eIF2, not GTP hydrolysis, is the step controlled by start-site selection during eukaryotic translation initiation. *Mol Cell* 20: 251–262
- Acker MG, Shin BS, Dever TE, Lorsch JR (2006) Interaction between eukaryotic initiation factors 1A and 5B is required for efficient ribosomal subunit joining. *J Biol Chem* 281: 8469–8475
- Acker MG, Shin BS, Nanda JS, Saini AK, Dever TE, Lorsch JR (2009) Kinetic analysis of late steps of eukaryotic translation initiation. *J Mol Biol* 385: 491–506
- Afonine PV, Poon BK, Read RJ, Sobolev OV, Terwilliger TC, Urzhumtsev A, Adams PD (2018) Real-space refinement in PHENIX for cryo-EM and crystallography. *Acta Crystallogr D Struct Biol* 74: 531–544

- Ameisemeier M, Cheng J, Berninghausen O, Beckmann R (2018) Visualizing late states of human 40S ribosomal subunit maturation. *Nature* 558: 249–253
- Andersen DS, Leever SJ (2007) The essential *Drosophila* ATP-binding cassette domain protein, pixie, binds the 40 S ribosome in an ATP-dependent manner and is required for translation initiation. *J Biol Chem* 282: 14752–14760
- Anger AM, Armache JP, Berninghausen O, Habeck M, Subklewe M, Wilson DN, Beckmann R (2013) Structures of the human and *Drosophila* 80S ribosome. *Nature* 497: 80–85
- Asano K, Clayton J, Shalev A, Hinnebusch AG (2000) A multifactor complex of eukaryotic initiation factors, eIF1, eIF2, eIF3, eIF5, and initiator tRNA(Met) is an important translation initiation intermediate in vivo. *Genes Dev* 14: 2534–2546
- Aylett CH, Boehringer D, Erzberger JP, Schaefer T, Ban N (2015) Structure of a yeast 40S-eIF1-eIF1A-eIF3-eIF3j initiation complex. *Nat Struct Mol Biol* 22: 269–271
- Barthelme D, Dinkelaker S, Albers SV, Londei P, Ermiler U, Tampe R (2011) Ribosome recycling depends on a mechanistic link between the FeS cluster domain and a conformational switch of the twin-ATPase ABCE1. *Proc Natl Acad Sci USA* 108: 3228–3233
- Barthelme D, Scheele U, Dinkelaker S, Janoschka A, Macmillan F, Albers SV, Driessen AJ, Stagni MS, Bill E, Meyer-Klaucke W, et al (2007) Structural organization of essential iron-sulfur clusters in the evolutionarily highly conserved ATP-binding cassette protein ABCE1. *J Biol Chem* 282: 14598–14607
- Becker T, Franckenberg S, Wickles S, Shoemaker CJ, Anger AM, Armache J-P, Sieber H, Ungewickell C, Berninghausen O, Daberkow I, et al (2012) Structural basis of highly conserved ribosome recycling in eukaryotes and archaea. *Nature* 482: 501–506
- Ben-Shem A, Garreau de Loubresse N, Melnikov S, Jenner L, Yusupova G, Yusupov M (2011) The structure of the eukaryotic ribosome at 3.0 Å resolution. *Science* 334: 1524–1529
- Beznoskova P, Cuchalova L, Wagner S, Shoemaker CJ, Gunisova S, von der Haar T, Valasek LS (2013) Translation initiation factors eIF3 and HCR1 control translation termination and stop codon read-through in yeast cells. *PLoS Genet* 9: e1003962
- Bienert S, Waterhouse A, de Beer TA, Tauriello G, Studer G, Bordoli L, Schwede T (2017) The SWISS-MODEL Repository-new features and functionality. *Nucleic Acids Res* 45: D313–D319
- Block KL, Vornlocher HP, Hershey JW (1998) Characterization of cDNAs encoding the p44 and p35 subunits of human translation initiation factor eIF3. *J Biol Chem* 273: 31901–31908
- Brown A, Baird MR, Yip MC, Murray J, Shao S (2018) Structures of translationally inactive mammalian ribosomes. *Elife* 7: e40486
- Brown A, Shao S, Murray J, Hegde RS, Ramakrishnan V (2015) Structural basis for stop codon recognition in eukaryotes. *Nature* 524: 493–496
- Cate JH (2017) Human eIF3: from 'blobology' to biological insight. *Philos Trans R Soc Lond B Biol Sci* 372: 20160176
- Buschauer R, Matsuo Y, Sugiyama T, Chen YH, Alhusaini N, Sweet T, Ikeuchi K, Cheng J, Matsuki Y, Nobuta R, et al (2020) The Ccr4-Not complex monitors the translating ribosome for codon optimality. *Science* 368
- Chen ZQ, Dong J, Ishimura A, Daar I, Hinnebusch AG, Dean M (2006) The essential vertebrate ABCE1 protein interacts with eukaryotic initiation factors. *J Biol Chem* 281: 7452–7457
- Cox J, Mann M (2008) MaxQuant enables high peptide identification rates, individualized p.p.b.-range mass accuracies and proteome-wide protein quantification. *Nat Biotechnol* 26: 1367–1372
- Cox J, Neuhauser N, Michalski A, Scheltema RA, Olsen JV, Mann M (2011) Andromeda: a peptide search engine integrated into the MaxQuant environment. *J Proteome Res* 10: 1794–1805
- Cuchalova L, Kouba T, Herrmannova A, Danyi I, Chiu WL, Valasek L (2010) The RNA recognition motif of eukaryotic translation initiation factor 3g (eIF3g) is required for resumption of scanning of posttermination ribosomes for reinitiation on GCN4 and together with eIF3i stimulates linear scanning. *Mol Cell Biol* 30: 4671–4686
- Das S, Ghosh R, Maitra U (2001) Eukaryotic translation initiation factor 5 functions as a GTPase-activating protein. *J Biol Chem* 276: 6720–6726
- des Georges A, Dhote V, Kuhn L, Hellen CUT, Pestova TV, Frank J, Hashem Y (2015) Structure of mammalian eIF3 in the context of the 43S preinitiation complex. *Nature* 525: 491–495
- Dong J, Lai R, Nielsen K, Fekete CA, Qiu H, Hinnebusch AG (2004) The essential ATP-binding cassette protein RLI1 functions in translation by promoting preinitiation complex assembly. *J Biol Chem* 279: 42157–42168
- Dong Z, Qi J, Peng H, Liu J, Zhang JT (2013) Spectrin domain of eukaryotic initiation factor 3a is the docking site for formation of the a:b:i:g subcomplex. *J Biol Chem* 288: 27951–27959
- ElAntak L, Tzakos AG, Locker N, Lukavsky PJ (2007) Structure of eIF3b RNA recognition motif and its interaction with eIF3j: structural insights into the recruitment of eIF3b to the 40 S ribosomal subunit. *J Biol Chem* 282: 8165–8174
- Elantak L, Wagner S, Herrmannova A, Karaskova M, Rutkai E, Lukavsky PJ, Valasek L (2010) The indispensable N-terminal half of eIF3j/HCR1 cooperates with its structurally conserved binding partner eIF3b/PRT1-RRM and with eIF1A in stringent AUG selection. *J Mol Biol* 396: 1097–1116
- Eliseev B, Yeramala L, Leitner A, Karuppasamy M, Raimondeau E, Huard K, Alkalaeva E, Aebersold R, Schaffitzel C (2018) Structure of a human cap-dependent 48S translation pre-initiation complex. *Nucleic Acids Res* 46: 2678–2689
- Emsley P, Cowtan K (2004) Coot: model-building tools for molecular graphics. *Acta Crystallogr D Biol Crystallogr* 60: 2126–2132
- Erzberger JP, Stengel F, Pellarin R, Zhang S, Schaefer T, Aylett CHS, Cimermancic P, Boehringer D, Sali A, Aebersold R, et al (2014) Molecular Architecture of the 40SEIF1eIF3 Translation Initiation Complex. *Cell* 159: 1227–1228
- Fraser CS, Berry KE, Hershey JW, Doudna JA (2007) eIF3j is located in the decoding center of the human 40S ribosomal subunit. *Mol Cell* 26: 811–819
- Fraser CS, Lee JY, Mayeur GL, Bushell M, Doudna JA, Hershey JW (2004) The j-subunit of human translation initiation factor eIF3 is required for the stable binding of eIF3 and its subcomplexes to 40 S ribosomal subunits in vitro. *J Biol Chem* 279: 8946–8956
- Gerovac M, Tampe R (2019) Control of mRNA Translation by Versatile ATP-Driven Machines. *Trends Biochem Sci* 44: 167–180
- Ghaemmaghami S, Huh WK, Bower K, Howson RW, Belle A, Dephoure N, O'Shea EK, Weissman JS (2003) Global analysis of protein expression in yeast. *Nature* 425: 737–741
- Goddard TD, Huang CC, Meng EC, Pettersen EF, Couch GS, Morris JH, Ferrin TE (2018) UCSF ChimeraX: Meeting modern challenges in visualization and analysis. *Protein Sci* 27: 14–25
- Gouridis G, Hetzert B, Kiosze-Becker K, de Boer M, Heinemann H, Nurenbeg-Goloub E, Cordes T, Tampe R (2019) ABCE1 Controls Ribosome Recycling by an Asymmetric Dynamic Conformational Equilibrium. *Cell Rep* 28: 723–734

- Hashem Y, des Georges A, Dhote V, Langlois R, Liao HY, Grassucci RA, Hellen CUT, Pestova TV, Frank J (2013) Structure of the mammalian ribosomal 43S preinitiation complex bound to the scanning factor DHX29. *Cell* 153: 1108–1119
- Herrmannova A, Daujotyte D, Yang JC, Cuchalova L, Gorrec F, Wagner S, Danyi I, Lukavsky PJ, Valasek LS (2012) Structural analysis of an eIF3 subcomplex reveals conserved interactions required for a stable and proper translation pre-initiation complex assembly. *Nucleic Acids Res* 40: 2294–2311
- Herzog F, Kahraman A, Boehringer D, Mak R, Bracher A, Walzthoeni T, Leitner A, Beck M, Hartl FU, Ban N, et al (2012) Structural probing of a protein phosphatase 2A network by chemical cross-linking and mass spectrometry. *Science* 337: 1348–1352
- Heuer A, Gerovac M, Schmidt C, Trowitzsch S, Preis A, Kötter P, Berninghausen O, Becker T, Beckmann R, Tampé R (2017) Structure of the 40S-ABCE1 post-splitting complex in ribosome recycling and translation initiation. *Nature Structural & Molecular Biology* 24: 453–460
- Hinnebusch AG (2006) eIF3: a versatile scaffold for translation initiation complexes. *Trends Biochem Sci* 31: 553–562
- Hopfner KP (2016) Invited review: Architectures and mechanisms of ATP binding cassette proteins. *Biopolymers* 105: 492–504
- Huang HK, Yoon H, Hannig EM, Donahue TF (1997) GTP hydrolysis controls stringent selection of the AUG start codon during translation initiation in *Saccharomyces cerevisiae*. *Genes Dev* 11: 2396–2413
- Hubner NC, Mann M (2011) Extracting gene function from protein-protein interactions using Quantitative BAC Interactomics (QUBIC). *Methods* 53: 453–459
- Hussain T, Llacer JL, Fernandez IS, Munoz A, Martin-Marcos P, Savva CG, Lorsch JR, Hinnebusch AG, Ramakrishnan V (2014) Structural changes enable start codon recognition by the eukaryotic translation initiation complex. *Cell* 159: 597–607
- Imai H, Abe T, Miyoshi T, Nishikawa SI, Ito K, Uchiumi T (2018) The ribosomal stalk protein is crucial for the action of the conserved ATPase ABCE1. *Nucleic Acids Res* 46: 7820–7830
- Karcher A, Schele A, Hopfner KP (2008) X-ray structure of the complete ABC enzyme ABCE1 from *Pyrococcus abyssi*. *J Biol Chem* 283: 7962–7971
- Katoh K, Rozewicki J, Yamada KD (2019) MAFFT online service: multiple sequence alignment, interactive sequence choice and visualization. *Brief Bioinform* 20: 1160–1166
- Kenner LR, Anand AA, Nguyen HC, Myasnikov AG, Klose CJ, McGeevra LA, Tsai JC, Miller-Vedam LE, Walter P, Frost A (2019) eIF2B-catalyzed nucleotide exchange and phosphoregulation by the integrated stress response. *Science* 364: 491–495
- Khoshnevis S, Gunisova S, Vlckova V, Kouba T, Neumann P, Beznoskova P, Ficner R, Valasek LS (2014) Structural integrity of the PCI domain of eIF3a/TIF32 is required for mRNA recruitment to the 43S pre-initiation complexes. *Nucleic Acids Res* 42: 4123–4139
- Kiosze-Becker K, Ori A, Gerovac M, Heuer A, Nürenberg-Goloub E, Rashid UJ, Becker T, Beckmann R, Beck M, Tampé R (2016) Structure of the ribosome post-recycling complex probed by chemical cross-linking and mass spectrometry. *Nature Communications* 7: 13248
- Lee AS, Kranzusch PJ, Doudna JA, Cate JH (2016) eIF3d is an mRNA cap-binding protein that is required for specialized translation initiation. *Nature* 536: 96–99
- Lee HH, Kim YS, Kim KH, Heo I, Kim SK, Kim O, Kim HK, Yoon JY, Kim HS, Kim DJ, et al (2007) Structural and functional insights into Dom34, a key component of no-go mRNA decay. *Mol Cell* 27: 938–950
- Lee JH, Pestova TV, Shin BS, Cao C, Choi SK, Dever TE (2002) Initiation factor eIF5B catalyzes second GTP-dependent step in eukaryotic translation initiation. *Proc Natl Acad Sci USA* 99: 16689–16694
- Liebschner D, Afonine PV, Baker ML, Bunkoczi G, Chen VB, Croll TI, Hintze B, Hung LW, Jain S, McCoy AJ, et al (2019) Macromolecular structure determination using X-rays, neutrons and electrons: recent developments in Phenix. *Acta Crystallogr D Struct Biol* 75: 861–877
- Llacer JL, Hussain T, Marler L, Aitken CE, Thakur A, Lorsch JR, Hinnebusch AG, Ramakrishnan V (2015) Conformational differences between open and closed states of the eukaryotic translation initiation complex. *Mol Cell* 59: 399–412
- Llacer JL, Hussain T, Saini AK, Nanda JS, Kaur S, Gordiyenko Y, Kumar R, Hinnebusch AG, Lorsch JR, Ramakrishnan V (2018) Translational initiation factor eIF5 replaces eIF1 on the 40S ribosomal subunit to promote start-codon recognition. *Elife* 7: e39273
- Mancera-Martinez E, Brito Querido J, Valasek LS, Simonetti A, Hashem Y (2017) ABCE1: A special factor that orchestrates translation at the crossroad between recycling and initiation. *RNA Biol* 14: 1279–1285
- Martin-Marcos P, Nanda JS, Luna RE, Zhang F, Saini AK, Cherkasova VA, Wagner G, Lorsch JR, Hinnebusch AG (2014) Enhanced eIF1 binding to the 40S ribosome impedes conformational rearrangements of the preinitiation complex and elevates initiation accuracy. *RNA* 20: 150–167
- Mohammad MP, Munzarova Pondelickova V, Zeman J, Gunisova S, Valasek LS (2017) In vivo evidence that eIF3 stays bound to ribosomes elongating and terminating on short upstream ORFs to promote reinitiation. *Nucleic Acids Res* 45: 2658–2674
- Natchiar SK, Myasnikov AG, Kratzat H, Hazemann I, Klaholz BP (2017) Visualization of chemical modifications in the human 80S ribosome structure. *Nature* 551: 472–477
- Nielsen KH, Valasek L, Sykes C, Jivotovskaya A, Hinnebusch AG (2006) Interaction of the RNP1 motif in PRT1 with HCR1 promotes 40S binding of eukaryotic initiation factor 3 in yeast. *Mol Cell Biol* 26: 2984–2998
- Notredame C, Higgins DG, Heringa J (2000) T-Coffee: A novel method for fast and accurate multiple sequence alignment. *J Mol Biol* 302: 205–217
- Nürenberg-Goloub E, Heinemann H, Gerovac M, Tampé R (2018) Ribosome recycling is coordinated by processive events in two asymmetric ATP sites of ABCE1. *Life Science Alliance* 1: e201800095
- Nürenberg-Goloub E, Kratzat H, Heinemann H, Heuer A, Kötter P, Berninghausen O, Becker T, Tampé R, Beckmann R (2020) Molecular analysis of the ribosome recycling factor ABCE1 bound to the 30S post-splitting complex. *The EMBO Journal* 39: e103788
- Nürenberg-Goloub E, Tampe R (2019) Ribosome recycling in mRNA translation, quality control, and homeostasis. *Biol Chem* 401: 47–61
- Obayashi E, Luna R, Nagata T, Martin-Marcos P, Hiraishi H, Singh C, Erzberger J, Zhang F, Arthanari H, Morris J, et al (2017) Molecular Landscape of the Ribosome Pre-initiation Complex during mRNA Scanning: Structural Role for eIF3c and Its Control by eIF5. *Cell Reports* 18: 2651–2663
- Passmore LA, Schmeing TM, Maag D, Applefield DJ, Acker MG, Algire MA, Lorsch JR, Ramakrishnan V (2007) The eukaryotic translation initiation factors eIF1 and eIF1A induce an open conformation of the 40S ribosome. *Mol Cell* 26: 41–50
- Paulin FE, Campbell LE, O'Brien K, Loughlin J, Proud CG (2001) Eukaryotic translation initiation factor 5 (eIF5) acts as a classical GTPase-activator protein. *Curr Biol* 11: 55–59

- Pettersen EF, Goddard TD, Huang CC, Couch GS, Greenblatt DM, Meng EC, Ferrin TE (2004) UCSF Chimera—a visualization system for exploratory research and analysis. *J Comput Chem* 25: 1605–1612
- Perez-Riverol Y, Csordas A, Bai J, Bernal-Llinares M, Hewapathirana S, Kundu DJ, Inuganti A, Griss J, Mayer G, Eisenacher M, et al (2019) The PRIDE database and related tools and resources in 2019: improving support for quantification data. *Nucleic Acids Res* 47: D442–D450
- Pestova TV, Lomakin IB, Lee JH, Choi SK, Dever TE, Hellen CU (2000) The joining of ribosomal subunits in eukaryotes requires eIF5B. *Nature* 403: 332–335
- Pisarev AV, Hellen CU, Pestova TV (2007) Recycling of eukaryotic posttermination ribosomal complexes. *Cell* 131: 286–299
- Pisarev AV, Skabkin MA, Pisareva VP, Skabkina OV, Rakotondrafara AM, Hentze MW, Hellen CU, Pestova TV (2010) The role of ABCE1 in eukaryotic posttermination ribosomal recycling. *Mol Cell* 37: 196–210
- Pisareva VP, Skabkin MA, Hellen CU, Pestova TV, Pisarev AV (2011) Dissociation by Pelota, Hbs1 and ABCE1 of mammalian vacant 80S ribosomes and stalled elongation complexes. *EMBO J* 30: 1804–1817
- Preis A, Heuer A, Barrio-Garcia C, Hauser A, Eyler DE, Berninghausen O, Green R, Becker T, Beckmann R (2014) Cryoelectron microscopic structures of eukaryotic translation termination complexes containing eRF1-eRF3 or eRF1-ABCE1. *Cell Rep* 8: 59–65
- Prokhorova I, Altman RB, Djumagulov M, Shrestha JP, Urzhumtsev A, Ferguson A, Chang CT, Yusupov M, Blanchard SC, Yusupova G (2017) Aminoglycoside interactions and impacts on the eukaryotic ribosome. *Proc Natl Acad Sci USA* 114: E10899–E10908
- Rohou A, Grigorieff N (2015) CTFFIND4: Fast and accurate defocus estimation from electron micrographs. *J Struct Biol* 192: 216–221
- Scheres SH (2012) RELION: implementation of a Bayesian approach to cryo-EM structure determination. *J Struct Biol* 180: 519–530
- Schlutzen F, Tocilj A, Zarivach R, Harms J, Gluehmann M, Janell D, Bashan A, Bartels H, Agmon I, Franceschi F, et al (2000) Structure of functionally activated small ribosomal subunit at 3.3 angstroms resolution. *Cell* 102: 615–623
- Schmitt E, Blanquet S, Mechulam Y (2002) The large subunit of initiation factor aIF2 is a close structural homologue of elongation factors. *EMBO J* 21: 1821–1832
- Schmitt E, Panvert M, Lazennec-Schurdevin C, Coureux PD, Perez J, Thompson A, Mechulam Y (2012) Structure of the ternary initiation complex aIF2-GDPNP-methionylated initiator tRNA. *Nat Struct Mol Biol* 19: 450–454
- Sha Z, Brill LM, Cabrera R, Kleinfeld O, Scheliga JS, Glickman MH, Chang EC, Wolf DA (2009) The eIF3 interactome reveals the translatome, a supercomplex linking protein synthesis and degradation machineries. *Mol Cell* 36: 141–152
- Shao S, Brown A, Santhanam B, Hegde RS (2015) Structure and assembly pathway of the ribosome quality control complex. *Mol Cell* 57: 433–444
- Shoemaker CJ, Green R (2011) Kinetic analysis reveals the ordered coupling of translation termination and ribosome recycling in yeast. *Proc Natl Acad Sci USA* 108: E1392–E1398
- Simonetti A, Brito Querido J, Myasnikov AG, Mancera-Martinez E, Renaud A, Kuhn L, Hashem Y (2016) eIF3 Peripheral Subunits Rearrangement after mRNA Binding and Start-Codon Recognition. *Mol Cell* 63: 206–217
- Sokabe M, Fraser CS, Hershey JW (2012) The human translation initiation multi-factor complex promotes methionyl-tRNAi binding to the 40S ribosomal subunit. *Nucleic Acids Res* 40: 905–913
- Srivastava S, Verschoor A, Frank J (1992) Eukaryotic initiation factor 3 does not prevent association through physical blockage of the ribosomal subunit-subunit interface. *J Mol Biol* 226: 301–304
- Tyanova S, Temu T, Sinitcyn P, Carlson A, Hein MY, Geiger T, Mann M, Cox J (2016) The Perseus computational platform for comprehensive analysis of (prote)omics data. *Nat Methods* 13: 731–740
- Valasek L, Hasek J, Trachsel H, Imre EM, Ruis H (1999) The *Saccharomyces cerevisiae* HCR1 gene encoding a homologue of the p35 subunit of human translation initiation factor 3 (eIF3) is a high copy suppressor of a temperature-sensitive mutation in the Rpg1p subunit of yeast eIF3. *J Biol Chem* 274: 27567–27572
- Valasek L, Mathew AA, Shin BS, Nielsen KH, Szamecz B, Hinnebusch AG (2003) The yeast eIF3 subunits TIF32/a, NIP1/c, and eIF5 make critical connections with the 40S ribosome in vivo. *Genes Dev* 17: 786–799
- Valasek L, Nielsen KH, Hinnebusch AG (2002) Direct eIF2-eIF3 contact in the multifactor complex is important for translation initiation in vivo. *EMBO J* 21: 5886–5898
- Valasek L, Nielsen KH, Zhang F, Fekete CA, Hinnebusch AG (2004) Interactions of eukaryotic translation initiation factor 3 (eIF3) subunit NIP1/c with eIF1 and eIF5 promote preinitiation complex assembly and regulate start codon selection. *Mol Cell Biol* 24: 9437–9455
- Valasek L, Phan L, Schoenfeld LW, Valaskova V, Hinnebusch AG (2001) Related eIF3 subunits TIF32 and HCR1 interact with an RNA recognition motif in PRT1 required for eIF3 integrity and ribosome binding. *EMBO J* 20: 891–904
- Valasek LS, Zeman J, Wagner S, Beznoskova P, Pavlikova Z, Mohammad MP, Hronova V, Herrmannova A, Hashem Y, Gunisova S (2017) Embraced by eIF3: structural and functional insights into the roles of eIF3 across the translation cycle. *Nucleic Acids Res* 45: 10948–10968
- Walker SE, Zhou F, Mitchell SF, Larson VS, Valasek L, Hinnebusch AG, Lorsch JR (2013) Yeast eIF4B binds to the head of the 40S ribosomal subunit and promotes mRNA recruitment through its N-terminal and internal repeat domains. *RNA* 19: 191–207
- Walzthoeni T, Claassen M, Leitner A, Herzog F, Bohn S, Forster F, Beck M, Aebersold R (2012) False discovery rate estimation for cross-linked peptides identified by mass spectrometry. *Nat Methods* 9: 901–903
- Waterhouse A, Bertoni M, Bienert S, Studer G, Tauriello G, Gumienny R, Heer FT, de Beer TAP, Rempfer C, Bordoli L, et al (2018) SWISS-MODEL: homology modelling of protein structures and complexes. *Nucleic Acids Res* 46: W296–W303
- Waterhouse AM, Procter JB, Martin DM, Clamp M, Barton GJ (2009) Jalview Version 2—a multiple sequence alignment editor and analysis workbench. *Bioinformatics* 25: 1189–1191
- Wessel D, Flugge UI (1984) A method for the quantitative recovery of protein in dilute solution in the presence of detergents and lipids. *Anal Biochem* 138: 141–143
- Yamamoto Y, Singh CR, Marintchev A, Hall NS, Hannig EM, Wagner G, Asano K (2005) The eukaryotic initiation factor (eIF) 5 HEAT domain mediates multifactor assembly and scanning with distinct interfaces to eIF1, eIF2, eIF3, and eIF4G. *Proc Natl Acad Sci USA* 102: 16164–16169
- Young DJ, Guydosh NR (2019) Hcr1/eIF3j Is a 60S Ribosomal Subunit Recycling Accessory Factor In Vivo. *Cell Rep* 28: 39–50
- Yu Y, Marintchev A, Kolupaeva VG, Unbehauen A, Varyasova T, Lai SC, Hong P, Wagner G, Hellen CU, Pestova TV (2009) Position of eukaryotic translation initiation factor eIF1A on the 40S ribosomal subunit mapped by directed hydroxyl radical probing. *Nucleic Acids Res* 37: 5167–5182
- Zeman J, Itoh Y, Kukacka Z, Rosulek M, Kavan D, Kouba T, Jansen ME, Mohammad MP, Novak P, Valasek LS (2019) Binding of eIF3 in complex

- with eIF5 and eIF1 to the 40S ribosomal subunit is accompanied by dramatic structural changes. *Nucleic Acids Res* 47: 8282–8300
- Zhang E, Khanna V, Dacheux E, Namane A, Doyen A, Gomard M, Turcotte B, Jacquier A, Fromont-Racine M (2019) A specialised SKI complex assists the cytoplasmic RNA exosome in the absence of direct association with ribosomes. *EMBO J* 38: e100640
- Zhang K (2016) Gctf: Real-time CTF determination and correction. *J Struct Biol* 193: 1–12
- Zheng SQ, Palovcak E, Armache J-P, Verba KA, Cheng Y, Agard DA (2017) MotionCor2: anisotropic correction of beam-induced motion for improved cryo-electron microscopy. *Nature methods* 14: 331–332
- Zimmermann L, Stephens A, Nam SZ, Rau D, Kubler J, Lozajic M, Gabler F, Soding J, Lupas AN, Alva V (2018) A Completely Reimplemented MPI Bioinformatics Toolkit with a New HHpred Server at its Core. *J Mol Biol* 430: 2237–2243
- Zivanov J, Nakane T, Forsberg BO, Kimanius D, Hagen WJ, Lindahl E, Scheres SH (2018) New tools for automated high-resolution cryo-EM structure determination in RELION-3. *Elife* 7: e42166



License: This is an open access article under the terms of the Creative Commons Attribution-NonCommercial-NoDerivs 4.0 License, which permits use and distribution in any medium, provided the original work is properly cited, the use is non-commercial and no modifications or adaptations are made.

Expanded View Figures

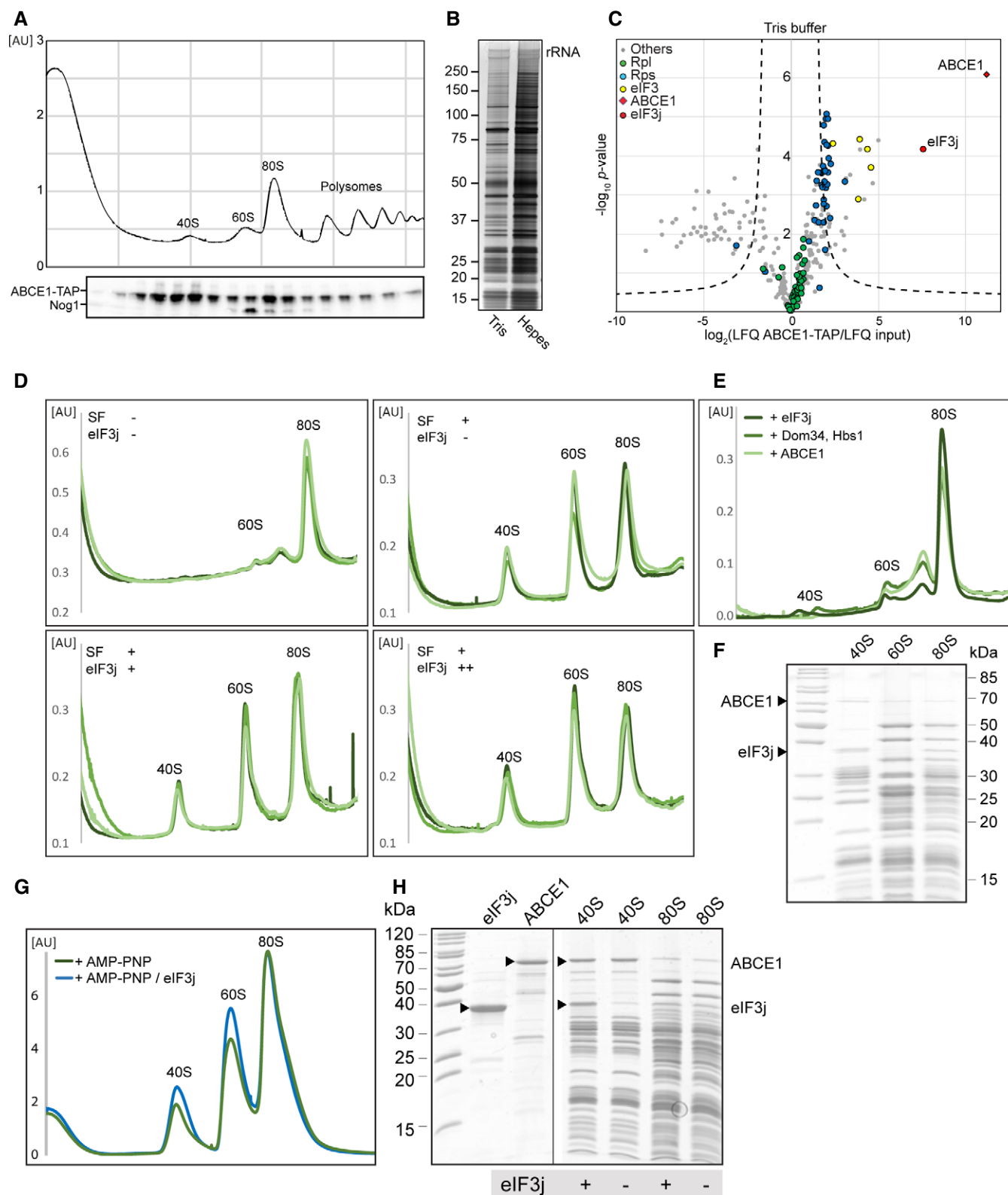


Figure EV1.

Figure EV1. Enrichment of ABCE1 and eIF3j on 40S complexes and assessment of their role in splitting of 80S ribosomes.

- A Total cellular extracts from yeast cells expressing ABCE1-TAP were separated on a sucrose gradient (10–50%) by ultracentrifugation. Proteins of each fraction were analyzed by Western blot using a PAP antibody for the detection of the ABCE1-TAP fusion protein and anti-Nog1 antibody to mark the 60S fraction. AU—absorption units at 260 nm.
- B Silver-stained NuPAGE gel showing elution from affinity purification using ABCE1-TAP performed in Tris or HEPES buffer (see Materials and Methods for details).
- C Volcano plot showing the fold enrichment of proteins in the elution fraction from the ABCE1-TAP purification in Tris buffer followed by mass spectrometry analysis (LC-MS/MS). The enrichment was calculated relative to an “input” corresponding to an aliquot of the ABCE1-TAP cell lysate used for the affinity purification. It is represented, on the x-axis, as $\log_2(\text{LFQ ABCE1-TAP}/\text{LFQ input})$ where LFQ stands for label-free quantification. The y-axis represents the P-value distribution ($-\log_{10} p\text{-value}$) calculated using Student's t-test for all identified proteins represented by a circle. Proteins above the curved lines show a statistically significant enrichment according to the t-test value. The assay was performed in triplicates.
- D UV profiles from *in vitro* splitting reaction triplicates with and without splitting factors (SF; ABCE1, Dom34, Hbs1, and eIF6) and eIF3j. Samples were separated on a sucrose gradient (10–50%) by ultracentrifugation. (+) = 4-fold molar excess of eIF3j; (++) = 20-fold molar excess of eIF3j.
- E Relative abundance of 80S and subunits in each experiment, as calculated from triplicates shown in (D).
- F SDS-PAGE of the 40S, 60S, and 80S peaks obtained from the *in vitro* splitting experiment (D) containing SFs and high amounts of eIF3j.
- G UV profiles from *in vitro* “facilitated” splitting reactions. Samples were separated on a sucrose gradient (10–50%) by ultracentrifugation.
- H SDS-PAGE of the input factors (eIF3j and ABCE1) as well as 40S and 80S peaks from the “facilitated” splitting experiment. ABCE1 and eIF3j are marked by arrows, respectively.

Figure EV2. Resolution and model fitting of the human 43S PIC.

- A Gold standard Fourier Shell Correlation (FSC) curve for individual bodies in multi-body refinements (40S head including eIF3d, 40S body including eIF3c-NTD and eIF1A, two bodies of the eIF3 PCI-MPN core) and focused refinements using soft binary masks (ABCE1 and the TC).
- B Composite map of 40S head and body after multi-body refinement colored and low-pass filtered according to local resolution.
- C Composite map of the eIF3 MPN-PCI core (left) after multi-body refinement with two bodies (right), filtered according to local resolution. Structural hallmarks are color coded in the composite map as shown in Fig 5A, and the two bodies are colored according to local resolution.
- D Focused refined map of the masked region containing ABCE1, filtered according to local resolution, and colored for ABCE1 (left). Two views are shown colored according to local resolution (right).
- E Same as in (D) for eIF1, eIF1A, and the TC.

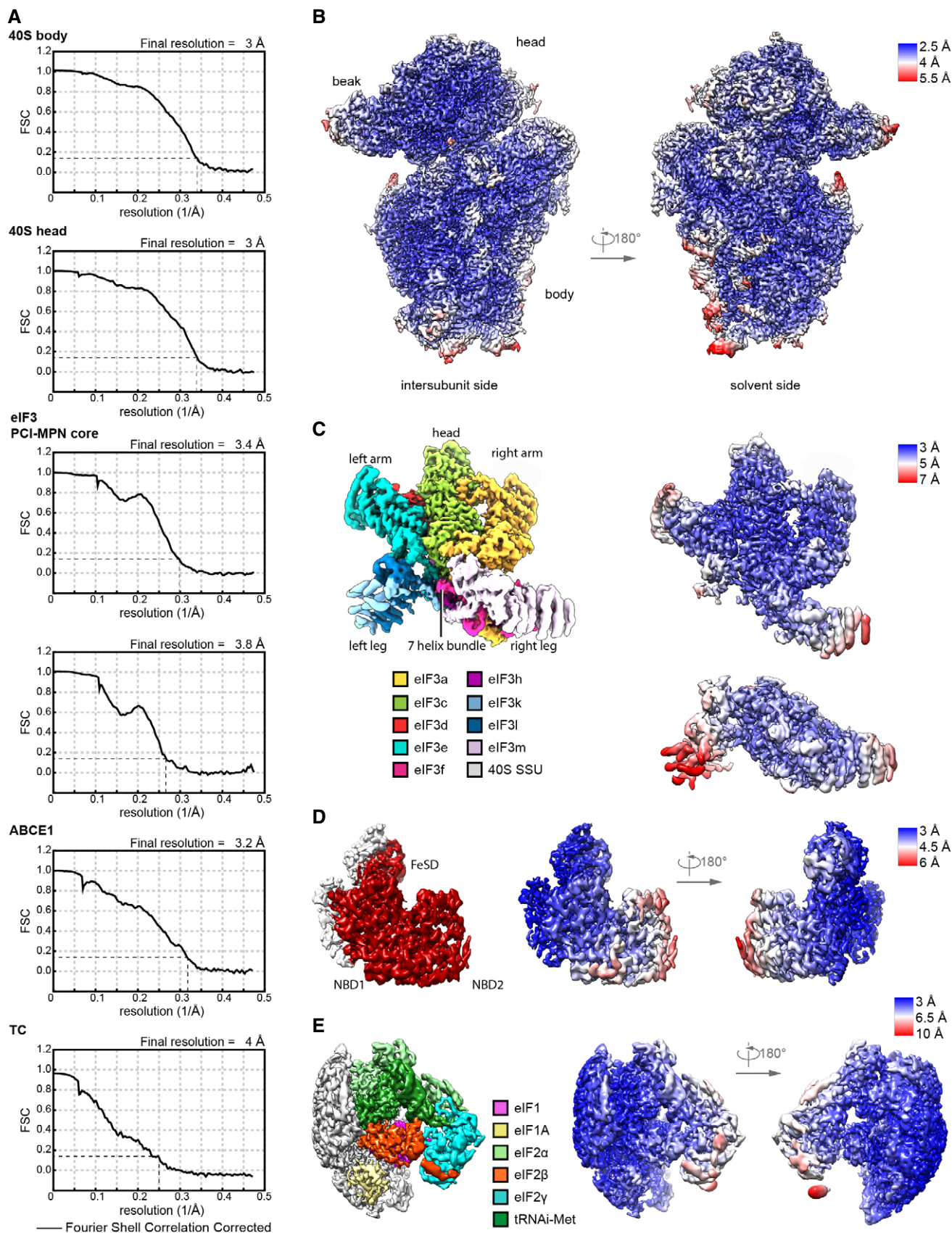


Figure EV2.

Figure EV3. Density fits of ABCE1 and alignment, model and ribosome binding of human and yeast eIF3j.

- A Model for ABCE1 fit into low-pass-filtered density to demonstrate the hybrid semi-open/closed conformation of ABCE1 in native yeast and human 43S PICs.
- B Schemes of *H.s.* and *S.c.* eIF3j indicating the length of N- and C-termini; the three helices present in the crystal structure of human eIF3j (PDB 3BPJ) are indicated.
- C View highlighting the rearrangement (100-degree rotation) of eIF3 in the human (eIF1A-lacking) and yeast (eIF1A-containing) 43S PICs.
- D Alignment between *H.s.* and *S.c.* eIF3j shows 24.6% identity and 53.1% similarity for the full-length protein. Dark blue boxes indicate conservation, light blue boxes indicate similarity. For the sequence (three α -helices) present in the human X-ray structure (PDB 3BPJ) from residues 144-213 in protomer 1 and 144-216 in protomer 2, identity/similarity is 32.4%/66.2%, corroborating the reliability of the yeast homology model.
- E, F Fits of the human eIF3j crystal structure and the yeast homology model into the corresponding density.
- G Interactions of the eIF3j C-terminus (protomer 2) with the 40S head and body shown with models fit into the cryo-EM map of the crosslinked yeast 43S-PIC.
- H Schematic representation summarizing interactions of the eIF3j C-terminus with the 40S. Colored boxes indicate residues interacting with eIF3j, with brown representing 18S rRNA, purple representing uS3, and green representing eS10.

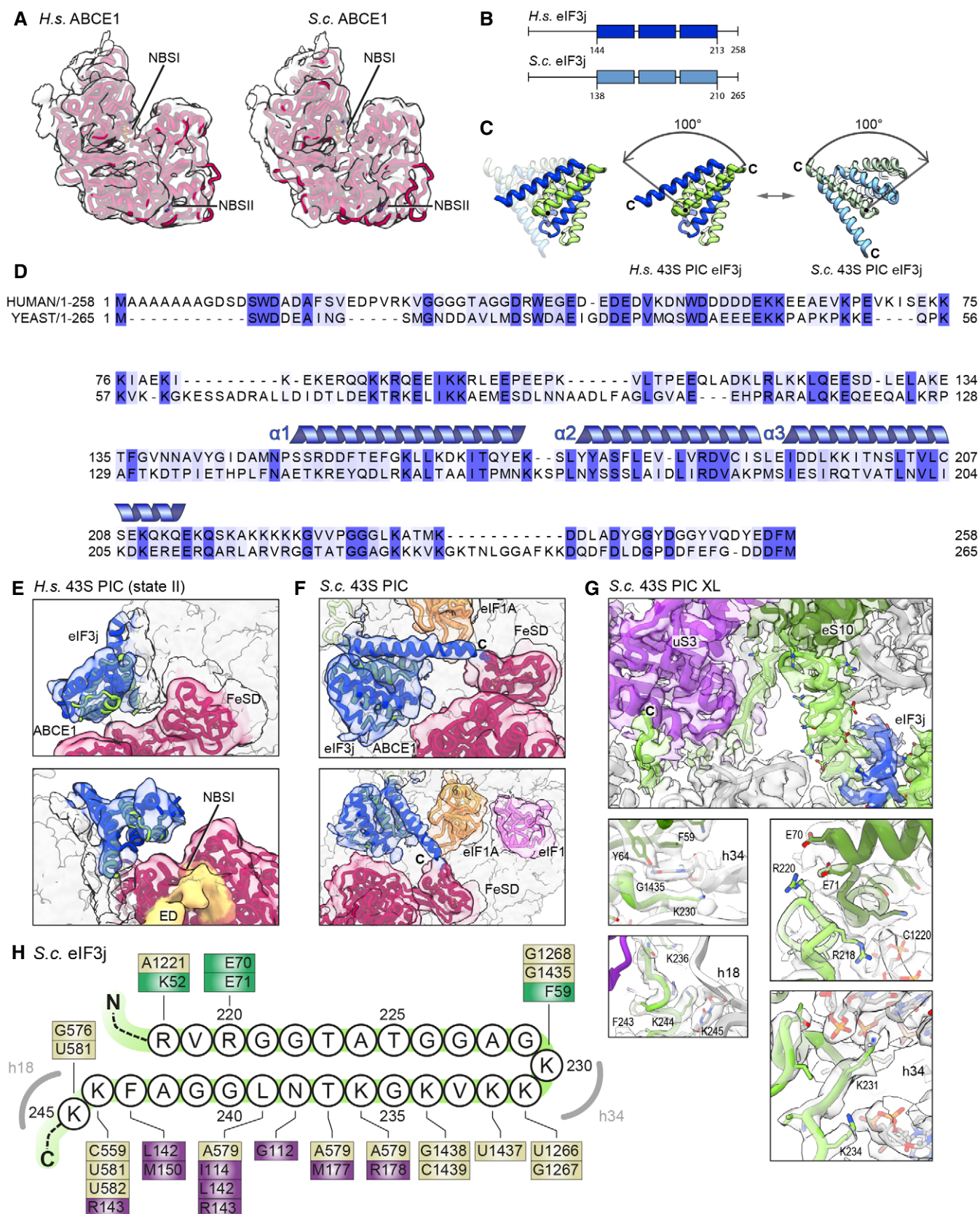


Figure EV3.

Figure EV4. Molecular interactions of eIF3d and the PCI-MPN core in the 43S PIC shown with density.

- A PCI arc of the PCI-MPN core; zoomed views highlighting fits of the eIF3 PCI arc into the refined density and interactions between the subunits in the PCI-MPN core.
- B eIF3a and eIF3c interactions with the 40S.
- C Left, Middle: Interactions of the eIF3d N-terminal tail with the PCI-MPN core: Interactions of the ultimate eIF3d N-terminus (Phe4-Pro18) with eIF3e are established *via* Phe4 (to Tyr32 in loop between PCI helices $\alpha 2$ and $\alpha 3$), Gln10 (to His12 in $\alpha 1$), Ile9 and Asp11 (to Arg16 in $\alpha 2$), Ser14 (to Asn164 $\alpha 9$ and Phe132 in $\alpha 7$), Trp16 (to Gly171 in $\alpha 10$), and Gly17 (to Trp170 in $\alpha 10$). eIF3d residues 25-36 are bridging eIF3e and eIF3c. Residues involved are Tyr30 (to Leu208 in eIF3e PCI helix $\alpha 12$), Phe33 (to the peptide backbone of Leu590 in eIF3c $\alpha 11$), and Lys35 (to Gln283 in eIF3e $\alpha 16$). eIF3c-specific interactions are established by Leu39 (to Gln595), Trp45 (Pro603, Ile607, and Glu666), and Thr46 (to Arg641) (see Table S3). For clarity, only density for eIF3d is shown (gray transparent surface). Right: Detailed view of the interaction of F80 (eIF3d) with K36 and R80 (eS27). Density is shown for both proteins (gray transparent surface). Below: MSA of the conserved N-terminal region of eIF3d is shown. Coloring according to default Clustal X color scheme (blue: hydrophobic, magenta: negative charge, red: positive charge, green: polar, orange: glycine, yellow: proline, pink: cysteine, cyan: aromatic).
- D Interactions of the eIF3d C-terminal domain with the 40S head and zoomed views of uS7 and eS28 interaction sites shown with density.

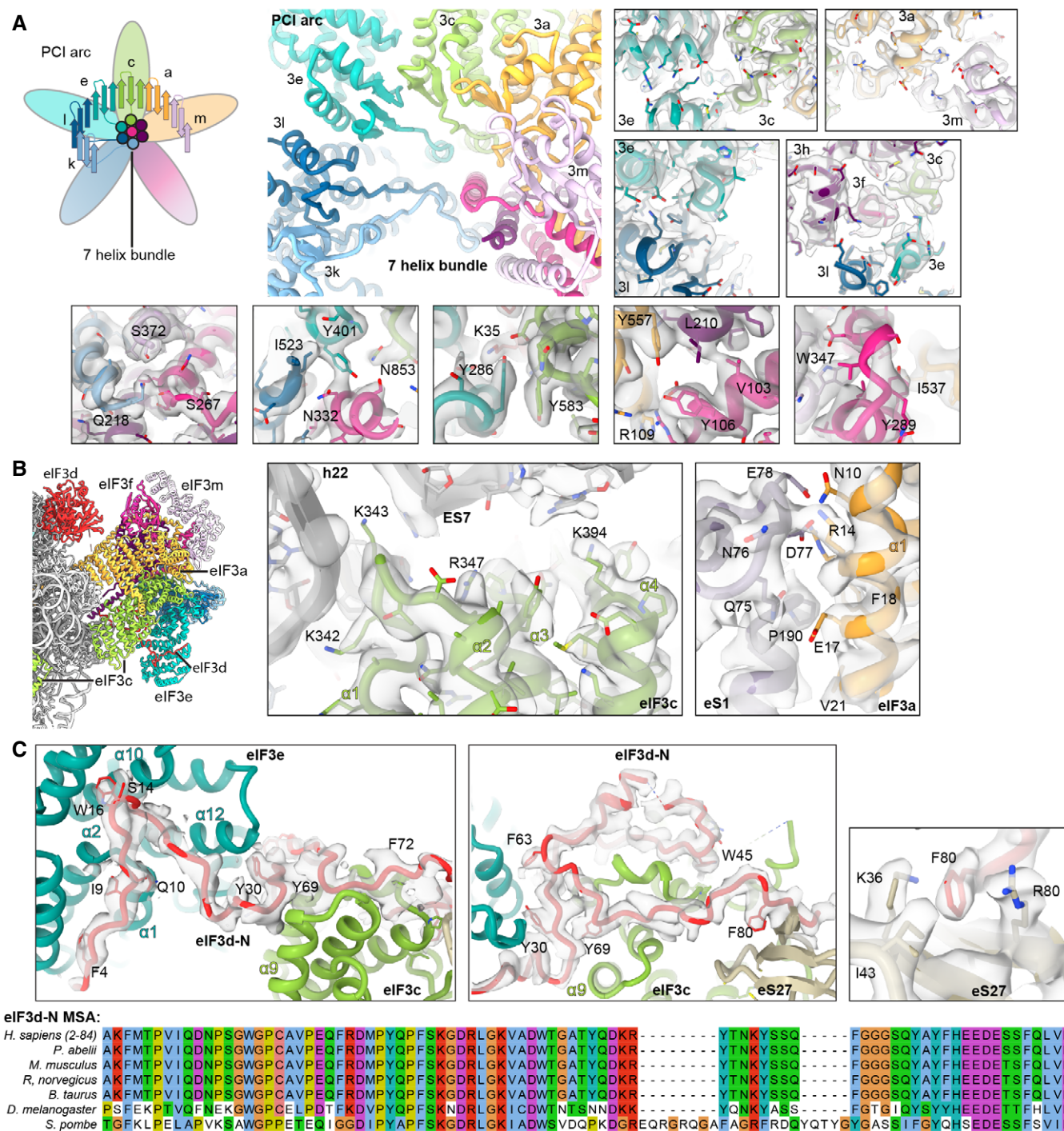


Figure EV4.

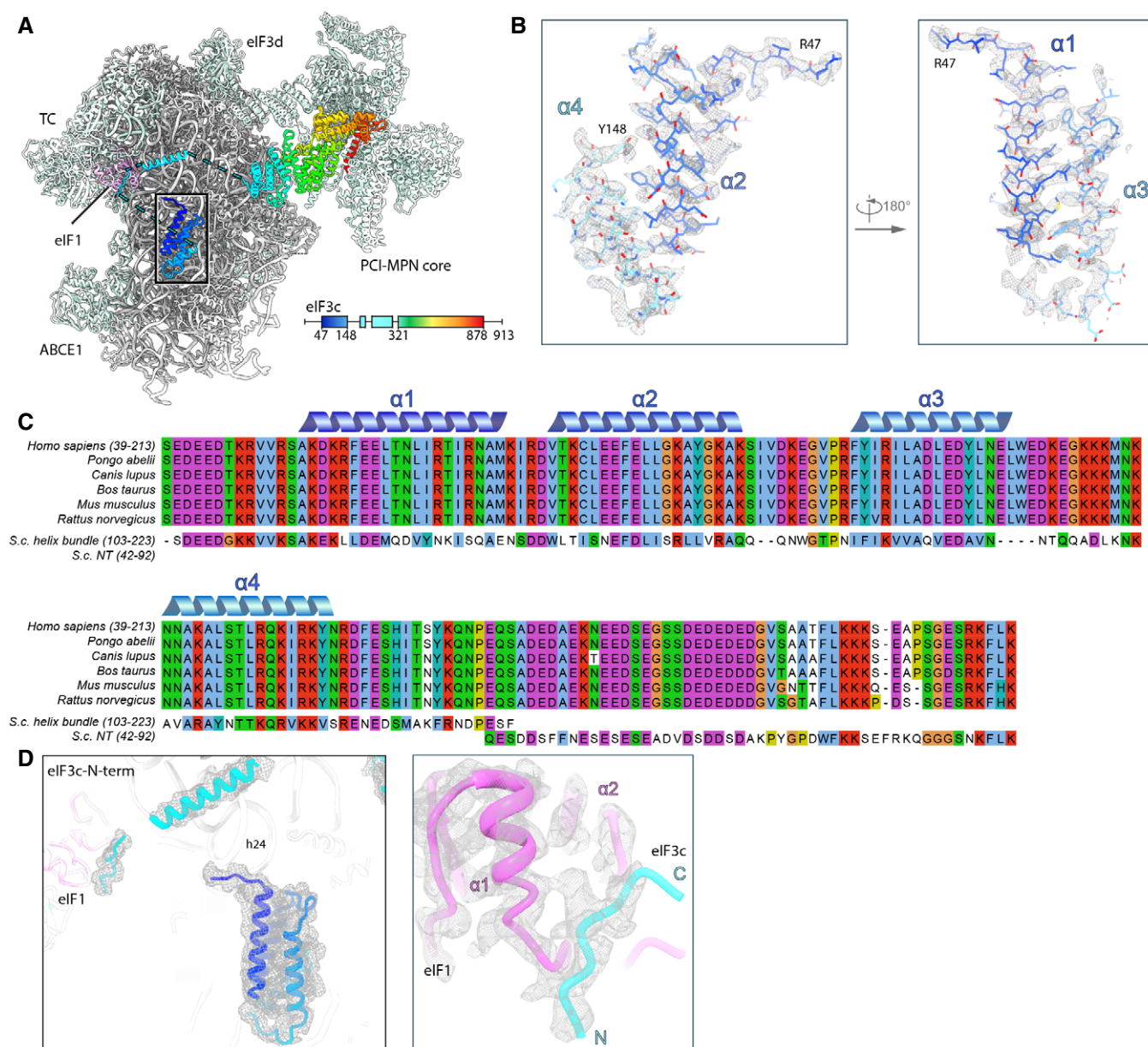


Figure EV5. Model fitting and sequence alignment of the eIF3c-NTD.

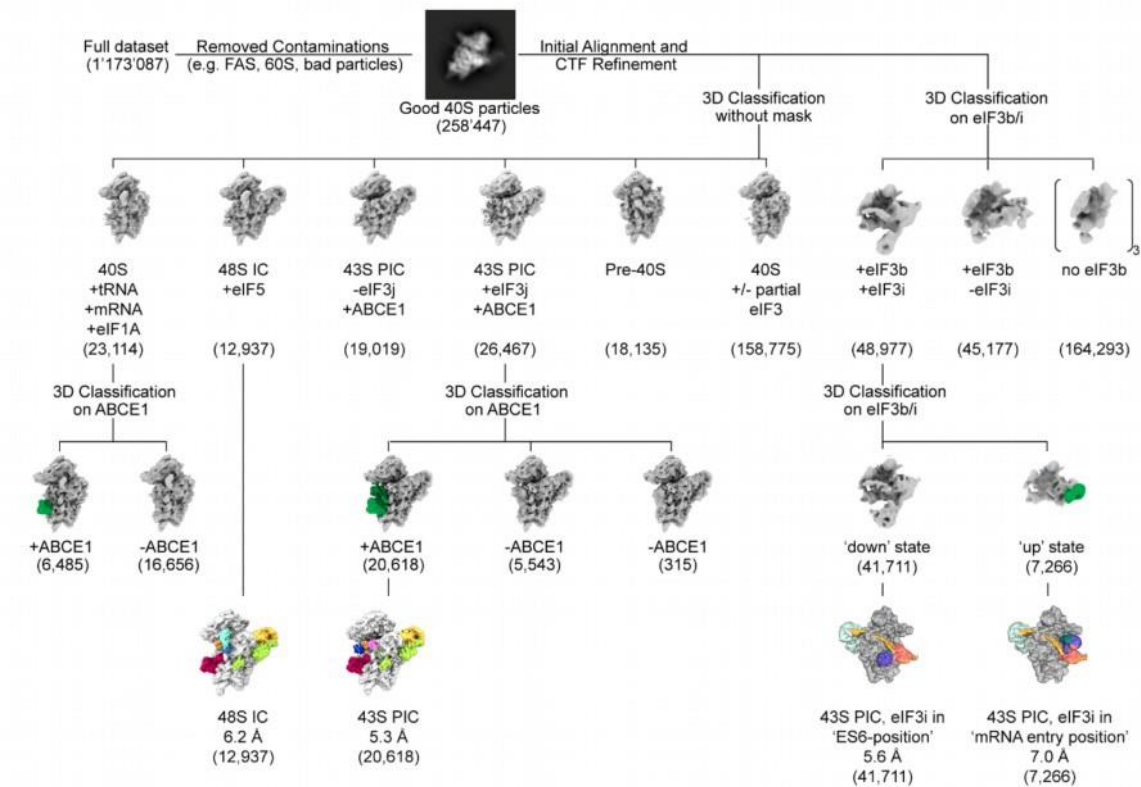
- A Overview of the TC-containing human 43S PIC as shown in Fig 6 and scheme indicating the parts of eIF3c modeled. Black box indicates section of eIF3c highlighted in (B).
- B Zoomed views highlighting fits of the eIF3c-NTD 4-helix bundle into the refined density (gray transparent mesh). The N- and C-terminal residues are marked.
- C MSA of the conserved N-terminal region of eIF3c in mammals (Ser39-Lys213 in *H.s.*), aligned with segments of the NTD from *S.c.*. Coloring according to default Clustal X color scheme (blue: hydrophobic, magenta: negative charge, red: positive charge, green: polar, orange: glycine, yellow: proline, pink: cysteine, cyan: aromatic). The 4-helix bundle shows 31.1/67.2% sequence identity/similarity, and the eIF1-interacting stretch present in the N-terminus of *S.c.* eIF3c (Gln42-Lys92) shows 32.0/56.0% sequence identity/similarity with a mammalia-specific insert C-terminal of the conserved 4-helix bundle.
- D eIF3c-NTD in the human 43S PIC fitted into the cryo-EM map and zoomed view showing the fit of the eIF1-interacting stretch of eIF3c into the cryo-EM map.

Appendix

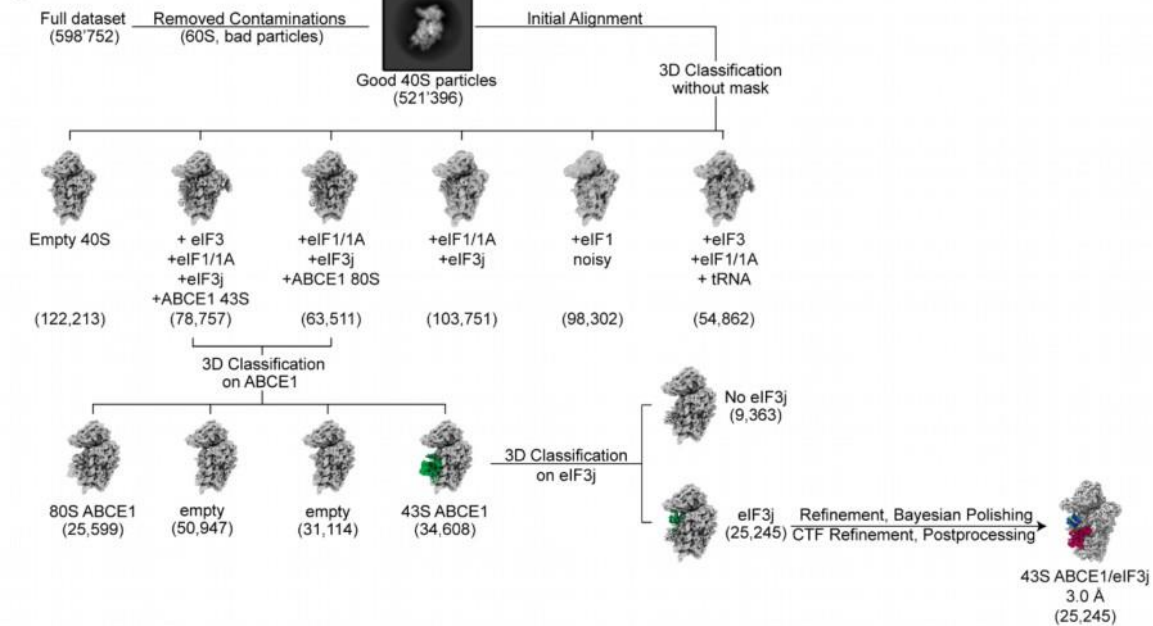
Table of contents

Appendix Figure S1 - Sorting scheme for the yeast native 40S sample and the 43S-PIC-XL sample.	2
Appendix Figure S2 - Sorting scheme for the human native small 40S sample.	3
Appendix Figure S3 - Overview and resolution of the yeast 43S PIC and 48S IC.	5
Appendix Figure S4 - Sample preparation and cryo-EM structure of the yeast 43S PIC-XL.	6
Appendix Figure S5 - Crosslink derived connectivity network of the yeast ABCE1 43S PIC.	7
Appendix Figure S6 - Corrected register shifts in the helices of the PCI-MPN core in the human 43S PIC.	8
Appendix Figure S7 - Position of the eIF3 YLC and the eIF3a-CTD in yeast and human 43S PICs.	9
Appendix Figure S8 - Position of the eIF3g or eIF4b RRM and density in the mRNA channel.	10
Appendix Figure S9 - Molecular interactions of the TC in the complete human 43S PIC.	11
Appendix Table S1 - Data collection, refinement, and model composition of the yeast initiation complexes.	12
Appendix Table S2 - Data collection, refinement, and validation statistics of the human 43S PIC.	13
Appendix Table S3 - Crosslinks identified on a yeast ABCE1-43S PIC.	14
Appendix Table S4 - Molecular interactions between eIF3 subunits and 40S.	19
Appendix Text 1 - Molecular interactions between eIF3j and the 40S subunit in the yeast 43S-PIC.	20
Appendix References	21

A



B

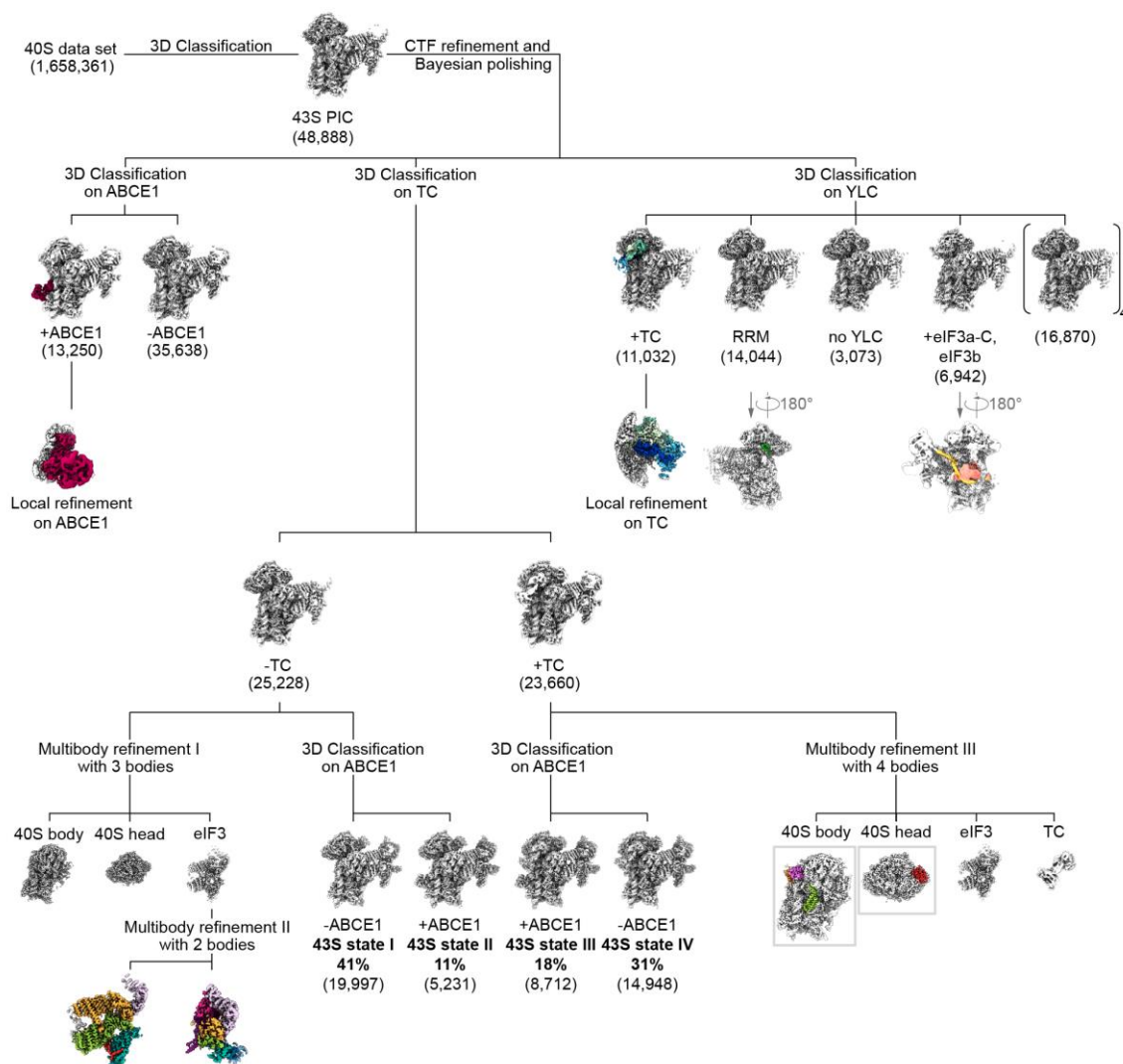


Appendix Figure S1 - Sorting scheme for the yeast native 40S sample and the 43S-PIC-XL sample.

A After 2D classification of the full dataset, approximately 260.000 particles representing 40S subunits were selected. By 3D classification into six classes, 29% of the particles were unambiguously identified as pre-initiation complexes, amongst them a 43S PIC class containing eIF1, eIF1A, eIF3 and ABCE1 with stably bound eIF3j and one class representing a partial 48S initiation complex containing eIF1A, eIF3, eIF5, the TC, and ABCE1. The 48S IC was refined to 6.2 Å and the eIF3j-containing 43S was sub-classified for ABCE1, yielding a 5.3 Å

reconstruction of the 43S PIC. In total, 62% of the found initiation-factor-containing 40S particles contained ABCE1 after focused classification for ABCE1 presence. Independently, focused classification on the particles containing the eIF3b/i/g module was performed to assess conformational distribution of eIF3i/g with respect to eIF3b. 85% of the particles contained eIF3i in the “ES6-position”, while in 15% of particles, eIF3i was in the “mRNA entry-position”.

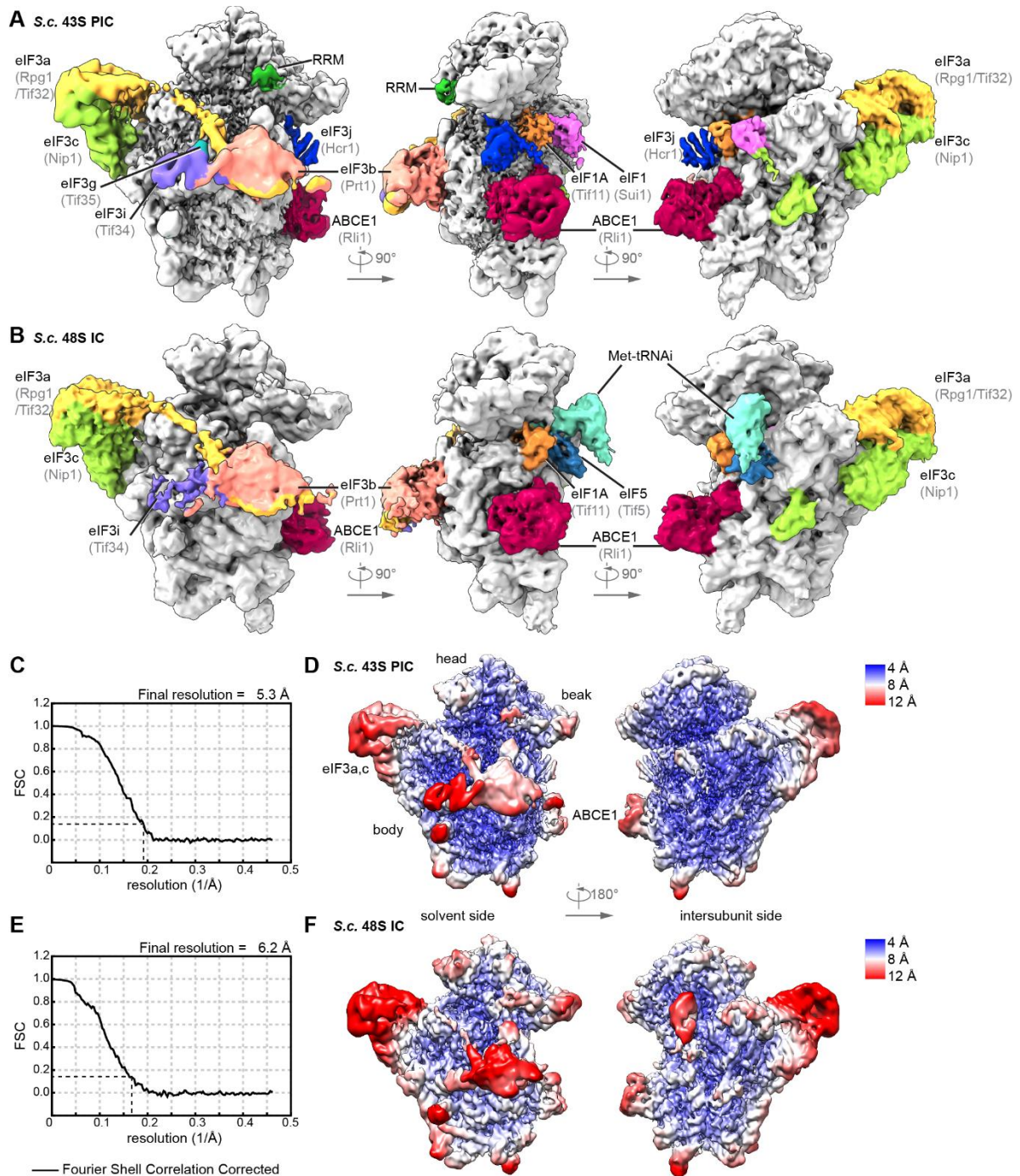
B After 2D classification of the full dataset, 521,396 particles representing 40S subunits were selected. By 3D classification into six classes, two classes containing ABCE1 were identified. These were subclassified by sequentially using a mask on the ABCE1 region as well as a mask on eIF3j, in order to identify one class containing both eIF3j and ABCE1 in the semi-open conformation as observed in the native sample. This class represents 4.8% of the total dataset and was refined to 3.0 Å.



Appendix Figure S2 - Sorting scheme for the human native small 40S sample.

The data set was first classified for presence of initiation factors (see Materials and Methods). 2.9% of all particles contained the eIF3 PCI-MPN core at the back side of the 40S and partial densities for the YLC at the mRNA entry site, the TC in the ISS, and ABCE1. Focused classifications were performed using a binary mask with soft edges

to obtain homogenous populations of 43S complexes. Focused classification on the TC yielded two classes with and without the TC that also differed in the conformation of the 40S head (closed latch without TC and P_{OUT} state). These two classes were sub-classified focusing on ABCE1, yielding the four main classes shown in Fig. 2. To obtain the highest possible resolution, we independently performed multi-body refinements on TC-bound and -unbound classes. The TC-lacking class containing the eIF3-PCI-MPN core was refined in two steps: first, the 43S was divided into three bodies (40S body, 40S head and eIF3; multi-body refinement I). Then the body containing the eIF3-PCI-MPN core was re-centered, the 40S SSU signal subtracted and a multi-body refinement with two bodies was performed (multi-body refinement II) that were used for model building. Particles containing the TC were subjected to multi-body refinement III with four bodies (40S body and head, eIF3-PCI-MPN core and TC) yielding well-resolved densities for the eIF3c-NTD on the body and eIF3d on the head used for model building. Classification of the entire 43S data set focusing on ABCE1 followed by focused refinement yielded a well-resolved map from 27% ABCE1-containing particles used for model building. Focused classification on the YLC revealed various compositional and conformational states. One class represented a very stable complete 43S complex in P_{OUT} state and focused refinement yielded a well-resolved map of the TC used for model building. A focused refinement resulted in the best resolved map for the TC, which could be used for model building; two other classes were enriched in stably bound YLC, one showing the clear connection between the PCI-MPN core and the YLC and one with a well-resolved density for a RRM adjacent to the mRNA entry site and density in the mRNA channel.

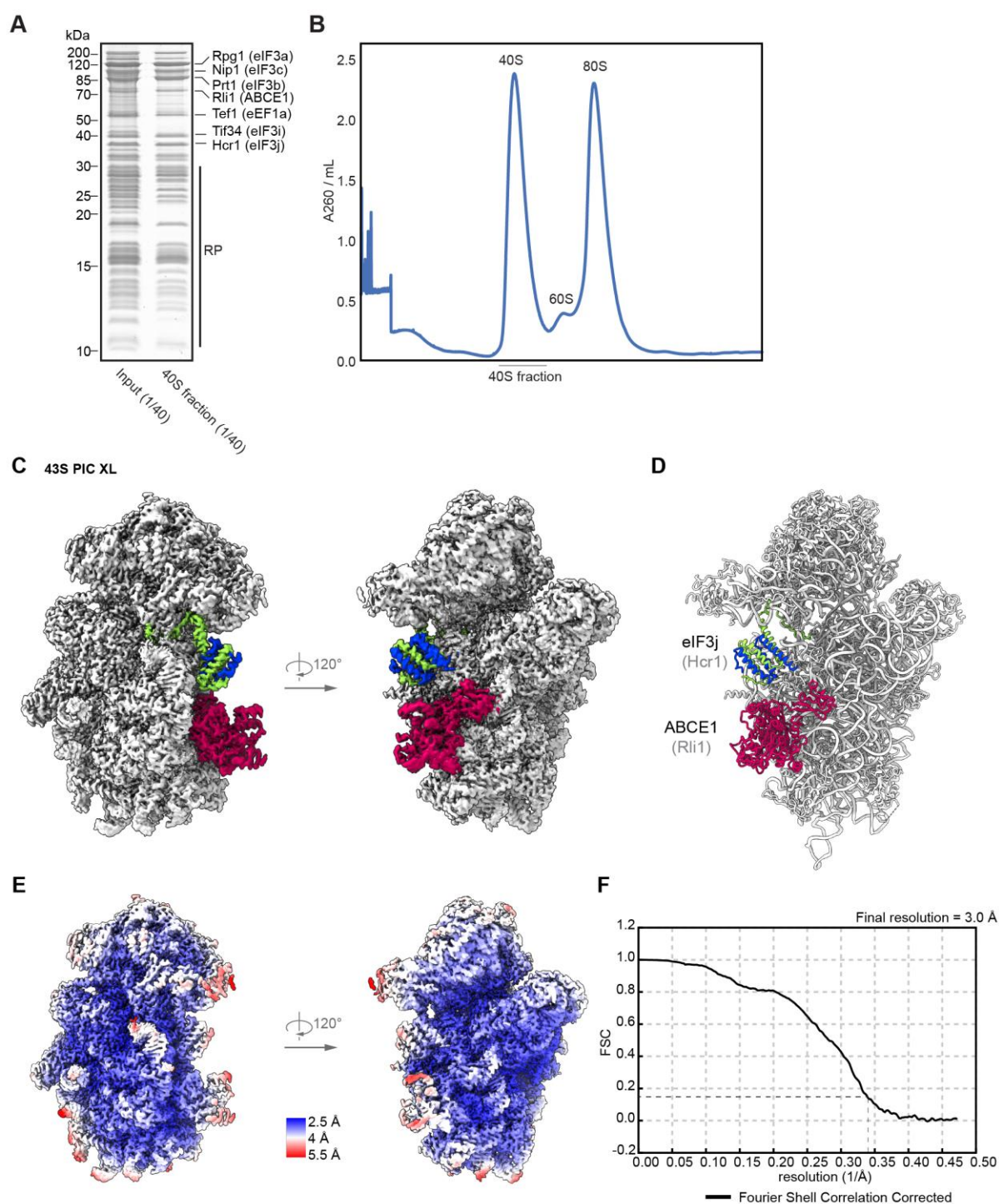


Appendix Figure S3 - Overview and resolution of the yeast 43S PIC and 48S IC.

A, B Three views on the 3D reconstructions of the yeast 43S PIC (A) and the 48S IC (B) low-pass filtered according to local resolution.

C, D Gold standard Fourier Shell Correlation (FSC) curve (C) and 3D reconstruction the yeast 43S PIC colored and filtered according to local resolution (D).

E, F Gold standard Fourier Shell Correlation (FSC) curve (E) and 3D reconstruction the yeast 48S IC colored and low-pass filtered according to local resolution (F).



Appendix Figure S4 - Sample preparation and cryo-EM structure of the yeast 43S PIC-XL.

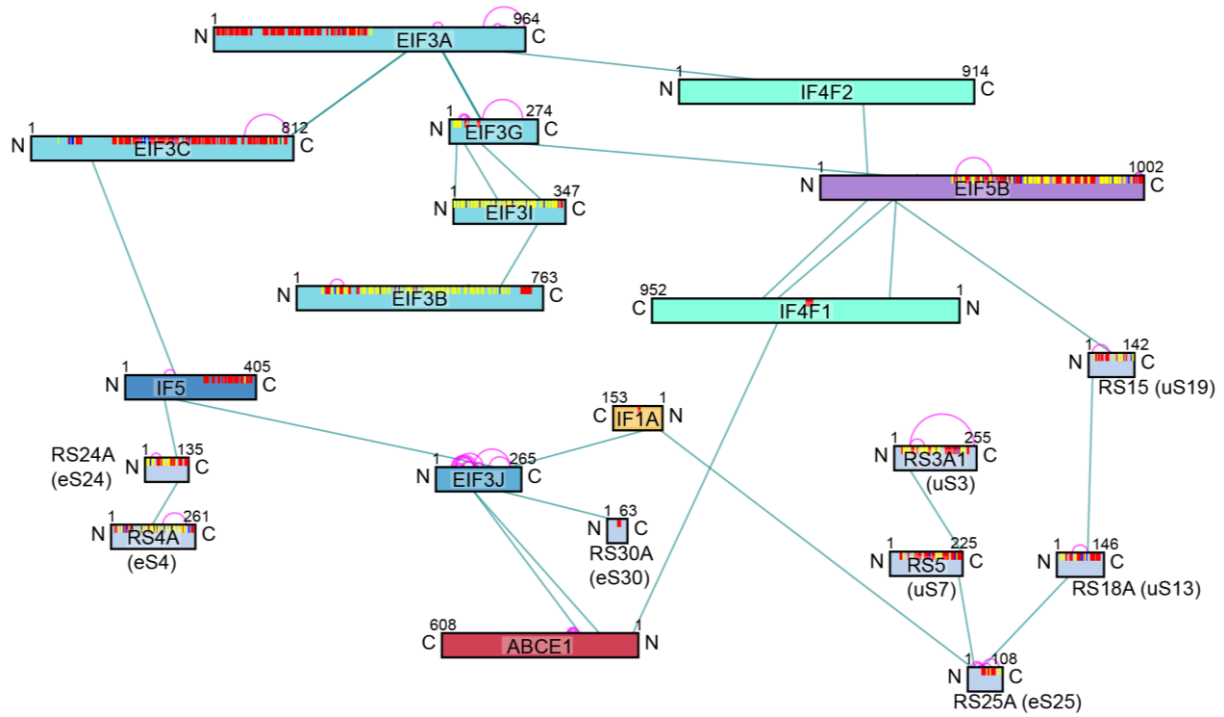
A SDS-PAGE gel of the Nip1-TAP pullout sample before and after sucrose gradient purification.

B UV profile from Nip1-TAP pullout elution fraction separated on a sucrose gradient (10–50%) by ultracentrifugation.

C Two views of the 3D reconstruction of the yeast 43S PIC-XL, low-pass filtered at local resolution.

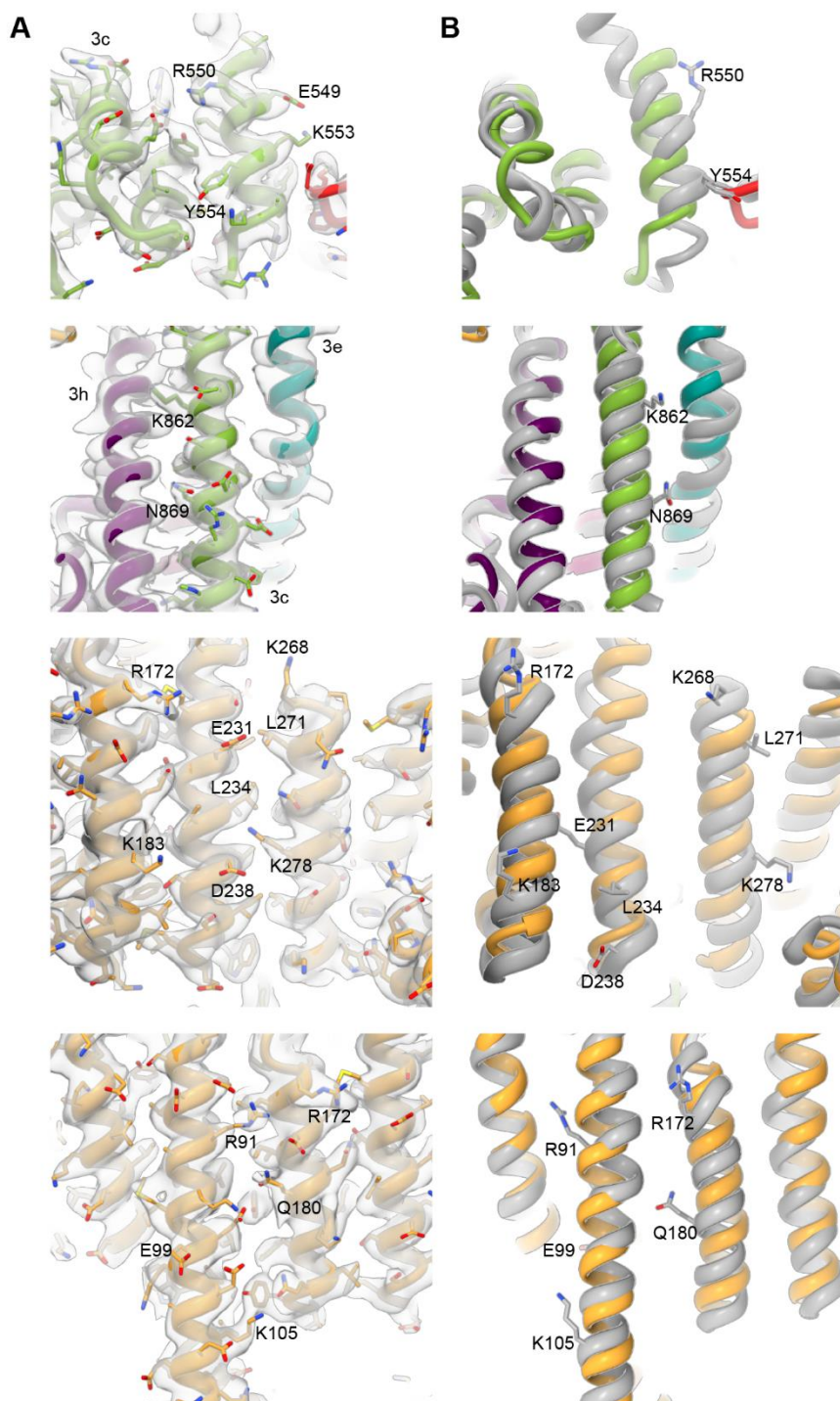
D Atomic model of the yeast 43S PIC-XL.

E, F 3D reconstruction the yeast 43S PIC-XL colored and low-pass filtered according to local resolution (E) and gold standard Fourier Shell Correlation (FSC) curve (F).



Appendix Figure S5 - Crosslink derived connectivity network of the yeast ABCE1 43S PIC.

ABCE1-43S pre-initiation complex was affinity-purified from yeast cell extracts using TAP-tagged Nip1 (eIF3c) protein. Schematic representation of the obtained 43 inter-protein and 74 intra-protein crosslinks (Appendix Table 3) with a focus on initiation factors and ABCE1. Proteins are represented as bars with subunits and secondary structures indicated according to UniProt color scheme. The lengths of protein and crosslinks are scaled to the amino acid sequence.

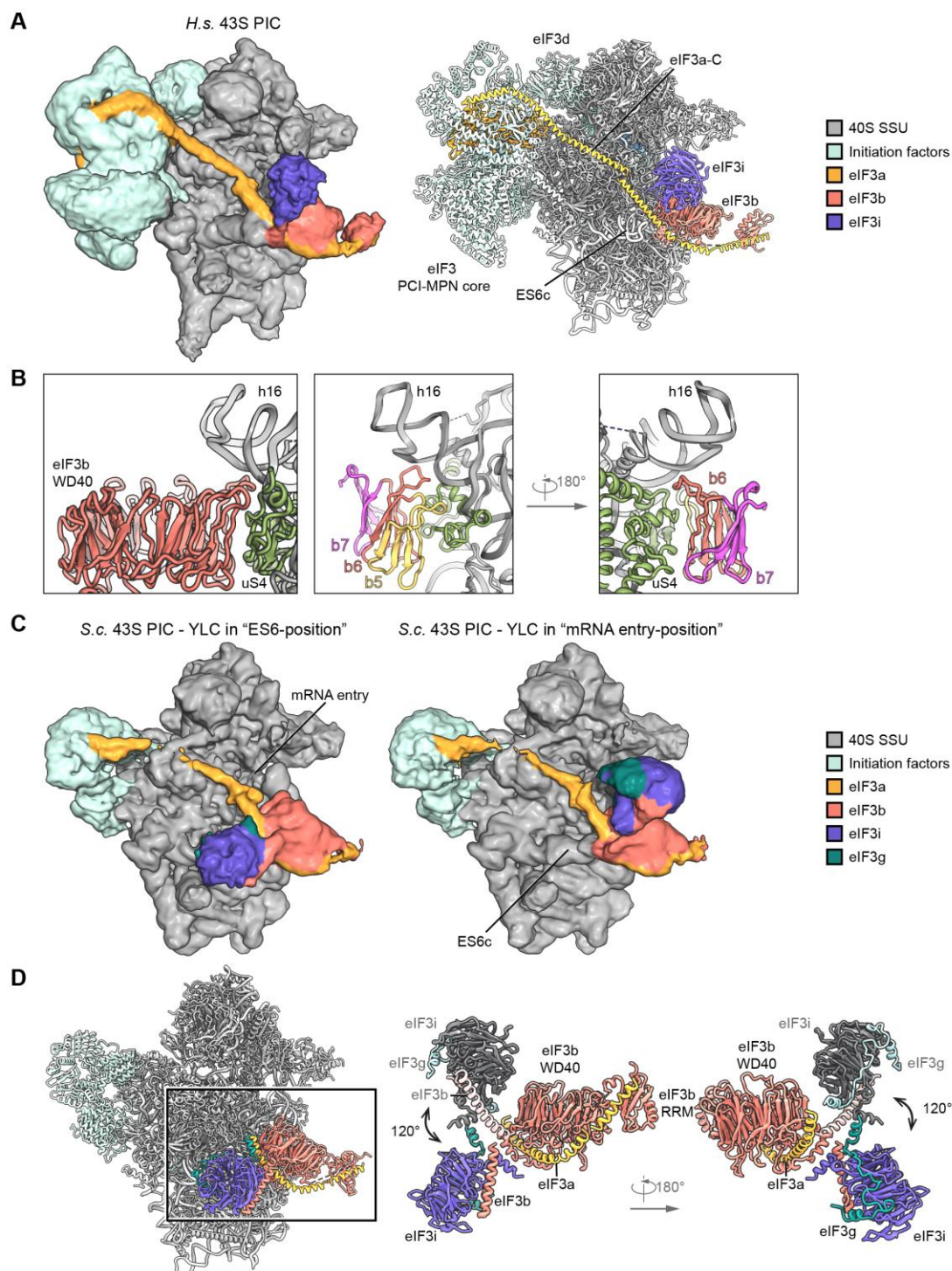


Appendix Figure S6 - Corrected register shifts in the helices of the PCI-MPN core in the human 43S PIC.

A Selected sites of the PCI-MPN core shown with cryo-EM density

B Comparison of the new model and the starting model (PDB 5A5T, des Georges *et al.*, 2015) coloured in grey.

Same view and colours as in (A). Side chains are labelled to highlight the register shifts.



Appendix Figure S7- Position of the eIF3 YLC and the eIF3a-CTD in yeast and human 43S PICs.

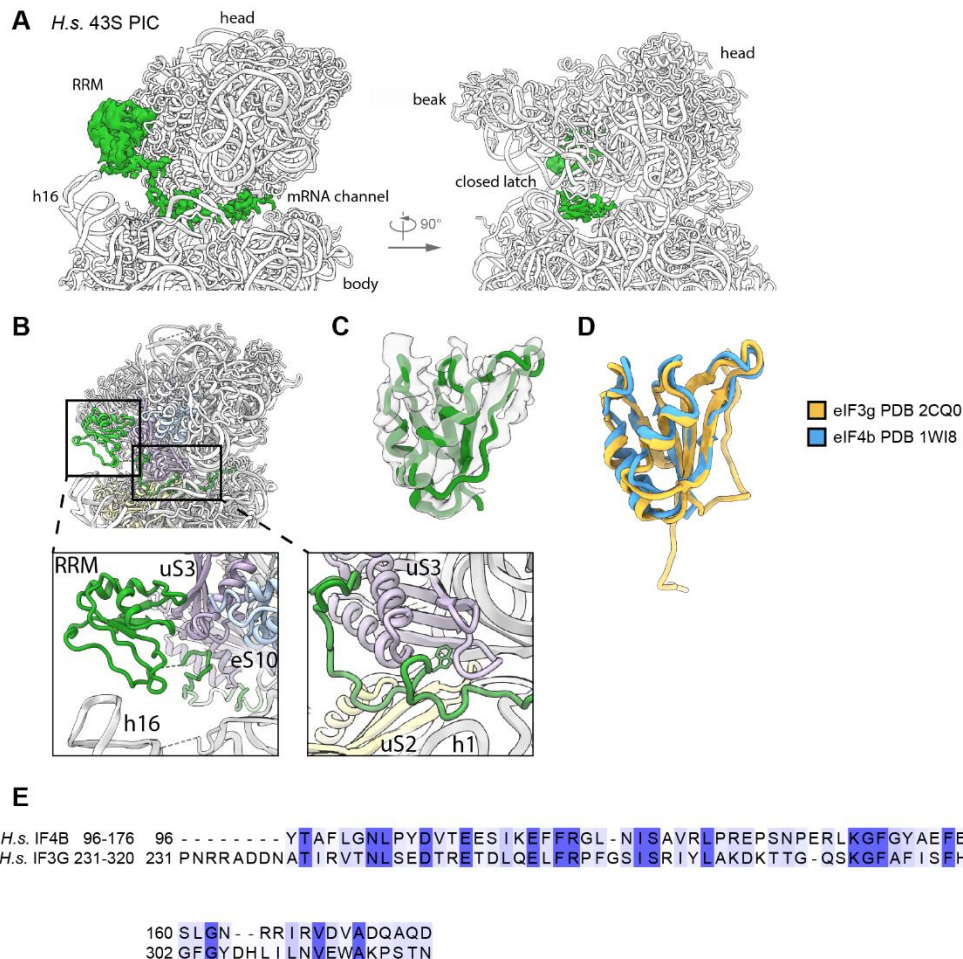
A Cryo-EM map of the human 43S PIC class obtained after local classification on the YLC (see Appendix Fig S2), low-pass filtered at 6 Å (left). Composite model of the human 43S PIC as in Fig. 2 (right). The view focuses on the mRNA entry side of the 40S, showing the YLC and the rod-like eIF3a density representing its C-terminus spanning from the back side of the 40S to the YLC.

B Interactions of eIF3b with the ribosome; models for eIF3g and eIF3a not shown. Two different views show only WD40 blades (b) 5 to 7 of eIF3b. In β -strand D5 (nomenclature refers to Liu *et al.*, 2014) Arg505, Arg507 and

Leu509 and in β -strand D6 Val558, Glu560 are facing towards uS4. The loop between B5-C5 (485-490) interacts with the rRNA backbone of the h16-h17 junction and uS4 (Tyr 165) and the loop between D5 and A6 (especially Phe510) interacts with Lys121 of uS4. h16 is contacted *via* the loop B6-C6 (res 532-541) *via* backbone interactions.

C Two different states of the yeast YLC obtained after focused classification. In one state (“ES6-position”) the eIF3g-eIF3i module bound to the eIF3b most C-terminal helix is facing towards expansion segment ES6c, in the other state (“mRNA entry-position”) it faces towards the mRNA entry, similar as in the human 43S PIC and as described previously (Erzberger *et al.*, 2014; Llacer *et al.*, 2018). 85% of the particles contained eIF3i in the ES6-position and 15% of particles in the mRNA entry-position (see Appendix Fig S1).

D Molecular model of the yeast 43S PIC with the YLC in (left) and overlay of the two positions. In the overlay the mRNA entry-position eIF3i is colored grey and eIF3g light blue and the eIF3b C-terminal helix white. The loop between the two most C-terminal helices of the eIF3b CTD (Thr697-Asp701) serves as a hinge for rotation.



Appendix Figure S8 - Position of the eIF3g or eIF4b RRM and density in the mRNA channel.

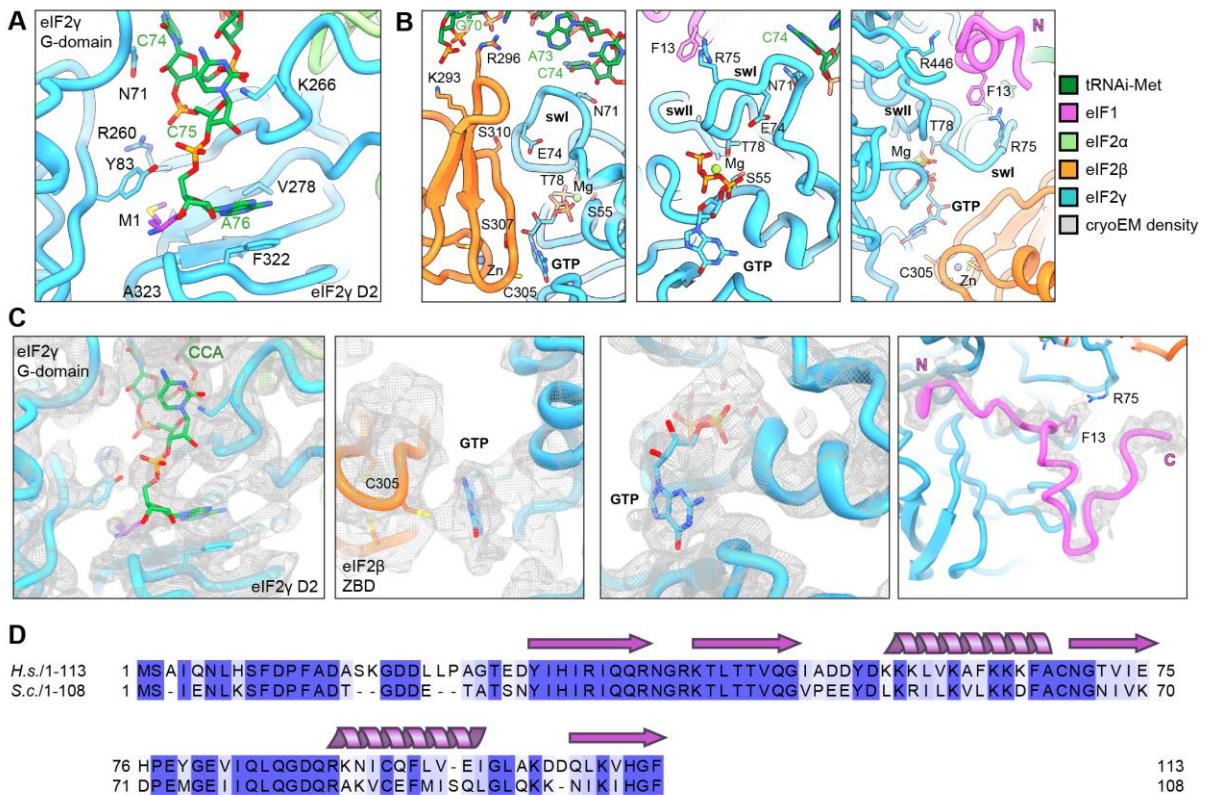
A Zoomed views on the mRNA channel as viewed from the ISS focusing on an extra density (green) on top of rRNA h16 and inside the mRNA channel. The isolated density is low-pass filtered according to local resolution.

B Overview and zoomed views on the poly-alanine model for an RRM on top of h16 and for the density in the mRNA channel in context of the 43S PIC. Interacting r-proteins and rRNA and the clearly visible tryptophan residue interacting with uS3 in the mRNA entry channel are highlighted.

C Model for a typical RRM-fold fitted into the corresponding isolated density.

D Overlay of the RRM of eIF4b and eIF3g.

E Sequence alignment of the RRM of human eIF4b and eIF3g, which shows 21.7/55.4% sequence identity/similarity.



Appendix Figure S9 - Molecular interactions of the TC in the complete human 43S PIC.

A, B View focusing on the interactions of methionylated tRNA_i with eIF2γ (A), the ZBD of eIF2β packing upon the nucleotide binding pocket of eIF2γ (B) as shown in Figure 7. Binding to tRNA_i (left) and the switch loops (sw) of eIF2γ contacting the *de novo* built eIF1 N-terminal tail (middle and right).

C Zoomed views of fits of the TC model into the cryo-EM map. Highlighted are the CCA-end of tRNA_i bound to eIF2γ, the guanine base lock-up by the eIF2β ZBD, the GTP in the eIF2γ nucleotide binding pocket and the *de novo* built N-terminal tail (res 4-30) of eIF1.

D Sequence alignment between the yeast and human eIF1 shows a sequence identity of 61.1% and a sequence similarity of 87.0% (N-terminus of eIF1 (4-30) shows 55.6/74.1% sequence identity/similarity) indicating a high degree of conservation.

Appendix Table S1 - Data collection, refinement, and model composition of the yeast initiation complexes.

	S.c. 43S PIC PDB 6ZCE EMDB 11160	S.c. 48S IC PDB 6ZU9 EMDB 11439	S.c. 43S PIC-XL PDB 7A1G EMDB 11608
Data collection			
Voltage (kV)	300		
Electron exposure (e-/Å ²)	25		44.8
Defocus range (μm)	-1.1 to -2.3		-0.5 to -2.5
Pixel size (Å)	1.084		1.059
Symmetry imposed	C1		
Refinement			
Particle images (no.)	20,618	12,937	25,245
Map resolution (Å)	5.3	6.2	3.0
FSC threshold	0.143		
Map sharpening B factor (Å ²)	-48.5	-100	-24
Model composition			
Correlation coefficient (%; Phenix)	64	60	82
Models used (PDB codes)	5NDG, 6FYY, 4U1E, 3BPJ, 6FEC	6TB3, 6FYX, 4U1E	6TB3, 3BPJ
Non-hydrogen atoms	76,380	78,384	81,866
Protein residues	8,027	7,845	5,612
RNA bases	1,719	1,852	1,771
R.m.s. deviations			
Bond lengths (Å)			0.009
Bond angles (°)			1.245
Validation			
MolProbity score			1.26
Clash score			4.91
Rotamer outliers (%)			0.19
Ramachandran plot			
Favored (%)			99.17
Allowed (%)			0.78
Disallowed (%)			0.05
Validation RNA			
Correct sugar pucker (%)			99
Good backbone conf. (%)			71

Appendix Table S2 - Data collection, refinement, and validation statistics of the human 43S PIC.

Atomic models were built into the best-resolved maps as obtained after local focused refinement or multi-body refinement. Validation statistics are shown for each individual part, as well as for the final composite models. The model for State II includes 40S SSU, eIF1, eIF3 PCI-MPN core, eIF3d, eIF3c-N, eIF3a-C, eIF3b, eIF3i, eIF3j, RRM and ABCE1. The model for State III includes 40S SSU, eIF1, eIF1A, eIF2 $\alpha/\beta/\gamma$, tRNA_i, eIF3 PCI-MPN core, eIF3d, eIF3c-N, eIF3a-C, eIF3b, eIF3i, RRM and ABCE1.

H.s. 43S	40S eIF1A eIF3c-N eIF3d	eIF3 PCI- MPN core (3a, 3c, 3d- N, 3e, 3f, 3h, 3k, 3l, 3m)	Ternary complex (eIF2$\alpha/\beta/\gamma$, tRNA_i eIF1)	ABCE1	composite model (state II) (PDB 6ZVJ, EMDB 11458)	composite model (state III) (PDB 7A09, EMDB 11602)
Data collection						
Voltage (kV)	300					
Electron exposure (e ⁻ /Å ²)	48					
Defocus range (μm)	-0.5 to -2.5					
Pixel size (Å)	1.059					
Symmetry imposed	C1					
Refinement						
Particle images (no.)	23,660	25,228	11,032	13,250	5,231	8,712
Map resolution (Å)	3.0/3.0 (40S body/head)	3.4/3.8 (a,c,d,e,f,h, k,l,m)	4	3.2	3.8	3.5
FSC threshold	0.143					
Map sharpening B factor (Å ²)	-29.98/ -35.86	-61.34/- 89.07	-50.55	-45.58	-36.79	-34.39
Model composition						
Correlation coefficient (%; mask; Phenix)	85/84	81	51	80	69	75
Starting model (PDB codes)	40S: 6G5H eL41: 6EK0 eIF1A: 3J81 eIF3d: 5K4B	5A5T	tRNA: 6FEC eIF2 β : 6GSM eIF2 α,γ : 6O85 eIF1: 6GSM	5LL6		
Non-hydrogen atoms	50,220/ 27,787	25,291	7,889	4,619	115,031	122,211
Protein residues	3,043/ 2,239	3,104	973	576	10,127	10,954
RNA bases	1208/ 464	0	75	0	1,720	1,796
R.m.s. deviations						
Bond lengths (Å)	0.017/0.024	0.016	0.013	0.017	0.010	0.010
Bond angles (°)	1.425/1.757	1.587	1.578	1.558	1.337	1.203

Validation						
MolProbity score	1.79/2.05	1.5	1.93	2.21	1.4	1.98
Clash score	2.82/4.36	6.52	7.9	6.45	5.45	8.57
Rotamer outliers (%)	8.9/12.64	1.53	3.83	13.44	1.39	0.02
Ramachandran plot						
Favored (%)	99.63/99.18	99.74	97.74	99.48	99.76	90.96
Allowed (%)	0.37/0.77	0.26	1.54	0.52	0.24	8.98
Disallowed (%)	0/0.05	0	0.71	0	0	0.06
Validation RNA						
Correct sugar pucker (%)	99.17/98.71	-	100	-	100	100
Good backbone conf. (%)	73.43/75	-	69.33	-	70	70

Appendix Table S3 - Crosslinks identified on a yeast ABCE1-43S PIC.

ABCE1-bound 43S PIC was affinity-purified from yeast cell extracts using TAP-tagged Nip1 (eIF3c) protein and crosslinked with BS2G. 43 inter-protein (dark green) and 74 intra-protein (light green) crosslinks were obtained from the analysis. The crosslinks are listed according to the Id.Score (xQuest identification score).

No	Topology	Protein1	Protein2	AbsPos1	AbsPos2	Mz	z	Error	Id.Score
1	TLVNKSTGLK-VAKSNR-a5-b3	sp P33442 RS3A1_YEAST	sp P26783 RS5_YEAST	50	222	610.686	3	-1.1	42.07
2	NKDDLEKISK-IAKER-a7-b3	sp P38249 EIF3A_YEAST	sp P32497 EIF3C_YEAST	596	802	476.015	4	0.1	40.46
3	ALQKEQEEQALK-STALKILAGK-a4-b5	sp Q05775 EIF3J_YEAST	sp Q03195 RLI1_YEAST	118	121	628.607	4	0.7	39.23
4	TGPKALPDVAITIEPK-VKQLENVSSNIVK-a4-b2	sp P05750 RS3_YEAST	sp P38701 RS20_YEAST	200	32	801.455	4	1.2	39.09
5	DDLEKISK-IAKER-a5-b3	sp P38249 EIF3A_YEAST	sp P32497 EIF3C_YEAST	596	802	553.637	3	-0.9	37.91
6	ENKVSPADAAK-VIKVLGR-a3-b3	sp P39938 RS26A_YEAST	sp Q3E7X9 RS28A_YEAST	108	14	503.041	4	0.5	37.53
7	GISFKLQEEERER-SFKEPR-a5-b3	sp P02407 RS17A_YEAST	sp P32905 RSSA1_YEAST	72	116	496.658	5	-0.3	35.5
8	DSATHELTKVSEPIHK-VHKSVAER-a9-b3	sp P40217 EIF3I_YEAST	sp Q04067 EIF3G_YEAST	138	47	589.106	5	-1.4	34.7
9	GISFKLQEEER-SFKEPR-a5-b3	sp P02407 RS17A_YEAST	sp P32905 RSSA1_YEAST	72	116	732.043	3	0.1	34.7
10	NKSELESRIQKEK-a2-b3	sp P38249 EIF3A_YEAST	sp Q04067 EIF3G_YEAST	709	97	568.305	3	1.2	34.63
11	ISKIVDER-IAKER-a3-b3	sp P38249 EIF3A_YEAST	sp P32497 EIF3C_YEAST	599	802	557.653	3	-1	34.28
12	EKVVEEQEQQQQIIK-VTPTKTEVIIR-a2-b5	sp P38701 RS20_YEAST	sp P05750 RS3_YEAST	8	45	809.941	4	1.1	34.14
13	ANDIGFHKYR-ITLTSTKVK-a8-b7	sp P41058 RS29B_YEAST	sp P38701 RS20_YEAST	54	30	577.319	4	1.3	33.77
14	QTVATLNLVIKDK-AGKVK-a11-b3	sp Q05775 EIF3J_YEAST	sp POCX33 RS3OA_YEAST	205	13	510.808	4	1.1	33.54
15	ALQKEQEEQALK-AIKGPVQK-a4-b3	sp Q05775 EIF3J_YEAST	sp Q03195 RLI1_YEAST	118	181	588.331	4	0.8	31.95
16	LTGDDQKFGVPVR-KAFTSYDR-a7-b1	sp P38011 GBLP_YEAST	sp POCX51 RS16A_YEAST	53	107	629.322	4	0.5	31.91
17	LAAPENKPPAPVRTHMR-EKAKR-a8-b4	sp Q01855 RS15_YEAST	sp P39730 IF2P_YEAST	72	226	881.813	3	3.2	31.89

18	KVQLGK-VEKASR-a1-b3	sp POCX35 RS4 A_YEAST	sp POCX31 RS2 4A_YEAST	128	102	364. 968	4	- 0.7	31.8 4
19	EFIILGGGQEAQDVTTTSANEGK- HKVEHGKY-a12-b2	sp P40217 EIF31 _YEAST	sp P06103 EIF3 B_YEAST	261	632	865. 188	4	1.2	31.7 3
20	AVLKFAAHTGATPIAGR- KDQYVPEVSALDLSR-a4-b1	sp P32905 RSSA 1_YEAST	sp P02407 RS17 A_YEAST	88	81	699. 979	5	0.7	31.2 1
21	LVEGLANDPENKVPLIK- VDAEGKVTk-a12-b6	sp P48589 RS12 _YEAST	sp P05759 RS31 _YEAST	85	113	723. 401	4	0.5	31.1 3
22	AAAAAALAGGK-NTKGGK-a3-b3	sp Q3E792 RS2 5A_YEAST	sp P38912 IF1A _YEAST	12	7	566. 988	3	- 1.1	30.5 1
23	NKSELESR-EKASLTk-a2-b2	sp P38249 EIF3 A_YEAST	sp Q04067 EIF3 G_YEAST	709	99	611. 991	3	0.6	30.4 8
24	AAAAALAGGK-KKDELER-a9-b1	sp Q3E792 RS2 5A_YEAST	sp P26783 RS5_ YEAST	21	213	468. 265	4	- 1.3	30.0 6
25	TGPKALPDAVTIIEPKEEEPILAPSVK- VKQLENVSSNIVK-a4-b2	sp P05750 RS3_ YEAST	sp P38701 RS20 _YEAST	200	32	879. 894	5	2.3	29.6 5
26	YIDLEAPVQIVKR-VTPKTKEVIIR-a12- b5	sp P38701 RS20 _YEAST	sp P05750 RS3_ YEAST	101	45	724. 67	4	0.7	29.5 8
27	DVTTTSANEGKFEAR-EKASLTk-a11- b2	sp P40217 EIF31 _YEAST	sp Q04067 EIF3 G_YEAST	272	99	833. 087	3	0.9	29.2 1
28	REDDKPK-EKAKR-a5-b4	sp P39935 IF4F 1_YEAST	sp P39730 IF2P _YEAST	564	226	538. 627	3	2.7	29
29	GGTATGGAGKK-VEASCFDGNKR- a10-b10	sp Q05775 EIF3 J_YEAST	sp P38912 IF1A _YEAST	230	56	761. 367	3	0.6	28.4 2
30	AAAEKSQKSK-KMKSLLNK-a8-b3	sp P39730 IF2P _YEAST	sp P39935 IF4F 1_YEAST	147	611	702. 066	3	0.7	28.2
31	AAAEKSQKSK-KMKSLLNK-a8-b3	sp P39730 IF2P _YEAST	sp P39936 IF4F 2_YEAST	147	571	702. 066	3	0.7	28.2
32	QVIIAEVSKNK-IQKEK-a9-b3	sp P38249 EIF3 A_YEAST	sp Q04067 EIF3 G_YEAST	707	97	493. 039	4	0	28.1 9
33	AIKLTGHERPLTQVK-SIITYKIEDGVK- a3-b6	sp P40217 EIF31 _YEAST	sp Q04067 EIF3 G_YEAST	5	23	631. 161	5	- 0.2	27.5 1
34	KAATASANVR-NKA VAR-a1-b2	sp P38431 IF5_ YEAST	sp P32497 EIF3 C_YEAST	156	189	581. 326	3	- 2.5	26.7 3
35	AEGKLLTRK-KAALEKK-a4-b1	sp P39730 IF2P _YEAST	sp P39935 IF4F 1_YEAST	235	217	633. 386	3	- 0.1	26.4 2
36	AQHAVILDQEKYDR- IVYALTTIKGVGR-a11-b9	sp Q3E792 RS2 5A_YEAST	sp POCX55 RS1 8A_YEAST	46	36	793. 683	4	- 2.1	26.1 4
37	AGNREPPSTPSTLPKATVSPDK- KNGLISETEK-a15-b1	sp P38249 EIF3 A_YEAST	sp P39936 IF4F 2_YEAST	889	243	693. 563	5	-2	25.4 9
38	QNDITDGKDYHTLANNVESK- VFKTHSYR-a8-b3	sp POCX55 RS1 8A_YEAST	sp Q01855 RS1 5_YEAST	96	13	679. 733	5	1.5	25.1
39	IAIVSADKCKPK-EDDKPK-a10-b4	sp Q03195 RLI1 _YEAST	sp P39935 IF4F 1_YEAST	17	564	539. 787	4	- 1.9	24.7 7
40	VSVVRNKETGK-LANEEKMK-a7-b6	sp Q04067 EIF3 G_YEAST	sp P39730 IF2P _YEAST	227	210	569. 308	4	-1	23.0 8
41	DVAKPMSIESIR-KKAATASANVR-a4- b2	sp Q05775 EIF3 J_YEAST	sp P38431 IF5_ YEAST	186	156	640. 102	4	2.2	22.9 2
42	DVLDELKNYISKR-EIVKSNTSSKK-a7- b4	sp P20459 IF2A _YEAST	sp P39015 STM 1_YEAST	170	27	485. 598	6	-4	22.7 3
43	YGLAEKVEK-DCKACGK-a6-b3	sp POCX31 RS2 4A_YEAST	sp P38431 IF5_ YEAST	99	122	657. 319	3	2.6	22.6 1
44	VGELLKLR-SPEDVKR-a6-b6	sp Q03195 RLI1 _YEAST	sp Q03195 RLI1 _YEAST	192	203	464. 018	4	- 0.9	43.0 8
45	ILQLENVLKR-VGELLKLR-a9-b6	sp Q03195 RLI1 _YEAST	sp Q03195 RLI1 _YEAST	216	192	562. 85	4	0.4	42.5
46	FNVVKVSAAAGK-NAGLGFKTPK-a5- b7	sp POCX48 RS1 1B_YEAST	sp POCX48 RS1 1B_YEAST	141	43	580. 329	4	1.8	41.3 7
47	NTEEGWVVPVK-LVKAGK-a5-b3	sp P25443 RS2_ YEAST	sp P25443 RS2_ YEAST	33	46	700. 057	3	1	41.0 6
48	AQHAVILDQEKYDR-LKIGGSLAR- a11-b2	sp Q3E792 RS2 5A_YEAST	sp Q3E792 RS2 5A_YEAST	46	70	539. 897	5	0.5	40.7 2

49	GPVQKVGELLK-ILQLENVLKR-a5-b9	sp Q03195 RLI1_YEAST	sp Q03195 RLI1_YEAST	186	216	622.878	4	1.4	39.24
50	SDWLLLLK-SIDTLKDK-a7-b6	sp P39730 IF2P_YEAST	sp P39730 IF2P_YEAST	993	976	505.037	4	0.7	38.85
51	AQHAVILDQEKYDR-AAAAAGGKK-a11-b9	sp Q3E792 RS25A_YEAST	sp Q3E792 RS25A_YEAST	46	21	528.486	5	0.4	38.73
52	EKVEEQEQQQQIIK-YIDLEAPVQIVKR-a2-b12	sp P38701 RS20_YEAST	sp P38701 RS20_YEAST	8	101	881.722	4	0.5	38.37
53	ASLTKTGLQCR-IQKEK-a5-b3	sp Q04067 EIF3G_YEAST	sp Q04067 EIF3G_YEAST	104	97	659.027	3	0.9	38.32
54	ALTSLSFKAGK-SFHGKR-a8-b5	sp P06103 EIF3B_YEAST	sp P06103 EIF3B_YEAST	105	147	488.021	4	-1.2	38.05
55	LSSESVIEQIVKYAR-KGLTPSQIGVLLR-a12-b1	sp P05756 RS13_YEAST	sp P05756 RS13_YEAST	39	43	800.459	4	0.6	37.83
56	RKEEIANAER-LAKGGR-a2-b3	sp P38249 EIF3A_YEAST	sp P38249 EIF3A_YEAST	835	961	478.765	4	-0.6	37.72
57	VQTKLTR-ELEKK-a4-b4	sp P26786 RS7A_YEAST	sp P26786 RS7A_YEAST	76	83	529.642	3	-0.9	37.4
58	KLDYVLALK-VGVLSDEKK-a1-b8	sp P05755 RS9B_YEAST	sp P05755 RS9B_YEAST	92	90	533.811	4	0	37.27
59	ALQKEQEEQALK-KGKESSADR-a4-b3	sp Q05775 EIF3J_YEAST	sp Q05775 EIF3J_YEAST	118	62	622.573	4	-0.2	37.1
60	ILQLENVLKR-SPEDVKR-a9-b6	sp Q03195 RLI1_YEAST	sp Q03195 RLI1_YEAST	216	203	538.56	4	0.6	37.08
61	APFVVALNKIDR-TKLLDK-a9-b2	sp P39730 IF2P_YEAST	sp P39730 IF2P_YEAST	531	420	539.568	4	0	36.93
62	DIEKLSGGELQR-ILQLENVLKR-a4-b9	sp Q03195 RLI1_YEAST	sp Q03195 RLI1_YEAST	221	216	889.17	3	2.3	36.86
63	KAPFVVALNKIDR-TKLLDK-a10-b2	sp P39730 IF2P_YEAST	sp P39730 IF2P_YEAST	531	420	571.592	4	0.4	36.58
64	LNNVFVIGEQQKPYISLPK-VNDTVKIDLASGK-a12-b6	sp POCX35 RS4A_YEAST	sp POCX35 RS4A_YEAST	233	161	893.492	4	0.8	36.39
65	VCEFMISQLGLQKK-NIKIHGF-a13-b3	sp P32911 SUI1_YEAST	sp P32911 SUI1_YEAST	100	104	651.848	4	-0.2	36.2
66	AQHAVILDQEKYDR-AAKAAAALAGGK-a11-b3	sp Q3E792 RS25A_YEAST	sp Q3E792 RS25A_YEAST	46	12	556.9	5	-0.5	36.03
67	YGSEKSPAGPSAVTAR-IEDGVKYK-a5-b6	sp Q04067 EIF3G_YEAST	sp Q04067 EIF3G_YEAST	62	29	671.092	4	0.5	35.94
68	ALQKEQEEQALK-GKESSADR-a4-b2	sp Q05775 EIF3J_YEAST	sp Q05775 EIF3J_YEAST	118	62	590.549	4	-0.9	35.75
69	AQHAVILDQEKYDR-ILKEVPTYR-a11-b3	sp Q3E792 RS25A_YEAST	sp Q3E792 RS25A_YEAST	46	52	580.711	5	-1.9	35.63
70	KAATASANVR-DCKACGK-a1-b3	sp P38431 IF5_YEAST	sp P38431 IF5_YEAST	156	122	641.312	3	-1.3	35.61
71	YGSEKSPAGPSAVTAR-VHKSVAER-a5-b3	sp Q04067 EIF3G_YEAST	sp Q04067 EIF3G_YEAST	62	47	664.594	4	1.8	35.58
72	NVKEETVAK-SKNAER-a3-b2	sp POCX39 RS8A_YEAST	sp POCX39 RS8A_YEAST	128	137	649.332	3	-0.9	35.57
73	FYAPETKEK-TDVIKR-a7-b5	sp P06103 EIF3B_YEAST	sp P06103 EIF3B_YEAST	529	536	647.011	3	0	35.56
74	DIEKLSGGELQR-GPVQKVGELLK-a4-b5	sp Q03195 RLI1_YEAST	sp Q03195 RLI1_YEAST	221	186	869.818	3	1.3	35.54
75	ALLDIDTLDEKTR-GKESSADR-a11-b2	sp Q05775 EIF3J_YEAST	sp Q05775 EIF3J_YEAST	79	62	612.562	4	0	35.39
76	AAKLAAPENEPAPVR-VFKTHSYR-a3-b3	sp Q01855 RS15_YEAST	sp Q01855 RS15_YEAST	64	13	466.589	6	-1.7	35.26
77	TGPKALPDAVTIIIEPK-DPAKSR-a4-b4	sp P05750 RS3_YEAST	sp P05750 RS3_YEAST	200	194	605.336	4	-2.1	34.52
78	ALQKEQEEQALK-KEQPKK-a4-b5	sp Q05775 EIF3J_YEAST	sp Q05775 EIF3J_YEAST	118	56	567.563	4	1.1	34.31
79	GGTATGGAGKK-GKTNLGGAFK-a10-b2	sp Q05775 EIF3J_YEAST	sp Q05775 EIF3J_YEAST	230	236	664.688	3	-1.7	34.19

80	TTQENASEAIKSDSK-KDSEVVPDDELK-a11-b1	sp P39730 IF2P_YEAST	sp P39730 IF2P_YEAST	298	303	770.123	4	1.1	34.13
81	ASLTKTGLQCR-NKETGK-a5-b2	sp Q04067 EIF3G_YEAST	sp Q04067 EIF3G_YEAST	104	227	669.351	3	1.1	34.09
82	ALQKEQEEQALK-ELIKK-a4-b4	sp Q05775 EIF3J_YEAST	sp Q05775 EIF3J_YEAST	118	86	714.067	3	-0.2	33.94
83	YIDLEAPVQIVKR-VLKISTR-a12-b3	sp P38701 RS20_YEAST	sp P38701 RS20_YEAST	101	64	614.614	4	1	33.77
84	KQFVVDVLHPNR-LAEVYKAEK-a1-b6	sp POCX31 RS24A_YEAST	sp POCX31 RS24A_YEAST	21	49	650.107	4	-1	33.63
85	RPAFTKDTPIETHPLFNAETK-ALQKEQEEQALK-a6-b4	sp Q05775 EIF3J_YEAST	sp Q05775 EIF3J_YEAST	132	118	654.677	6	0.9	33.38
86	ALLDIDTLDEKTRK-ELIKK-a11-b4	sp Q05775 EIF3J_YEAST	sp Q05775 EIF3J_YEAST	79	86	786.117	3	0.3	33.35
87	ATVSPDKAK-LDMIAQQR-a7-b7	sp P38249 EIF3A_YEAST	sp P38249 EIF3A_YEAST	896	905	529.288	4	0.7	33.28
88	AQHAVILDQEKYDR-SMKDR-a11-b3	sp Q3E792 RS25A_YEAST	sp Q3E792 RS25A_YEAST	46	33	605.053	4	-0.4	32.77
89	GKESSADR-ELIKK-a2-b4	sp Q05775 EIF3J_YEAST	sp Q05775 EIF3J_YEAST	62	86	525.618	3	0.4	32.67
90	SLEHYDKLSFQGGPETLR-LNKEYK-a7-b3	sp P32497 EIF3C_YEAST	sp P32497 EIF3C_YEAST	661	796	752.386	4	-0.9	32.18
91	NPPDSVSGSKK-KAATASANVR-a10-b1	sp P38431 IF5_YEAST	sp P38431 IF5_YEAST	152	156	550.54	4	-0.3	31.91
92	EKVEEQEQQQQIIK-VLKISTR-a2-b3	sp P38701 RS20_YEAST	sp P38701 RS20_YEAST	8	64	699.884	4	0	31.42
93	MITEVNAKGHVYIDPNEAK-NKSELESR-a8-b2	sp P38249 EIF3A_YEAST	sp P38249 EIF3A_YEAST	679	709	797.399	4	0.1	31.28
94	ALQKEQEEQALK-KPAPKPK-a4-b5	sp Q05775 EIF3J_YEAST	sp Q05775 EIF3J_YEAST	118	49	569.573	4	0.4	31.24
95	EQEEQALKRPAFTK-ALQKEQEEQALK-a8-b4	sp Q05775 EIF3J_YEAST	sp Q05775 EIF3J_YEAST	126	118	637.737	5	0.8	30.87
96	YGSEKGSPAGPSAVTAR-ITQVKV-a5-b4	sp Q04067 EIF3G_YEAST	sp Q04067 EIF3G_YEAST	62	35	612.331	4	1.8	30.64
97	VDEVQGGKLLTNFHGMDFTTDK-TLVNKSTGLK-a7-b5	sp P33442 RS3A1_YEAST	sp P33442 RS3A1_YEAST	94	50	916.969	4	-0.5	30.62
98	DTPIETHPLFNAETKR-GKESSADR-a15-b2	sp Q05775 EIF3J_YEAST	sp Q05775 EIF3J_YEAST	147	62	704.099	4	0.7	30.5
99	LRVDEVQGGKLLTNFHGMDFTTDK-TLVNKSTGLK-a9-b5	sp P33442 RS3A1_YEAST	sp P33442 RS3A1_YEAST	94	50	787.612	5	-2.7	30.1
100	GFLFVECGSMNDACK-IKSFHGK-a14-b3	sp P06103 EIF3B_YEAST	sp P06103 EIF3B_YEAST	138	142	682.596	4	-1.7	29.94
101	LKVVFGE-SIDTLKDK-a2-b6	sp P39730 IF2P_YEAST	sp P39730 IF2P_YEAST	996	976	640.363	3	-0.1	29.77
102	DTPIETHPLFNAETKR-ALQKEQEEQALK-a15-b4	sp Q05775 EIF3J_YEAST	sp Q05775 EIF3J_YEAST	147	118	845.435	4	-0.8	29.56
103	AGNREPPSTPSTLPKATVSPDK-AKLDMIAQK-a15-b2	sp P38249 EIF3A_YEAST	sp P38249 EIF3A_YEAST	889	898	673.359	5	0	29.43
104	DLSEASVYPEYALPKTYNK-ENKVSPADAAK-a15-b3	sp P39938 RS26A_YEAST	sp P39938 RS26A_YEAST	66	108	853.926	4	0.2	29.34
105	ALQKEQEEQALK-TRKELIK-a4-b3	sp Q05775 EIF3J_YEAST	sp Q05775 EIF3J_YEAST	118	82	480.273	5	-0.1	29.06
106	AGNREPPSTPSTLPKATVSPDK-KSTPYSFR-a15-b1	sp P38249 EIF3A_YEAST	sp P38249 EIF3A_YEAST	889	867	666.946	5	0.9	28.39
107	AQHAVILDQEKYDR-HSKQAIYTR-a11-b3	sp Q3E792 RS25A_YEAST	sp Q3E792 RS25A_YEAST	46	97	577.7	5	-0.9	28.21
108	EPPSTPSTLPKATVSPDK-KSTPYSFR-a11-b1	sp P38249 EIF3A_YEAST	sp P38249 EIF3A_YEAST	889	867	733.879	4	-0.7	25.78
109	EQEEQALKRPAFTK-KEQPK-a8-b1	sp Q05775 EIF3J_YEAST	sp Q05775 EIF3J_YEAST	126	52	600.568	4	-2.8	25.66
110	AASAKIESSVESQFSAGR-NVKEETVAK-a5-b3	sp POCX39 RS8A_YEAST	sp POCX39 RS8A_YEAST	151	128	767.388	4	1.4	25.61

111	VVAQVEDAVNNTQQADLKNK-NKAVARAYNTTK-a18-b2	sp P32497 EIF3 C_YEAST	sp P32497 EIF3 C_YEAST	187	189	904.724	4	0.4	25.46
112	VTGFKDEVLETV-TLVNKSTGLK-a5-b5	sp P33442 RS3 A1_YEAST	sp P33442 RS3 A1_YEAST	248	50	831.456	3	1.3	25.42
113	QNDITDGKDYHTLANNVESK-KADVDLHKR-a8-b1	sp POCX55 RS1 8A_YEAST	sp POCX55 RS1 8A_YEAST	96	49	688.544	5	0.6	24.42
114	ALQKEQEEQALK-GGTATGGAGKK-a4-b10	sp Q05775 EIF3 J_YEAST	sp Q05775 EIF3 J_YEAST	118	230	604.317	4	-2.8	24.37
115	EPPSTPSTLPKATVSPDK-AKLDMIAQK-a11-b2	sp P38249 EIF3 A_YEAST	sp P38249 EIF3 A_YEAST	889	898	741.895	4	-1.3	24.37
116	KADVPPPSADPSK-EIVKSNTSSK-a1-b4	sp P39015 STM 1_YEAST	sp P39015 STM 1_YEAST	34	27	832.765	3	-1.2	23.52
117	ALTAAITPMNKK-GGTATGGAGKK-a11-b10	sp Q05775 EIF3 J_YEAST	sp Q05775 EIF3 J_YEAST	166	230	565.311	4	0.7	22.52

Appendix Table S4 - Molecular interactions between eIF3 subunits and 40S.

eIF3a									
3a	eS1	3a	3c	3a	3f	3a	3h	3a	3m
Q6	E78	E125	K474	N521	S232	N521	S232	S444	K342
N10	E78	V132	N678	H565	R109	A525	Q314	I446	I325
R14	E78, D77	R140	P464, S466			E547	K220	Y447	K342
E17	N75	R143	D463			H550	W216	Q448	I325
		W246	P729			E564	H209	S449	D326, Q327
		Q247	Q724			R571	E77	E451	Q327
		D337	K745			E576	R108	R454	E309
		L342	R719			R578	E145, E146	N512	C323
		E468	Y799						
		R483	S797, D800						
		I484	D800						

eIF3b			
3b	18S rRNA	3b	uS4
K487	A560	R507	D158
D488	A560	V556	K155

3c-N		eIF3c (PCI-MPN core)											
3c	18S rRNA	3c	18S rRNA	3c	eS27	3c	3d	3c	3e	3c	3f	3c	3h
R47	C1039, A1181	K342	G929	G341	Q65	D562	A70	Y583	Y286	Q852	D333	Y557	L210
K55	C1180	K343	G929	N388	Q75	M591	Q31	D587	Y286	N870	N351, Q347	L859	M247
K92	U1178			L389	Q75	H593	P32, G64	D602	Y41			K862	M247
K132	C369					Q595	L39	S820	N302			V873	N261
K136	U367					H600	H73	L835	I347, Q349			H876	N261
Q143	U367, U368					D602	H73	Q837	S352				
K144	U367					P603	W45	H845	N395				
						Q606	W45						
						Y609	K41						
						N610	A43						
						N631	R38						
						D635	Y59						
						R641	T46						
						E666	W45						

eIF3d									
3d	3e	3d	uS27	3d	18S rRNA	3d	eS28	3d	uS7
F4	Y32	E75	K36	R212	C1470	Q416	R51, E52	K472	Q29
Q10	H12	E77	R80			T423	R13	S478	N31
D11	R16	Q81	S78, F79			K426	F34, T38		
W16	S167, G171	V83	G76						
G17	W170								
A20	Q209								
Y30	L208								
F33	N244, L590								
K35	Q283, E284								

eIF3e	
3e	3l
R369	D480
Y401	I523
Q416	D532

eIF3f							
3f	3h	3f	3k	3f	3m	3f	3l
R108	D113	S267	Q218	Q280	N362	N332	I523
V163	Y99	N328	E203	D301	W347		
S164	E56			R306	H339		
Y239	L218, E217			N313	S337		
N260	K206						
R261	H209, N207						
I263	I205						
D268	Q336						
Q271	S161						
P316	Q348						
I318	Q348						
N342	K331						
Q345	N324						
N356	R313						

eIF3h			
3h	3l	3h	3k
E195	R545	K331	S217
		K345	K204

eIF3l	
3l	3k
K534	S216

Appendix text 1 - Molecular interactions between eIF3j and the 40S subunit in the yeast 43S-PIC.

Molecular details of the eIF3j-40S interaction were derived from the high-resolution structure of the cross-linked 43S-PIC (43S-PIC-XL) at an overall resolution of 3.0 Å and a local resolution of eIF3j ranging from 3 to 5 Å (Appendix Fig S4). Ribosome-bound eIF3j forms a dimer folding into a stable entangled 6-helix bundle as observed in crystal structure of human eIF3j (PDB 3BPJ; lacking 137 residues at the N- and 28 residues at the C-terminus). A yeast homology model based on this structure could be unambiguously fitted into the EM density (Fig EV3). It accommodates between the 40S body and head *via* interactions of both protomers. The 40S body is contacted by Arg148 and Arg154 of the N-terminal helix 1 of protomer 1 *via* A542 in the h17-h18 junction and *via* Glu22 of eS30, respectively. This contact to eS30 is also confirmed by the XL-MS data (Appendix Fig S5 and Appendix Table 3). 40S body and head are bridged by the C-terminal helix 3 of protomer 1. Here, Gln195 and Thr199 contact the backbone of eS30 in the body (at Lys15 and Lys20, respectively), while Arg215 contacts G1264 of h33 on the head. Helix 3 of the second protomer projects into the opposite direction and likely contacts Glu31 of eIF1A *via* a basic patch consisting of Lys205, Arg209, and Arg212. Following helix 3, the second eIF3j protomer forms a highly basic loop inside a pocket formed by h33, h34 and eS10 (Figs 4E, F and EV3). Here, Lys230 of eIF3j and Phe59 of eS10 are sandwiching the flipped-out G1435 base of h34. H34 is also contacted by Lys234 (at G1438), whereas Lys231 contacts U1266 and G1267 of h33. The loop is further stabilized by salt bridges between Arg220 and Glu70-Glu71 of eS10. From the loop, the C-terminus projects towards the mRNA entry channel (Fig 4G). It interacts with h18 (*via* Lys236) and then forms several contacts with uS3, mainly *via* hydrophobic interactions between Leu239 and Phe243 with Ile114, Leu142, and Arg143 of uS3 and the flipped-out base of A579 (h18). Finally, the C-terminus is anchored at h18 by the interaction of Lys244 with C559 (phosphate) and U581 (stacking), as well as Lys245 with U581 and U582 (phosphates). From here, the eIF3j C-terminus makes another kink into the mRNA entry channel, in which eleven more residues are visible (Asp246-Phe257). This part is not forming any specific interactions and thus is more flexible.

Appendix References

des Georges A, Dhote V, Kuhn L, Hellen CU, Pestova TV, Frank J, Hashem Y (2015) Structure of mammalian eIF3 in the context of the 43S preinitiation complex. *Nature* 525: 491-495

Erzberger JP, Stengel F, Pellarin R, Zhang S, Schaefer T, Aylett CHS, Cimermancic P, Boehringer D, Sali A, Aebersold R et al (2014) Molecular Architecture of the 40S eIF1eIF3 Translation Initiation Complex. *Cell* 159: 1227-1228

Liu Y, Neumann P, Kuhle B, Monecke T, Schell S, Chari A, Ficner R (2014) Translation initiation factor eIF3b contains a nine-bladed beta-propeller and interacts with the 40S ribosomal subunit. *Structure* 22: 923-930

Llacer JL, Hussain T, Saini AK, Nanda JS, Kaur S, Gordiyenko Y, Kumar R, Hinnebusch AG, Lorsch JR, Ramakrishnan V (2018) Translational initiation factor eIF5 replaces eIF1 on the 40S ribosomal subunit to promote start-codon recognition. *Elife* 7

Ribosome collisions in bacteria promote ribosome rescue by triggering mRNA cleavage by SmrB

Kazuki Saito¹, Hanna Kratzat², Annabelle Campbell¹, Robert Buschauer², A. Maxwell Burroughs³, Otto Berninghausen², L. Aravind³, Roland Beckmann², Rachel Green^{1,4}, Allen R. Buskirk^{1,*}

¹Department of Molecular Biology and Genetics and ⁴Howard Hughes Medical Institute, Johns Hopkins University School of Medicine, Baltimore, United States.

²Gene Center and Center for Integrated Protein Science Munich, Department of Biochemistry, University of Munich, Munich, Germany.

³Computational Biology Branch, National Center for Biotechnology Information, National Library of Medicine, National Institutes of Health, Bethesda, United States.

*To whom correspondence should be addressed: buskirk@jhmi.edu

Abstract

Ribosome rescue pathways recycle stalled ribosomes and target problematic mRNAs and aborted proteins for degradation. In bacteria, it remains unclear how rescue pathways distinguish ribosomes stalled in the middle of a transcript from actively translating ribosomes. In a genetic screen in *E. coli*, we discovered a novel rescue factor that has endonuclease activity. SmrB cleaves mRNAs upstream of stalled ribosomes, allowing the ribosome rescue factor tmRNA (which acts on truncated mRNAs) to rescue upstream ribosomes. SmrB is recruited by ribosome collisions; cryo-EM structures of collided disomes from *E. coli* and *B. subtilis* reveal a distinct and conserved arrangement of the individual ribosomes and the composite SmrB binding site. These findings reveal the underlying mechanism by which ribosome collisions trigger ribosome rescue in bacteria.

Introduction

Ribosomes often encounter obstacles that stop them in their tracks: the synthesis of roughly 1 out of every 250 proteins in *E. coli* ends in failure (1). Problems arise in many ways. Ribosomes arrest when they reach the 3'-end of transcripts that lack a stop codon, for example, due to premature transcriptional termination or mRNA decay (2). Ribosomes also stall on intact messages when they encounter chemical damage in the mRNA (2, 3), codons that are decoded very slowly (4), or specific nascent peptide sequences that inhibit their own translation (5, 6). Although stalling is sometimes resolved productively, prolonged pauses often lead to aborted protein synthesis. Such translational failures are dangerous because they trap ribosomes in inactive complexes and produce incomplete proteins that can be toxic. To meet these challenges, bacteria have evolved ribosome rescue mechanisms that selectively recognize stalled ribosomes, rescue the ribosomal subunits, and target problematic mRNAs and nascent proteins for degradation (reviewed in (7)).

How do ribosome rescue factors in bacteria distinguish stalled ribosomes from actively translating ribosomes? There are two rescue pathways active in *E. coli*: the main one (mediated by tmRNA and its protein partner, SmpB) and a backup pathway (mediated by ArfA) that is induced when tmRNA is overwhelmed (8). These pathways differ in fundamental ways: the tmRNA-SmpB complex enters ribosomes and encodes a short peptide tag to target the nascent peptide for proteolysis (9) whereas ArfA simply promotes peptidyl hydrolysis by recruiting the canonical release factor RF2 (10). Because both factors bind in the mRNA channel, their activity is inhibited by intact mRNA downstream of the stall site (7, 11-13). In cases where translation stalls on intact messages, the current model is that mRNA cleavage yields truncated mRNAs that become good substrates for rescue pathways. For example, ribosome stalling during termination in an inefficient context, Glu-Pro-stop (EP*), leads to mRNA cleavage in the ribosomal A site (14). mRNA cleavage is an attractive mechanism that could explain how rescue factors identify ribosomes that have irreversibly arrested. Yet the signal that triggers mRNA cleavage and the identity of the nucleases involved have remained elusive.

Recent work has revealed insights into how eukaryotic cells recognize and rescue stalled ribosomes. The E3 ubiquitin ligase Hel2 was identified in a genetic screen in yeast as a factor that promotes ribosome rescue by adding ubiquitin to specific ribosomal proteins (15). Hel2 is thought to recognize the interface between two small ribosomal subunits formed when an upstream ribosome collides into a stalled ribosome (16, 17). Collisions are the trigger that leads to ubiquitination of r-proteins and activation of downstream quality control pathways including subunit splitting, mRNA decay, and degradation of the nascent polypeptide (18). In the absence of ubiquitination systems and Hel2 homologs, however, it has been unclear whether similar mechanisms are at play in bacteria.

Here, we report that the *E. coli* protein SmrB cleaves mRNA upstream of stalled ribosomes, promoting ribosome rescue. SmrB contains an SMR domain associated with nuclease activity (19-21); SMR-domain proteins are broadly conserved in bacteria and eukaryotes as well as in a few archaeal lineages, one of the few rescue factors with a widespread presence across the three superkingdoms of life. We show that following SmrB cleavage at the 5'-boundary of the stalled ribosome, upstream ribosomes translate to the 3'-end of the upstream mRNA fragment and are rapidly rescued by tmRNA. We show that SmrB binds preferentially to collided ribosomes and only cleaves at stalling motifs where collisions occur, arguing that SmrB recognizes aberrant translation through recruitment to collided ribosomes. Moreover, we present cryo-EM structures of ribosome dimers stalled at specific stalling motifs in *B. subtilis* and *E. coli*, revealing a distinct and conserved architecture of disomes formed by collisions. In SmrB-bound disomes we define a composite binding site that explains how SmrB is specifically recruited to and activated by ribosome collisions. These findings establish that ribosome collisions are the trigger for ribosome rescue in *E. coli* through recruitment of the nuclease SmrB.

Results

A genetic selection for novel rescue factors

To identify novel factors that act early in the ribosome rescue pathway in *E. coli*, we performed a genetic selection similar to the one used previously to discover Hel2 in eukaryotes (15), searching for mutants that allow ribosomes to translate through a strong stalling motif and complete the translation of a downstream ORF. Our selection is based on a reporter construct encoding a fusion of NanoLuc upstream of the bleomycin resistance protein (Ble) that will confer growth on selective media (Fig 1A). Two control constructs are shown: one has a stop codon in between the genes and produces NanoLuc alone (Stop); the second is a direct fusion without any intervening stalling motif (Non-stall) and produces full-length fusion protein. In a third construct, we inserted the strong SecM arrest motif at the junction of NanoLuc and Ble (SecM); overexpression of reporters containing this stalling motif leads to mRNA cleavage and tagging of the nascent peptide by tmRNA (5).

We first confirmed that the SecM reporter undergoes stalling and ribosome rescue using antibodies against the Strep-tag at the N-terminus of the NanoLuc-Ble fusion protein. Although abundant full-length protein is visible in the Non-stall control, no full-length protein is detectable for the SecM reporter due to the strong arrest sequence (Fig 1B). To visualize the aborted protein product, we introduced the SecM reporter into cells lacking tmRNA (encoded by *ssrA*). Using the anti-Strep antibody, we observed truncated protein that is roughly the same size as NanoLuc produced from the Stop control (Fig 1B).

As another control, we developed a reporter with eight consecutive isoleucine residues at the fusion site; this reporter yields relatively little full-length protein detected by the anti-Strep

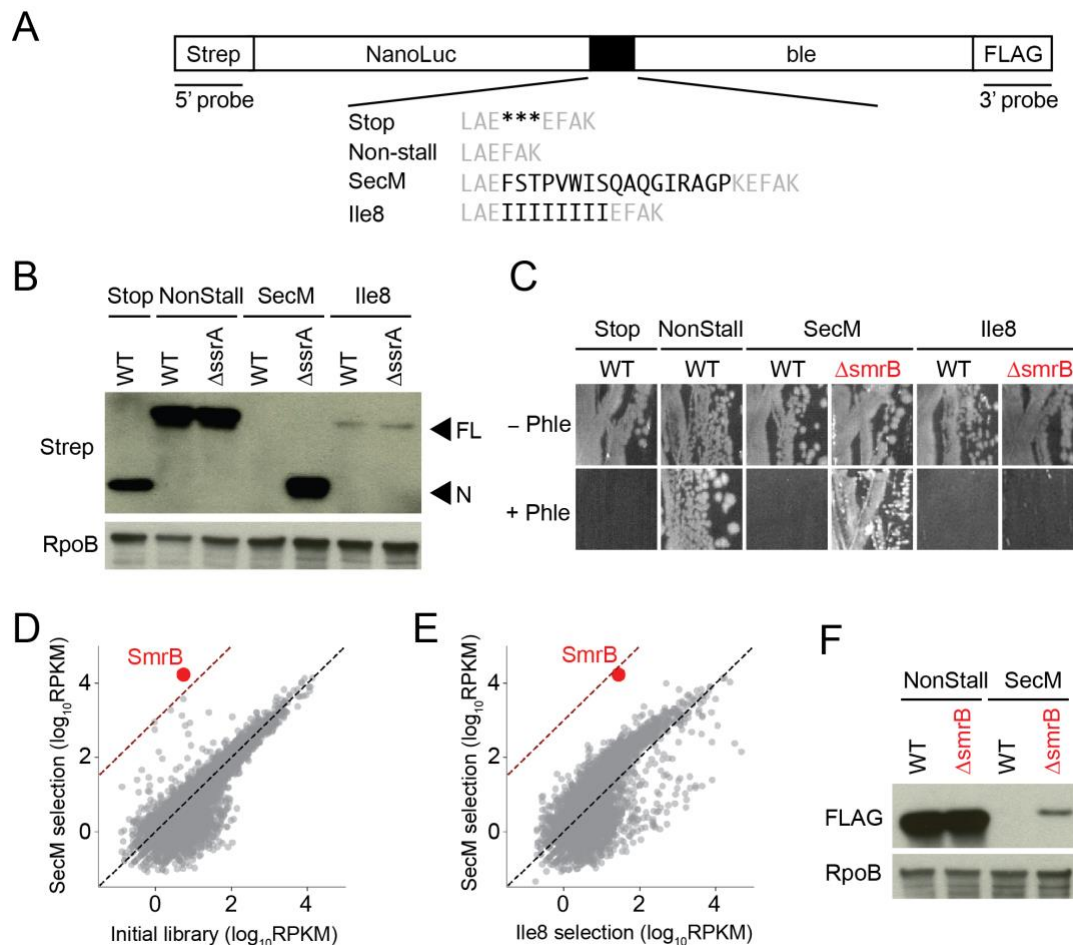


Figure 1. A genetic selection for novel rescue factors. (A) Reporters for studying ribosome rescue in *E. coli*. Between the NanoLuc gene and bleomycin resistance gene, we inserted either stop codons, no added sequence, the SecM stalling motif, or eight Ile codons (black). (B) Reporter protein from wild-type and Δ ssrA strains was detected by antibodies against the N-terminal Strep-tag. Arrows indicate the full-length fusion protein (FL) and shorter NanoLuc protein (N). The RpoB protein serves as a loading control. (C) Growth of wild-type and Δ ssrB strains expressing various reporters on media with or without 50 μ g/mL phleomycin. (D) and (E) The results of TN-seq are shown as a scatter plot of mapped reads (rpkm) for each gene corresponding to the number of transposon insertions. The dashed line indicates 1000-fold enrichment. (F) Full-length reporter protein was detected using antibodies against the FLAG-tag.

antibody, likely because the protein is misfolded and degraded (Ile8, Fig 1B). No truncated protein from the Ile8 reporter was observed in the Δ ssrA strain. The relatively low levels of full-length protein independent of ribosome stalling and rescue makes the Ile8 reporter a useful control in our genetic selection, as discussed below.

Using the NanoLuc-Ble reporters, we found that expression of the full-length reporter protein from the Non-stall construct conveys resistance to 50 μ g/mL phleomycin (an antibiotic structurally related to bleomycin) (Fig 1C). In contrast, cells expressing NanoLuc alone from the Stop construct are sensitive to this concentration of phleomycin, as expected. Next, we tested the SecM and Ile8 constructs and observed that wild-type cells expressing these reporters are also phleomycin sensitive, in line with the finding that the full-length protein is expressed at very

low levels from these constructs. These results establish parameters for the screen to identify gene deletions that increase the level of full-length reporter protein.

To perform the genetic selection we adopted a Tn-seq approach (22, 23), creating a knock-out library of about 5 million colonies through random insertion of Tn5 transposase into *E. coli* K12 MG1655. We transformed this library with a plasmid expressing the SecM or the Ile8 reporter and plated the transformants on media containing 50 µg/mL phleomycin. After harvesting phleomycin-resistant cells, we counted the number of transposon insertions per gene (normalized by length) in units of reads per kilobase per million mapped reads (rpkm) (Fig 1D). Compared to the initial library, 29 genes in the SecM reporter strain and 109 genes in the Ile8 reporter strain exhibited a more than 10-fold enrichment in transposon insertions. Many of these genes are false positives relevant to phleomycin toxicity. By comparing the results of the SecM selection with the Ile8 selection, we can remove false positives from consideration, focusing instead on genes that are selectively enriched in the SecM selection because they affect ribosome stalling and rescue (Fig 1E).

We found a single gene, *smrB*, where transposon insertions were strongly enriched in the SecM reporter strain compared to the Ile8 reporter strain (~600-fold, Fig 1E). To confirm this phenotype, we constructed a clean *smrB* deletion strain and found that Δ *smrB* cells expressing the SecM reporter are resistant to phleomycin whereas cells expressing the Ile8 reporter remain sensitive (Fig 1C). Furthermore, using the anti-FLAG antibody, we observe that deletion of *smrB* yields increased levels of full-length NanoLuc-Ble protein from the SecM reporter (Fig 1F) and from similar reporters with other stalling motifs, such as 12 rare Arg codons or the Glu-Pro-stop motif (EP*) (Fig S1). In contrast, loss of *smrB* has no effect on expression of the Non-stall reporter.

SmrB is a conserved nuclease involved in ribosome rescue

The *E. coli* SmrB protein is 183 amino acids long and contains a domain of the Small MutS Related (SMR) superfamily first proposed to act as a DNase in MutS-like proteins in bacteria and plants. However, more recent studies have shown that SMR domains possess endonucleolytic RNase activity (19, 24, 25). Indeed, we recently identified an SMR protein, Cue2, as the endonuclease that cleaves mRNA upstream of stalled ribosomes in yeast (20). A systematic analysis of the SMR domains across the tree of life revealed independent fusions to a diverse array of RNA-binding domains supporting the hypothesis that it primarily operates on RNA (21).

To better understand the evolutionary trajectories of the SMR proteins, we performed phyletic pattern (Fig 2A) and phylogenetic analyses (Fig S2). We find that SMR domains are broadly conserved in bacteria, though notably underrepresented in the PVC group and the actinobacteria (Fig 2A). They are found across all sampled eukaryotic lineages, but are relatively uncommon in Archaea, where they are found mainly in Asgardarchaeota and Thermoplasmata.

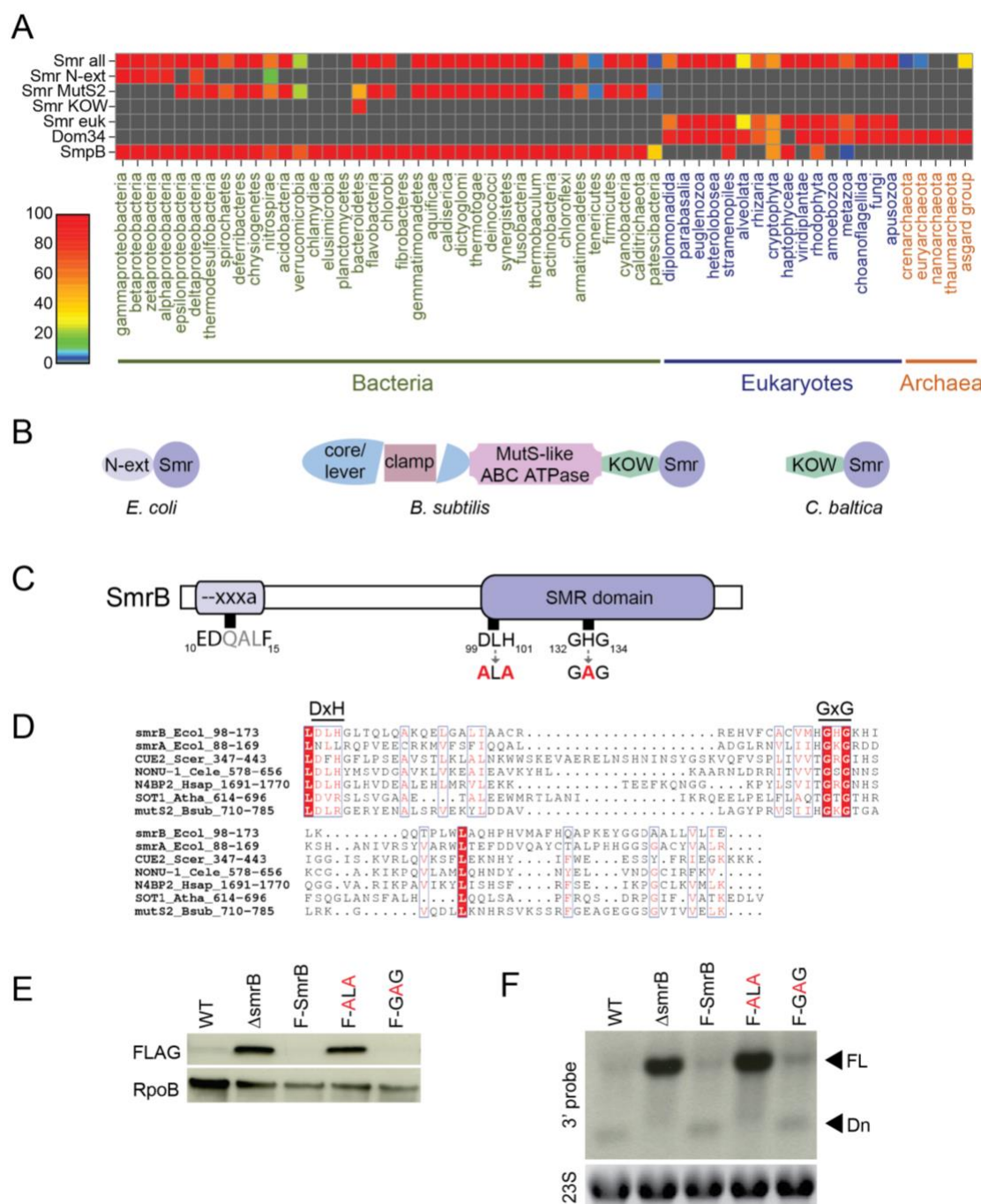


Figure 2. SMR-domain proteins are conserved RNA nucleases. (A) Heat map demonstrating the conservation and distribution of SMR-domain proteins and other related translational quality control factors. Smr-all includes all types of SMR-domain proteins; Smr-euk includes only the eukaryotic branch. (B) Domain organization of three representative bacterial proteins containing an SMR domain. (C) Domain organization of *E. coli* SmrB. Mutations at the two conserved DxH and GxG motifs are indicated by red bold letters. (D) Sequence alignment of SMR domains of representative proteins. Identical residues are shown in white with a red background; conserved residues are shown in red. The identity of each sequence is represented by the gene name, species name, and numbers indicating the beginning and the end of the residues used for the alignment. Ecol, *Escherichia coli*; Scer, *Saccharomyces cerevisiae*; Cele, *Caenorhabditis elegans*; Hsap, *Homo sapiens*; Atha, *Arabidopsis thaliana*; Bsub, *Bacillus subtilis*. (E) Full-length SecM reporter protein was detected with antibodies against the FLAG-tag. The RpoB protein serves as a loading control. F-SmrB, F-ALA, and F-GAG indicate endogenously FLAG-tagged SmrB and its variants. (F) The SecM reporter mRNA was detected on northern blots using a probe which anneals to the 3'-end of the reporter. Ethidium bromide staining of 23S rRNA serves as a loading control. FL = full-length and Dn = the downstream mRNA fragment.

These data suggest that the SMR domain might have entered the eukaryotic stem lineage at some point from a bacterial source.

The bacterial SMR domains cluster into three major clades. *E. coli* SmrB together with other proteobacterial versions form the first of these clades (Fig 2B) typified by a characteristic extension N-terminal to the SMR domain. This extension contains a predicted helix (residues 9-20) with a strongly conserved “--xxxa” motif (two negatively charged residues followed by three variable and one aromatic residue; E₁₀DQALF₁₅ in *E. coli* SmrB; Fig 2C and Fig S3) followed by a poorly conserved, largely unstructured segment. In gammaproteobacteria, like *E. coli*, a duplication led to two copies of these SMR proteins per genome; one with active site residues conserved (SmrB) and the other predicted to be enzymatically inactive (SmrA). The second clade contains the most common bacterial version typified by the *B. subtilis* MutS2 protein. From N- to C-terminus, these proteins contain the core/lever and clamp domains, the MutS DNA mismatch repair protein-type P-loop ABC ATPase domain, as well as an additional KOW domain with a SH3-like fold and a C-terminal SMR domain (Fig 2B). Notably, the MutS2 proteins lack the mismatch recognition and connector domains typical of the canonical MutS protein involved in mismatch repair. We identified several independent occasions where the predicted active site residues have been lost in this clade. The third clade is the smallest, restricted to the *Bacteroidetes* lineage, with an N-terminal KOW domain and C-terminal SMR domain.

An alignment of the SMR domain (residues 98-173) reveals that SmrB contains the conserved residues associated with endonuclease and RNA-binding activity (21, 26): residues D₉₉LH₁₀₁ correspond to the DxH motif implicated in catalysis and residues G₁₃₂HG₁₃₄ with the GxG motif marking the loop predicted to interact with RNA substrates (Fig 2D). We generated *E. coli* strains where the DxH and GxG motifs were mutated to ALA and GAG, respectively (Fig 2C), at the endogenous *smrB* locus tagged with an N-terminal FLAG epitope. The FLAG tag does not inhibit SmrB activity; like the wild-type, little or no full-length reporter protein is detectable in this strain (Fig 2E). Importantly, we observe that the ALA mutation increased full-length protein to a similar extent as deletion of *smrB*, whereas the GAG mutation had no discernable effect in vivo activity. These results suggest that the DxH motif is critical for SmrB activity while the central residue in the GxG motif is not required, consistent with its lower conservation. We note that loss of a second SMR-domain protein encoded in the *E. coli* genome, SmrA, which lacks the DxH motif did not affect expression of the stalling reporter (Fig S4).

To observe more directly the activity of SmrB on the reporter mRNA in vivo, we performed northern blots with a probe binding to the 3'-end of the reporter construct (Fig 2F). In the wild-type strain, the full-length reporter mRNA is barely detectable while the strongest signal comes from a shorter mRNA fragment whose size suggests that cleavage is occurring somewhere near the SecM motif. In the Δ smrB strain, the downstream fragment disappears and the levels of the full-length mRNA are dramatically higher. As expected, the strains with FLAG-tagged SmrB and the GAG mutant show robust levels of RNA cleavage, whereas the ALA mutant strain shows high

levels of reporter mRNA. These results confirm that SmrB cleaves the reporter mRNA in vivo and reveal that SmrB cleavage is the dominant pathway that targets the reporter mRNA for degradation.

Reporter mRNAs decayed via multiple pathways

We next asked whether we could detect the upstream fragment using a probe against the 5'-end of the reporter mRNA. We began by comparing the mRNA levels of the SecM-short reporter and the EP* reporter in the wild-type strain versus strains lacking either tmRNA or SmrB or both. Whereas we see little reporter RNA in the wild-type strain (since it is cleaved and degraded), the 5'-probe reveals the upstream fragment from both reporters in the Δ ssrA strain (Fig 3A), consistent with prior reports that the loss of tmRNA stabilizes the upstream fragment (5, 14). As expected, there is no detectable upstream fragment in the Δ smrB strain. Surprisingly, however, the upstream fragment is present for both reporters in the Δ ssrA Δ smrB strain ($\Delta\Delta$); this unexpected result reveals that this truncated mRNA can be produced by one or more mechanisms that are independent of SmrB. It is unlikely that other endonucleases are responsible, given that the downstream fragment detected by the 3'-probe disappears in strains lacking SmrB (Fig 3A). We speculate that in the absence of SmrB, the upstream fragment is generated by exonucleolytic decay of the mRNA back to the stalled ribosome; *E. coli* has three processive 3'-5' exonucleases implicated in mRNA decay but lacks 5'-3' exonucleases (27).

SmrB cleaves mRNA at the 5'-boundary of stalled ribosomes

The reporter mRNA is degraded by at least two mechanisms, one that depends on SmrB and another that likely involves exonucleases. To better characterize these pathways, we used RACE to identify the 5'- and 3'-ends of the mRNA fragments produced by these decay events coupled to ribosome stalling (Fig 3B). 5'-RACE experiments reveal the 5'-end of the downstream fragment which is generated solely by endonucleolytic cleavage by SmrB: there is a sharp peak 11 nt upstream of the SecM stall site (Fig 3C). This peak is also evident in the Δ ssrA strain, but disappears in the Δ smrB and the Δ smrB Δ ssrA knockout strains. These data are consistent with the northern blots showing that the downstream fragment is not detectable in strains lacking SmrB (Fig 3A, 3'-probe). We see very similar results from the EP* reporter where the 5'-end of the downstream fragment is 10 nt upstream of the stop codon in the A site of the ribosome (Fig 3D). Based on ribosome footprinting experiments (28), we know that the 5'-boundary of the ribosome is roughly 12 nt upstream of the A-site codon, suggesting that SmrB cleaves mRNA at the site where it exits the ribosome.

We also used 3'-RACE to determine the 3'-end of the upstream mRNA fragment (Fig 3B). The data from these experiments are more complex because multiple pathways generate truncated mRNAs near the stall site. For the SecM reporter, in the wild-type and Δ ssrA strains, the strongest peak in the 3'-RACE data is 11 nt upstream of the stall site (Fig 3E); in the absence

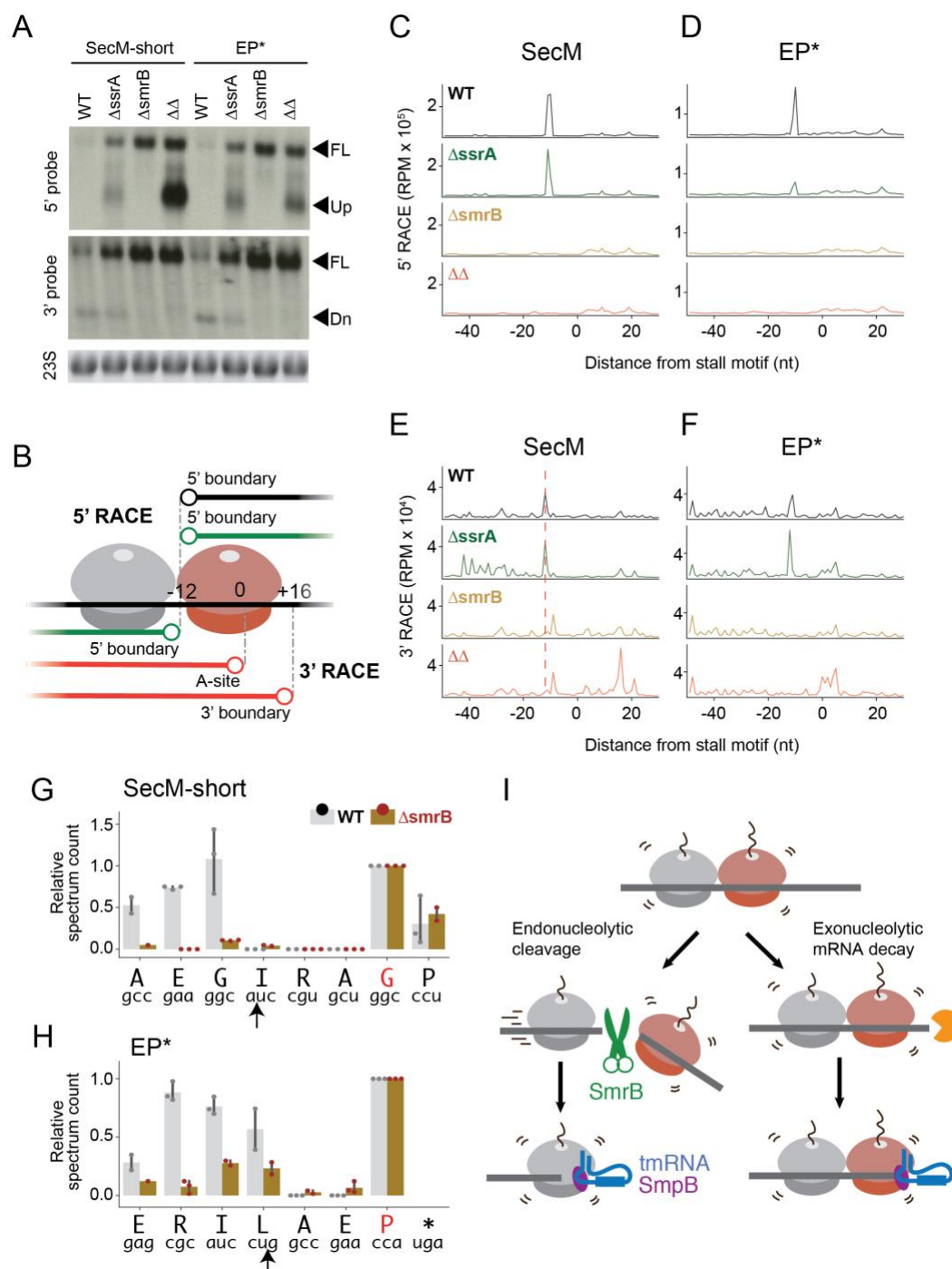


Figure 3. SmrB cleaves at the 5' boundary of stalled ribosomes. (A) Northern blots of reporter mRNA using the 5'-probe and the 3'-probe. Arrows indicate the full-length (FL) or truncated RNAs (upstream or downstream fragments). Ethidium bromide staining of 23S rRNA serves as a loading control. (B) Schematic representation of RNA fragments observed in the RACE data. (C) and (D) The results of 5' RACE showing the 5'-ends of downstream fragments in reads per million on the reporter sequence. The first nt in the A site codon in the stall motif is designated as zero. (E) and (F) The results of 3' RACE showing the 3'-ends of upstream fragments in reads per million on the reporter sequence. The first nt in the A site codon in the stall motif is designated as zero. (G) and (H) tmRNA tagging near the stall motif in wild-type and $\Delta smrB$ strains. The tagging site is the residue immediately preceding the tmRNA tag in peptide sequences detected by targeted LC-MS/MS. The red letter indicates the residue encoded by the P site codon at the stall site. The arrow indicates the SmrB cleavage site demonstrated by 5' RACE. The relative spectrum count is shown, normalized by the count at the stall site where tmRNA tagging was expected to occur in both the wild-type and $\Delta smrB$ strains. (I) A model for mRNA processing during ribosome rescue. In the endonucleolytic cleavage pathway, SmrB cleaves the mRNA at the 5' boundary of stalled ribosomes, at the interface of ribosome collisions. Upstream ribosomes then resume translation, reaching the 3'-end of the cleaved mRNA, and are quickly rescued by tmRNA-SmpB. In the secondary pathway, 3'-to-5' exonucleases degrade mRNA until they hit the 3' boundary of the stalled ribosome, after which the stalled ribosome is eventually rescued by tmRNA-SmpB.

of SmrB, this peak disappears. This same phenomenon was also observed in the EP* reporter (Fig 3F). For both reporters, these positions correspond perfectly with the site of cleavage identified on the downstream fragment by 5'-RACE, suggesting that these upstream fragments are derived from SmrB cleavage at the 5' boundary of stalled ribosomes.

In strains lacking both SmrB and tmRNA ($\Delta\Delta$) the 3'-RACE data provide additional information about other pathways that act on the upstream mRNA fragment. In the absence of both factors, the strongest 3'-RACE signal for the SecM reporter is 16 nt downstream of the first nt in the A site codon, roughly corresponding to the 3'-boundary of the ribosome stalled at the SecM motif (Fig 3E), likely the products of exonucleolytic decay. In contrast, the strongest 3'-RACE signal from the double knockout strain expressing the EP* reporter is at the A-site codon (Fig 3F). These results are broadly consistent with previous reports of mRNA cleavage at both the 5'- and 3'-boundaries of ribosomes stalled on SecM (5) and of A-site cleavage within ribosomes stalled during termination at EP* (14). Taken together, the 5'- and 3'-RACE data on these stalling reporter mRNAs reveal that SmrB cleaves at the 5'-boundary of stalled ribosomes and that in the absence of SmrB, other pathways lead to mRNA decay up to the A-site codon or the 3'-boundary of the lead stalled ribosome.

SmrB cleavage liberates stacked ribosomes upstream of stalled ribosomes

Our analyses of the reporter mRNA indicate that SmrB cleaves upstream of stalled ribosomes forming an upstream fragment whose decay is promoted by tmRNA. To ask which ribosome complexes are rescued by tmRNA, we determined where the tmRNA tag is added on both the short-SecM and EP* reporters. We immunoprecipitated reporter protein (using the N-terminal Strep-tag) from both the wild-type and ΔsmrB strains containing a tmRNA variant that tags the reporter protein with a ClpXP-resistant AANDENYALDD sequence (4).

We determined the sites of tmRNA tagging by digesting the immunoprecipitated reporter protein with lysyl endopeptidase and subjecting the resulting peptides to LC-MS-MS. For the SecM reporter, where ribosomes stall with the second Gly codon in GIRAGP in the P site (29), there is strong signal from the peptide produced when the tmRNA tag is added at the second Gly residue (Fig 3G), as previously reported (5). Importantly, robust tagging at this site is observed in both the wild-type and ΔsmrB strains, suggesting that SmrB cleavage is not essential for tagging at the SecM stall site. We also observe strong tagging four residues upstream (at the first Gly) in the wild-type strain (Fig 3G). This result correlates precisely with the SmrB cleavage site determined by RACE; tagging at this site is dramatically reduced in the ΔsmrB strain. Likewise, consistent with previous studies (6), we observe tmRNA tagging of the EP* reporter protein at the C-terminal Pro residue in both the wild-type and ΔsmrB strains (Fig 3H). We also observe tagging at the residues upstream of the stalling site at positions where mRNA is cleaved by SmrB in the wild-type strain; this signal is diminished in the ΔsmrB strain.

Taken together, the RACE and tmRNA tagging results lead us to propose the following model for ribosome rescue within ORFs in *E. coli* (Fig 3I). Ribosome stalling leads to endonucleolytic cleavage by SmrB at the 5'-boundary of the first, stalled ribosome (red). No longer impeded by the ribosome trapped on the stalling motif, upstream ribosomes (grey) translate to the end of the upstream mRNA fragment and arrest at the 3'-end generated by SmrB cleavage. The tmRNA-SmpB complex then rescues and releases these ribosomes, consistent with its well-characterized preference for truncated mRNAs. This model highlights how SmrB cleavage and tmRNA activity rapidly clear upstream ribosomes from the message and target it for decay. Consistent with previous studies, tmRNA also releases the initial stalled ribosome (red), tagging the nascent peptide right at the stall site. Decay of the reporter mRNA back to the 3'-boundary of the ribosome (in the case of SecM) or the A-site codon (in the case of EP*) by exonucleases likely allows tmRNA to gain access to these stalled ribosomes (5, 14, 30).

SmrB preferentially binds collided ribosomes

We next asked how SmrB selectively recognizes stalled ribosomes. Although ribosome collisions have not been implicated in bacterial ribosome rescue, our data suggest that SmrB, like Cue2, recognizes collided ribosomes. First, as shown above, 5'-RACE of the downstream fragment in the SecM reporter reveals that SmrB cleavage occurs precisely at the 5'-boundary of the SecM-stalled ribosome; additional peaks are seen (with lower intensity) further upstream of the stall site that cluster in sets centered roughly 25 nt apart, the length of a ribosome footprint (Fig 4A). Second, ribosome profiling data from the Δ ssrA Δ smrB strain expressing a related reporter reveal a strong peak of ribosome density at the SecM stall site, as expected, as well as sets of peaks roughly 25 nt apart extending upstream (Fig 4A). The 5'-boundaries of the SecM stalled ribosome and the first three stacked ribosomes align well with the sites of SmrB cleavage seen in the RACE data. These findings suggest that SmrB cleavage happens in the context of ribosome collisions, arguing that collisions may serve as a signal for SmrB recruitment or activation.

Our work so far has focused on strong stalling motifs in reporter genes. To ask what effects collisions have on SmrB binding to ribosomes globally, we induced collisions throughout the transcriptome using the antibiotic mupirocin (MPC) which inhibits isoleucine tRNA synthetase and globally slows down the rate of decoding of Ile codons (28, 31). In untreated cells, FLAG-SmrB is distributed broadly across the sucrose gradient, extending from the subunit fractions to the polysome fractions (Fig 4B), arguing that most SmrB is ribosome-bound. After inducing collisions for 5 min with 50 μ g/mL MPC, we observed that FLAG-SmrB moves deeper into the polysome fraction, consistent with preferential binding to collided ribosomes on messages that are heavily translated (Fig 4B).

Further, we treated cell lysates with RNase A to generate nuclease-resistant disomes, a hallmark of ribosome collisions (17). As expected, RNase A treatment collapses polysomes to yield a strong monosome peak and a small nuclease-resistant disome peak (Fig 4C). The disome

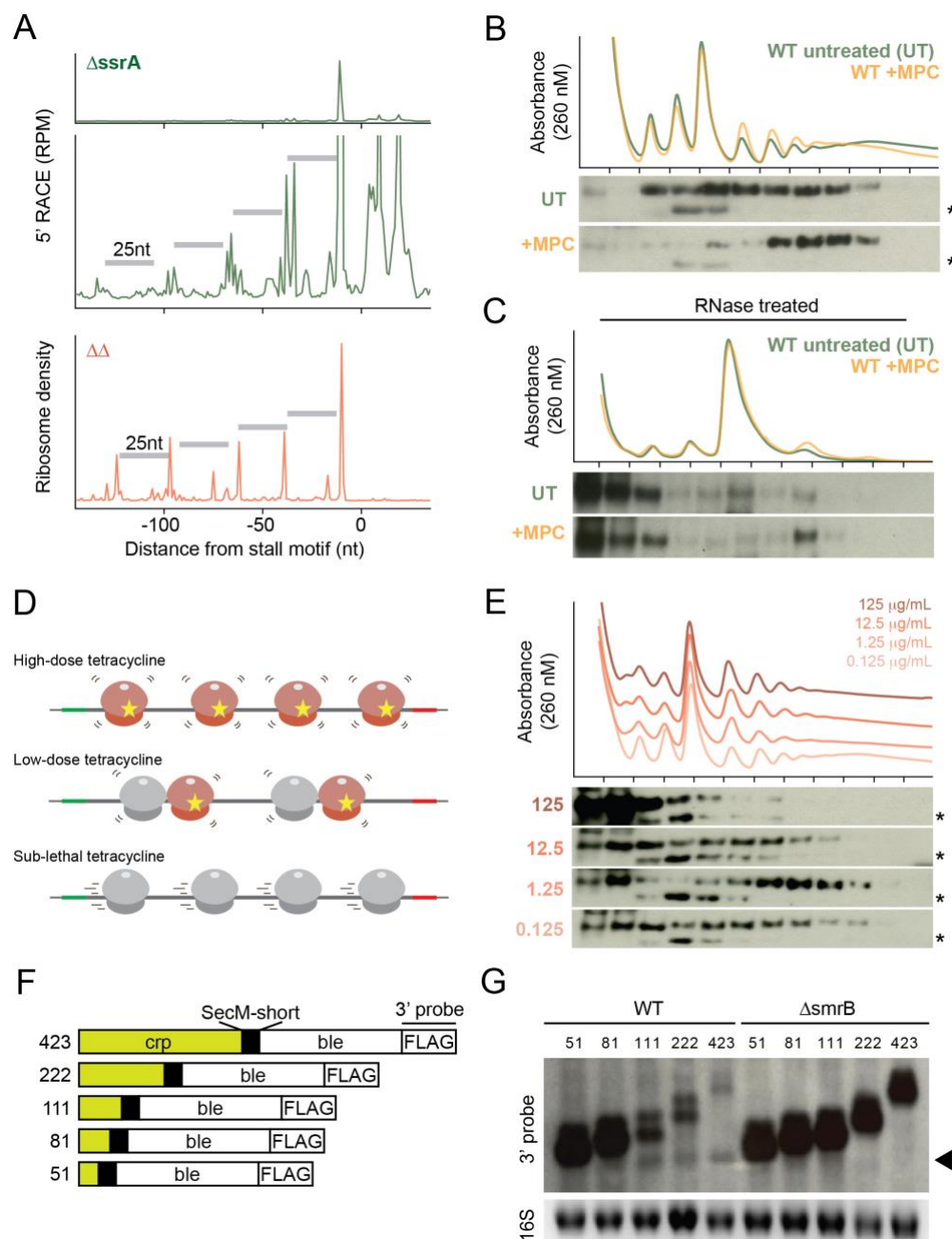


Figure 4. SmrB preferentially binds and cleaves upstream of collided ribosomes. (A) Top: 5'-RACE data reveal the SmrB cleavage sites as in Fig 4C, zoomed in to show smaller peaks upstream. Bottom: ribosome profiling data showing the 5'-boundary of ribosomes on the SecM reporter in the strain lacking tmRNA and SmrB. (B) The distribution of FLAG-SmrB with and without mupirocin (MPC) treatment (which induces pauses at Ile codons) was determined by fractionation over sucrose gradient and detection with an anti-FLAG antibody. A non-specific band is marked with *. (C) Lysates from cells with and without mupirocin treatment were treated with RNase A, fractionated over sucrose gradients, and the binding of FLAG-SmrB to nuclease resistant disomes was detected with an anti-FLAG antibody. (D) and (E) Low doses of tetracycline induce collisions whereas high doses stall ribosomes without inducing collisions. Following treatment with four different tetracycline concentrations, the distribution of FLAG-SmrB was determined by fractionation over sucrose gradient and detection with an anti-FLAG antibody. (F) and (G) In a new series of reporters, the Crp gene and bleomycin resistant gene are fused with the short SecM motif between them. The Crp gene is trimmed to reduce the number of ribosomes that can be loaded between the start codon and the stall site (the number shown). Reporter mRNA was detected on northern blots using the 3'-probe. An arrow indicates the downstream fragments. Ethidium bromide staining of 16S rRNA serves as a loading control.

peak is modestly but reproducibly higher in the MPC treated samples, consistent with the expectation that there are more ribosome collisions in MPC-treated cells. Although much of the SmrB dissociates from ribosomes under these conditions, moving into the top fractions, we see a strong SmrB band in the nuclease-resistant disome peak in the MPC-treated sample; quantitation of the amount of SmrB bound to various fractions shows strong enrichment for SmrB binding on colliding ribosomes relative to monosomes.

Another strategy to differentiate the effects of stalling and ribosome collisions is to treat cells with antibiotics that target the ribosome and then compare the effects of high doses, which stall all ribosomes quickly, versus lower doses that only stall some ribosomes, allowing others to translate until collisions occur (Fig 4D) (18). In untreated samples SmrB is broadly distributed in sucrose gradients while SmrB is enriched in polysomes deeper in the gradient when 1.25 $\mu\text{g/mL}$ tetracycline is used (Fig 4E). Importantly, the enrichment of SmrB in the polysomes is lost in cells treated with 10- or 100-fold higher concentrations of tetracycline.

Ribosome collisions promote SmrB cleavage

As previously performed in yeast (18), we generated a series of reporters to test whether ribosome collisions are required for mRNA cleavage. In these reporters, different lengths of the *crp* gene were fused upstream of the short SecM stalling motif, while the downstream *ble* sequence remains constant (Fig 4F). The reporters are numbered by the distance from the start codon to the stall site (in nt). We anticipated that the closer the short SecM motif is to the 5'-end of the ORF, the less room there is for ribosomes to load onto the mRNA and collide at the stalling motif. Using the 3'-probe against the reporter mRNA to follow the activity of SmrB, we observe the downstream mRNA fragment characteristic of SmrB cleavage and a strong reduction in full-length mRNA in the 111, 222, and 423 reporters (Fig 4G). In contrast, the downstream mRNA fragment is reduced in the 51 and 81 reporters and we see much higher levels of full-length mRNA. In the 51 and 81 reporters, only one or two ribosomes can be loaded upstream of the SecM stalled ribosome, respectively, suggesting that multiple collisions may be required to recruit SmrB. In the ΔsmrB strain, the amount of full-length mRNA is strongly increased in all five reporters and no downstream fragment is observed. These findings show that SmrB activity is triggered by collisions.

The structure of collided ribosomes from B. subtilis and E. coli

Ribosomal collisions in yeast and mammalian cells create a distinct architecture of disomes with new composite interaction surfaces that are recognized by collision sensors (16, 17). To ask whether bacterial ribosomes display a similar behavior, we generated collided ribosomes in cell-free translation systems, translating mRNAs encoding the arrest peptides MifM (32) in *B. subtilis* extracts and VemP (33) in the commercially available *E. coli* PURE system.

Following separation by sucrose density gradient centrifugation, disome and trisome peaks were collected and subjected to structural analysis by cryo-EM.

3D reconstruction of the *E. coli* disomes (details in Fig S5) revealed a defined arrangement of two ribosomes (Fig 5A). The leading (stalled) ribosome closely resembles the previously described VemP-stalled 70S in a non-rotated state, carrying a peptidyl-tRNA in the P site, a highly structured nascent peptide chain in the ribosomal tunnel, and an aminoacyl-tRNA in the A site (34). The collided ribosome is found in a mixture of rotated and non-rotated states carrying two tRNAs in the canonical or hybrid state conformation. The stalled ribosome engages the collided ribosome in an intricate interaction mainly involving protein-protein and protein-rRNA interactions between the two juxtaposed small 30S subunits. These interactions involve ribosomal proteins uS10, uS2, 16S rRNA helix h16, uS4, and 16S rRNA helices h5 and h17 in the collided ribosome interacting with uS9, uS2, 25S rRNA helix H78, uS11 and bS6, and uL9 of the stalled ribosome, respectively (Fig 5B,C). In addition, the L1 stalk in the large subunit of the stalled ribosome was observed in its “out” conformation forming a new bridge between its rRNA helix H78 and 16S helix h16 of the collided ribosome (Fig 5C).

Another substantial difference between the conformation of the stalled and collided ribosome is the dramatic rearrangement of the uL9 protein of the large ribosomal subunit. In individual 70S ribosomes, from its binding site on the 50S subunit below the L1 stalk, L9 contacts uS6 and uL2 in the 30S subunit (not shown). While this conformation was also observed in the collided ribosome, the L9 protein of the stalled ribosome flipped out of this position to engage in a novel mode of interaction via its C-terminal domain with the 30S subunit of the collided ribosome. This interaction involves rRNA helices h5 and h17 of the collided ribosome, thereby effectively forming another bridge between the stalled 50S subunit and the collided 30S subunit (Fig 5C). Although a similar bridging interaction of L9 between individual 70S ribosomes was observed previously in crystallized 70S ribosomes from *E. coli* and other bacteria (35, 36), the L9 binding site on the neighboring 30S subunit does not overlap with the site observed here in collided disomes and may be an artifact caused by crystallization conditions.

Notably, the largest protein of the 30S subunit, S1, is missing in the stalled ribosome but present in the collided one (Fig 5A). The arrangement of the interface between the solvent sides of the two 30S subunits results in very limited accessible space and would lead to a steric clash of the S1 protein with the collided ribosome. We conclude that formation of the observed disome architecture requires dissociation of S1 from the stalled ribosome. S1 dissociation may serve as a checkpoint in order to discriminate between short-lived ribosome collisions in productive polysomes and longer lasting stalling events.

When analyzing *E. coli* trisomes, we found that the structural features of the interface between the second and third ribosomes are essentially identical to the interface observed between the stalled and first collided ribosomes (e.g. the L1 and L9 bridges) (Fig 5D). This suggests that during long-lived stalling events, additional collisions can accumulate and yield a multitude

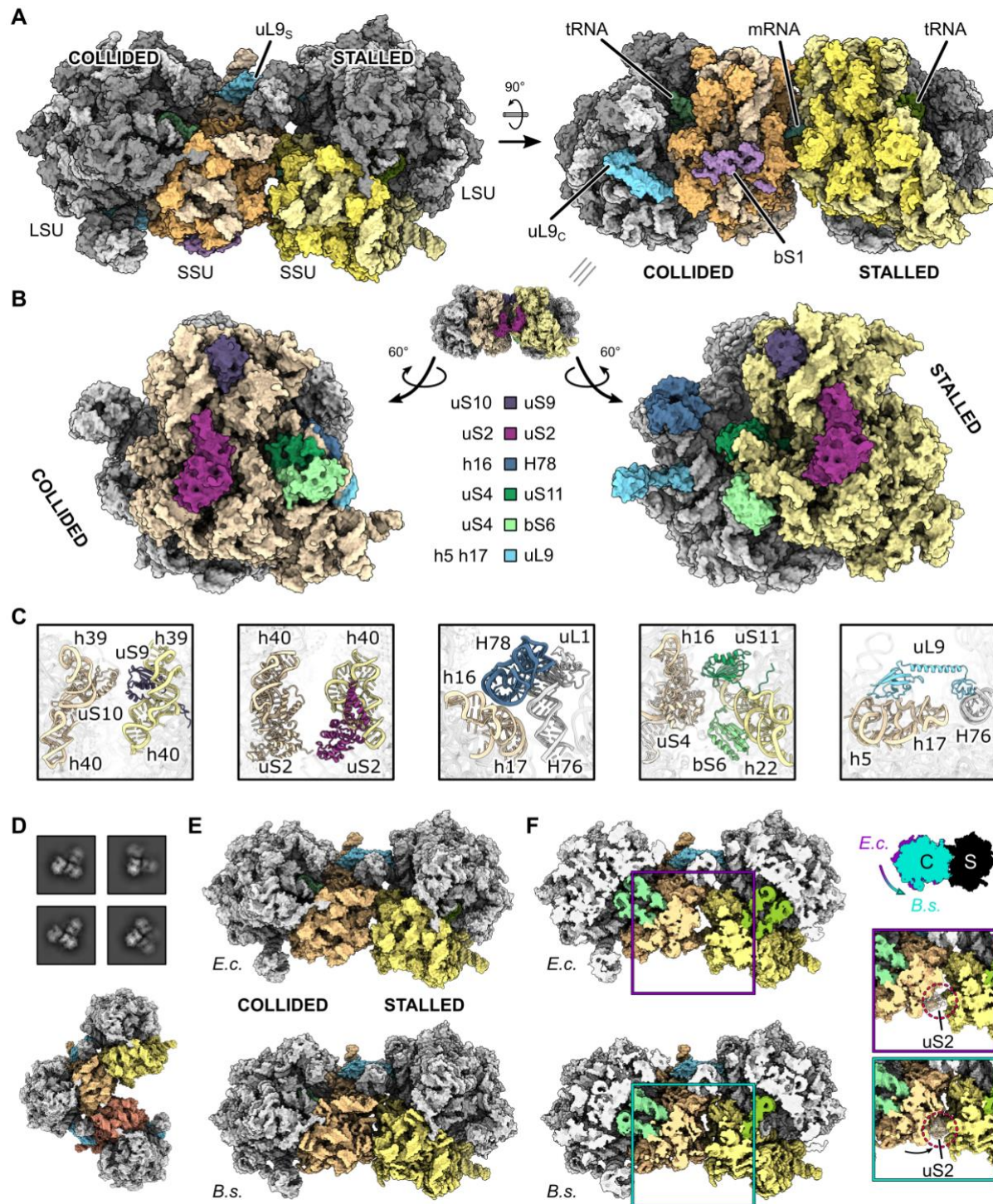


Figure 5. Cryo-EM structure of the *E. coli* disome. (A) Surface representation of the structural model of the *E. coli* disome. The uL9 proteins from stalled (uL9_s) and collided (uL9_c) adopt different conformations. (B) Interactions between stalled and collided ribosome at the disome interface. The disome interface is opened up by rotation of the stalled and collided ribosomes and interaction partners are shown in matching colors. (C) Cartoon representation of the individual interactions as they occur at the interface. (D) 2D class averages and cryo-EM structure model of an *E. coli* trisome. (E and F) Comparison of the *E. coli* (*E.c.*) and *B. subtilis* (*B.s.*) disomes displaying full and cut views. Note the smaller space between stalled and collided ribosomes in the *B.s.* disome interface as illustrated by comparing the positions of uS2 proteins in the zoomed view in (F).

of composite ribosome-ribosome interfaces. This may explain our observation of gradually increasing efficiency of ribosome rescue with longer reporter mRNAs allowing for more ribosomes to collide (Fig 4F,G).

We wondered whether the observed disome formation is unique to *E. coli* and compared our structures to those of the MifM-stalled disomes from the Gram-positive bacterium *B. subtilis*. We found that ribosome collisions in *B. subtilis* result in disomes adopting an essentially identical conformation as observed in *E. coli*: the overall orientation and interactions of the ribosomes are highly similar, the bridge by the L1 stalk to rRNA helix h16 is formed, and L9 of the stalled ribosome reaches over to the 30S subunit of the collided one (Fig 5E). One notable difference is that the 30S subunits are positioned closer in the *B. subtilis* disome when compared to *E. coli* (Fig 5F). This high degree of overall similarity indicates that the observed mode of collided disome formation is likely to be conserved in bacteria, with subtle differences at the disome interface. Notably, the overall architecture of these collided disomes is very different from hibernating, so-called 100S disomes formed under stress conditions (Fig S6) (37, 38). We conclude that, similar to eukaryotes, the observed disome (and trisome) architecture of collided ribosomes is a conserved feature in bacteria that can provide a unique interface used by rescue factors such as SmrB to recognize stalled ribosomes.

In vitro cleavage of mRNA and the SmrB-disome structure

Next, we reconstituted SmrB recruitment to collided disomes and endonucleolytic cleavage of mRNA *in vitro*. We incubated purified SmrB or the nuclease deficient ALA mutant with purified VemP-stalled disomes and analyzed the reaction products by sucrose density gradient centrifugation (Fig 6A). In a control reaction without SmrB we observed disomes, as expected, as well as some 70S ribosomes likely arising from ribosome dissociation from the mRNA and/or background nucleolytic activity. In contrast, after incubation with wild-type but not mutant SmrB, we observed an almost complete loss of the disome signal and a corresponding increase in the 70S signal, consistent with cleavage between the collided ribosomes by the endonuclease activity of SmrB.

We reconstituted the nuclease-deficient SmrB mutant with our *E. coli* VemP-stalled disomes and subjected the complexes to structural analysis by cryo-EM (details in Fig S7). Compared to disomes alone, this reconstruction revealed an extra density between the 30S ribosomal subunits in the immediate vicinity of the mRNA stretching from the mRNA exit site of the stalled ribosome to the mRNA entry of the collided ribosome (Fig 6B). Although the overall resolution of the SmrB-bound disome is 3.3 Å, we observed limited local resolution in this region of the map. Therefore, we could only partially build the molecular structure of SmrB and relied on the AF2-driven prediction for rigid body docking of SmrB (39) (Fig S8).

The binding site for SmrB involves both the stalled and the collided ribosome: on the collided ribosome the SMR domain interacts with uS3, uS2 and uS5, whereas on the stalled

ribosome it binds rRNA helices h40 and h26 as well as ribosomal proteins uS11 and uS21 (Fig 6C-E). Notably, in several bacteria the genes encoding uS21 and SMR-domain proteins are tightly linked in conserved operons, suggesting that this interaction might be a conserved aspect of binding of SMR domains to collided ribosomes. The N-terminal extension region of SmrB forms a hook-like structure that wraps around uS2 of the collided ribosome (Fig 6D). Interestingly, the N-terminal alpha-helix contains the --xxxa motif conserved in other SMR-domain proteins in proteobacteria (Fig 2C and Fig S3). We observed this hook-like N-terminus of SmrB on the stalled ribosome as well, although in that position it cannot be connected to the SMR domain between the subunits and thus represents a second copy of SmrB in the complex. We speculate that this N-terminal helix may promote the initial recruitment of SmrB to elongating 70S ribosomes and that when collisions occur, the subsequent binding of the SMR domain at the composite binding site between collided ribosomes further stabilizes SmrB binding. In agreement with this idea, a truncated SmrB mutant consisting of only the SMR domain (residues 88-183) does not bind ribosomes (Fig 6H). The observed binding mode of SmrB therefore explains how SmrB is specifically recruited to collided disomes (or trisomes).

The active site of SmrB interacts with the bridging mRNA, poised for cleavage in between the individual ribosomes (Fig 6F,G). From the structure, it is difficult to determine the exact mRNA residues to be cleaved, however, and the nuclease-deficient mutant of SmrB may engage in a somewhat different interaction with its mRNA substrate. Nevertheless, the observed positioning indicates that SmrB can execute endonucleolytic cleavage of the mRNA between position -9 and -16, counting from the first nucleotide in the A site of the stalled ribosome, in agreement with our biochemical data. We speculate that activation of SmrB specifically on collided disomes is a result of precise positioning with respect to its substrate.

Disruption of the SmrB-binding pocket on collided ribosomes

We asked if disruption of the disome interface or the SmrB binding pocket formed between collided ribosomes would interfere with mRNA cleavage by SmrB. The L9 protein from the stalled ribosome makes contacts with the 30S subunit in the collided ribosome (Fig 5C) and strains lacking L9 are known to have high levels of frameshifting (40, 41). We found, however, that SmrB still cleaves the CRP reporters in a collision dependent manner in an L9 knockout strain; the reporter mRNA processing is indistinguishable from that seen in wild-type strains (Fig S9). Moreover, fusion of mCherry to the C-terminus of L9 (on the domain that contacts 16S rRNA in the collided ribosome) also has no effect on SmrB activity (Fig S9). These results suggest that this contact between the disomes does not play an essential role in stabilizing the disome interaction. In contrast, we observe that fusion of MBP to the N-terminus of S21 dramatically stabilizes full-length mRNA in the 111 and 222 CRP reporters compared to the wild-type strain (Fig 6I). To a lesser extent, fusion of GFP to the C-terminus of S6 also stabilizes the 111 CRP reporter compared to the wild-type strain (Fig 6I). These results are consistent with a reduction in SmrB activity and

stabilization of the reporter mRNA due to a disruption of the SmrB binding pocket formed between the collided ribosomes, validating the structural findings reported here.

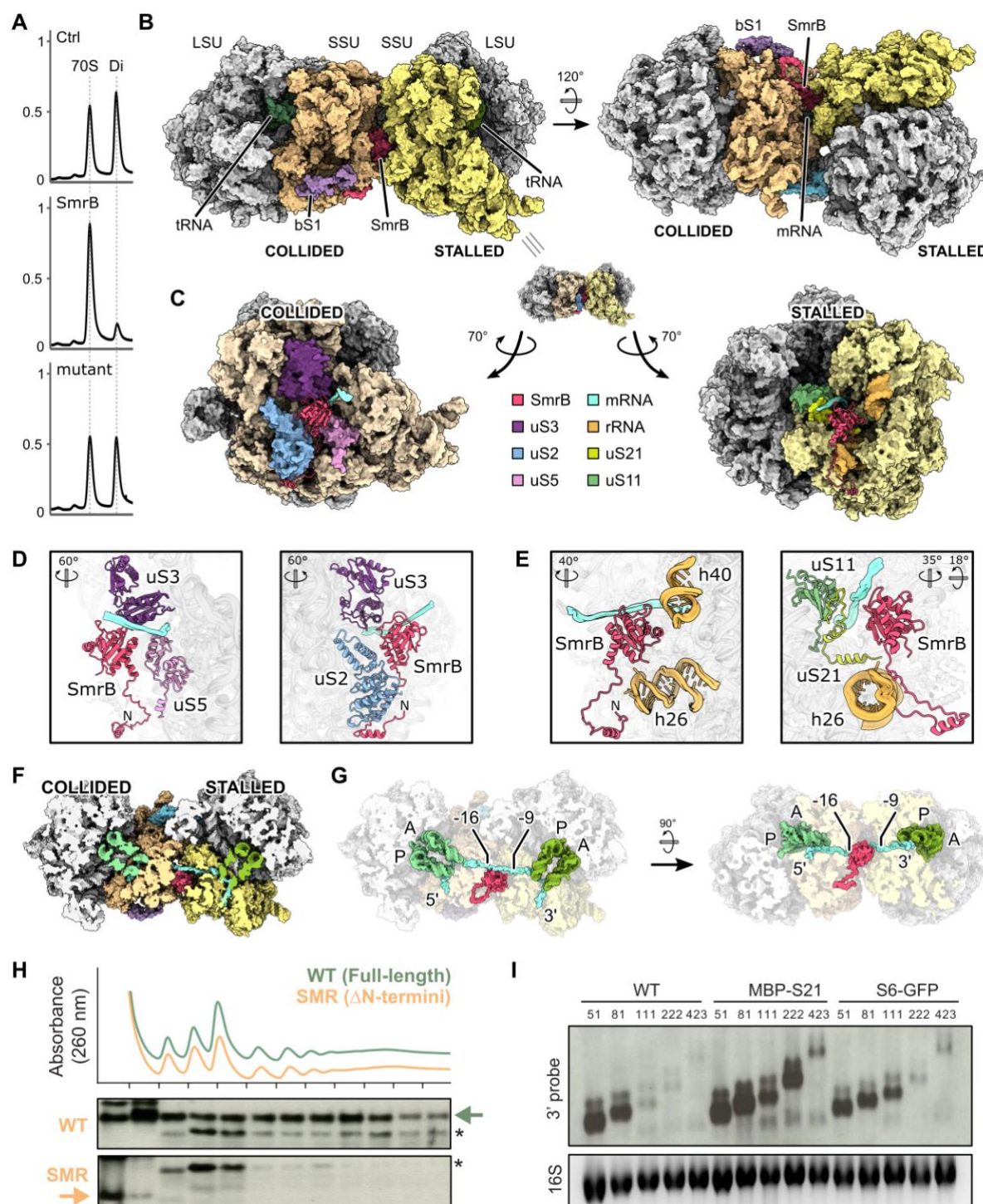


Figure 6. Cryo-EM structure of the SmrB-bound *E. coli* disome. (A) Disome nuclease assay. Sucrose density gradient profiles of VemP-stalled disomes alone (Ctrl), incubated with SmrB (SmrB) and incubated with nuclease deficient SmrB (mutant), respectively. The Y-axes show the absorption at 260 nm. (B) Surface representation structural model of SmrB bound to the *E. coli* disome. (C) Interactions between SmrB and the stalled and collided ribosomes at the disome interface. The disome interface is opened up by rotation of the stalled and collided ribosomes and SmrB is shown in cartoon representation. *Continued on next page...*

Figure 6. (D and E) Cartoon representation of the individual interactions of SmrB with the collided ribosome in (D) and the stalled ribosome in (E). The orientations of the individual views with respect to (C) are indicated. (F) Cut view of the SmrB bound disome showing the mRNA path. (G) Interaction of SmrB with the mRNA. The disome orientation in the left part of (G) corresponds to the one shown in (F). Approximately 8 nucleotides of the mRNA are exposed at the disome interface, in reach for SmrB cleavage. The nucleotides at the ribosome boundaries are indicated, counting the first nucleotide in the A-site of the stalled ribosome as 0. (H) The distribution of FLAG-tagged full-length SmrB and a construct with only the SMR domain (residues 88-183) was determined by fractionation over sucrose gradient and detection with an anti-FLAG antibody. A non-specific band is marked with *. (I) Northern blots using the 3'-probe against the CRP reporters with the short SecM stalling motif in wild-type cells, a strain where MBP is fused to the N-terminus of S21, and a strain where GFP is fused to the C-terminus of S6.

Discussion

Our findings indicate that ribosome collisions are the critical trigger for ribosome rescue in *E. coli*: collisions recruit the endonuclease SmrB, triggering mRNA cleavage and rescue of upstream ribosomes by tmRNA. Under normal conditions, SmrB is distributed broadly across sucrose gradients, suggesting that it binds ribosomes generally, scanning for problems. When collisions are induced throughout the transcriptome, SmrB moves deep into the polysome fraction and binds preferentially to nuclease-resistant disomes that are a hallmark of collisions. Importantly, we find that SmrB recruitment is triggered by low doses of tetracycline that promote collisions but not by high doses that promote stalling without collisions. Furthermore, SmrB is unable to cleave mRNA at stalling motifs positioned too close to the 5'-end of an ORF for sufficient collisions to occur. We conclude that ribosome collisions serve as a signal to recruit ribosome rescue factors in bacteria as well as in eukaryotes.

The importance of collisions is fully validated by our cryo-EM structures of collided ribosomes from both Gram negative *E. coli* cells and Gram positive *B. subtilis* cells that reveal a specific architecture of closely interacting individual 70S ribosomes. Their architecture is similar to, but distinct from, the collided disome structures previously characterized in eukaryotic yeast and mammalian cells (16, 17). In both cases, the interaction between stalled and collided ribosomes primarily involves the two small ribosomal subunits, but also employs contacts between the large subunit of the stalled ribosome and the small subunit of the collided one. However, these contacts are not conserved between the kingdoms: in eukaryotes they are established by 25S rRNA helix H31L and ribosomal protein eL27 of the large subunit, whereas in bacteria by the L1 stalk and the ribosomal protein uL9. The collided disome architecture is likely to be conserved in bacteria and, importantly, differs completely from the structure of hibernating disomes in *E. coli* and *B. subtilis*. This makes the observed collided disomes a valid proxy for sensing ribosome stalling in bacteria.

A role for collisions in ribosome rescue is consistent with previous studies in bacteria. Structural studies of polysomes and the crystal packing interactions in x-ray structures show that bacterial ribosomes pack closely together through interactions between their small subunits (35, 42). Moreover, in ribosome profiling studies in *E. coli*, Subramaniam et al. observed reduced ribosome density downstream of pausing sites due to the removal of stalled ribosomes by tmRNA

(43); these researchers later argued that reductions in protein output were most consistent with a mathematical model in which collisions are the trigger that recruits rescue factors to remove stalled ribosomes (44). Finally, two recent studies suggest that ribosome collisions influence the level of frameshifting at pause sites in *E. coli* (45, 46).

It is striking that collided ribosomes are recognized in *E. coli* by an SMR-domain protein (SmrB) given that the same domain plays a similar role in yeast (Cue2) (20). Prior to this study, only Rqc2, the factor that promotes CAT-tailing in yeast and has homologs in some bacteria (47, 48), has been shown to mediate ribosome rescue pathways in both bacteria and eukaryotes. Our analysis identified SMR-domain proteins in all but a few bacterial phyla (Fig 2A), suggesting that a role for SMR proteins in ribosome rescue may be widespread in bacteria just as it is in eukaryotes.

In yeast (20), worms (21), and now *E. coli*, ribosome collisions lead to mRNA cleavage by SMR-domain proteins upstream of the ribosome stalling site, targeting the problematic mRNA for decay. Cleavage leads to the rescue of upstream ribosomes which, no longer impeded by a downstream stalled ribosome, translate to the 3'-end of the upstream fragment and are released by rescue factors, tmRNA-SmpB in bacteria and Dom34-Hbs1 in yeast. Despite these general similarities, there are also a few apparent differences between the activity of SmrB and the Cue2 protein in yeast. While our RACE and MS data place the SmrB cleavage site at the 5' boundary of the stalled ribosome (Fig 3), Cue2 cleavage has been mapped to the A site of the collided ribosome in a wild-type yeast strain and to the 5' boundary of the stalled ribosome in strains lacking rescue factors Hel2 or Slh1 (16, 20, 49). A second difference is that loss of Cue2 alone has little or no effect on the stability of reporter mRNAs in yeast because the processive 5'-3' exonuclease Xrn1 is primarily responsible for their decay (20). In contrast, loss of SmrB leads to a dramatic increase in full-length mRNA in our reporters in *E. coli* (Fig 2F).

We observe two pathways by which stalled ribosome complexes are resolved (Fig 3I). The main pathway is cleavage at the 5'-boundary of the stalled ribosome by SmrB. In the second pathway, 3'-to-5' exonucleases degrade mRNA until they encounter the stalled ribosome, allowing tmRNA access for rescue to occur (30, 50). *E. coli* possesses three major 3'-to-5' exonucleases involved in mRNA turnover: RNase II, RNase R, and polynucleotide phosphorylase. Previous studies showed that strains with single knockouts of any of these exonucleases still exhibited trimming of mRNA back to the 3'-boundary of ribosomes stalled at the SecM motif (50); the triple deletion strain is not viable.

The structure of the disome-bound SmrB illustrates how this rescue factor can generally screen translating ribosomes and, in case of problematic events such as mRNA damage by oxidative or alkylating agents (3), is able to specifically recognize the new composite interface formed between the individual collided 70S ribosomes. Through its N-terminus, SmrB associates generally with elongating ribosomes for screening, whereas the composite binding site between the adjacent collided 30S subunits is required to position the SMR domain of SmrB proximal to

the bridging mRNA for endonucleolytic cleavage. In contrast, eukaryotic SMR-domain proteins frequently contain ubiquitin-binding domains (e.g. CUE, UBA, UIM, and UBL) to bind ribosome proteins ubiquitinated by E3 ligases such as Hel2. This diversity suggests that recruitment to collided ribosomes can occur through multiple alternate mechanisms.

In this report, we reveal a novel ribosome rescue factor in bacteria, SmrB, that recognizes ribosome collisions and specifically targets stalled ribosomes for mRNA decay and ribosome rescue. Bacteria and eukaryotes both rely on collisions to sense ribosome stalling and SMR-domain proteins to cleave the mRNA so that upstream stalled ribosomes can then be rescued by factors known to act on truncated mRNAs. These common features substantiate the universal significance of ribosome collisions and endonucleolytic cleavage in ribosome rescue. We anticipate the bacterial system to be as complex as the eukaryotic counterpart that enables recognition of stalled ribosomes, triggering RNA and proteolytic processing, and rescuing ribosomes. Our present work provides the initial scaffold for additional studies to fully appreciate this phenomenon.

Acknowledgements: The authors thank Suparna Sanyal for sharing *E. coli* strains QC101 and QC901, Haiping Hao at the JHMI Transcriptomics and Deep Sequencing Core for assistance with high-throughput sequencing, Bob Cole and Tatiana Boronina at JHMI in the Mass Spectrometry and Proteomics Facility, Joanna Musial for assistance during protein purifications, C. Ungewickell and S. Rieder for technical assistance, and L. Kater and K. Best for support with the pre-processing pipeline of cryo-EM data. **Funding:** This work was supported by NIH grant GM136960 (ARB), HHMI (RG), the Intramural Research Program of the National Library of Medicine at the NIH (AMB and LA), and by German Research Council (TRR174) (RB). HK is supported by a DFG fellowship through the Graduate School of Quantitative Bioscience Munich (QBM). **Author contributions:** K.S. performed the genetic screen, the analyses of the nanoLuc-ble reporters, and sucrose gradients. A.C. analyzed the CRP reporters and prepared samples for the MS experiments. M.B. and L.A. performed the phylogenetic analyses. H.K. performed in vitro translation and in vitro nuclease assays and prepared samples for cryo-EM analysis. O.B. and R.Bu. collected cryo-EM data. H.K. processed the cryo-EM data and R.Bu. prepared molecular models. H.K., R.Bu. and R.Be. analyzed and interpreted the structures and R.Bu. prepared structural figures. A.B., R.G., and R.Be. supervised the project. **Competing Interests:** The authors declare that there are no competing interests. **Data and materials availability:** The ribosome profiling data are available at the GEO with accession number GSE179691. Cryo-EM volumes and molecular models have been deposited at the Electron Microscopy Data Bank and Protein Data Bank with accession codes EMD-XXXX (*E. coli* maps) and PDB-YYYY (stalled 70S) PDB-ZZZZ (collided 70S-SmrB), EMD-YYYY (*B. subtilis* maps).

Supplementary Materials

Materials and Methods

Table S1

Fig S1 – S9

References (51 – 74)

References:

1. S. D. Moore, R. T. Sauer, Ribosome rescue: tmRNA tagging activity and capacity in Escherichia coli. *Molecular Microbiology* **58**, 456-466 (2005).
2. L. L. Yan, H. S. Zaher, How do cells cope with RNA damage and its consequences? *The Journal of Biological Chemistry* **294**, 15158-15171 (2019).
3. E. N. Thomas, K. Q. Kim, E. P. McHugh, T. Marcinkiewicz, H. S. Zaher, Alkylative damage of mRNA leads to ribosome stalling and rescue by trans translation in bacteria. *eLife* **9**, e61984 (2020).
4. E. D. Roche, R. T. Sauer, SsrA-mediated peptide tagging caused by rare codons and tRNA scarcity. *The EMBO journal* **18**, 4579-4589 (1999).
5. T. Sunohara, K. Jojima, H. Tagami, T. Inada, H. Aiba, Ribosome stalling during translation elongation induces cleavage of mRNA being translated in Escherichia coli. *The Journal of Biological Chemistry* **279**, 15368-15375 (2004).
6. C. S. Hayes, B. Bose, R. T. Sauer, Proline residues at the C terminus of nascent chains induce SsrA tagging during translation termination. *The Journal of Biological Chemistry* **277**, 33825-33832 (2002).
7. C. Müller, C. Crowe-McAuliffe, D. N. Wilson, Ribosome Rescue Pathways in Bacteria. *Frontiers in Microbiology* **12**, 652980 (2021).
8. F. Garza-Sánchez, R. E. Schaub, B. D. Janssen, C. S. Hayes, tmRNA regulates synthesis of the ArfA ribosome rescue factor. *Molecular Microbiology* **80**, 1204-1219 (2011).
9. K. C. Keiler, P. R. Waller, R. T. Sauer, Role of a peptide tagging system in degradation of proteins synthesized from damaged messenger RNA. *Science (New York, N.Y.)* **271**, 990-993 (1996).
10. Y. Chadani, K. Ito, K. Kutsukake, T. Abo, ArfA recruits release factor 2 to rescue stalled ribosomes by peptidyl-tRNA hydrolysis in Escherichia coli. *Molecular Microbiology* **86**, 37-50 (2012).
11. N. Ivanova, M. Y. Pavlov, B. Felden, M. Ehrenberg, Ribosome rescue by tmRNA requires truncated mRNAs. *Journal of Molecular Biology* **338**, 33-41 (2004).
12. C. Neubauer, R. Gillet, A. C. Kelley, V. Ramakrishnan, Decoding in the absence of a codon by tmRNA and SmpB in the ribosome. *Science (New York, N.Y.)* **335**, 1366-1369 (2012).
13. D. Kurita, Y. Chadani, A. Muto, T. Abo, H. Himeno, ArfA recognizes the lack of mRNA in the mRNA channel after RF2 binding for ribosome rescue. *Nucleic Acids Research* **42**, 13339-13352 (2014).
14. C. S. Hayes, R. T. Sauer, Cleavage of the A site mRNA codon during ribosome pausing provides a mechanism for translational quality control. *Molecular Cell* **12**, 903-911 (2003).
15. O. Brandman *et al.*, A ribosome-bound quality control complex triggers degradation of nascent peptides and signals translation stress. *Cell* **151**, 1042-1054 (2012).

16. K. Ikeuchi *et al.*, Collided ribosomes form a unique structural interface to induce Hel2-driven quality control pathways. *The EMBO journal* **38**, e100276 (2019).
17. S. Juskiewicz *et al.*, ZNF598 Is a Quality Control Sensor of Collided Ribosomes. *Molecular Cell* **72**, 469-481.e467 (2018).
18. C. L. Simms, L. L. Yan, H. S. Zaher, Ribosome Collision Is Critical for Quality Control during No-Go Decay. *Molecular Cell* **68**, 361-373.e365 (2017).
19. W. Zhou *et al.*, PPR-SMR protein SOT1 has RNA endonuclease activity. *Proceedings of the National Academy of Sciences of the United States of America* **114**, E1554-E1563 (2017).
20. K. N. D'Orazio *et al.*, The endonuclease Cue2 cleaves mRNAs at stalled ribosomes during No Go Decay. *eLife* **8**, e49117 (2019).
21. M. L. Glover *et al.*, NONU-1 Encodes a Conserved Endonuclease Required for mRNA Translation Surveillance. *Cell Reports* **30**, 4321-4331.e4324 (2020).
22. T. van Opijnen, K. L. Bodi, A. Camilli, Tn-seq: high-throughput parallel sequencing for fitness and genetic interaction studies in microorganisms. *Nature Methods* **6**, 767-772 (2009).
23. G. C. Langridge *et al.*, Simultaneous assay of every Salmonella Typhi gene using one million transposon mutants. *Genome Research* **19**, 2308-2316 (2009).
24. D. Bhandari, K. Guha, N. Bhaduri, P. Saha, Ubiquitination of mRNA cycling sequence binding protein from Leishmania donovani (LdCSBP) modulates the RNA endonuclease activity of its Smr domain. *Febs Lett* **585**, 809-813 (2011).
25. W. J. Wu *et al.*, SOT1, a pentatricopeptide repeat protein with a small MutS-related domain, is required for correct processing of plastid 23S-4.5S rRNA precursors in Arabidopsis thaliana. *Plant J* **85**, 607-621 (2016).
26. S. Liu, J. Melonek, L. M. Boykin, I. Small, K. A. Howell, PPR-SMRs: ancient proteins with enigmatic functions. *RNA biology* **10**, 1501-1510 (2013).
27. D. H. Bechhofer, M. P. Deutscher, Bacterial ribonucleases and their roles in RNA metabolism. *Critical Reviews in Biochemistry and Molecular Biology* **54**, 242-300 (2019).
28. F. Mohammad, R. Green, A. R. Buskirk, A systematically-revised ribosome profiling method for bacteria reveals pauses at single-codon resolution. *eLife* **8**, e42591 (2019).
29. H. Muto, H. Nakatogawa, K. Ito, Genetically encoded but nonpolypeptide prolyl-tRNA functions in the A site for SecM-mediated ribosomal stall. *Molecular Cell* **22**, 545-552 (2006).
30. B. D. Janssen, F. Garza-Sánchez, C. S. Hayes, A-site mRNA cleavage is not required for tmRNA-mediated ssrA-peptide tagging. *PloS One* **8**, e81319 (2013).
31. J. Hughes, G. Mellows, Inhibition of isoleucyl-transfer ribonucleic acid synthetase in Escherichia coli by pseudomonic acid. *The Biochemical Journal* **176**, 305-318 (1978).
32. S. Chiba, A. Lamsa, K. Pogliano, A ribosome-nascent chain sensor of membrane protein biogenesis in Bacillus subtilis. *The EMBO journal* **28**, 3461-3475 (2009).

33. E. Ishii *et al.*, Nascent chain-monitored remodeling of the Sec machinery for salinity adaptation of marine bacteria. *Proceedings of the National Academy of Sciences of the United States of America* **112**, E5513-5522 (2015).
34. T. Su *et al.*, The force-sensing peptide VemP employs extreme compaction and secondary structure formation to induce ribosomal stalling. *eLife* **6**, e25642 (2017).
35. B. S. Schuwirth *et al.*, Structures of the bacterial ribosome at 3.5 Å resolution. *Science (New York, N.Y.)* **310**, 827-834 (2005).
36. M. Selmer, Y. G. Gao, A. Weixlbaumer, V. Ramakrishnan, Ribosome engineering to promote new crystal forms. *Acta Crystallogr D* **68**, 578-583 (2012).
37. B. Beckert *et al.*, Structure of the *Bacillus subtilis* hibernating 100S ribosome reveals the basis for 70S dimerization. *Embo Journal* **36**, 2061-2072 (2017).
38. B. Beckert *et al.*, Structure of a hibernating 100S ribosome reveals an inactive conformation of the ribosomal protein S1. *Nat Microbiol* **3**, 1115-+ (2018).
39. J. Jumper *et al.*, Highly accurate protein structure prediction with AlphaFold. *Nature*, (2021).
40. K. L. Herbst, L. M. Nichols, R. F. Gesteland, R. B. Weiss, A mutation in ribosomal protein L9 affects ribosomal hopping during translation of gene 60 from bacteriophage T4. *Proceedings of the National Academy of Sciences of the United States of America* **91**, 12525-12529 (1994).
41. R. Leipuvienė, G. R. Björk, Alterations in the two globular domains or in the connecting alpha-helix of bacterial ribosomal protein L9 induces +1 frameshifts. *Journal of Bacteriology* **189**, 7024-7031 (2007).
42. F. Brandt *et al.*, The native 3D organization of bacterial polysomes. *Cell* **136**, 261-271 (2009).
43. A. R. Subramaniam, B. M. Zid, E. K. O'Shea, An integrated approach reveals regulatory controls on bacterial translation elongation. *Cell* **159**, 1200-1211 (2014).
44. M. A. Ferrin, A. R. Subramaniam, Kinetic modeling predicts a stimulatory role for ribosome collisions at elongation stall sites in bacteria. *eLife* **6**, e23629 (2017).
45. C. L. Simms, L. L. Yan, J. K. Qiu, H. S. Zaher, Ribosome Collisions Result in +1 Frameshifting in the Absence of No-Go Decay. *Cell Reports* **28**, 1679-1689.e1674 (2019).
46. A. M. Smith, M. S. Costello, A. H. Kettring, R. J. Wingo, S. D. Moore, Ribosome collisions alter frameshifting at translational reprogramming motifs in bacterial mRNAs. *Proceedings of the National Academy of Sciences of the United States of America* **116**, 21769-21779 (2019).
47. P. S. Shen *et al.*, Protein synthesis. Rqc2p and 60S ribosomal subunits mediate mRNA-independent elongation of nascent chains. *Science (New York, N.Y.)* **347**, 75-78 (2015).
48. I. Lytvynenko *et al.*, Alanine Tails Signal Proteolysis in Bacterial Ribosome-Associated Quality Control. *Cell* **178**, 76-90.e22 (2019).

49. A. Navickas *et al.*, No-Go Decay mRNA cleavage in the ribosome exit tunnel produces 5'-OH ends phosphorylated by Trl1. *Nature Communications* **11**, 122 (2020).
50. F. Garza-Sánchez, B. D. Janssen, C. S. Hayes, Prolyl-tRNA(Pro) in the A-site of SecM-arrested ribosomes inhibits the recruitment of transfer-messenger RNA. *The Journal of Biological Chemistry* **281**, 34258-34268 (2006).

SUPPLEMENTARY INFORMATION

MATERIALS & METHODS

Bacterial strains and plasmids

A list of strains and plasmids and the details of their construction are given in Table S1.

The L9 knockout strain (BW25113 *rplI::kan*) was obtained from the *E. coli* Genetic Stock Center. Strains QC101 and QC901 containing the L9-mCherry and S6-GFP, respectively, were gifts from Suparna Sanyal (51). Additional knockout strains of MG1655 were constructed using one-step genomic replacement with a PCR fragment with λ Red recombinase as described (52). Gene deletions and the endogenous epitope-tagged SmrB mutants were verified by PCR and sequencing.

The nanoLuc-ble reporter construct pKS-nonstall was expressed from plasmids containing an AmpR marker and a p15A origin of replication. DNA encoding various stalling motifs was inserted between the genes for nanoLuc and ble using Gibson assembly.

To construct the Crp collision reporters, the first 39, 69, 99, 109, and 411 bases of the *crp* coding region were amplified from MG1655 genomic DNA. The PCR also added the sequence encoding the short SecM ribosome stalling motif (GIRAGP) in-frame immediately downstream of the *crp* fragment. The PCR products were inserted into EcoRI and BglII digested pKS-nonstall to produce the pCRP51, pCRP81, pCRP111, pCRP121, and pCRP423 reporter plasmids using Gibson assembly. The names of the plasmids and numbers in the text represent the distance from the AUG to the stall site (the second Gly codon in GIRAGP) in each reporter.

To construct the plasmid pAC01 encoding tmRNA-DD, we switched the origin of replication of the pKW23 plasmid (4) from p15A to pBR322 for compatibility. This was accomplished by Gibson assembly of two PCR products: 1) everything in pKW23 except the origin and 2) the pBR322 origin from pBAD-GFPuv (53).

For overexpression and purification of SmrB, we amplified the *smrB* gene from genomic DNA from MG1655, adding a Twin-Strep tag, a TEV cleavage site, and a FLAG tag to the N-terminus of SmrB using nested PCR primers. This amplicon was inserted into pET24b cleaved with NdeI and BamHI using Gibson assembly.

Genetic screening

A library with random transposon insertions throughout the genome was constructed using the EZ-Tn5 <KAN-2>Tnp Transposome Kit (Lucigen). The EZ-Tn5 transposome was electroporated into the parental *E. coli* strain MG1655 and the cells were plated on LB + kanamycin (50 mg/L). After one overnight incubation, approximately 5 million colonies were collected and stored at -80°C in LB + 20% glycerol. Subsequently, either the SecM or Ile8 reporter plasmid was electroporated into the random insertion library and transformants were plated on LB + ampicillin (50 mg/L) + phleomycin (50 mg/L). After one overnight incubation, phleomycin resistant colonies were collected and stored in at -80°C in LB + 20% glycerol.

To quantify the number of transposon insertions in each gene throughout the genome, Tn-seq was performed on the random insertion library as well as the libraries of phleomycin-resistant colonies from both the SecM and Ile8 screens. Sequencing libraries were prepared from genomic DNA from each library using the NEBNext Ultra II FS DNA Library Prep Kit for Illumina (NEB) following the manufacturer's protocol. During PCR amplification of the adapter-ligated DNA, we use two PCR steps with primers that specifically bind to the mosaic end of EZ-Tn5 <KAN-2> Transposon to prepare libraries enriched in transposon insertion sites. Between

the PCR steps, we included an additional enrichment step based on biotin-streptavidin purification. The two-PCR steps were performed using NEBNext Ultra II Q5 Master Mix (NEB) as follows: The 1st PCR enrichment was performed with primers KS_Tn5_1stPCR_F_biotin and KS_Tn5_1stPCR_R (Table S1) with the following program: 30 s at 98 °C; 15 cycles of 10 s at 98 °C, 20 s at 59 °C, 60 s at 65 °C; and 5 min at 65 °C. The PCR products were purified first with DNA Clean & Concentrator-5 columns (Zymo Research) and then Dynabeads MyOne Streptavidin C1 beads (Thermo Fisher). The streptavidin beads were washed four times with binding and washing buffer (5 mM Tris-HCl pH 7.5, 0.5 mM EDTA pH 8.0, 1M NaCl); the PCR products were added and incubated for 30 min at 25 °C; and the beads were washed twice with the binding and washing buffer and then twice by 0.1x TE buffer (1 mM Tris pH 8.0, 0.1 mM EDTA pH 8.0). The beads bound to the PCR products were used directly as the template for the 2nd PCR enrichment using KS_Tn_library_F and one of our custom Index primers for Tn-seq (Table S1) with the following program: 30 s at 98 °C; 7 ~ 9 cycles of 10 s at 98 °C, 20 s at 59 °C, 60 s at 65 °C; and 5 min at 65 °C. The products from the 2nd PCR were gel purified on a non-denaturing 5% TBE gel, analyzed on a BioAnalyzer high sensitivity DNA kit (Agilent), and sequenced on the NextSeq 500 instrument (Illumina).

The Tn-seq data were analyzed with custom scripts written in Python 2.7. The adaptor sequence AGATCGGAAGAGCACACGTC was removed from the 3'-ends of reads with Skewer (54). Reads of interest contain the Tn5 transposase sequence at the 5'-end and genomic DNA sequence at the 3'-end. Reads lacking the Tn5 transposase sequence GGTGAGATGTGTATAAGAGACAG at their 5'-ends were discarded using cutadapt. After trimming this sequence, the remaining reads were aligned to *E. coli* MG1655 genome build NC_000913.2 using bowtie version 1.1.2 (55). The site of the transposon insertion was assigned using the 5'-end of the aligned reads. The number of transposon insertion sites for each gene was counted and normalized as reads per kilobase per million mapped reads (RPKM), normalizing for both the sequencing depth for each library and the length of each gene.

Sequence Analyses

PSI-BLAST (56) and JACKHMMER programs (57) were used to carry out iterative sequence profile searches to collect Smr domain-containing sequences. Proteins were clustered using BLASTCLUST (<https://ftp.ncbi.nih.gov/blast/documents/blastclust.html>) to identify shared domain architectural themes. Additional domains fused to the Smr domain were annotated using a database of domain sequence profiles including pfam A models (58). For contextual analysis of prokaryotic gene neighborhoods, the GenBank genome files corresponding to unique GenBank genome assemblies (GCA ids) were used as starting material. Specific neighborhoods were extracted using a Perl script that reports upstream and downstream genes of the anchor Smr domain-containing gene. Proteins encoded by these genes were then clustered using BLASTCLUST to identify conserved gene neighborhoods based on conservation between different taxa. Additional filters outputted valid neighborhoods for further analysis: (1) nucleotide distance constraint (generally 50 nucleotides), (2) conservation of gene directionality within the neighborhood, and (3) presence in more than one phylum. Multiple sequence alignments were built using the Kalign program (59), and manually improved based on the alignments outputted by sequence homology searches. Secondary structure prediction was done using the JPred program (60). Phylogenetic relationships were determined using an approximate maximum likelihood (ML) method as implemented in the FastTree program (61): corresponding local support values were also estimated as implemented. To increase accuracy of topology, the rounds of minimum-evolution subtree-prune-regraft (SPR) moves were increased to 4 (-spr 4) and we utilized options -mlacc and -slownni to survey more exhaustively the ML nearest neighbor interchanges (NNIs).

Western blots

Cells were grown in LB + ampicillin (50 mg/L) to OD₆₀₀ = 0.5, harvested by centrifugation, resuspended in 12.5 mM Tris pH 6.8 with 4% SDS, and lysed by heating to 90 °C for 10 min. 5x loading dye (250 mM Tris pH 6.8, 20%

glycerol, 30% β -mercaptoethanol, 10% SDS, saturated bromophenol blue) was added and the lysate was denatured at 90 °C for 10 min. Protein was separated on a 4–12% Criterion XT Bis-Tris protein gel (Bio-Rad) using XT MES buffer and transferred to PVDF membrane using the Trans-Blot Turbo Transfer system (Bio-Rad). Membranes were blocked in 5% milk for 1 h at room temperature, washed, and then probed with antibodies diluted in TBS-tween. Antibodies dilutions were: anti-FLAG-HRP 1:10000 (Sigma); anti-Strep•Tag II-HRP 1:5000 (Millipore Sigma); anti-rpoB 1:1000 (BioLegend); anti-rpoC 1:1000 (BioLegend); and anti-mouse-HRP 1:2000 (Thermo Fisher). Chemiluminescent signals from HRP were detected using SuperSignal West Pico PLUS Chemiluminescent Substrate (Thermo Fisher) or SuperSignal West Femto Maximum Sensitivity Substrate (Thermo Fisher) and visualized on Amersham Hyperfilm ECL (GE).

Northern blots

Cells were grown in LB + ampicillin (50 mg/L) to $OD_{600} = 0.5$, harvested by centrifugation, and resuspended in 100 mM NaCl, 10 mM Tris pH 8.0, 1 mM EDTA pH 8.0, and 1% SDS. RNA was extracted twice by phenol, pH 4.5 (once at 65°C and once at room temperature) followed by chloroform extraction. RNA in the aqueous layer was then precipitated by isopropanol and 0.3 M NaOAc (pH 5.5), washed with 80% ethanol, and resuspended in water. Purified RNA was separated on a 1.2% agarose-formaldehyde denaturing gel and transferred to a nylon membrane (Hybond-N+, Cytiva) in 10 x SSC buffer using a Model 785 Vacuum Blotter (Bio-Rad). RNA was crosslinked to the membrane with the Stratalinker UV crosslinker (Stratagene). Pre-hybridization and hybridization was performed in PerfectHyb Plus Hybridization Buffer (Millipore Sigma). RNA was probed with 50 nM 5'-digoxigenin labeled DNA oligos (IDT). Digoxigenin was detected with anti-Digoxigenin-AP antibodies diluted 1:1000 (Millipore Sigma). Chemiluminescent signals from alkaline phosphatase were detected with CDP-Star (Millipore Sigma) and visualized on Amersham Hyperfilm ECL (GE).

5'-RACE

RNA was extracted as described above. DNA contamination was depleted by treatment with RQ1 DNase (Promega). 5 μ g of purified RNA was 5'-phosphorylated by incubating with T4 polynucleotide kinase (NEB) in 1 mM ATP at 37 °C for 30 min, after which PNK was denatured by heating to 75 °C for 10 min. The RNA adapter KS_5RACE_linker was ligated to the 5'-end of the RNA by incubating with T4 RNA ligase 1 (NEB) in 1 mM ATP and 15% PEG8000 at 25 °C for 3 h. Ligated samples were purified by 2.2x volume of RNAClean XP (Beckman). The 1st strand cDNA was synthesized using the KS_5RACE_RT primer and SuperScript III Reverse Transcriptase (Thermo Fisher) by incubating at 54 °C for 60 min after which RT was denatured by heating to 85°C for 5 min. Denatured reverse transcription products were used directly in the 1st PCR reaction. The 1st PCR was performed with Phusion High-Fidelity DNA Polymerase (NEB) and a set of primers of KS_5RACE_F1 and KS_5RACE_R1; with the program: 30 s at 98 °C; 25 cycles of 10 s at 98 °C, 10 s at 65 °C, 60 s at 72 °C; and 5 min at 72 °C. The 1st PCR products were purified using DNA Clean & Concentrator-5 columns (Zymo Research). The 2nd PCR was performed with Phusion High-Fidelity DNA Polymerase (NEB) and a set of primers of NI-NI-2 and one of our custom Index primers for 5'RACE (Table S1) with the program: 30 s at 98 °C; 25 cycles of 10 s at 98 °C, 10 s at 65 °C, 60 s at 72 °C; and 5 min at 72 °C. The 2nd PCR products were purified using DNA Clean & Concentrator-5 columns (Zymo Research), analyzed on a BioAnalyzer high sensitivity DNA kit (Agilent), and sequenced on the MiSeq Nano instrument (Illumina).

The 5'-RACE data were analyzed using custom scripts written in Python 2.7. The RNA adapter sequence TGCCCGAGTG was removed from the 5'-end of reads using cutadapt. Reads without the RNA adapter sequence were discarded. The reverse primer sequence GCGGTCGAGTTCTGGACCGA from the 2nd PCR was removed from the 3'-ends of reads by cutadapt. The processed reads were aligned to the SecM or EP* reporter plasmid sequences using bowtie version 1.1.2 (55). The 5' ends of mapped reads were counted and normalized as reads per million mapped reads (RPM), normalizing for the sequencing depth of each library.

3'-RACE

RNA was extracted as described above. DNA contamination was depleted by treatment with RQ1 DNase (Promega). 5 µg of purified RNA was 3'-dephosphorylated by incubating with T4 polynucleotide kinase (NEB) without ATP at 37 °C for 30 min, after which PNK was denatured by heating to 75 °C for 10 min. The 3' DNA adapter was 5' adenylated using the 5' DNA Adenylation Kit (NEB) and purified with an Oligo Clean & Concentrator column (Zymo Research). This adaptor was ligated to 3'-end of dephosphorylated RNA by incubating with T4 RNA ligase 2 truncated (NEB) in 15% PEG8000 at 37 °C for 3 hours. Ligated samples were purified with RNAClean XP (Beckman). The 1st strand cDNA was synthesized with KS_3RACE_RT and SuperScript III Reverse Transcriptase (Thermo Fisher) by incubating at 54 °C for 60 min, after which RT was denatured by heating to 85°C for 5 min. Denatured reverse transcription products were used directly in the 1st PCR reaction. The 1st PCR was performed with Phusion High-Fidelity DNA Polymerase (NEB) and primers KS_3RACE_F1 and KS_3RACE_RT with the program: 30 s at 98 °C; 9 cycles of 10 s at 98 °C, 10 s at 65 °C, 60 s at 72 °C; and 5 min at 72 °C. The PCR products were purified using DNA Clean & Concentrator-5 columns (Zymo Research). The 2nd PCR was performed with Phusion High-Fidelity DNA Polymerase (NEB) and one of our custom Index primers for 3'RACE (Table S1) and KS_3RACE_R with the program: 30 s at 98 °C; 25 cycles of 10 s at 98 °C, 10 s at 65 °C, 60 s at 72 °C; and 5 min at 72 °C. The 2nd PCR products were purified by DNA Clean & Concentrator-5 columns (Zymo Research), analyzed on a BioAnalyzer high sensitivity DNA kit (Agilent), and sequenced on the MiSeq Nano (Illumina).

The 3'-RACE data were analyzed by custom scripts written in Python 2.7. The DNA adapter sequence TCCTTGTTGCCCGAGTGNNNNNNN was removed from the 5'-end of reads using cutadapt. Reads without the adapter sequence were discarded. The forward primer sequence AGATCGGAAGAGCACACGTC from the 2nd PCR was removed from 3'-end of reads using cutadapt. Processed reads were aligned to the SecM or EP* reporter plasmid sequences using bowtie version 1.1.2 (55). The 5' ends of mapped reads were counted and normalized as reads per million mapped reads (RPM), normalizing for the sequencing depth of each library.

Mass spectrometric analysis of tmRNA tagging sites

Immunoprecipitation and processing of the reporter proteins

The EP* and the short-SecM (GIRAGP) reporters were expressed in both the wild-type MG1655 strain and the Δ smrB strain. In addition, a modified tmRNA encoding ANDENYALDD was also expressed from the pAC01 plasmid to stabilize the products of tmRNA tagging. (pAC01 is a derivative of pKW23 (4) modified to contain a pBR322 origin). For each of these four samples, reporter protein was purified from three biological replicates as follows: 100 mL LB cultures were grown to OD₆₀₀ = 0.5 and harvested by centrifugation. The pellet was frozen at -80 °C and thawed in 2x CellLytic B cell lysis reagent (Sigma) for 10 minutes. The lysate was clarified by centrifugation for 30 min at 20,000 x g. 50 µL Strep-tactin sepharose beads (IBA) were added to the supernatant and incubated at 4 °C for 1 h. The beads were washed with IP wash buffer (20 mM Tris pH 8.0, 100 mM NH₄Cl, 0.4% Triton, 0.1% NP-40) for 5 min at 4 °C four times. Protein was eluted from the beads by shaking at 4 °C in elution buffer (20 mM Tris pH 8.0, 100 mM NH₄Cl, 5 mM desthiobiotin) for 1 h. 36 µL of each immunoprecipitated sample was reduced with 1.5 mg/mL DTT in 50 µL of 50 mM tri-ethyl ammonium bicarbonate (TEAB) buffer at 57 °C for 60 min, then alkylated with 10 mg/mL iodoacetamide in 50 µL of 50 mM TEAB buffer in the dark at room temperature for 45 min. The samples were reconstituted in 36 µL of 50 mM HEPES pH 8.5 and digested with 2 ng/µL LysC at 37 °C overnight as described (62). Peptides were desalted on Oasis u-HLB plates (Waters), eluted with 60% ACN / 0.1% TFA, dried, and reconstituted with 2% ACN / 0.1% formic acid.

LC/MS/MS analysis

Desalted peptides cleaved by LysC were analyzed by liquid chromatography/tandem mass spectrometry (LC/MS/MS). The peptides were separated by reverse-phase chromatography (2% - 90% acetonitrile / 0.1% formic acid gradient over 60 min at 300 nL/min) on an 75 μ m x 150 mm ProntoSIL-120-5-C18 H column (Bischoff) using the nano-EasyLC 1200 system (Thermo). Eluting peptides were sprayed into an Orbitrap-Lumos_ETD mass spectrometer through a 1 μ m emitter tip (New Objective) at 2.7 kV. Scans were acquired within 360-1700 Da m/z targeting the C-terminal SsrA fusion peptides with no dynamic exclusion. Precursor ions were individually isolated with 0.8 Da (no offset) and fragmented (MS/MS) using HCD activation collision energy 30. Precursor and the fragment ions were analyzed at resolution at 200Da 120,000 AGC target 1xe6, max IT 50ms and 60000, AGC target 1xe5, mx IT118ms, respectively, 3 cycles. Tandem MS/MS spectra were processed by Proteome Discoverer v2.4 (Thermo Fisher) and analyzed with Mascot v.2.6.2 (Matrix Science) using RefSeq2017_83Ecoli and a database with peptides from the nanoLuc-ble reporter protein. Peptide identifications from Mascot searches were processed within the Proteome Discoverer-Percolator to identify peptides with a confidence threshold of a 0.01% False Discovery Rate, based on a concatenated decoy database search to calculate the protein and peptide ratios. Only Peptide Rank 1 were considered.

Ribosome profiling

The plasmid encoding the nanoLuc-ble reporter with the short SecM motif (IRAGP) was introduced into four strains: wild-type *E. coli* MG1655, the Δ ssrA mutant, the Δ smrB mutant, and the Δ ssrA Δ smrB double knockout. 200 mL cultures of each strain were grown at 37 °C in MOPS EZ Rich Defined media (Teknova) with ampicillin at 37 °C starting from a 1:100 dilution of an overnight culture to a final OD₆₀₀ = 0.3. The cells were harvested by filtration using a Kontes 99 mm filtration apparatus with a 0.45 μ m nitrocellulose filter (Whatman) and then flash frozen in liquid nitrogen. 0.65 mL frozen lysis buffer (20 mM Tris pH 8.0, 10 mM MgCl₂, 100 mM NH₄Cl, 5 mM CaCl₂, 0.1% NP-40, 0.4% TritonX-100, 100 U/mL DNase I (Roche), and 1 mM chloramphenicol) was added to the frozen pellets and The cells were cryogenically pulverized using a Spex 6870 freezer mill with 5 cycles of 1 min grinding at 5 Hz and 1 min cooling. Following lysis, the RNA was digested with MNase and the resulting ribosome footprints were cloned and sequenced as described (63).

Custom Python scripts were used to analyze the resulting ribosome profiling data. Raw reads were filtered for quality and trimmed using Skewer v0.2.2. Bowtie v0.12.7 was used to map reads uniquely to genome build NC_000913.2 (allowing two mismatches) and separately to the reporter plasmid sequence after reads mapping to tRNA or rRNA were discarded. Ribosome density was assigned to the 3'-end of reads using read sizes 10–40 nt.

Polysome profiling

Cells were cultured at 37 °C in 500 mL of LB (and antibiotics where appropriate) to OD₆₀₀ = 0.5, harvested by filtration using a Kontes 99 mm filtration apparatus with a 0.45 μ m nitrocellulose filter (Whatman), and flash frozen in liquid nitrogen. Cells were lysed in lysis buffer (20 mM Tris pH 8.0, 10 mM MgCl₂, 100 mM NH₄Cl, 5 mM CaCl₂, 100 U/mL DNase I, and 1 mM chloramphenicol) using a Spex 6870 freezer mill with 5 cycles of 1 min grinding at 5 Hz and 1 min cooling. Lysates were centrifuged at 20,000 x g for 30 min at 4 °C to pellet cell debris. 10–54% sucrose density gradients were prepared using the Gradient Master 108 (Biocomp) with gradient buffer (20 mM Tris pH 8.0, 10 mM MgCl₂, 100 mM NH₄Cl, and 2 mM DTT). 5–40 AU of *E. coli* lysate was loaded on top of sucrose gradient and centrifuged in a SW41 rotor at 35,000 rpm for 2.5 h at 4 °C. Fractionation was performed on a Piston Gradient Fractionator (Biocomp). To process each fraction for western blots, proteins were precipitated in 10% trichloroacetic acid (TCA) and the pellets were washed twice by ice-cold acetone, vacuum-dried briefly, resuspended in 5x loading dye, and neutralized with Tris-HCl pH 7.5.

Purification of *E. coli* SmrB and inactive SmrB mutant (99DLH₁₀₁-ALA).

The plasmids pET24b coding for *E. coli* SmrB and *E.coli* SmrB mutant with N-terminal TwinStrep-tag, TEV cleavage site and FLAG-tag were transformed in *E. coli* stain BL21 (DE3). Cells were grown in 3 L LB medium to mid-log phase ($OD_{600} = 0.6$) at 37 °C and induced with 1 mM IPTG at 18 °C for 20 h. Cells were harvested by centrifugation at 5,471 *g* and 4 °C for 8 min, resuspended with buffer A (25 mM HEPES/KOH pH 7.8, 300 mM KCl, 5 mM β -Mercaptoethanol, 1:1000 protease inhibitor (pill/mL), 10% glycerol) and lysed using a microfluidizer (Microfluidics M-110L). Cell debris was removed by centrifugation at 30,597 *g* and 4 °C for 20 min. The cleared lysate was then incubated with 5 mL of prewashed Strep-Tactin XT Superflow beads for 1 h. Afterwards the beads were washed with 10 column volumes (CVs) buffer B (25 mM HEPES/KOH pH 7.8, 1 M KCl, 5 mM β -mercaptoethanol, 10% glycerol), with CVs buffer C (25 mM HEPES/KOH pH 7.8, 300 mM KCl, 5 mM β -mercaptoethanol, 10% glycerol), and eluted with 1 CV Buffer D (25 mM HEPES/KOH pH 7.8, 300 mM KCl, 5 mM β -mercaptoethanol, 10% glycerol, 50 mM biotin).

275 μ g of TEV protease were added to the elution fraction and incubated on a rotating wheel at 4 °C overnight. To remove the TEV protease, Dynabeads™ (Invitrogen, Thermo Fisher Scientific) were added and incubated for 30 minutes. The cleaved tag was removed by incubation with Strep-Tactin XT Superflow beads. SmrB was concentrated using an Amicon 10k MWCO and subjected to size-exclusion chromatography using a Superdex 75 in buffer C. SmrB-containing fractions were again concentrated and stored at -80 °C.

***E.coli in vitro* translation and isolation of disomes and trisomes**

The VemP-encoding mRNA, which contains the VemP peptide without N-terminal signal sequence, FLAG-tag and a cleavable His-tag, was prepared as described before by PCR amplification, DNA purification, *in vitro* transcription and Phenol/Chloroform precipitation (34). RNCs were generated with the PURExpress In Vitro Protein Synthesis Kit (New England Biolabs #E6800S, transcription and translation coupled) using 21 ng of mRNA per 25 μ L reaction. 10 reactions were incubated at 30 °C for 35 min and subsequently loaded on sucrose density gradients (25 mM HEPES/KOH pH 7.5, 100 mM KOAc, 10 mM $Mg(OAc)_2$, 0.01% DDM; 10-50% sucrose) and spun in a SW 40 Ti rotor (Beckman Coulter) at 54,322 *g* for 16 h at 4 °C. The gradient was fractionated at a BioComp Gradient Station *ip* using a Triax Flow Cell for UV measurement. The disome and trisomes peak fractions were collected and pelleted by centrifugation in a TLA110 rotor (Beckman Coulter) at 434,513 *g* for 2 h at 4 °C. After resuspension in RNC buffer (25 mM HEPES/KOH pH 7.5, 150 mM KOAc, 10 mM $Mg(OAc)_2$, 2 mM DTT), samples were frozen in liquid nitrogen and stored at -80 °C.

***B. subtilis in vitro* translation and isolation of disomes**

The MifM-encoding mRNA, which contains the MifM leader peptide with shortened C-terminus, a defined stalling site, the MifM N-terminal transmembrane segment (TM), a V5-tag and a cleavable His-tag, was prepared as described before by PCR amplification, DNA purification, *in vitro* transcription and Phenol/Chloroform precipitation (64). The translation extract was prepared from the *Bacillus subtilis* strain 168 Δ hpf Δ ssrA Δ SAS1-2 (65). Cells were grown in LB medium supplemented with 1% glucose, harvested at an OD_{600} between 0.6 and 0.8 and pelleted by centrifugation at 5,471 *g* and room temperature for 5 min. Afterwards, cells were resuspended in PBS (137 mM NaCl, 2.7 mM KCl, 10 mM Na_2HPO_4 , 2 mM KH_4PO_4 , pH 7.4), pelleted again by centrifugation at 5,471 *g* and 4 °C for 15 min and resuspended in as little as possible lysis buffer (10 mM HEPES pH 8.2, 60 mM K glutamate, 14 mM $Mg(OAc)_2$). Cell lysis was performed using a microfluidizer (Microfluidics M-110L) and cell debris was removed by centrifugation at 30,597 *g* and 4 °C for 20 min. The extract was aliquoted and frozen in liquid nitrogen. Activity of the extract as well as Mg buffer concentration was determined using the Luciferase Assay System (Promega).

The *in vitro* translation reaction was performed in 4 x 500 μ L reaction volume. 640 μ L cell extract were mixed with energy buffer (final concentration in 2 mL: 2% PEG 8000, 50 mM HEPES/KOH pH 8.2, 10 mM NH_4OAc , 130 mM KOAc, 30 mM Na-pyruvate, 4 mM Na-oxalate, 50 μ g ml^{-1} tRNA (from *E. coli*; Sigma 10109541 001), 0.2 mg

ml⁻¹ folinic acid, 0.1 µg ml⁻¹ creatine kinase, 20 mM creatine phosphate, 4 mM ATP, 3 mM GTP, 0.1 mM amino acid mix, 1 mM DTT, 0.08 U SUPERase•In™ RNase Inhibitor (Invitrogen), 15 mM Mg(OAc)₂). After heating the mixture to 32°C for 2 min, 50 µg of mRNA were added to each aliquot and the *in vitro* translation was incubated at 32 °C for 40 min while shaking at 900 rpm. For affinity purification of ribosome nascent chain complexes, the *in vitro* translation was incubated with 400 µL of prewashed TALON metal affinity resin for 45 min on a wheel. The flow-through was collected, beads were washed with 5 CVs buffer A (30 mM HEPES pH7.5/KOH, 250 mM KOAc, 25 mM Mg(OAc)₂, 20 mM imidazole, 0.1% DDM) and eluted by incubation for 2 h with 1 CV buffer B (30 mM HEPES pH 7.5/KOH, 250 mM KOAc, 25 mM Mg(OAc)₂, 0.1% DDM), 1.1 mg ml⁻¹ 3C protease). The sample was loaded on a 10-40% sucrose gradient (30 mM HEPES pH 7.5/KOH, 250 mM KOAc, 25 mM Mg(OAc)₂, 0.1% DDM, 10-40% (w/v) sucrose) and spun in a SW 40 Ti rotor (Beckman Coulter) at 54,322 *g* for 16 h at 4°C. The disome peak fractions were combined pelleted by centrifugation in a TLA110 rotor (Beckman Coulter) at 434,513 *g* for 2 h at 4°C. The pellet was resuspended in buffer C (25 mM HEPES pH 7.5/KOH, 150 mM KOAc, 10 mM Mg(OAc)₂, 2 mM DTT), frozen in liquid nitrogen and stored at -80 °C.

Nuclease Assay

Purified *E. coli* disomes were mixed with 10 times molar excess of protein (SmrB wt/ SmrB mut). As a control the same volume of buffer C (25 mM HEPES pH 7.5/KOH, 150 mM KOAc, 10 mM Mg(OAc)₂, 2 mM DTT) was added to disomes. Samples were incubated at 30°C for 3 h and then loaded on sucrose density gradients (25 mM pH 7.5 HEPES-KOH, 100 mM KOAc, 10 mM Mg(OAc)₂, 0.01% DDM; 10-50% sucrose). The gradients were spun in a SW 40 Ti rotor (Beckman Coulter) at 54,322 *g* for 16 h at 4°C. The gradient was fractionated at a BioComp Gradient Station *ip* using a Triax Flow Cell for UV measurement.

Cryo-EM analysis

Data collection and processing of the E. coli disome and E. coli trisome.

A volume of 3.5 µL was applied to 2 nm pre-coated Quantifoil R3/3 holey carbon support grids and vitrified in liquid ethane using a Vitrobot mark IV (FEI Company, Netherlands) (wait time 45 s, blotting time 2 s). 2,437 and 14'849 movies were collected for the *E. coli* disome and trisome sample, respectively. Data were collected on a Titan Krios TEM using a Falcon II DED at 300 kV, with an electron dose of 2.5 e⁻/Å² per frame for 16 frames (defocus range of 0.5 to 4 µm). The magnified pixel size was 1.09 Å/pixel. For the *E. coli* disome sample, frames were gain corrected, aligned and summed using MotionCor2 (66) and CTF parameters were determined using CTFFIND (67). Particles were picked using Gautomatch (<http://www.mrc-lmb.cam.ac.uk/kzhang/>). The particles were extracted and processed following the standard workflow in RELION 3.1 (68). The particles containing the stalled ribosome of the disomes were extracted with a box size of 380 pixel, imported to Cryosparc v3.2.0 (69) and refined to a final resolution of 3.8 Å (Fig S5). For the *E. coli* trisome, data were processed following the standard workflow in cryoSPARC v3.2.0 (69).

Data collection and processing of the B. subtilis disome

All samples were vitrified as described above. Two datasets of 8,842 and 19'354 movies were collected on a Titan Krios TEM using a Falcon II DED at 300 kV, with an electron dose of 2.5 e⁻/Å² per frame for 16 frames (defocus range of 0.5 to 4 µm). The magnified pixel size was 1.084 Å/pixel. All frames were gain corrected and subsequently aligned and summed using MotionCor2 (66). The data were processed following the standard workflow in cryoSPARC v3.2.0 (69).

Sample preparation, data collection and processing of the E. coli disome SmrB complex.

For reconstitution, disomes and SmrB mutant (99DLH₁₀₁-ALA) were thawed on ice. Disomes were mixed with

10 times molar excess of protein, incubated for 10 min at room temperature and subsequently analysed by cryo-EM. 8,350 movies were collected on a Titan Krios at 300 kV recorded on a K2 Summit direct electron detector (DED) with an electron dose of approx. $1.06 \text{ e}^-/\text{\AA}^2$ per frame for 40 frames (defocus range of 0.5 to 3.5 μm). The magnified pixel size was 1.059 $\text{\AA}/\text{pixel}$. All frames were gain corrected and subsequently aligned and summed using MotionCor2 (66). The data were processed following the standard workflow in cryoSPARC v3.2.0 (69). The processing scheme and final local resolution for SmrB are shown in Fig S7.

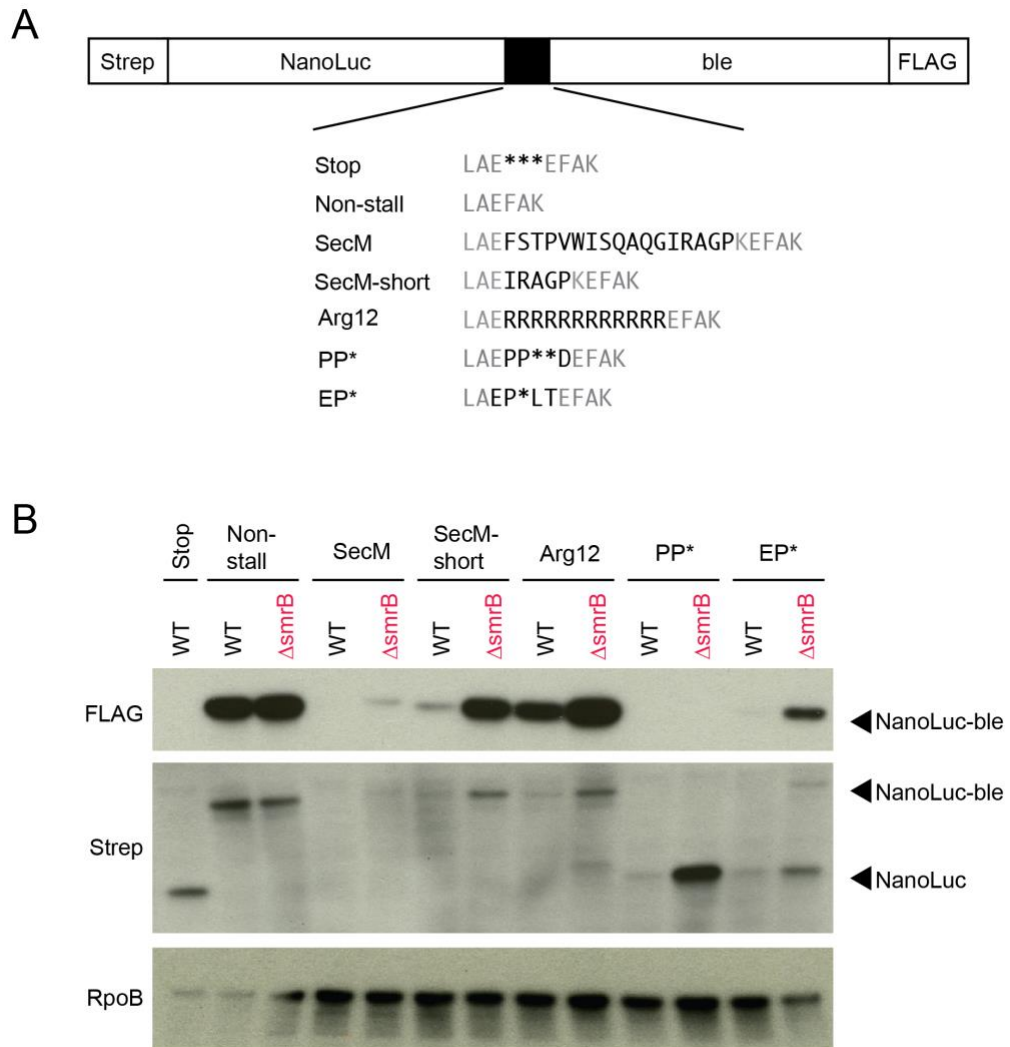
Model building and refinement

The *E. coli* disome model was prepared by rigid body docking of the model from Su *et al.* (PDB code 5NWY (34)). uL9 was taken from PDB-6WD1 (70) and the N-terminal part (residues 1-52) and the C-terminal part (residues 53-149) were rigid body docked individually and rejoined to match the bridged conformation of uL9 in the stalled ribosome. uL1 and the L1-stalk rRNA (nucleotides 2099-2190) were taken from PDB-6WD1 and rigid body docked into the cryo-EM density. tRNA-Phe was taken from PDB-3L0U (71) and rigid body docked into the A-sites of stalled and collided ribosomes although the identity of the tRNA in the A-site of the collided could not be determined. uS1 was taken from PDB-6BU8 and docked into the density map of the collided ribosome. The resolution of the mRNA between the two ribosomes was insufficient for modeling with nucleotide precision. Despite that, the mRNA of PDB-5NWY was extended at the 5'-end according to the sequence of the construct to provide an approximation of the number of nucleotides stretching from the exit of the stalled to the entry of the collided ribosome. The SmrB model was prepared using AlphaFold 2 (AF2) (39) predictions and Mmseqs2 (72) for multiple sequence alignment of SmrB alone and of SmrB fused to the ribosomal interaction partner uS2 as described in Fig S8. AF2 predictions were performed using an API provided by the Söding lab.

The *E. coli* trisome model was prepared by docking the two copies of the stalled 70S from the disome in the first and second ribosome and one copy of the collided 70S in the third ribosome. The *B. subtilis* disome model was prepared by docking two copies of the MifM-stalled ribosome complex (PDB 3J9W; (64)) into the cryo-EM map.

All model adjustments were performed using coot (73). Structural figures were prepared using ChimeraX (74).

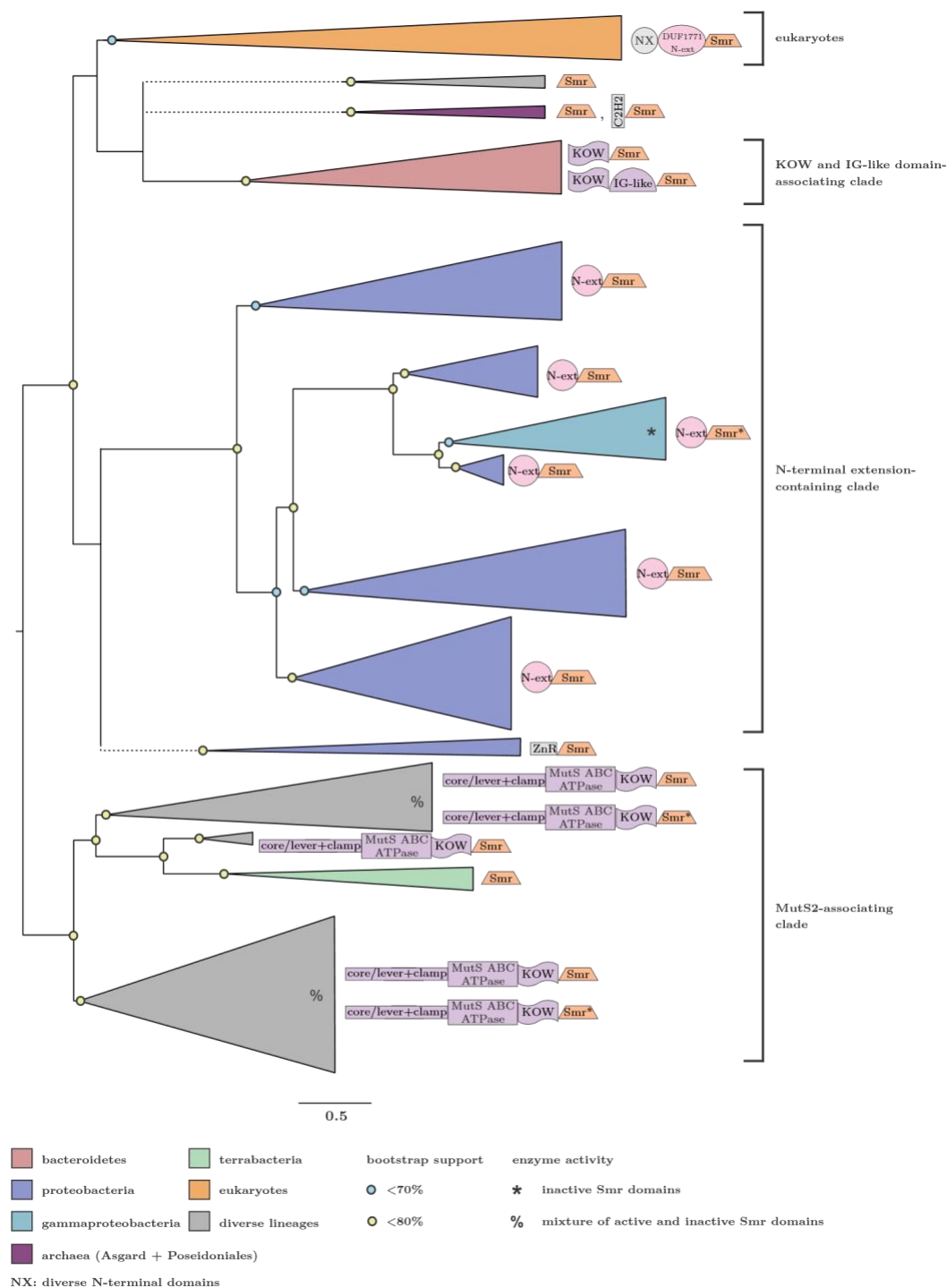
Figure S1



Supplemental Figure 1. SmrB is a general quality control factor

(A) Additional reporters to study ribosome rescue in *E. coli* with various stall motifs. **(B)** The expression of full-length NanoLuc-Ble protein was monitored an anti-FLAG antibody; anti-Strep antibodies reveal both full-length NanoLuc-Ble and truncated NanoLuc proteins. The RpoB protein serves as a loading control.

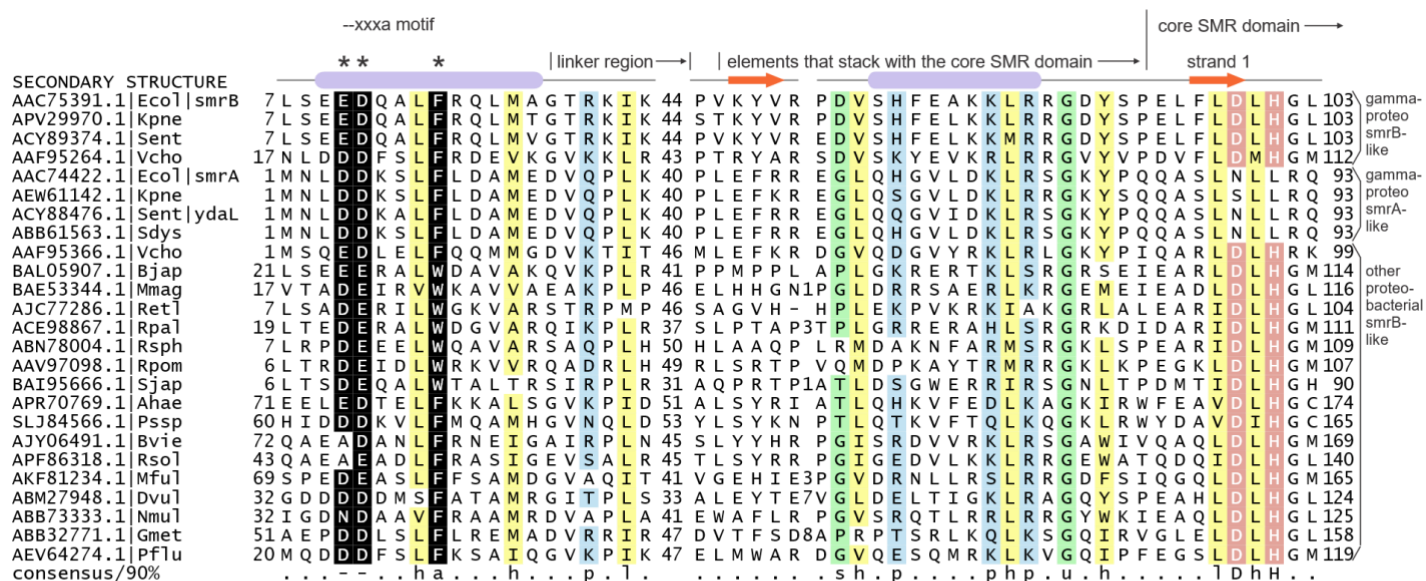
Figure S2



Supplemental Figure 2. Phylogenetic tree of SMR domain proteins

Stylized phylogenetic tree depicting relationships between SMR domain clades. Clades with indicated bootstrap support are marked with circles. Clade names are given to the right of the tree. Dotted lines indicate positions with little or no bootstrap support.

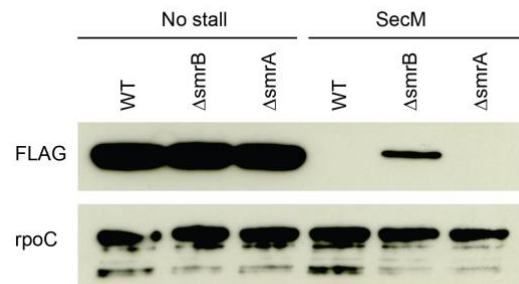
Figure S3



Ecol : Escherichia coli; Kpne : Klebsiella pneumoniae; Sent : Salmonella enterica; Vcho : Vibrio cholerae; Sdys : Shigella dysenteriae; Bjap : Bradyrhizobium japonicum; Mmag : Magnetospirillum magneticum; RetI : Rhizobium etli; Rpal : Rhodopseudomonas palustris; Rsph : Rhodobacter sphaeroides; Rpom : Ruegeria pomeroyi; Sjap : Sphingobium japonicum; Ahae : Acinetobacter haemolyticus; Pssp : Psychrobacter sp; Bvie : Burkholderia vietnamiensis; Rsol : Ralstonia solanacearum; Mful : Myxococcus fulvus; DvuI : Desulfovibrio vulgaris; Nmul : Nitrosospora multiformis; Gmet : Geobacter metallireducens; Pflu : Pseudomonas fluorescens;

Supplemental Figure 3. Multiple alignment of the conserved regions in the N-terminal extension of SMR proteins from proteobacteria. Columns in the alignment are shaded and labeled according to biochemical character: -, negatively charged; h, hydrophobic in yellow; a, aromatic; p, polar in blue; l, aliphatic in yellow; s, small in green; u, tiny in green. Residue positions in the --xxxa motif are colored in white and shaded in black, marked by asterisks above the alignment. Residue positions forming part of the active site of the core SMR domain are colored in white and shaded in red. Sequences are labeled with NCBI accession number and organism abbreviation, abbreviations are provided below alignment. Secondary structure provided at top of alignment. Numbers to left and right of alignment denote positioning of the region. Internal numbers give the size of excised variable insert regions.

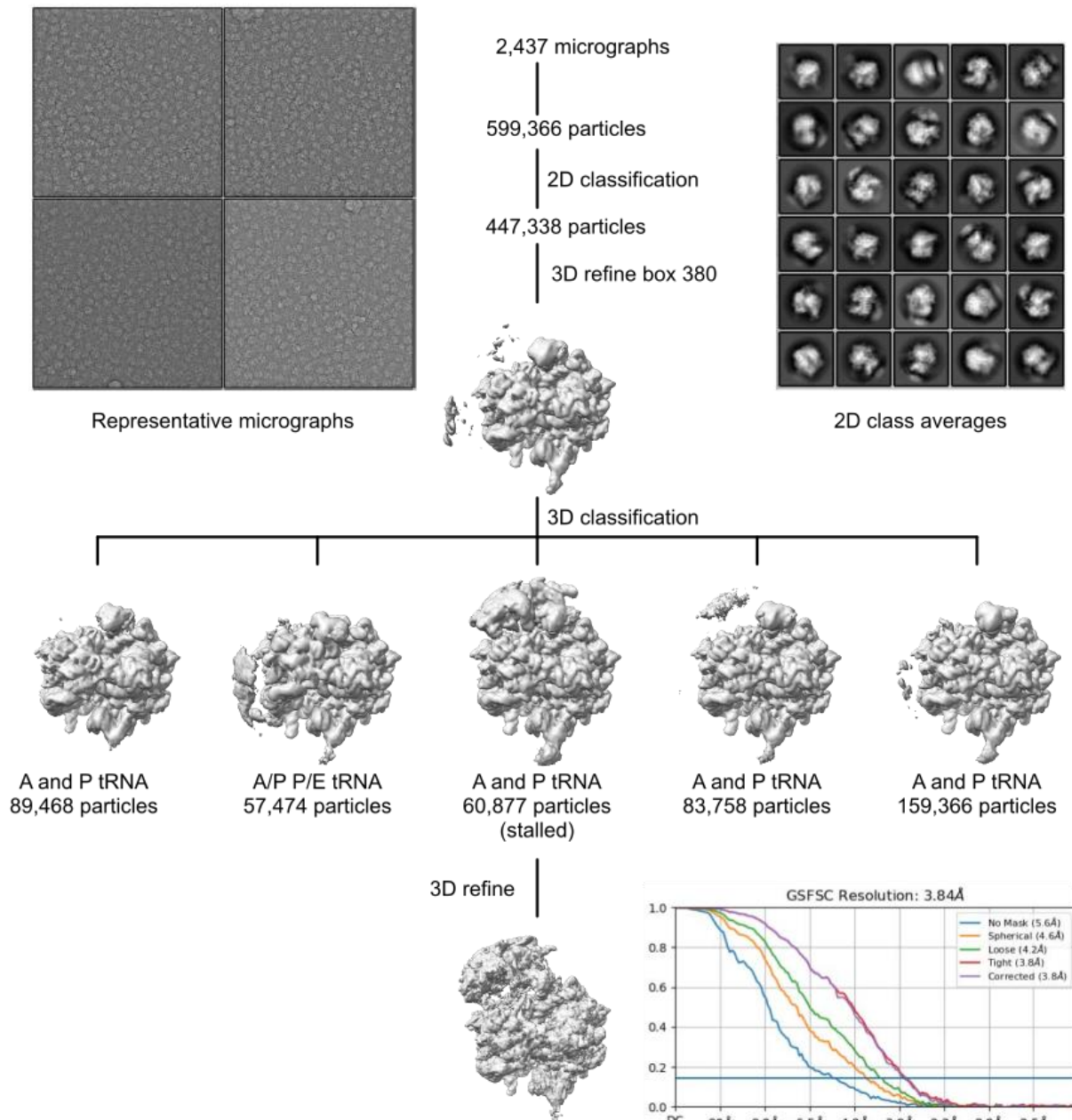
Figure S4.



Supplemental Figure 4. Loss of SmrA does not affect expression of the stalling reporter

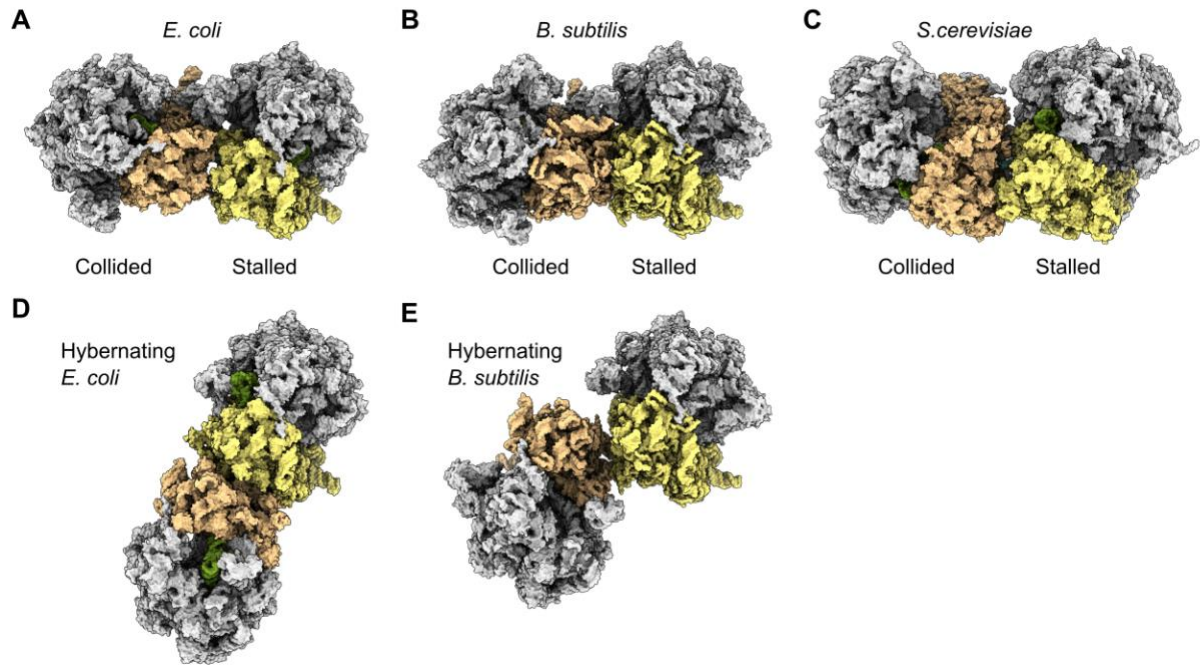
The level of SecM reporter protein was monitored using an anti-FLAG antibody. The RpoC protein serves as a loading control.

Figure S5.



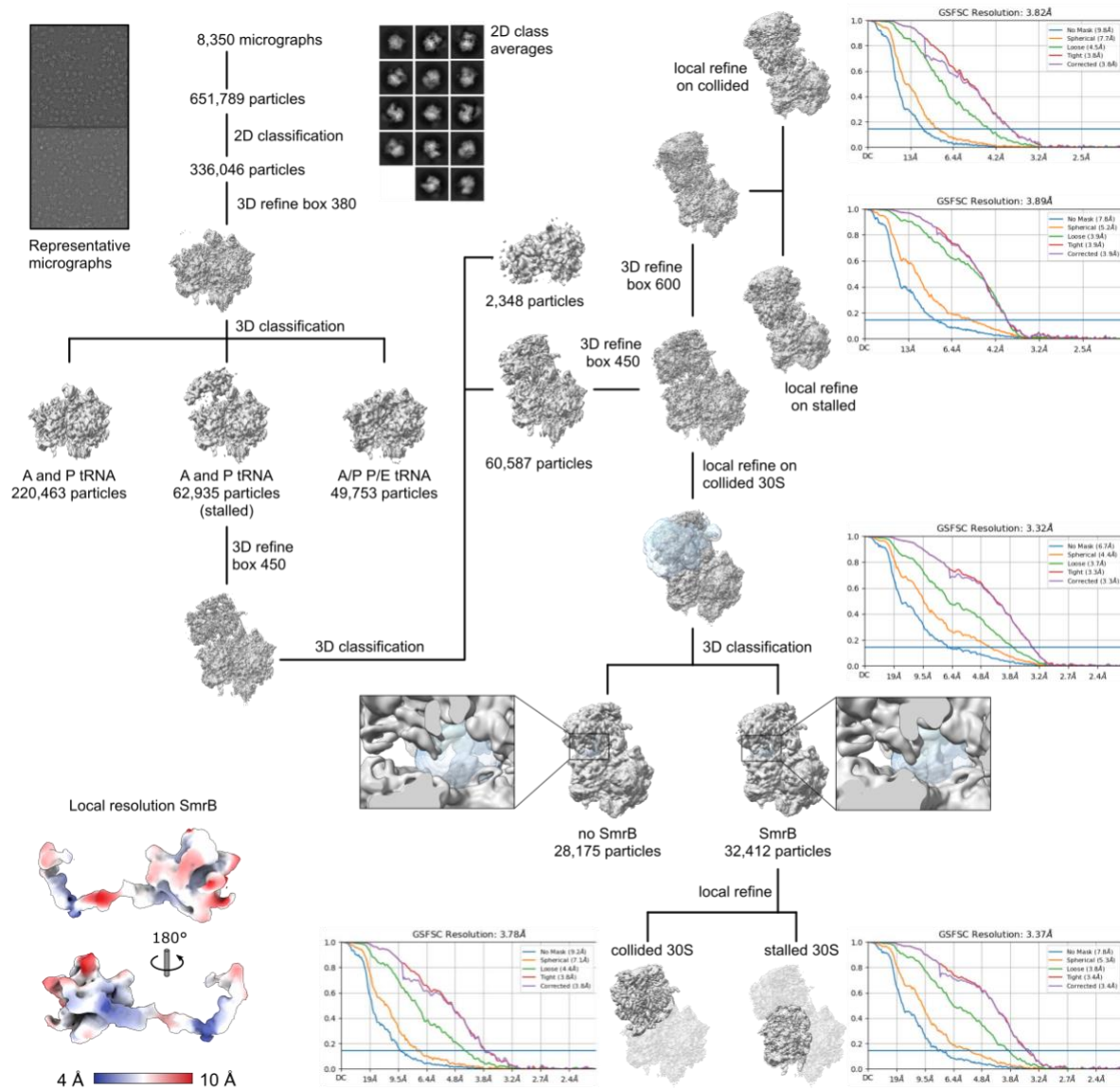
Supplemental Figure 5. Cryo-EM data processing for the *E. coli* disome sample. Shown are the classification scheme, representative micrographs, 2D class averages and the Gold standard Fourier Shell Correlation (GSFSC) curve for the final volume containing the 70S stalled ribosome as well as the 30S of the collided ribosome.

Figure S6



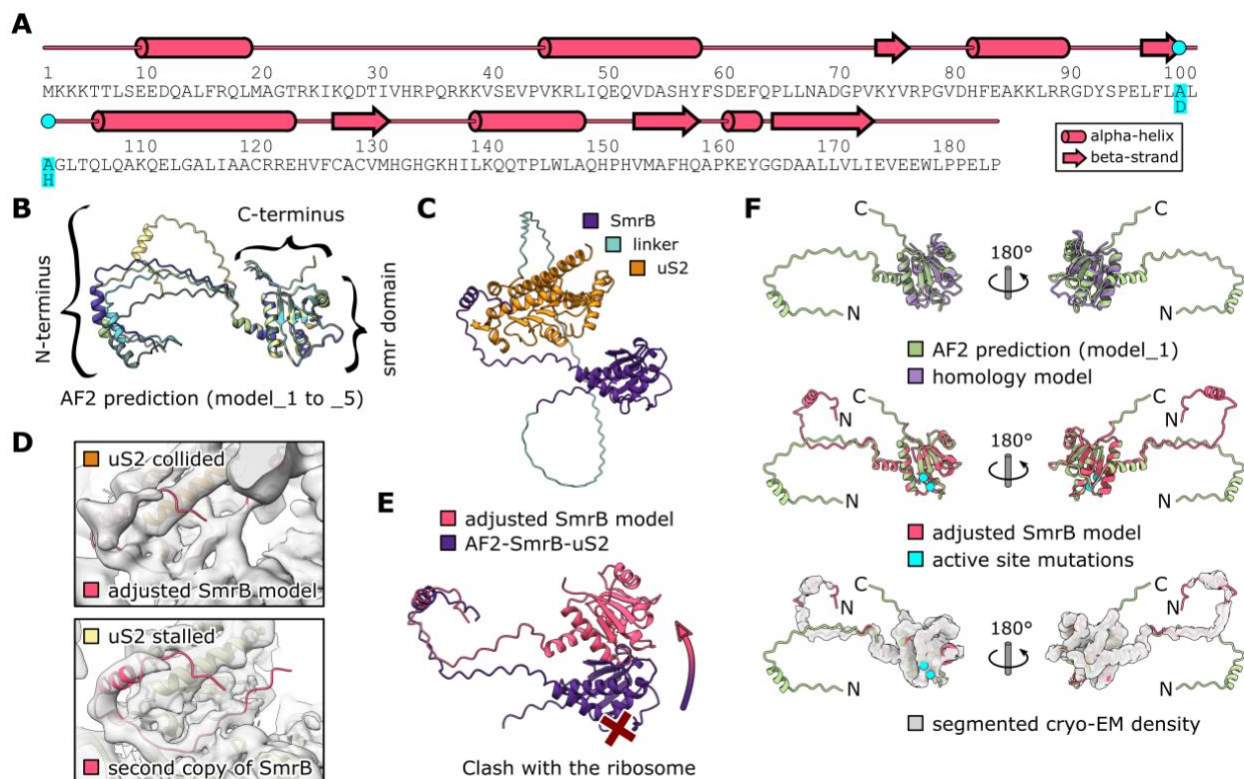
Supplemental Figure 6. Comparison of different disomes. The *E. coli* and *B. subtilis* disomes from ribosome collision are compared to the *S. cerevisiae* ribosome collision disome and hibernation disomes.

Figure S7



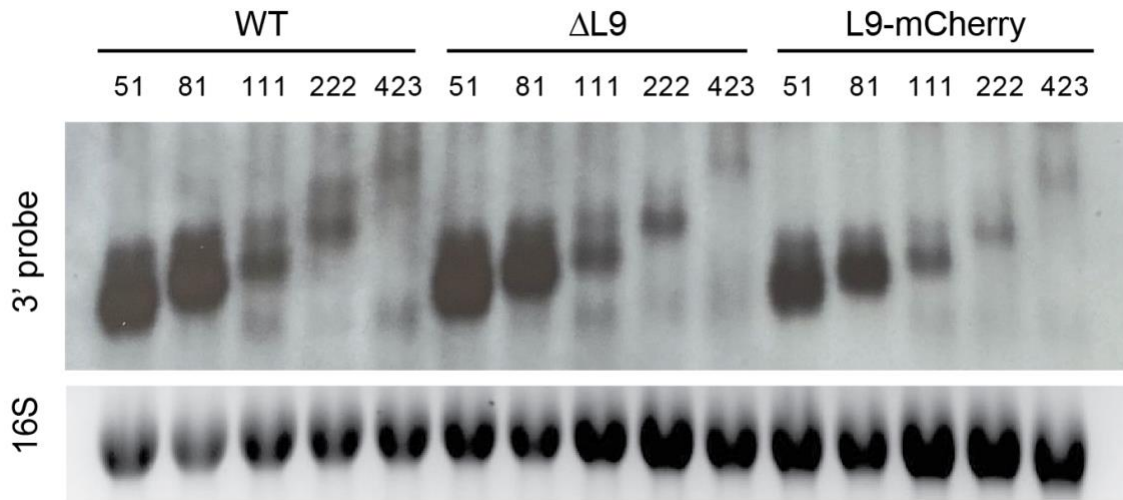
Supplemental Figure 7. Cryo-EM data processing for the *E. coli* disome sample. Shown are the classification scheme, representative micrographs, 2D class averages and the Gold standard Fourier Shell Correlation (GSFSC) curve for the respective 3D reconstructions. The segmented density for SmrB is colored according to local resolution.

Figure S8



Supplemental Figure 8. Structural model of SmrB. (A) Secondary structure of SmrB. The DLH to ALA mutation is indicated. (B) AF2 prediction models 1-5. The SMR domain is predicted with high confidence, while the linker to the N-terminal helix appears flexible. (C) AF2 prediction of the interaction between SmrB and uS2. For this prediction uS2 was fused to the C-terminus of SmrB with a glycine serine linker (39 copies of GS). The prediction shows the N-terminal helix of SmrB folded back onto uS2. (D) Top: Cryo-EM density and adjusted model of the SmrB. Bottom: Cryo-EM density and rigid body docked model of the N-terminus of SmrB from the collided 30S onto the stalled 30S. A second copy of SmrB was found anchored to uS2 of the stalled ribosome. However, there was no density for the SMR domain of the second SmrB, indicating a high degree of flexibility due to the lack of another ribosome in front of the stalled one. (E) Adjustment of the AF2 predicted model of SmrB-uS2. Without adjustment according to the cryo-EM density (as shown in D) the SMR domain would clash with the ribosome. (F) Comparison of the AF2 prediction, the homology model and the adjusted model of SmrB. Compared to the AF2 prediction, the homology model is missing the two N-terminal helices and most of the loops are slightly different (top). The AF2 prediction almost perfectly matched the cryo-EM density map and the corresponding adjusted model (middle and bottom). Only the catalytic loop (carrying the active site mutations) had to be slightly adjusted to prevent clashes with the mRNA. The N-terminus was adjusted as discussed above.

Figure S9



Supplemental Figure 9. RNA processing via collision is independent of the L9 bridge

Northern blots using the 3'-probe against the CRP reporters with the short SecM stalling motif in wild-type cells, L9-deletion strain (Δ L9), and a strain where mCherry is fused to the C-terminus of L9 (L9-mCherry). Ethidium bromide staining of 16S rRNA serves as a loading control.

Supplemental References

51. Q. Chai *et al.*, Organization of Ribosomes and Nucleoids in Escherichia coli Cells during Growth and in Quiescence. *Journal of Biological Chemistry* **289**, 11342-11352 (2014).
52. K. A. Datsenko, B. L. Wanner, One-step inactivation of chromosomal genes in Escherichia coli K-12 using PCR products. *Proceedings of the National Academy of Sciences of the United States of America* **97**, 6640-6645 (2000).
53. A. Cramer, E. A. Whitehorn, E. Tate, W. P. C. Stemmer, Improved green fluorescent protein by molecular evolution using DNA shuffling. *Nature Biotechnology* **14**, 315-319 (1996).
54. H. S. Jiang, R. Lei, S. W. Ding, S. F. Zhu, Skewer: a fast and accurate adapter trimmer for next-generation sequencing paired-end reads. *Bmc Bioinformatics* **15**, (2014).
55. B. Langmead, C. Trapnell, M. Pop, S. L. Salzberg, Ultrafast and memory-efficient alignment of short DNA sequences to the human genome. *Genome Biology* **10**, (2009).
56. S. F. Altschul *et al.*, Gapped BLAST and PSI-BLAST: a new generation of protein database search programs. *Nucleic Acids Research* **25**, 3389-3402 (1997).
57. S. R. Eddy, A new generation of homology search tools based on probabilistic inference. *Genome Informatics. International Conference on Genome Informatics* **23**, 205-211 (2009).
58. R. D. Finn *et al.*, The Pfam protein families database: towards a more sustainable future. *Nucleic Acids Research* **44**, D279-D285 (2016).
59. T. Lassmann, O. Frings, E. L. L. Sonnhammer, Kalign2: high-performance multiple alignment of protein and nucleotide sequences allowing external features. *Nucleic Acids Research* **37**, 858-865 (2009).
60. C. Cole, J. D. Barber, G. J. Barton, The Jpred 3 secondary structure prediction server. *Nucleic Acids Research* **36**, W197-W201 (2008).
61. M. N. Price, P. S. Dehal, A. P. Arkin, FastTree 2-Approximately Maximum-Likelihood Trees for Large Alignments. *PloS One* **5**, (2010).
62. A. Shevchenko, M. Wilm, O. Vorm, M. Mann, Mass spectrometric sequencing of proteins from silver stained polyacrylamide gels. *Analytical Chemistry* **68**, 850-858 (1996).
63. F. Mohammad, A. Buskirk, Protocol for Ribosome Profiling in Bacteria. *Bio-Protocol* **9**, (2019).
64. D. Sohmen *et al.*, Structure of the Bacillus subtilis 70S ribosome reveals the basis for species-specific stalling. *Nature Communications* **6**, (2015).
65. H. Schafer *et al.*, The alarmones (p)ppGpp are part of the heat shock response of Bacillus subtilis. *Plos Genetics* **16**, (2020).
66. S. Q. Zheng *et al.*, MotionCor2: anisotropic correction of beam-induced motion for improved cryo-electron microscopy. *Nature Methods* **14**, 331-332 (2017).
67. A. Rohou, N. Grigorieff, CTFFIND4: Fast and accurate defocus estimation from electron micrographs. *Journal of Structural Biology* **192**, 216-221 (2015).
68. J. Zivanov, T. Nakane, S. H. W. Scheres, Estimation of high-order aberrations and anisotropic magnification from cryo-EM data sets in RELION-3.1. *Iucrj* **7**, 253-267 (2020).
69. A. Punjani, J. L. Rubinstein, D. J. Fleet, M. A. Brubaker, cryoSPARC: algorithms for rapid unsupervised cryo-EM structure determination. *Nature Methods* **14**, 290-+ (2017).

70. A. B. Loveland, G. Demo, A. A. Korostelev, Cryo-EM of elongating ribosome with EF-Tu center dot GTP elucidates tRNA proofreading. *Nature* **584**, 640-+ (2020).
71. R. T. Byrne, A. L. Konevega, M. V. Rodnina, A. A. Antson, The crystal structure of unmodified tRNA(Phe) from Escherichia coli. *Nucleic Acids Research* **38**, 4154-4162 (2010).
72. M. Mirdita, M. Steinegger, J. Soding, MMseqs2 desktop and local web server app for fast, interactive sequence searches. *Bioinformatics* **35**, 2856-2858 (2019).
73. P. Emsley, K. Cowtan, Coot: model-building tools for molecular graphics. *Acta Crystallographica Section D-Structural Biology* **60**, 2126-2132 (2004).
74. T. D. Goddard *et al.*, UCSF ChimeraX: Meeting modern challenges in visualization and analysis. *Protein Science* **27**, 14-25 (2018).